

STUDY OF THE DYNAMICAL AND MORPHOLOGICAL PROPERTIES OF MASSIVE STARS WITH HIGH ANGULAR RESOLUTION TECHNIQUES



Universidad de Granada

Programa de Doctorado en Física y Ciencias del Espacio

Tesis Doctoral

memoria presentada al Departamento de Física Teórica y del Cosmos de la Universidad
de Granada para optar al grado de **Doctor en Física y Ciencias del Espacio**.

por

Joel SÁNCHEZ BERMÚDEZ

Directores

Dr. Antonio Alberdi Odriozola

Dr. Rainer Schödel



Abril, 2015
Granada, España

This thesis has been approved by the supervisors:

Prof. Dr. A. Alberdi and **Dr. R. Schödel**

from the Instituto de Astrofísica de Andalucía (IAA-CSIC)

Front & Back: Artistic representation of an interferogram recorded with sparse aperture masking observations.

Copyright © 2015 by J. Sánchez Bermúdez

ISBN 000-00-0000-000-0

An electronic version of this dissertation is available through direct request to: joel@iaa.es

DECLARACIÓN

El doctorando **Joel Sánchez Bermúdez** y los directores de la tesis, **Dr. Antonio Alberdi Odriozola** y **Dr. Rainer Schödel**, garantizamos, al firmar esta tesis doctoral, que el trabajo ha sido realizado por el doctorando bajo la dirección de los directores de la tesis y, hasta donde nuestro conocimiento alcanza, en la realización del trabajo se han respetado los derechos de otros autores a ser citados cuando se han utilizado sus resultados o publicaciones.

Joel Sánchez Bermúdez

El doctorando

Dr. Antonio Alberdi Odriozola

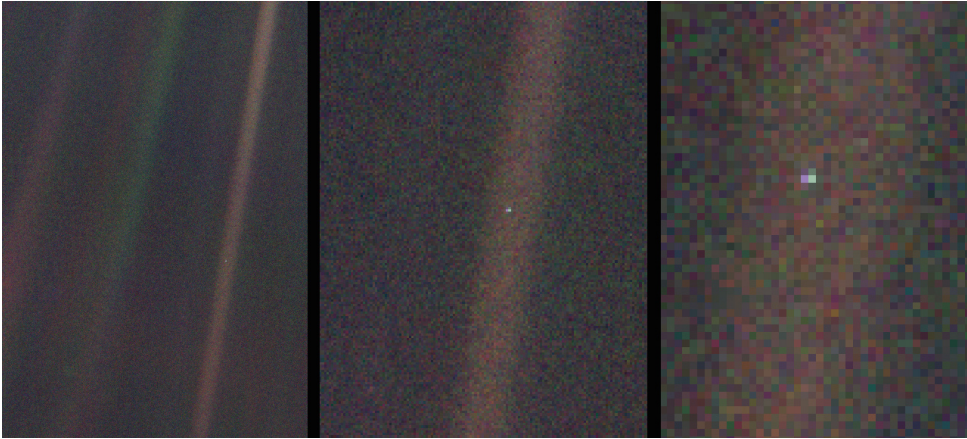
Tutor

Dr. Rainer Schödel

Tutor

Granada, 30 de abril de 2015.

PRÓLOGO



LA nave espacial Voyager 1 se encontraba muy lejos de casa, más allá de la órbita del planeta más exterior y muy por encima del plano de la eclíptica, una superficie plana imaginaria, algo así como una pista, en la que generalmente se hallan confinadas las órbitas de los planetas. El Voyager 1 se alejaba del Sol a 65000 kilómetros por hora. Pero a principios de febrero de 1990 recibió un mensaje urgente de la Tierra.

El buen funcionamiento de los Voyager sólo estaba garantizado hasta que efectuaran su encuentro con Saturno. Se me ocurrió que podía ser una buena idea que, una vez que éste se hubiera producido, echaran un último vistazo en dirección a la Tierra. Yo sabía que desde Saturno la Tierra se vería demasiado pequeña como para que el Voyager pudiera percibir detalles. Nuestro planeta aparecería como un mero punto de luz, un pixel solitario, apenas distinguible de los otros muchos puntos de luz visibles, planetas cercanos y soles remotos. Pero precisamente por la oscuridad de nuestro mundo puesta así de manifiesto, podía valer la pena disponer de esa imagen.

Me pareció que otra instantánea de la Tierra, como la icónica imagen obtenida por el Apolo 17 en el último viaje del hombre a la Luna, esta vez desde una distancia cien mil veces superior, podía ser útil en el constante proceso de revelarnos a nosotros mismos nuestra verdadera circunstancia y condición. Los científicos y filósofos de la antigüedad

clásica habían comprendido correctamente que la Tierra es un mero punto en la inmensidad del cosmos, pero nadie la había visto nunca como tal. Esa era nuestra primera oportunidad (y quizá también la última en décadas y décadas).

De modo que aquí están, un mosaico de cuadrados colocados sobre los planetas y un esbozo de lo que son las estrellas más distantes. Como consecuencia del reflejo de la luz solar de la nave hacia la Tierra, ésta parece envuelta en un haz de luz, como si ese pequeño mundo tuviera algún significado especial. Pero se trata solamente de un accidente achacable a la geometría y a la óptica. Desde la distancia, los planetas parecen sólo puntos de luz, con manchas o sin ellas, incluso a través del telescopio de alta resolución instalado a bordo del Voyager. Son como los planetas observados a simple vista desde la superficie de la Tierra, puntos luminosos más brillantes que la mayoría de estrellas. Con sólo mirar uno de esos puntos no somos capaces de decir lo que albergan, cuál ha sido su pasado y si, en esta época concreta, vive alguien allí.

Desde esa posición tan alejada puede parecer que la Tierra no reviste ningún interés especial. Pero para nosotros es distinta. Echemos otro vistazo a ese punto. Ahí está. Es nuestro hogar. Somos nosotros. Sobre él ha transcurrido y transcurre la vida de todas las personas a las que queremos, la gente que conocemos o de la que hemos oído hablar y, en definitiva, de todo aquel que ha existido. En ella conviven nuestra alegría y nuestro sufrimiento, miles de religiones, ideologías y doctrinas económicas, cada cazador y recolector, cada héroe y cobarde, cada creador y destructor de civilizaciones, cada rey y cada campesino, cada joven pareja de enamorados, cada madre y padre, cada niño ilusionado, inventores y exploradores, cada profesor de ética, cada político corrupto, cada “superestrella”, cada “líder supremo”, cada santo y cada pecador de toda la historia de nuestra especie vivió ahí: sobre una mota de polvo suspendida en un haz de luz solar.

La Tierra constituye solo una pequeña fase en medio de la vasta arena cósmica. Pensemos en los ríos de sangre derramada por tantos generales y emperadores con el único fin de convertirse, tras alcanzar el triunfo y la gloria, en dueños momentáneos de una fracción del punto. Pensemos en las interminables crueldades infligidas por los habitantes de un rincón de ese pixel a los moradores de algún otro rincón apenas distinguible. Cuán frecuentes sus malentendidos, cuán avidos están por matarse unos a otros, cuán ferviente su odio. Nuestros posicionamientos, la importancia que nos auto atribuimos, nuestra errónea creencia de que ocupamos una posición privilegiada en el universo, todo es puesto en tela de juicio por ese pequeño punto de pálida luz. Nuestro planeta no es más que una solitaria mota de polvo en la gran envoltura de la oscuridad cósmica. Y en nuestra oscuridad, en medio de esa inmensidad, no hay ningún indicio de que vaya a llegar ayuda de algún lugar capaz de salvarnos de nosotros mismos.

La Tierra es el único mundo hasta hoy conocido que alberga vida. No existe otro lugar a donde pueda emigrar nuestra especie, al menos en un futuro próximo. Visitar otros mundos es posible, pero no lo es establecernos en ellos. Nos guste o no, la

Tierra es, por el momento, nuestro único hábitat. Se ha dicho en ocasiones que la Astronomía es una experiencia de humildad y que imprime carácter. Quizá no haya mejor demostración de la locura de la vanidad humana que esa imagen a distancia de nuestro minúsculo mundo. En mi opinión, subraya nuestra responsabilidad de tratarnos mejor unos a otros, y preservar y amar nuestro punto azul pálido, el único hogar que conocemos.

The Pale Blue Dot
Carl Sagan (1934-1996)

AGRADECIMIENTOS

LEGAR a la conclusión de este trabajo doctoral ha sido un largo viaje, principalmente porque el deseo de estudiar Astronomía ha estado presente durante prácticamente toda mi vida. Desde mi infancia en aquella biblioteca, en donde leí mis primeros libros sobre las estrellas y donde prácticamente crecí, hasta mi llegada a Granada, cuando finalmente comencé a formarme profesionalmente como astrónomo.

Me gustaría agradecer a mis tutores, Antxon Alberdi y Rainer Schödel, por darme la oportunidad de realizar este sueño, por confiar en mí, por su paciencia, y por ser mis dos grandes maestros. Muchas gracias Antxon por tu amabilidad y ser un guía tanto profesional como personal estos años. Muchas gracias Rainer por compartir tu talento, por corregir mis errores y por ser un gran amigo. I am very grateful with you, Christian Hummel, for all your kindness and for sharing always you knowledge with me. Thank you for teaching me to be cautious and professional. También agradezco a mis colegas quienes con el tiempo se volvieron grandes amigos. En especial a Roberto Galván y Gráinne Costigan por su complicidad, por nuestras charlas científicas y por aguantarme en mis momentos de flaqueza, Vielen Dank. También quiero dar un sincero agradecimiento a todos mis compañeros del IAA y de la ESO, será un gusto encontrarnos nuevamente.

Una parte fundamental de este logro se lo debo a mis padres, Toribio y Paula, por enseñarme que la educación es lo más importante, y por haberme dado la lección más simple y profunda de mi vida: ser perseverante. Agradezco a mis hermanos, Anahí, Juan Carlos y Sergio, por aguantar mis locuras y por motivarme a ser un buen hermano mayor. A mi abuelita Marce, por enseñarme a escuchar y a observar la vida, muchas gracias donde quiera que estés. A mi tía Juanita por darme siempre ánimos para seguir adelante sin olvidarme de disfrutar del camino, como quien sube una montaña. A mi prima Carmen por ser mi hermana mayor y por su firme fe en mí. Ricardo, Arturo, Eduardo, Pepe, Eder y Carlos: gracias por aligerar el viaje y hacerlo más divertido, aún a la distancia.

Finalmente, agradezco a la persona quien me ayuda a recordar que la ciencia es mi pasión, quien me da fuerza para no dudar de mi mismo, a mi familia que todos los días hace de mi realidad un sueño, a mi esposa, Ana Laura, a ella le dedico esta tesis.

*Joel Sánchez Bermúdez
Granada, abril 2015.*

RESUMEN

NUESTRAS vidas están íntimamente relacionadas a las estrellas. Desde la luz que recibimos del Sol cada día, hasta el hecho de que la mayoría de los elementos en nuestra composición química fueron formados en el interior de las mismas. Entre los diferentes tipos de estrellas que conocemos, hay uno que es de especial relevancia debido a su rol clave en la evolución de las galaxias. Estas son “las estrellas masivas”. El término “masivas” se debe a que este tipo de estrellas tienen al menos ocho veces la masa del Sol. Esta condición hace que evolucionen rápidamente y que sus vidas duren solo unos pocos millones de años, comparadas con los miles de millones de años que viven las estrellas de baja masa.

Las estrellas masivas son raras y difíciles de observar con respecto a sus hermanas de baja masa. Por ejemplo, asumiendo una función inicial de masa de tipo Salpeter, por cada estrella que nace con una masa entre 64 y 128 masas solares, nacen más de 100 estrellas como el Sol. Lo cual significa que entre más masiva es la estrella más rara es la misma. Además de esto, las estrellas de alta masa se forman en las regiones más densas de las nubes moleculares. Así pues, sus fases iniciales pueden ser observadas solo en casos excepcionales, generalmente debido a que se encuentran envueltas por gas molecular denso y por polvo desde el momento inicial de su vida, y hasta que llegan a la secuencia principal. Además de que este tipo de estrellas son raras, las nubes moleculares en las que se forman se localizan a distancias mayores a 1 kpc. Por lo tanto, investigar este tipo de estrellas requiere de instrumentos con la mayor resolución angular posible.

Estas condiciones establecen una restricción importante en nuestro entendimiento sobre la formación de dichas estrellas. En años recientes, se ha hecho un importante trabajo teórico para explicar los posibles mecanismos de la formación de las estrellas masivas. Algunas de las teorías contemporáneas más aceptadas sugieren que las estrellas de alta masa se forman a través de discos de acreción, de forma semejante a las estrellas de baja masa. Sin embargo, estas predicciones teóricas necesitan ser confirmadas por pruebas observacionales.

No solamente las fases iniciales de las estrellas masivas son de interés. Durante toda su vida estos cuerpos son los precursores de fenómenos físicos que requieren estudio.

Por ejemplo, poseen fuertes vientos estelares con velocidades de hasta 10^3 km/s, y altas tasas de pérdida de masa (10^{-5} - 10^{-3} M_{\odot} /año). Esto significa que las estrellas de alta masa pueden interactuar fuertemente con el medio interestelar. En algunos sistemas binarios evolucionados, el intercambio de material producido por la pérdida de masa favorece la creación de ambientes ricos en polvo. Por otra parte, uno de los fenómenos más interesantes relacionados con las estrellas masivas es el de su muerte, que ocurre en forma de la explosión de una supernova, permitiendo el enriquecimiento del medio interestelar, estimulando o inhibiendo futuros procesos de formación estelar.

Otra característica observacional notable en este tipo de estrellas es el alto número de ellas que pertenecen a sistemas múltiples. Mientras solo el 30-40% de las estrellas de tipo solar pertenecen a un sistema múltiple, alrededor del 70-90% de las estrellas masivas forman parte de sistemas múltiples (desde sistemas binarios hasta múltiples jerárquicos). Esta propiedad establece importantes condiciones en los posibles escenarios de formación.

Gracias al surgimiento de técnicas de alta resolución angular en el infrarrojo, durante las últimas décadas, se ha logrado un importante progreso en el entendimiento de la física de las estrellas masivas. Por ejemplo, la óptica adaptativa, la interferometría óptica (tanto en la forma de *Sparse Aperture Masking* como de interferometría de larga base), y el incremento en la sensibilidad y resolución angular de los nuevos telescopios milimétricos. A longitudes de onda del infrarrojo existen importantes restricciones para realizar observaciones de alta resolución y sensibilidad desde la Tierra. Esto se debe principalmente al efecto de la atmósfera que deteriora la calidad de los frentes de onda observados, y a restricciones tecnológicas como el limitado número de actuadores y sensores usados para corregir las distorsiones atmosféricas.

El objetivo de esta tesis doctoral es el estudio de las estrellas masivas a través de técnicas de alta resolución angular en el infrarrojo. En particular, se hace uso de interferometría óptica en la forma de *Sparse Aperture Masking* y de larga base. Esas técnicas nos permiten observar objetos astronómicos combinando varios telescopios para lograr la máxima resolución angular posible. Esta resolución es proporcional a la distancia que existe entre los diferentes telescopios usados para una longitud de onda dada. Todos los estudios que aquí se presentan, se realizaron con los instrumentos del Observatorio Europeo Austral, que cuenta con el mayor interferómetro óptico del mundo: El Very Large Telescope Interferometer (VLTI). En este trabajo, se han abordado tres grandes problemas en el estudio de las estrellas masivas: a) el estudio de sus fases iniciales, b) el rol de la multiplicidad, y c) las interacciones de este tipo de estrellas con el medio interestelar.

Esta tesis esta compuesta de siete capítulos. En el primero de ellos se da una breve introducción sobre la misma. En el segundo capítulo se describen las diferentes técnicas observacionales utilizadas, prestando especial atención a la interferometría óptica.

El modelado de la función de transferencia de un interferómetro de tipo Fizeau es descrito también en este capítulo. Del capítulo tres al capítulo cinco se presentan los principales tópicos de investigación de esta tesis. Éstos incluyen los datos, los análisis y los resultados descritos en cuatro publicaciones arbitradas. A continuación se describen los tópicos:

La formación de estrellas masivas: Las teorías modernas de la formación de estrellas masivas sugieren la presencia de discos en el núcleo de los objetos masivos jóvenes. Sin embargo, esas estructuras han sido elusivas para los objetos más masivos. En este capítulo se presenta el estudio del objeto masivo: NGC 3603 IRS 9A* con la cámara infrarroja de alta resolución angular NACO del Very Large Telescope (VLT). Dichas observaciones se realizaron en el modo interferométrico de NACO, a través de la técnica conocida como *Sparse Aperture Masking*. Adicionalmente, se analizaron datos espectroscópicos con CRILES/VLT. Nuestros resultados, a través de modelos de transferencia radiativa, confirman la presencia de una componente compacta en el núcleo de IRS 9A, previamente propuesta por observaciones interferométricas en el infrarrojo medio. Adicionalmente, nuestros datos confirman la existencia de una envoltura alrededor de la componente compacta observada previamente. Modelos simultáneos a los datos interferométricos obtenidos y a la distribución espectral de esta fuente ponen de manifiesto la complejidad morfológica de IRS 9A. Lo cual enfatiza la necesidad de obtener datos de alta resolución angular a longitudes de onda adicionales, desde el infrarrojo hasta longitudes de onda de radio.

Multiplicidad en estrellas masivas: Esta tesis presenta el estudio, utilizando interferometría óptica de larga base, de dos sistemas múltiples masivos: HD 150 136 y Herschel 36. Observaciones espectroscópicas de ambos sistemas sugieren que éstos están formados por tres componentes atadas gravitacionalmente de manera jerárquica. Dos de ellas pertenecientes a una binaria espectroscópica y otra más localizada a una distancia mayor. HD 150 136 es un sistema extremadamente masivo, con una masa total estimada en más de 100 masas solares. Además de ello, una de las componentes que lo integran es una estrella de tipo O3 V, lo que significa que este sistema es muy joven con una edad de alrededor de un par millones de años. Por otro lado, Herschel 36 es un sistema joven con tres estrellas cuya luminosidad combinada parece corresponder a la de tres estrellas clasificadas como *Zero-age main-sequence*. Lo anterior sugiere que la edad de este sistema es de alrededor de un millón de años. Nuestras observaciones interferométricas en los filtros *J*, *H* y *K* con el instrumento AMBER del VLTI, resolvieron, por primera vez, la componente aislada adicional al sistema espectroscópico, tanto para HD 150 136 como para Herschel 36. Esto permitió determinar la posición proyectada de las componentes (de cada sistema múltiple) en el plano del cielo, su brillo relativo, así como dar una primera aproximación de su órbita.

Interacciones de las estrellas masivas con el medio interestelar: Aquí se presenta el

estudio de la morfología de las estrellas masivas que interactúan con los brazos de polvo y gas en el parsec central de la Galaxia: IRS 1W, IRS 5, IRS 10W, y IRS 21. La interacción entre el movimiento relativo de estas estrellas, y el choque de sus vientos estelares con el medio interestelar generan la formación de estructuras tipo *bow shock* alrededor de estos objetos. Para esta investigación, se utilizaron observaciones infrarrojas en el filtro L' con *Sparse Aperture Masking*, en combinación con observaciones asistidas por Óptica Adaptativa en los filtros H y Ks . Dichas observaciones junto con modelos de transferencia radiativa permitieron obtener la posición tridimensional y la geometría de los *bow shocks*. Además se investigaron los mecanismos responsables de la emisión infrarroja de las estructuras tipo *bow shocks*, y se determinaron los planos orbitales de las estrellas analizadas alrededor del agujero negro masivo SgrA*.

Finalmente, los capítulos seis y siete presentan las conclusiones generales y las futuras líneas de investigación de esta tesis.

CONTENTS

| | |
|---------------------------------------------------------------------------------|--------------|
| List of Figures | xxi |
| List of Tables | xxiii |
| Glossary | xxv |
| 1 Introduction | 1 |
| 2 High angular resolution techniques | |
| Stellar interferometry | 5 |
| 2.1 Interferometry in context | 5 |
| 2.2 Basic concepts of Interferometry | 8 |
| 2.2.1 The effect of the atmosphere on the interferometric observables | 9 |
| 2.3 Long-baseline interferometry | 11 |
| 2.4 Sparse Aperture Masking with Adaptive Optics | 14 |
| 2.4.1 Adaptive Optics | 14 |
| 2.4.2 Sparse Aperture Masking. | 15 |
| 2.5 Image reconstruction in optical interferometry | 22 |
| 3 The formation of massive stars | |
| The case of NGC 3603 IRS9A* | 35 |
| 3.1 Introduction: How are stars formed? | 37 |
| 3.1.1 Basic considerations | 37 |
| 3.1.2 Models of massive star formation | 38 |
| 3.1.3 Disks and envelopes in massive young stellar objects | 41 |
| 3.2 The MYSO NGC3603 IRS 9A* | 44 |
| 3.3 Observations and data reduction | 45 |
| 3.3.1 Sparse aperture masking data. | 45 |
| 3.3.2 CRIRES data | 48 |
| 3.4 Analysis and results | 49 |
| 3.4.1 The core of IRS 9A | 49 |
| 3.4.2 H ₂ and Bry spectroastrometric signals | 50 |
| 3.4.3 Radiative transfer model of IRS 9A | 54 |
| 3.5 Discussion | 59 |
| 3.6 Conclusions | 62 |

| | | |
|----------|-------------------------------------------------------------------------------------------|------------|
| 4 | Multiplicity in massive stars | |
| | The case of Herschel 36 and HD 150 136 | 65 |
| 4.1 | Introduction | 66 |
| 4.1.1 | Formation mechanisms of massive multiple systems | 67 |
| 4.1.2 | High-angular resolution techniques to study massive multiple systems | 69 |
| 4.2 | Herschel 36 | 71 |
| 4.3 | Herschel 36: observations and data reduction | 73 |
| 4.4 | Herschel 36: analysis and results | 74 |
| 4.5 | Herschel 36: discussion and conclusion | 77 |
| 4.6 | HD 150 136 | 78 |
| 4.7 | HD 150 136: observations and data reduction | 79 |
| 4.8 | HD 150 136: analysis | 80 |
| 4.9 | HD 150 136: results and discussion | 82 |
| 5 | Massive stars at the Galactic center | |
| | The bow shocks in the mini-spiral | 87 |
| 5.1 | Introduction | 88 |
| 5.2 | Observations and data reduction | 92 |
| 5.2.1 | AO imaging | 92 |
| 5.2.2 | Observations with sparse aperture masking | 94 |
| 5.2.3 | Extraction and calibration of the interferometric observables from the SAM data | 95 |
| 5.2.4 | SAM image reconstruction | 97 |
| 5.3 | Proper motions | 97 |
| 5.4 | Modeling the bow shocks | 99 |
| 5.4.1 | Bow-shock images | 99 |
| 5.4.2 | Bow-shock shape | 99 |
| 5.4.3 | Bow-shock emission | 101 |
| 5.4.4 | Bow-shock fitting | 103 |
| 5.4.5 | Contribution from dust scattering to the bow-shock emission | 105 |
| 5.4.6 | Properties of the individual sources | 106 |
| 5.5 | ISM velocity field and bow-shock orbital parameters | 112 |
| 5.5.1 | Northern Arm dust motion | 112 |
| 5.5.2 | Orbital motion of the bow-shock sources | 115 |
| 5.6 | Discussion and conclusions | 116 |
| 6 | Conclusions | 121 |
| 7 | Future work | 125 |
| A | Galactic Center orbits and proper motions (appendix) | 129 |
| A.1 | Proper motion measurements | 129 |

| | |
|-------------------------------------------------------------------|-----|
| A.2 Thiele-Innes method to determine orbital parameters | 129 |
|-------------------------------------------------------------------|-----|

LIST OF FIGURES

| | | |
|------|--------------------------------------------------------------------------------------------------------------------------------|----|
| 2.1 | Double-slit experiment | 8 |
| 2.2 | Comparison of the variance between phases and closure phases for a point-like source | 11 |
| 2.3 | Beam combination schemes | 12 |
| 2.4 | Delay line layout | 13 |
| 2.5 | VLTI layout | 14 |
| 2.6 | Comparison of Galactic center observations with and without AO | 15 |
| 2.7 | Sparse Aperture Masking layout. | 16 |
| 2.8 | Simulation of the SAM PSF in the detector of a given instrument | 17 |
| 2.9 | Interferometric SAM arrays, interferograms, and mutual transfer functions | 20 |
| 2.10 | Sparse Aperture Masking remapping pupil | 21 |
| 2.11 | Mapping spatial frequencies into the frequency space | 24 |
| 2.12 | Components of the dirty image | 25 |
| 2.13 | Components of the CLEAN algorithm | 26 |
| 2.14 | Comparison between regularizers | 29 |
| 2.15 | 2014 Beauty contest images | 32 |
| | | |
| 3.1 | Star formation in Orion: a picture of its structure at different spatial scales. | 36 |
| 3.2 | Kelvin-Helmholtz timescale as function of the stellar mass | 38 |
| 3.3 | Snapshot of massive star formation, assuming monolithic collapse. | 39 |
| 3.4 | Snapshot of massive star formation, assuming competitive accretion. | 40 |
| 3.5 | Accretion-time scale as function of the stellar mass | 41 |
| 3.6 | Diagram of the disk-outflow system of IRAS 13481-6124, taken from Kraus et al. (2010) | 42 |
| 3.7 | The place of IRS 9A in the giant molecular cloud NGC 3603 | 44 |
| 3.8 | u-v coverage of the mid-infrared interferometric data taken with T-ReCS/Gemini and MIDI/VLTI presented in Vehoff et al. (2010) | 45 |
| 3.9 | IRS 9A interferogram | 46 |
| 3.10 | IRS 9A aperture masking data | 48 |
| 3.11 | Uniform-disk model applied to the IRS 9A V^2 | 51 |
| 3.12 | Maximum-entropy images of IRS 9A | 52 |
| 3.13 | Spectroastrometric signal of the IRS 9A Br γ and H $_2$ lines | 53 |
| 3.14 | 2D plots of the Br γ spectroastrometric signals | 54 |
| 3.15 | Diagram of the IRS 9A morphology | 55 |

| | | |
|------|----------------------------------------------------------------------------------------------------------------------------|-----|
| 3.16 | Radiative transfer models of IRS9A at different inclinations | 57 |
| 3.17 | Radiative transfer models of IRS9A (V^2) | 59 |
| 3.18 | Radiative transfer models of IRS9A (SED) | 60 |
| 3.19 | Simulated RGB image of the IRS 9A morphology | 61 |
| 3.20 | Radial cut of the temperature distribution of the dust around IRS 9A | 62 |
| 3.21 | Spectral energy distribution of the best-fit radiative transfer model | 63 |
| | | |
| 4.1 | Scheme of the parameter space to search for multiple companions of high-mass stars | 68 |
| 4.2 | Multiple systems observed with the survey of Sana et al. (2014) | 69 |
| 4.3 | Multiplicity in the Orion Trapezium system | 70 |
| 4.4 | Radial velocity curves and diagram of Herschel 36 | 72 |
| 4.5 | $u - v$ coverage of our AMBER/VLTI observations of Herschel 36 | 73 |
| 4.6 | Best-fit model to the CPs and V^2 of Herschel 36 obtained with AMBER/VLTI | 74 |
| 4.7 | BSMEM reconstructed image of Herschel 36 | 75 |
| 4.8 | First-order estimate of the outer orbit of Herschel 36 | 77 |
| 4.9 | Radial velocity curves and diagram of HD 150 136 | 79 |
| 4.10 | $u - v$ coverage of the AMBER observations of HD 150 136 | 80 |
| 4.11 | CP and V^2 model fitting of HD 150 136 | 81 |
| 4.12 | BSMEM reconstructed image of HD 150 136 | 82 |
| 4.13 | First-order estimate of the outer orbit of HD 150 136 | 84 |
| | | |
| 5.1 | The center of the Milky Way | 89 |
| 5.2 | The Radio emission of the mini-spiral at the center of the Milky Way | 90 |
| 5.3 | The Galactic Center seen through Sparse Aperture Masking | 94 |
| 5.4 | Calibrated V^2 and CPs of the GC Aperture Masking observations | 95 |
| 5.5 | Images of the bow-shock sources | 100 |
| 5.6 | 3D Diagram of the bow-shock shell created by our model | 102 |
| 5.7 | H -band image of IRS5 with the three radial cuts used to estimate R'_0 | 104 |
| 5.8 | Sum of the squared residuals of the best-fit models with increasing relative contribution of scattering emission | 105 |
| 5.9 | L' -band (highpass filter) image of the surroundings of IRS 1W | 106 |
| 5.10 | Model of a bow shock in an ISM with a quadratic density gradient | 108 |
| 5.11 | L' -band image of the surroundings of IRS 10W | 110 |
| 5.12 | Bow-shock fitting of IRS 1W, IRS 5, IRS 10W and IRS 21 in H , K_s and L' wavelengths | 113 |
| 5.13 | Distribution of the bow-shocks orbital planes | 117 |
| | | |
| A.1 | Proper motion measurements of the reference stars IRS 16NW and IRS 33N | 129 |
| A.2 | Proper motion measurements of the bow-shock sources | 130 |
| A.3 | Keplerian orbital elements | 132 |

LIST OF TABLES

| | | |
|------|--------------------------------------------------------------------------------------------------------------------------------------|-----|
| 2.1 | Optical interferometric facilities | 7 |
| 2.2 | Regularizers for image reconstruction | 28 |
| 3.1 | Physical properties of giant molecular clouds and its fractal substructures | 37 |
| 3.2 | Log of the IRS 9A NACO/SAM observations | 47 |
| 3.3 | Parameters of best-fit uniform-disk model to the V^2 IRS 9A data | 50 |
| 3.4 | Radiative transfer models of IRS 9A. | 56 |
| 3.5 | Comparison of the root mean square error (RMSError) between the different models of IRS 9A. | 60 |
| 4.1 | Spectroscopic binary fraction of massive stars in nearby clusters | 67 |
| 4.2 | Best-fit parameters of a binary model for Herschel 36 | 76 |
| 4.3 | Best-fit parameters of a binary model for HD 150 136 | 83 |
| 4.4 | Strömgren and NIR Photometry of HD 150 136 | 83 |
| 5.1 | VLT/NACO imaging observations. | 93 |
| 5.2 | Iterations and reduced χ^2 for BSMEM image reconstruction | 97 |
| 5.3 | Measured proper motions in km/s of reference stars and bow-shock sources. | 101 |
| 5.4 | Best-fit parameters of our bow-shock models for IRS 5 (spherically symmetric stellar wind) | 107 |
| 5.5 | Best-fit parameters of our bow-shock models for IRS 1W (spherically symmetric stellar wind) | 109 |
| 5.6 | Best-fit parameters of our bow-shock models for IRS 1W (narrow solution) | 110 |
| 5.7 | Best-fit parameters of our bow-shock models for IRS 10W | 111 |
| 5.8 | Best-fit parameters of our bow-shock models for IRS 21 (spherically symmetric wind) | 112 |
| 5.9 | Velocities of the NA ISM considering the bow-shock model | 114 |
| 5.10 | 3D coordinates and velocities of IRS 1W, IRS 10W, IRS 21, and IRS 5 | 118 |
| 5.11 | Maxima of the PDFs orbital planes for the inclination angle (i) and angle of the line of nodes in the sky (Ω) | 119 |

GLOSSARY

- **AMBER:** Astronomical Multi-BEam combineR. Instrument built to perform long baseline optical interferometer. It operates in the bands *J*, *H*, and, *K* (i.e., ~ 1.0 to $2.4 \mu\text{m}$).
- **AO:** Adaptive Optics
- **ATs:** Auxiliary Telescopes of the Very Large Telescope Interferometer. The diameter of this telescopes is 2 meters.
- **CP:** Closure Phase
- **CRIRES:** CRyogenic high-resolution InfraRed Echelle Spectrograph. This instrument provides a solving power of up to 10^5 in the spectral range from 1 to $5.3 \mu\text{m}$.
- **ESO:** European Southern Observatory
- **FOV:** Field of view
- **FWHM:** Full Width at Half Maximum
- **GC:** Galactic Center. This term refers to the center of the Milky Way.
- **IDL:** Interactive Data Language
- **ISM:** Interstellar Medium
- **MIDI:** Mid-infrared Interferometric Instrument. It operates in the *N* band ($8\text{-}13 \mu\text{m}$), combining up to two telescopes.
- **MIR:** Mid-infrared
- **MTF:** Modulation Transfer Function
- **MYSO:** Massive Young Stellar Object
- **NACO:** Nasmyth Adaptive Optics System combined with the Near-Infrared Imager and Spectrograph. This instrument provides adaptive optics assisted imaging, imaging polarimetry, coronagraphy and spectroscopy, in the $1\text{-}5 \mu\text{m}$ range.
- **NIR:** Near-infrared

- **NRM:** Non-redundant mask. Mask used to perform Sparse Aperture Masking observations, in which the baselines formed by the pinholes in the mask are unique.
- **OIFITS:** This is a standard for exchanging calibrated, time-averaged data from astronomical optical interferometers, based on the FITS Standard.
- **PIONIER:** Precision Integrated-Optics Near-infrared Imaging Experiment. This instrument combines the light from four telescopes simultaneously, and operates at the near-infrared H -filter.
- **PSF:** Point Spread Function
- **SAM:** Sparse Aperture Masking
- **SED:** Spectral Energy Distribution
- **SNR:** Signal-to-noise ratio
- **UTs:** Unit Telescopes of the Very Large Telescope Interferometer. The diameter of this telescopes is 8.2 meters.
- **VLT:** Very Large Telescope
- **VLTI:** Very Large Telescope Interferometer

1

INTRODUCTION

*Heaven wheels above you displaying to you her eternal glories
and still your eyes are on the ground.*

Dante

OUR lives are intimately linked to the stars. From the light that we receive from the Sun each day to the fact that most of the elements in our chemical composition were formed at the interiors of stars. Among the different types of stars that we know, there is one that is of special relevance because of its key role in the evolution of galaxies. These are the “massive stars”. The term “massive” comes from the fact that they have at least eight times the mass of the Sun. Therefore, these stars evolve very rapidly. Their lives last around some millions of years instead of the billions of years of solar-type stars. However, our understanding on how they are born and evolve is still limited.

Massive stars are very rare and difficult to observe compared to their lower mass counterparts. For example, assuming a Salpeter initial mass function, for each massive star with a mass between $64-128 M_{\odot}$, there are more than 100 solar-type stars. Therefore, in general, the more massive a star is, the rarer it is. Moreover, these stars are formed in the densest regions of molecular clouds. Therefore, the initial phases of massive stars can only be observed in exceptional cases because generally they are enshrouded by dense molecular gas and dust from their very birth until they reach the main sequence. This poses a strong bias in our understanding of their formation. In the recent years, important theoretical work has been done in order to explain the possible mechanisms of massive star formation. Some of the contemporary theories suggest that high-mass stars are formed via accretion disks, in a similar way to lower mass stars. Nevertheless, theoretical predictions need to be confirmed by detailed observations. However, in addition to being rare, massive star formation regions are located at large distances from

the solar system, generally more than 1 kpc away. Therefore, investigating massive stars requires instruments with the highest possible resolution.

Nonetheless, not only the initial phases of massive stars are of interest. During all their lives, these stars drive physical phenomena that deserve study. For example, massive stars have very strong stellar winds with velocities up to some 10^3 km/s and huge mass loss rates (10^{-3} - 10^{-5} M_{\odot} /yr). Therefore, high-mass stars strongly interact with the interstellar medium (ISM). In some evolved binary systems, the exchange of material produced by the mass loss favors the creation of rich dusty environments. Perhaps one of the most astonishing phenomena related to massive stars is the end of their lives in the form of supernova explosions. Another interesting observational property of massive stars is the large number of multiple systems to which they belong. While only around 30-40% of solar type stars are multiples, around 70-90% of the massive stars form part of higher-order systems. Therefore, this property establishes important constraints on the different scenarios of massive star formation.

During the last decades considerable progress in our understanding of massive stars has been achieved thanks to the advent of technologies such as adaptive optics, infrared long baseline interferometry, or the improved sensitivity and angular resolution of millimeter interferometers. At infrared wavelengths, however, there are still important restrictions to perform ground-based high-contrast imaging, mainly because of the effect of the atmosphere which deteriorates the quality of the incoming wavefronts from the observed objects, and because of technological constraints, like the limited number of actuators and sensors to monitor and correct the distortions of the measured wavefronts.

This thesis is devoted to the study of massive stars using high angular resolution techniques in the infrared, in particular, optical interferometry in the form of sparse aperture masking and long-baseline interferometry. These techniques allow us to observe astronomical objects at infrared wavelengths combining several telescopes to achieve the highest angular resolution, which is proportional to the distance between the different combined telescopes at the observed wavelength. All the studies here presented were performed using the instrumental facilities of the European Southern Observatory (ESO), which has the largest interferometric facility in the world at infrared wavelengths: the Very Large Telescope Interferometer (VLTI). In this work we have addressed three main problems in the study of massive stars: a) the study of their initial phases; b) the role of multiplicity in massive stars, and c) the interactions of massive stars with the interstellar medium.

In addition to this brief introduction, this thesis is composed of seven chapters. The second chapter provides an overview of the different observational techniques used, paying special attention to optical interferometry. The modelling of the impulse response for Fizeau interferometers is described, together with the image reconstruction process for optical interferometry data. From chapter three to chapter five, the main research topics of the present thesis are described. These chapters include the data and

analysis presented in four peer-reviewed publications. The topics of these chapters are the following:

The formation of massive stars: The contemporary massive star formation theories suggest the presence of disk-like structures at the core of massive young stellar object (MYSO). However, these structures have been elusive for very massive young stellar objects. In this chapter, we present the study of the very massive young stellar object NGC 3603 IRS9A* with the adaptive optics assisted infrared camera NACO of the Very Large Telescope (VLT) in its sparse aperture masking mode, and with archival high-spectroscopic data with the CRyogenic high-resolution InfraRed Echelle Spectrograph (CRIRES).

Multiplicity in massive stars: Here, we present long-baseline optical interferometric observations of two massive triple hierarchical systems, HD 150 136 and Herschel36. The first of them is an extremely massive system with a total mass above $100 M_{\odot}$, and the second one is a young system with possibly three zero-age main-sequence stars in it. The objective of this research was to resolve, for the first time, the outer component of these triple hierarchical systems, to provide information on their position and brightness ratio with respect to the spectroscopic binary, and to obtain a first estimate of their orbits.

Interactions of massive stars with the ISM: Here, we studied bright massive stars associated with bow-shock structures in the inner parsec of the Galactic center (GC). To perform this research, we used near-infrared (NIR) aperture masking observations and adaptive optics images to obtain the 3D position and geometry of the bow-shock shells, investigating the mechanisms of the near-infrared bow-shock emission, and determining the orbital planes of the bow-shock sources around the massive black hole SgrA*.

Finally, chapters six and seven describe the general conclusions and prospectives of the presented research, respectively.

2

HIGH ANGULAR RESOLUTION TECHNIQUES

STELLAR INTERFEROMETRY

Any sufficiently advanced technology is indistinguishable from magic.

Arthur C. Clarke

High angular resolution techniques are a crucial tool for modern astrophysics. They have served to study many astronomical problems that range from the discovery of exo-planets, over the study of stellar physics, to the morphology of active galactic nuclei. For this thesis we have made an extensive use of them to study three different aspects of massive stars: (a) multiplicity, (b) early-phases of massive star formation, and (c) the physics of interactions of high-mass stars with the interstellar medium. We have made use of optical interferometry in the form of (i) long-baseline interferometry and (ii) sparse aperture masking in combination with adaptive optics. In this chapter, an overview of these techniques is presented, highlighting their basic principles and functioning.¹

2.1. INTERFEROMETRY IN CONTEXT

INTERFEROMETRY is a technique based upon the wave nature of light. It was Thomas Young who, in 1803, first quantitatively described the phenomenon of interference of light in his famous “double slit experiment”. Young observed the light of a sunbeam

¹This chapter uses as the main bibliography the works of [Monnier \(2003\)](#), [Monnier and Allen \(2013\)](#), [Lawson \(2000\)](#) and [Labeyrie et al. \(2006\)](#), unless others are explicitly mentioned.

that passed through a small pinhole and was subsequently split by an edge-on card, to be re-combined thereafter on a screen. He observed that the sunlight produced a series of interwoven dark and bright stripes, or “fringes”, on the screen. These fringes were produced by the difference in the path lengths between the two light beams and their successive interference on the screen.

The first experiments to obtain information of the brightness distribution of astronomical objects from interferometric fringes were performed at optical wavelengths more than one century ago. H. Fizeau hypothesized that interference fringes produced from a source with a finite size would be smeared depending on the size of the source. M. Stéphan was one of the first to corroborate this hypothesis. He used an 80-cm refractor telescope with an adapted mask (covering the entrance of light) with a pair of holes. With this instrument, he determined an upper limit of 0.16 arcsec for the angular size of the stars that he observed. Another example of the early development of interferometry, is the work of Michelson in 1891 to measure the diameters of the four major satellites of Jupiter, using a couple of variable slits to mask the 12-inch aperture telescope at Mount Hamilton². However, it was not until 1967 when a positive interferometric signal with two telescopes was obtained for the first time by Labeyrrie (1975). Nevertheless, restrictions imposed by the turbulent atmosphere, and the technological limitations to perform optical/infrared interferometric observations, delayed the further development of this technique until the last decade of the twentieth century. In contrast, the large coherence time, coherence length and the high transparency of the atmosphere at radio wavelengths ($\lambda \sim \text{cm}$) made the use of radio interferometry possible since the late 1940s, with this technique becoming widely used in the 1980s. For a complete review on radio interferometry, please see the text book of Thompson et al. (2001).

Optical interferometry³ resurged in the 1990s with the advent of complementary instrumentation like Adaptive Optics and the construction of interferometers that combine the light of, at least, three separate telescopes being capable to produce images. The interferometric array COAST was the first one to produce an optical synthesis image of the Capella binary system (Baldwin et al., 1996). Table 2.1 shows a list of the optical interferometers of the twentieth century along with a major astrophysical contribution for each one of them. Nowadays, one of the most prolific, in terms of scientific production, optical interferometers is the VLTI, which is able to perform observations combining up to four 8-m telescopes. This thesis is based on observations of massive stars performed with this array.

²Michelson, in combination with Edward W. Morley, won the Nobel prize for the determination of the standard meter in 1907 using an interferometer.

³The term “Optical Interferometry” refers to the use of optical elements (glass or mirrors) to obtain the interference fringes, not to the wavelength range of the observations. The current range of wavelengths covered by optical interferometry goes from the near-infrared to the mid-infrared ($\sim 1\text{-}20 \mu\text{m}$).

Table 2.1: List of the main optical interferometric facilities and their main-scientific results.

| Discovery | Year | Interferometry | Reference |
|--------------------------------------------------|------|----------------------------------------------|--------------------------------|
| Physical diameters of hot stars | 1974 | Narrabri Intensity Interferometer | Hanbury Brown et al. (1967a,b) |
| Empirical effective temperature scale for giants | 1987 | Infrared interferometer of CERGA | di Benedetto and Rabbia (1987) |
| Survey of IR Dust Shells | 1994 | Infrared Spatial Interferometer (ISI) | Danchi et al. (1994) |
| Geometry of Be star disks | 1997 | Mark III | Quirrenbach et al. (1996) |
| Near-IR Sizes of YSO disks | 2001 | Infrared Optical Telescope Array (IOTA) | Millan-Gabet et al. (2001) |
| Pulsating Cepheid Gem | 2001 | Palomar Tesbed Interferometer (PTI) | Lane et al. (2000) |
| Crystalline silicates in inner YSO disks | 2004 | Very Large Telescope Interferometer (VLTI) | van Boekel et al. (2004) |
| Vega is a rapid rotator | 2006 | Navy Precision Optical Interferometer (NPOI) | Peterson et al. (2006) |
| Imaging gravity-darkening on Altair | 2007 | CHARA interferometer | Monnier et al. (2007) |
| Near-IR sizes of AGN | 2009 | Keck-I | Kishimoto et al. (2009) |

Adapted from [Monnier and Allen \(2013\)](#).

2.2. BASIC CONCEPTS OF INTERFEROMETRY

THE capacity of a telescope to discern between two separate closely objects is known as “angular resolution” (θ). It depends on the wavelength of the observations, λ , and the size of the telescope, usually quantified by the diameter D of its primary mirror. According to the “Rayleigh” criterion the diffraction limited resolution of a circular telescope is thus given by:

$$\theta_{tel} = 1.22 \frac{\lambda}{D} \text{ rad}, \tag{2.1}$$

This means that a telescope cannot distinguish objects separated by an angular distance lower than θ_{tel} . In a similar fashion, one could determine the angular resolution of a two-station interferometer, taking as condition the full-constructive interference as:

$$\theta_{int} = \frac{\lambda}{B} \text{ rad}, \tag{2.2}$$

where B is the projected separation, in the plane of the sky, between the two telescopes (or the so-called “baseline length”). However, this criterion could be relaxed if partial-constructive interference is considered up to a limit of $\theta_{int} > \frac{\lambda}{2B}$, where the interference is completely destructive (see Fig. 2.1).

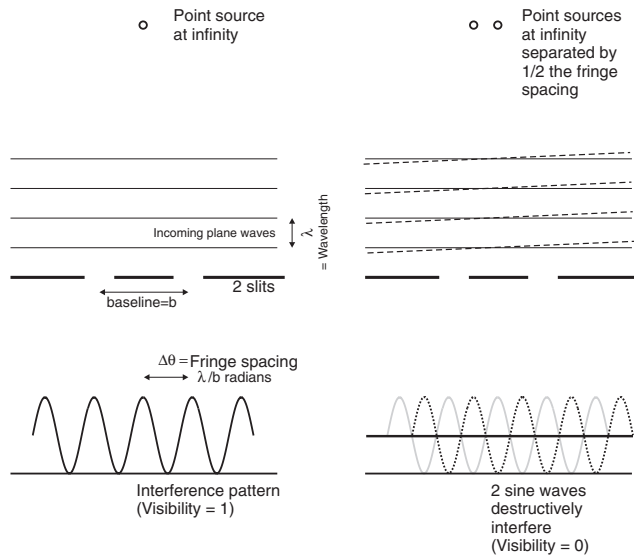


Figure 2.1: The *left* panel displays the interference pattern produced by a point-like source. The difference between two maxima in the fringes is known as the “fringe spacing” and is equal to θ_{int} . The *right* panel displays two point-like sources separated by an angular distance of one half the fringe spacing. The sets of fringes produced by the sources are shifted by 180° , thus interfering destructively, impeding the identification of the sources. Image taken from [Monnier \(2003\)](#).

The Van Cittert-Zernike theorem (see [Thompson et al., 2001](#)) relates the brightness distribution, I , of an object with the contrast of an interferometer's fringes through a Fourier transform in the following form ([Berger and Segransan, 2007](#)):

$$V(u, v) = |V|e^{i\phi_v} = \int_{l,m} A_N(l, m)I(l, m)e^{-2\pi i(ul+vm)} dl dm, \quad (2.3)$$

where $V(u, v)$ is the so-called *complex visibility*, (l, m) are cartesian coordinates in the plane of the sky in units of radians. $A_N(l, m)$ is the transfer function of the telescope, and (u, v) are the corresponding coordinates in Fourier space. The modulus of the complex visibility $|V|$ corresponds to the *fringe amplitude*, while the argument ϕ_v is the *fringe phase*. The visibility function $V(u, v)$ is usually normalized: $V(u, v) = V(u, v)/V(0,0)$. Therefore, its amplitude takes values between 0 and 1. $V(0,0)$ (usually named zero-spacing flux) is given by the integrated flux over the primary beam pattern of an individual telescope. The field-of-view (FOV) of an interferometer is roughly given by the size of the individual telescope/antenna: $\text{FOV} = \theta_{\text{telescope}} = \lambda/D$.

2.2.1. THE EFFECT OF THE ATMOSPHERE ON THE INTERFEROMETRIC OBSERVABLES

FLUCTUATIONS of the refractive index of the atmosphere introduce wavefront distortions. When these distortions are a considerable fraction of the wavelength across the aperture of a telescope, the quality of the image formed is not longer diffraction-limited, and rather depends on the coherence scale of the incoming wavefront (i.e., it is *seeing limited*). For a Kolmogorov model of the atmospheric turbulence, the root mean square path length of an incoming wavefront scales as $\sigma_d \sim (d/r_0)^{5/6}$, where d is the path separation between two given points of the wavefront and r_0 is the so-called ‘‘Fried parameter’’, which is a measurement of the quality of the atmospheric transmission. These variations in the length of the optical path are translated to fluctuations in the wavefront phase of the form: $\sigma_\phi = 2\pi\sigma_d/\lambda$. Therefore, when the phase variation σ_ϕ reaches π radians, the wavefront is incoherent at points separated by d_0 . At the infrared, d_0 scales as $d_0 \sim 10\lambda^{6/5}$ centimeters, where λ is given in microns. Therefore, for a wavefront at $2.2\mu\text{m}$, $d_0=25$ cm. To relate the spatial structure of the fluctuations with its temporal duration, the ‘‘coherence time’’, τ_d , is used. It characterizes the time over which the rms of the wavefront phase equals π radians and is given by: $\tau_d = d_0/v_s$, where v_s is the wind speed. Assuming a wind speed of 10 m/s, then $\tau_d=25$ milliseconds for $d_0=25$ cm.

The parameters r_0 and τ_d are important for interferometric observations because r_0 limits the useful size of the collecting aperture (without the assistance of techniques such as Adaptive Optics) and τ_d limits the coherent integration time. For interferometric observations at infrared wavelengths, the integrated atmospheric pathlength above each telescope generates phase shifts ζ in the recorded fringes. The phase shifts induced to the interferometric fringes are proportional to the difference of the phase shifts between the two telescopes that form a baseline. Those shifts (or pistons) affect the measured

phase of the visibilities, $\arg[V(u, v)]$, as:

$$\arg[V(u, v)] = \phi_{real} + (\zeta_j - \zeta_i), \quad (2.4)$$

One important consequence of the phase delays ζ , is that the visibility phase is not longer associated with the Fourier phase of the source's brightness distribution. To eliminate this effect a new interferometric observable is introduced: **the closure phase** (Baldwin et al., 1986; Jennison, 1958; Weigelt, 1977). This observable is constructed by multiplying the visibility functions of three different baselines that form a closed triangle. By doing this, the telescope-dependent errors are canceled:

$$\begin{aligned} \phi_{b1, meas} &= \phi_{b1, real} + (\zeta_1 - \zeta_2) \\ \phi_{b2, meas} &= \phi_{b2, real} + (\zeta_2 - \zeta_3) \\ \phi_{b3, meas} &= \phi_{b3, real} + (\zeta_3 - \zeta_1) \\ \phi_{b1, meas} + \phi_{b2, meas} + \phi_{b3, meas} &= \phi_{b1, real} + \phi_{b2, real} + \phi_{b3, real} \end{aligned} \quad (2.5)$$

This triple product of visibilities is known as the bispectrum (Roddier, 1986). The closure phases (CPs) are the argument of the bispectrum, and provide information that only depends on the structure of the source. If the source has point symmetry, the closure phases will be zero, while, if the target is asymmetric, variations of the closure phases will be observed between -180° to 180° , depending on the degree of the asymmetries. Fig 2.2 displays an example of the variation of the phases in comparison with the closure phases for interferometric observations taken at $8.8 \mu\text{m}$ of a point-like object. The total number of visibilities for a given interferometric array of N elements is $N(N-1)/2$, while the total number of independent closure phases is equal to $(N-1)(N-2)/2$. This means that the number of closure phases are smaller than the number of interferometric phases.

The sensitivity of an interferometer is affected by (i) the flux density of the source, (ii) the background radiation and/or (iii) the detector noise. In the case of optical interferometry, the noise is produced by random arrivals of photons, therefore the noise follows a Poisson statistics. Variations of the average number of photons N (that arrive to the detector at a given time) is given by: $\Delta N = \sqrt{N}$. Thus, the total number of photons recorded in a given interval is expressed as:

$$N = \eta \frac{P_\nu \Delta \nu}{h\nu} \tau, \quad (2.6)$$

where η is the total efficiency of the optical transmission system, P_ν is the power spectral density, τ is the time interval, ν is the frequency of the observation, h the Planck constant and $\Delta \nu$ the bandwidth used. Since the coherence time is very small at infrared wavelengths (e.g., at $2.2 \mu\text{m}$: $\tau_c = 25 \text{ ms}$ and at 1 mm : $\tau_c = 14 \text{ sec}$) compared to the radio regime, the number of photons recorded is considerably lower in a single exposure. To alleviate this problem, series of short exposures are taken and the final detected signal, over which the fringe contrast is measured, corresponds to the average of the total power

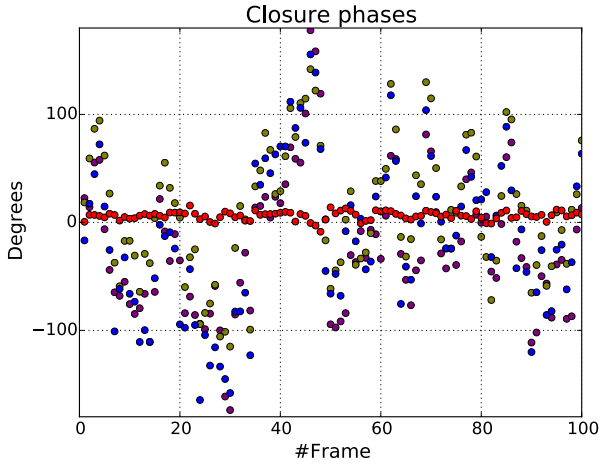


Figure 2.2: Comparison of the variance between phases and closure phases for a point-like source. The panel displays the different phases for a triplet of baselines (purple, green and blue dots) and their corresponding closure phase (red dot) for 100 different observations. It is appreciated that the phases largely variate along the entire phase range, while the closure phases remain close to zero. Variance of the phases is induced by delays due to phase errors at each aperture that forms a given baseline.

in the recorded exposures. The signal-to-noise ratio (SNR) for optical interferometers scales as NV^2 . For this reason, in optical interferometry the total power of the visibility, V^2 , is a better observable than the amplitude V (for a more complete description of the sensitivity in optical interferometry see: [Monnier and Allen, 2013](#); [Paresce, 1996](#)). The astrometric precision, $\Delta\Phi$, provided by an interferometer is also related to the SNR of the observations in the following manner:

$$\Delta\Phi \sim \frac{\theta}{SNR}, \quad (2.7)$$

where θ is the resolution of the interferometer.

2.3. LONG-BASELINE INTERFEROMETRY

TO record interferometric fringes at near-infrared wavelengths, a series of optical elements are required. Once the light is collected by the telescopes, the light should be interfered. Depending on the type of beam combination, there are two ways to perform the interference: “Fizeau” and “Michelson” interferometry. The first one performs the interference of the light in the image plane, while the second one does the combination in the pupil plane. In the case of optical long-baseline interferometry, “Michelson” beam combination is usually performed. On the other hand, an example of “Fizeau” interferometry is the technique known as Sparse Aperture Masking. Figure 2.3 displays a diagram with the two different types of beam combination.

In optical long-baseline interferometry, before the two light beams are combined, they are transported to a central station. To transport the light, vacuum optical paths are used. The vacuum condition is necessary to minimize the differential chromatic dispersion of the light. The size of the mirrors used to guide the light along the optical path should be taken into account to limit the diffraction effects. In order (i) to track the motion of the object in the plane of the sky during the observing time, (ii) to compensate for the geometric delay of the beams for a given baseline configuration, and (iii) to correct for the rapid path length variations due to atmospheric turbulence or mechanical vibrations, a movable delay line is used. Typical specifications of the movable delay line include nanometer precision at speeds of cm/s, over distances of ~ 100 meters and dynamic range of 10^{10} .

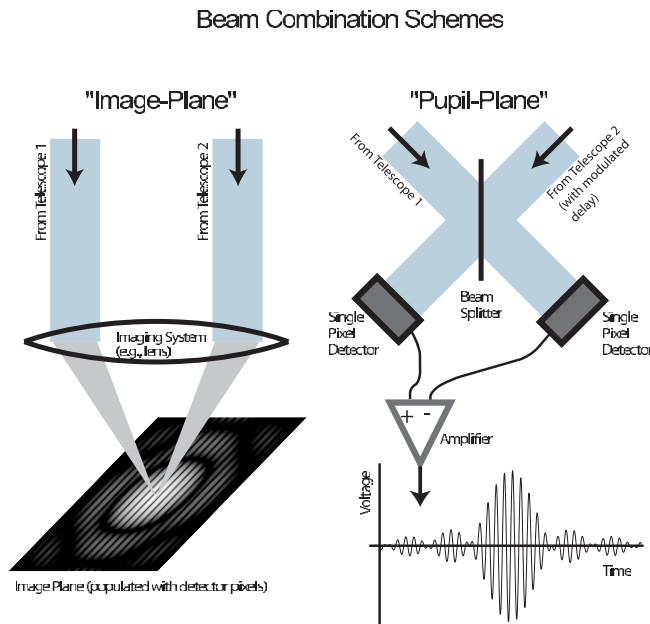


Figure 2.3: The Figure displays the two types of beam combination used in optical interferometry. The “image plane” method which is used by Sparse Aperture Masking, and “Pupil-plane” which is widely used for long-baseline interferometric observations. Image taken from [Monnier \(2003\)](#).

A widely used movable delay line is based on the Mark III interferometer ([Colavita et al., 1991](#); [Shao et al., 1988](#)). This system consists of a retro-reflector mirror system mounted on a moving base which can change its position being moved using precision rails on a timing belt. The optical elements of the delay line system include a parabolic mirror and a flat mirror located at its focus. This system is known as “Cat’s Eye”. The flat mirror is coupled with a piezo-electric stack, which samples the path differences, a voice coil positions the “Cat’s Eye” over the base and a high precision motor moves the base via a timing belt to compensate for the path differences. The metrology system to measure

the carriage position is driven by a laser beam that follows the same path as the beam lights via the “Cat’s Eye” (see Fig. 2.4).

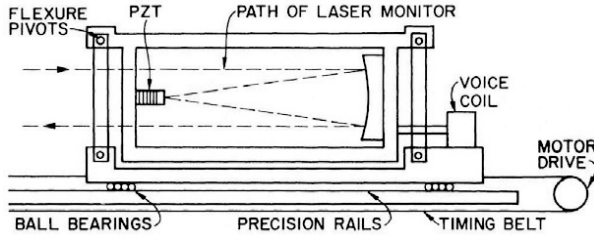


Figure 2.4: Schematic of the delay line based on the Mark III interferometer. This type of systems is widely used in current interferometric facilities like the VLTI. Image taken from [Monnier \(2003\)](#).

Once the light has been properly delayed, it is combined. For this purpose, a beam combiner is used. In the case of “Michelson” interferometry, the light beams are overlapped on a beam-splitter. Subsequently, the light on both sides of the beam-splitter is recorded and the fringes measured. In the case of Fig. 2.3, single pixel detectors are used. Nevertheless, current facilities use 2D CCD detectors. There are two methods to perform beam combination: “pair-wise” or “all-in-one”. In the first method, the light beams are split several times and the interference of each baseline is constructed afterwards. In the second method the light beams from several telescopes are interfered at the same time. In this method, each baseline is recognized by a specific modulation such that the baseline has a unique fringe temporal frequency in the readout.

To track the interference pattern in the presence of atmospheric fluctuations, “Fringe Tracking” is performed. This technique, also called “co-phasing”, measures the optical path delay fluctuations over sub-wavelength scales in real time. These observations are obtained on the guide stars and the results are applied to the science target. A common method to perform the fringe tracking is known as ABCD. In this method, two beams are combined pairwise, and the intensity of the fringes are measured at four points spaced by $\lambda/4$. Each one of the measurements represents different fringe phases from which the average phase of the fringe is estimated from a given reference point. This phase information is sent back to the delay line to correct it. Pupil-tracking is very useful to perform high-spectral resolution interferometry because white light fringe (i.e., the coherence envelope set by the spectral bandpass) can be used for fringe tracking while the remaining output channels can be dispersed. Moreover, pupil-tracking allows one to use longer integration times and therefore reach higher sensitivity.

The largest optical interferometer in the world is the VLTI. It combines the light beams of up to four telescopes. The VLTI is part of the European Southern Observatory facilities⁴, and is operational since 2000. The array consists of four Unit Telescopes (UTs) with 8m diameter and four Auxiliary Telescopes (ATs) of 2m. The position of the UTs is

⁴Spain became the 12th Member State of ESO on 14th February 2007.

fixed, while the ATs are movable on rails, providing 30 different baseline configurations to achieve efficient $u-v$ coverage. Figure 2.5 displays a layout of the VLTI telescopes. The first generation of VLTI instruments allows to observe from near-infrared ($2.2 \mu\text{m}$) up to mid-infrared ($13 \mu\text{m}$): the Astronomical Multi-BEam combineR (AMBER) and the Precision Integrated-Optics Near-infrared Imaging Experiment (PIONIER) at near-infrared wavelengths and the Mid-infrared Interferometric Instrument (MIDI) for mid-infrared observations. In this thesis we make use of data collected with AMBER in its low resolution mode, which includes simultaneous observations with the $J-$ ($1.19-1.41 \mu\text{m}$), $H-$ ($1.44-1.87 \mu\text{m}$), and $K-$ ($1.90-2.56 \mu\text{m}$) filters.

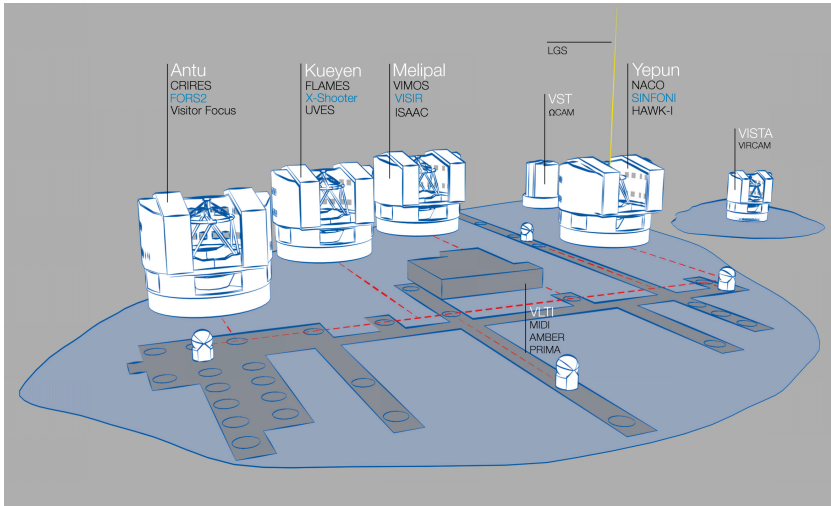


Figure 2.5: The image displays the layout of Paranal Observatory. The four main telescopes (Antu, Kueyen, Melipal, and Yepun), as well as the four Auxiliary Telescopes are displayed. These telescopes are the stations of the so-called Very Large Telescope Interferometer. The red dotted lines represent the delay lines that link the different telescopes to form an optical interferometer. The paths for the movable ATs are also displayed together with the available positions of the stations (blue ellipses). The names of the different instruments available at these telescopes are also displayed. Taken from the European Southern Observatory image gallery.

2.4. SPARSE APERTURE MASKING WITH ADAPTIVE OPTICS

2.4.1. ADAPTIVE OPTICS

ADAPTIVE Optics (AO) is a powerful technique which is used to overcome the degrading effects (mainly induced by the atmospheric turbulence) in the wavefront of a specific source, while keeping high sensitivity. AO systems consist of a real time sensor that monitors the incoming wavefronts; subsequently, a deformable mirror compensates the distortion of the wavefront before it reaches the pupil plane. Figure 2.6 displays an example of how the central parsec of the Galactic Center is seen with and without AO. Nevertheless, in spite of the great promise of AO to provide diffraction limited images, it

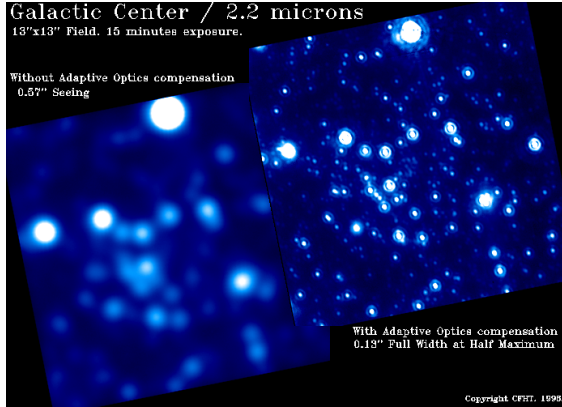


Figure 2.6: Comparison of observations of the Galactic Center with and without AO. The panel displays two images of the GC observed at $2.2\mu\text{m}$ with the Canada-France-Hawaii Telescope (CFHT). Notice how the image taken with AO is sharper, and more fine details of the sources structures are appreciated.

still faces a number of problems that makes a precise and stable point spread function (PSF) calibration very difficult. Among these problems we can mention: (a) The PSF of the AO systems is variable on different timescales and highly sensitive to the observing conditions (e.g. seeing, airmass, etc); (b) the AO performance is constrained by technological limitations of the system (e.g., the number of sensors and actuators that measure and correct the incoming wavefront); and (c) the wavefront of the guide star is not the same as the one of the scientific target. The latter effects are due to the wavefronts suffering different distortions because they take slightly different paths through the atmosphere. For a more complete description of AO in Astronomy see [Beckers \(1993\)](#); [Roddier \(2004\)](#).

2.4.2. SPARSE APERTURE MASKING

SPARSE Aperture Masking (SAM) interferometry is a technique which transforms a telescope into a non-redundant Fizeau interferometer by placing a mask with some holes in the pupil plane of the telescope (see Fig. 2.7). The first experiments with this technique in the modern era of optical interferometry were performed by John Baldwin of Cambridge University using the University of Hawaii 88-inch telescope ([Baldwin et al., 1986](#)), and by Bob Frater, from University of Sidney, using the 3.9 m AAT telescope ([Frater et al., 1986](#)). The main advantage of SAM interferometry is that the non-redundant mask removes most of the incoherent noise produced by the atmospheric turbulence, obtaining a very well defined and stable transfer function. The transfer function of the system resembles the diffraction pattern of the mask.

The nominal angular resolution achieved by this technique is of the order of $\theta \sim$

$\lambda/2D$. This is a factor of two better than the resolution obtained in standard imaging. Nevertheless, due to the fact that the non-redundant mask (NRM) covers most of the telescope pupil, SAM suffers from low photon efficiency and is limited to bright objects (e.g. in the case of the VLT the magnitudes of the targets range between 4 to 12, depending on the mask used). Early SAM experiments could only apply short exposure times to freeze the atmospheric seeing. However, AO provides a much higher encircled energy, and an image that is stable on longer timescales. Therefore the sensitivity is increased significantly over early applications of this technique. Thus, a combination of SAM and AO offers us a unique tool to recover high fidelity images (SNR \sim 200 at λ/D) and, hence, study structures between one and a few times the size of the interferogram (e.g., in the case of the NACO/VLT, SAM allows us to analyze objects with angular sizes from 50 to 150 mas), with the robust transfer-function calibration provided by SAM, and the higher dynamic range obtained by the AO systems (Tuthill et al., 2000).

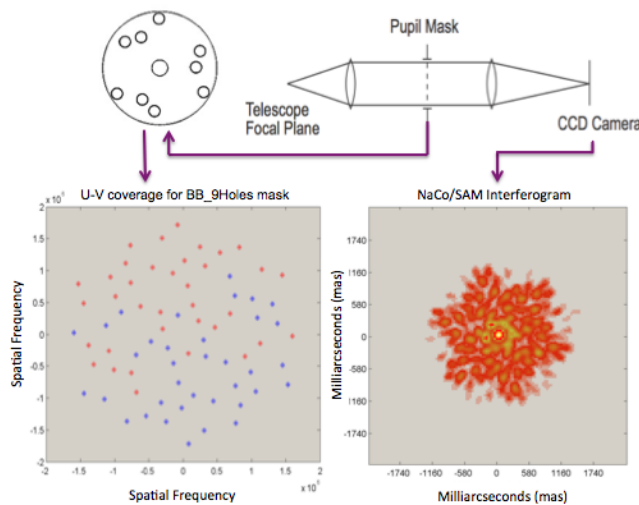


Figure 2.7: Sparse Aperture Masking layout. In the figure a NRM with nine holes is located in the pupil of the telescope. It is thus transformed into an interferometer with a non-redundant u-v coverage (lower-left gray scheme); note that the number of points sampled in the Fourier space correspond to all baselines formed by all the possible pair of holes combinations plus their complex conjugates (in this case, 36 red dots + 36 blue dots). The lower-right gray scheme shows the SAM interferogram of a point-like source obtained at the camera detector, with a shape that only depends on the geometry of the interferometric array. The upper part of the scheme was adapted from the NACO manual and Tuthill et al. (2006).

SIMULATIONS OF INTERFEROGRAMS USING NON-REDUNDANT MASKS ARRAYS

THE intensity fringe pattern $I(\theta_x, \theta_y)$, formed at the telescope detector, is known as *interferogram*, and it is the response to the object's brightness distribution $O(\theta_x, \theta_y)$ convolved with the instrument's transfer function $PSF(\theta_x, \theta_y)$. This is:

$$I(\theta_x, \theta_y) = O(\theta_x, \theta_y) \otimes PSF(\theta_x, \theta_y) \tag{2.8}$$

where (θ_x, θ_y) are coordinates in the *image plane* (or focal plane) in units of radians/pixel, and \otimes denotes convolution. In the case of aperture masking, the instrument's transfer function corresponds to the fringe pattern created by the geometry of the NRM. Here, we describe how to simulate the PSF of a NRM with a given geometry. The characterization of the PSF in Aperture Masking observations is particularly important to subsequently extract and calibrate the visibility functions of the scientific targets. Mapping the transfer function of a NRM into the detector of a telescope takes several steps. First, we must consider that the mask is physically placed at the *pupil plane* of the telescope and that the positions of the pinholes are given in cartesian coordinates (x, y) in units of meters. Placing the mask in the *pupil plane* is equivalent to having a large mask placed over the primary mirror of the telescope. Subsequent treatment of the position and sizes of the pinholes uses the projected geometry of the mask over the primary mirror.

The $PSF(\theta_x, \theta_y)$ in the plane of the detector is proportional to the square of the Fourier transform of the transmission function of the pupil $G(x, y)$. This is:

$$PSF(\theta_x, \theta_y) = |FT[G(x, y)]|^2 \tag{2.9}$$

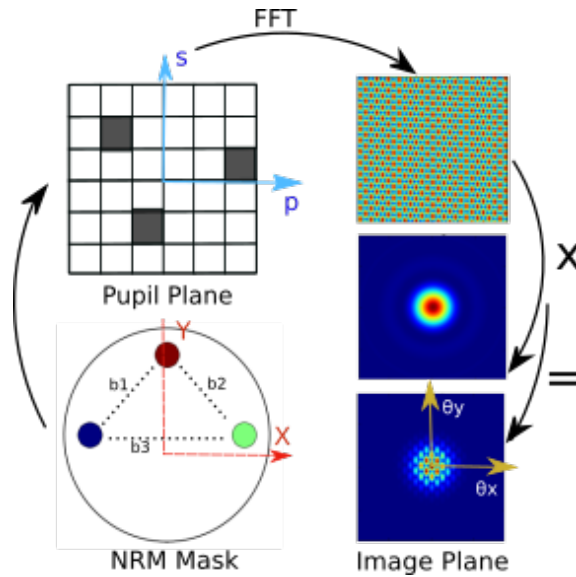


Figure 2.8: The panel displays an interferometric array of three non-redundant baselines. The transmission function of the interferometric array is mapped into an $N \times N$ pixel array. A posteriori, it is converted to the *image plane* through a Fourier Transform. The final interference pattern is modulated by the diffraction function of the pinhole geometry. In the case of circular apertures, it corresponds to an “airy disk”. Thus, forming the PSF of the interferometer.

In the case of a NRM, $G(x, y)$ takes values of ones at the surfaces of the pinholes in the mask, and zeros at the rest of the pupil where the entrance of light is blocked. Since the $PSF(\theta_x, \theta_y)$ is created in an array of pixels, $G(x, y)$, it must be mapped into a $N \times N$ discrete array with coordinates (s, p) in units of pixels. The conversion factor to discretize the transmission function of the pupil is given by:

$$\begin{aligned} s_i &= \frac{x_i}{\lambda} 2Y^{-1} \text{ pixels} \\ p_i &= \frac{y_i}{\lambda} 2Y^{-1} \text{ pixels} \end{aligned} \quad (2.10)$$

where λ is the wavelength of interest in units of meters, and Y the pixel scale of the detector normalized by half the total number of pixels in the image. The index i corresponds to the i th element of the transmission function to be discretized. Considering this, $PSF(\theta_x, \theta_y)$ equals:

$$PSF(\theta_x, \theta_y) = |FT[G(x, y)]|^2 = |FT[G(s, p)]|^2 \quad (2.11)$$

Once the pupil is discretized, we can take advantage of the linearity of the Fourier transform and go from the (s, p) plane to the (θ_x, θ_y) in two steps. First, we consider the discrete transmission function assuming that the sizes of the pinholes are negligible: $D(s, p)$. Therefore, at each pixel, with coordinates (s, p) that correspond to the mean position of the pinholes, the transmission function corresponds to unity, while the rest of the pixels in the $N \times N$ array remains equal to zero. Due to the discrete sampling of the pixel array, sometimes the positions of the pinholes do not correspond to a specific pixel, and the transmission should be divided into adjacent pixels to the mean position. Therefore, each pinhole might be represented by a “splodge” of pixels in the (s, p) plane. To project $D(s, p)$ onto the image plane, the square of its Fourier transform is computed. Second, to take into account the size and geometry of the apertures, $|FT[D(s, p)]|^2$ is modulated by the diffraction pattern of the aperture $\Gamma(\theta_x, \theta_y)$. In the case of a circular aperture or radius R , represented by $f(\vec{r}) = \text{circ}(r/R)$, the diffraction pattern corresponds to an “airy disk” of the form: $[2\pi R^2 J_1(\rho R)/\rho R]^2$, where $J_n(x)$ is the n -th order Bessel function, and $\rho = \sqrt{\theta_x^2 + \theta_y^2}$. Therefore, the PSF of an array of pinholes is written as:

$$PSF(\theta_x, \theta_y) = |FT[G(s, p)]|^2 = \Gamma(\theta_x, \theta_y) |FT[D(s, p)]|^2 \quad (2.12)$$

Figure 2.8 displays a schematic of the process to simulate the PSF for a given array. When a target is observed, the PSF is convolved with the real brightness distribution of the target, $O(\theta_x, \theta_y)$, to produce the images acquired at the detector. Extended objects dilute the fringe contrast and the interferogram appears blurry. However, point-like targets produce crispy interferograms.

Figure 2.9 displays, for different arrays, their PSFs and their Modulation Transfer Functions (MTF; i.e., the absolute value of the Fourier transform of the PSF), indicating the spatial frequencies from which the visibility function is measured. Notice that in the

case of a NRM with two holes, three bright spots are generated in the MTF. The brightest middle spot corresponds to the DC Fourier component and it is proportional to the square of the total transmission of the pinholes. The other two spots correspond to the sampled spatial frequencies, and their complex conjugate in the $u - v$ plane. The third row of Fig. 2.9 shows the PSF of the 7-holes mask that is available at the near-infrared camera NACO mounted at the VLT.

REDUNDANCY AND MASK DESIGN CONSIDERATIONS

ONE of the main restrictions of SAM interferometry, is the necessity to have a mask with non-redundant baselines. This condition allows one to relate each fringe to a specific baseline (Haniff et al., 1987). In contrast, when the mask has two or more baselines of the same length, a random phase is created in the fringes that is caused by these redundant baselines. This random phase is known as “redundancy noise”. This noise in the phase of the fringes is not cancelled by closure phases. Moreover, despite having non-redundant baselines, “redundancy noise” is still present in the data, and it is produced due to the finite size of the pinholes (Readhead et al., 1988). Even in the presence of AO correction, “redundancy noise” is responsible for the uncertainties in the closure phases (Tuthill et al., 2006). Therefore, the size of the pinholes are selected to be smaller than Fried’s parameter to minimize this problem (Bernat et al., 2012).

This condition imposes strong constraints on the mask’s design. First, because ill-designed masks could lead to non-uniform $u - v$ coverage. Moreover, the design of the masks should take into consideration the possible obstruction by the telescope spider and the secondary mirror of the telescope. Otherwise, some of the pinholes might be totally (or partially) obscured. The size of the pinholes is also important, very small pinholes reduce the number of photons detected, limiting the magnitudes of the sources that could be observed. On the other hand, large pinholes deal worse with noise and wavefront fluctuations. Carlotti and Groff (2010) proposed a triple correlation between some initial pinholes to determine the optimal place of new ones (see also Carlotti et al., 2012).

THE FUTURE OF APERTURE MASKING

OVER the last ten years, SAM interferometry has become very valuable to obtain high-angular resolution observations of many different astrophysical scenarios. Tuthill (2012) gives a complete description of the history and future perspectives for aperture masking interferometry. Among the future developments to this technique are: a) the combination of SAM with polarimetry; b) the combination of SAM with extreme-AO systems; c) the combination of SAM with integral field spectroscopy (Zimmerman et al., 2012); d) the implementation of SAM in the James Webb Space Telescope (Perrin et al., 2012; Sivaramakrishnan et al., 2014); e) the use of SAM to perform metrology; f) the Pupil Remapping and; g) the implementation of the Kernel-Phases technique in ground based observations.

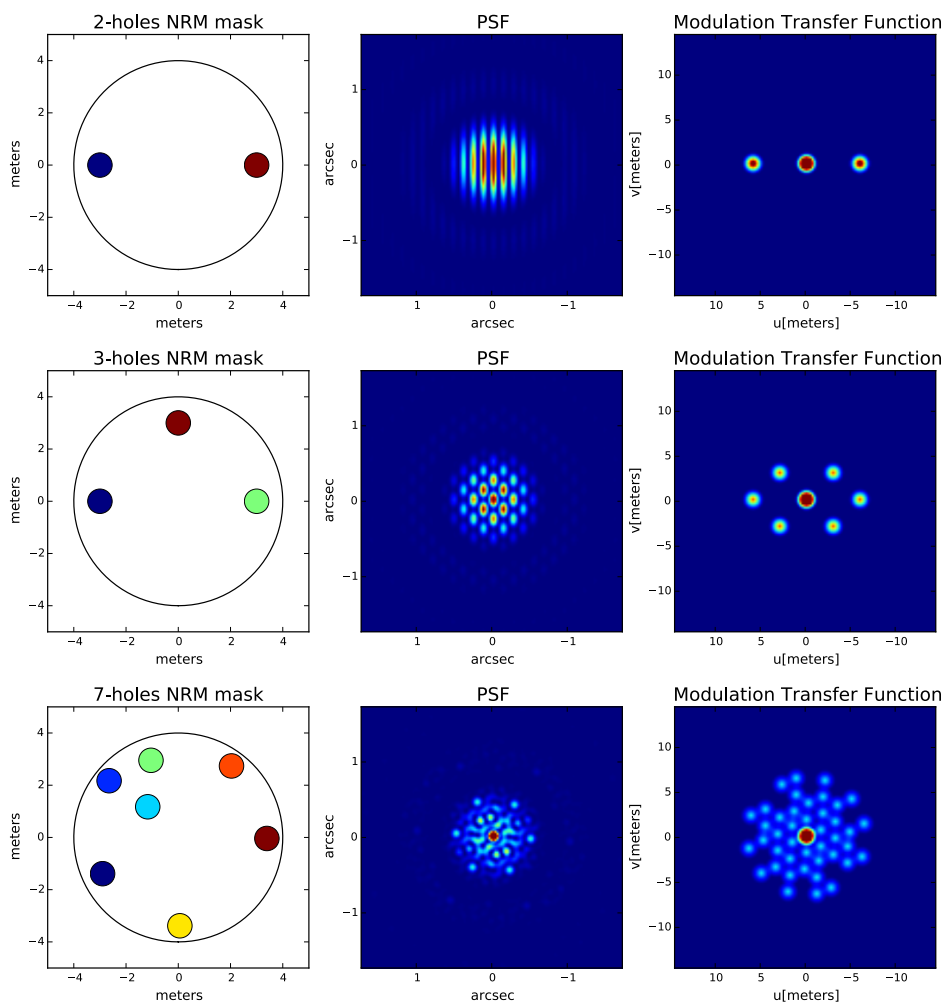


Figure 2.9: The figure displays three interferometric SAM arrays, their PSFs, and mutual transfer functions (i.e. the auto-correlation function of the transfer function of the NRM). The *left* column displays the position of the holes in the mask, each one identified with a different color. The column in the *middle* displays the interference pattern produced by the given arrays for a point-like object. This pattern is the point spread function of the given arrays and it is known as “interferogram”. The *right* column shows the absolute value of the Fourier transform of the interferograms, known as MTF.

Among the future SAM implementations and modifications, there are two very promising ones: the Pupil Remapping and the Kernel Phases. Pupil remapping takes advantage of high-transmission light systems (e.g., fiber optics) to guide the light from different segments of a mirror to create a beam combiner array. Therefore, simultaneous interference patterns could be created at the detector from different segments of the telescope. Some advantages of this implementation include: i) dedicated sampling of separated short and long baselines; b) efficient $u-v$ coverage; c) mitigation of frequency smearing due to spatial filtering with the single-mode fibers (waveguide optics) (Lacour et al., 2007; Perrin et al., 2007; Tuthill et al., 2010). Figure 2.10 displays an example of pupil remapping with the James Webb Space Telescope.

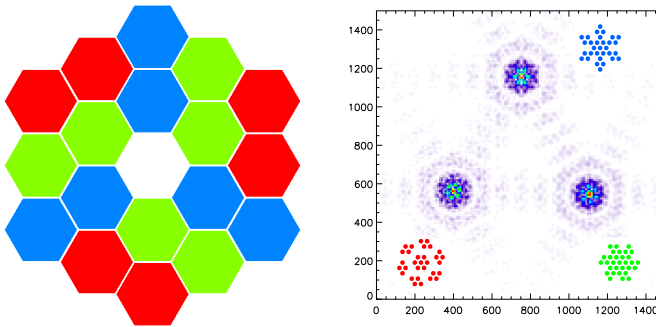


Figure 2.10: *Left* panel displays the segmented mirror of the James Webb Space Telescope. Different colors in the diagram correspond to segments of the mirror that will be used together to remap the pupil in different interferograms. Since this telescope will be located in orbit, the data are not affected by the atmosphere. Therefore, the size of the segments used for the pupil remapping is not restricted. When this technique is applied on ground-based facilities, the size of the segments should be smaller than the isoplanatic patch, unless they are AO-assisted. *Right* panel shows the interference patterns created with the three different arrays. These interferograms are recorded simultaneously at the detector of the telescope. The different $(u-v)$ coverage are also displayed in similar colors than the used segments of the telescope. Image taken from Tuthill (2012).

On the other hand, Kernel Phases (Martinache, 2010) uses a generalization of the closure phases concept to discretize a full-pupil telescope. This is done in order to obtain the linear independent phase information from the different combinations of the discrete elements of the pupil. This technique uses a Single Value Decomposition (SVD) method to solve the transfer matrix that maps the pupil phase into the Fourier space (Ireland, 2013; Martinache, 2011, 2014). This method has been successful to perform high-contrast detections for space observations. For example, Pope et al. (2013) used this technique to resolve brown dwarf binaries with contrast ratios up to ~ 160 , using Hubble Space Telescope observations. However, up to now, it is limited to observations with very-high Strehl ratios. For instance, for ground based observations, this technique could be used only with extreme-AO systems.

2.5. IMAGE RECONSTRUCTION IN OPTICAL INTERFEROMETRY

INTERFEROMETERS provide sparse measurements of the Fourier transform of the brightness distribution for a given source in the plane of the sky (the so-called visibility functions). Therefore, images must be reconstructed from these observables. Image reconstruction from interferometric data is, in principle, a Fourier inversion problem. Nevertheless, there are some details to take into account, particularly for the case of data obtained with optical interferometers. For example, (a) the sparseness of the $u - v$ coverage and; (b) the poor calibration of the amplitude of the visibilities due to the strong non modeled variations produced by the atmosphere turbulence.⁵

IMAGING THE DATA

If $O(\theta_x, \theta_y)$ is the true image that we would like to recover from the observed data $I(\theta_x, \theta_y)$, imaging process can be formulated as:

$$I(\theta_x, \theta_y) = PSF(\theta_x, \theta_y) \otimes O(\theta_x, \theta_y) + e(\theta_x, \theta_y) \quad (2.13)$$

where $e(\theta_x, \theta_y)$ is the additive noise. On the other hand, the Fourier domain version of this imaging model is:

$$V^{data}(u, v) = OTF(u, v)V^{real}(u, v) + e(u, v) \quad (2.14)$$

where $OTF(u, v)$ in the Optical Transfer Function of the system, and it is equivalent to the Fourier transform of the PSF. Having a set of measured visibilities $V_{j1, j2, m}^{data}$, Eq. 2.14 can be represented as follows:

$$V_{j1, j2, m}^{data} = \mathbf{OTF}(j1, j2, m)\mathbf{V}^{real}(\mathbf{v}_{j1, j2, m}) + \mathbf{e}_{j1, j2, m} \quad (2.15)$$

where $\mathbf{V}(\mathbf{v}_{j1, j2, m})$ is the Fourier transform of the intrinsic brightness distribution of the observed object, the indices $(j1, j2, m)$ are part of a set B_k , that correspond to the m th number of measurements of a given pair of telescopes $(j1, j2,)$ which measure the k th spatial frequency \mathbf{v}_k , that is:

$$(j1, j2, m) \in B_k \iff \frac{\mathbf{r}_{j2, m} - \mathbf{r}_{j1, m}}{\lambda} = \mathbf{v}_k \quad (2.16)$$

where, \mathbf{r} is the projected position of the telescopes and λ the observed wavelength. Since an image is the representation of a given brightness distribution into pixels, performing the image reconstruction requires a discrete model of the brightness distribution, and of its Fourier transform. The discretized representation of the intensity distribution of a given source in the plane of the sky is given as follows:

$$\mathbf{I}(\boldsymbol{\theta}) = \sum_{n=1}^N x_n b_n(\boldsymbol{\theta} - \boldsymbol{\theta}_n) \xrightarrow{F.T.} \mathbf{V}(\mathbf{v}) = \hat{\mathbf{b}}(\mathbf{v}) \sum_{n=1}^N x_n e^{-2i\pi\boldsymbol{\theta}_n \cdot \mathbf{v}} \quad (2.17)$$

⁵The following sections are based on the papers of Thiébaud (2009), Thiébaud and Giovannelli (2010) and Thiébaud (2013), unless others are explicitly mentioned.

where $b_n(\boldsymbol{\theta} - \boldsymbol{\theta}_n)$ corresponds to the basis functions -the pixels- $b_n(\boldsymbol{\theta})$ shifted at the grid nodes, and x_n are the image parameters that define the value of the brightness distribution at each pixel. Therefore, with this discretization, $V_{j_1, j_2, m}^{data}$ can be represented in the following way:

$$V_{j_1, j_2, m}^{data} = \mathbf{OTF}(j_1, j_2, m)(\mathbf{A} \cdot \mathbf{x})_k + e_{j_1, j_2, m} \quad (2.18)$$

where $\mathbf{A} = \hat{b}(\mathbf{v})e^{-2i\pi\boldsymbol{\theta}_n \cdot \mathbf{v}k}$. Since this model of the visibilities is linear with respect to \mathbf{x} , it can be described with matrix notation in the following way:

$$\mathbf{d} = \mathbf{OTF} \cdot \mathbf{A} \cdot \mathbf{x} + \mathbf{e} = \mathbf{M} \cdot \mathbf{x} + \mathbf{e} \quad (2.19)$$

The image reconstruction process aims at finding the values of the parameters \mathbf{x} such they minimize the differences between the model matrix \mathbf{M} and the data \mathbf{d} . There are two ways to map the matrix \mathbf{M} into the frequel plane (i.e., the Fourier transform of the pixel plane). The first one is to *interpolate* the discrete Fourier transform of the image with the sampled spatial frequencies. Nevertheless, rarely, the sampled spatial frequencies lie on top of one frequel (like in the case of “splodges” in SAM). Therefore, to represent the position of the spatial frequencies, an *interpolation* of the adjacent frequels to the mean position is performed. This method is equivalent to a convolution of the data with the kernel of the interpolation (e.g., a box of nearest neighbor frequels). The second method consists of interpolating the data onto a grid of frequels. This method is known as *regridding*. There are some considerations to take into account when this method is used. (i) When there are a lot of data with similar spatial frequencies, some of them could lie in the same frequel. This means that some of the data in the frequel space are correlated. Usually, these correlations are ignored and the data per frequel are assumed to be independent. This, however, might be a poor representation of the likelihood of the data. (ii) There are some observables that are not easy to *regrid*, particularly in optical interferometry, like the closure phases. This is because this observable is not smooth, and its range is limited to $-\pi$ and π . Figure 2.11 displays a schematic of interpolation and regridding of the spatial frequencies in an image.

As a consequence of mapping the data into a discrete grid, the number of pixels determines the resolution of our model. Therefore, (a) field-of-view aliasing should be avoided, and (b) the field-of-view of the image should be large enough to sample all the measured spatial frequencies. Hence, the chosen pixel size of the reconstructed image should be of the order of:

$$\Delta\theta \lesssim \frac{\lambda}{4B_{max}} \quad (2.20)$$

The best representation of the image is thus the one with the minimum discrepancies between the model and the real data. It is represented as follows:

$$\mathbf{x}_{ML} = \arg \min f_{ML}(\mathbf{x}) \quad (2.21)$$

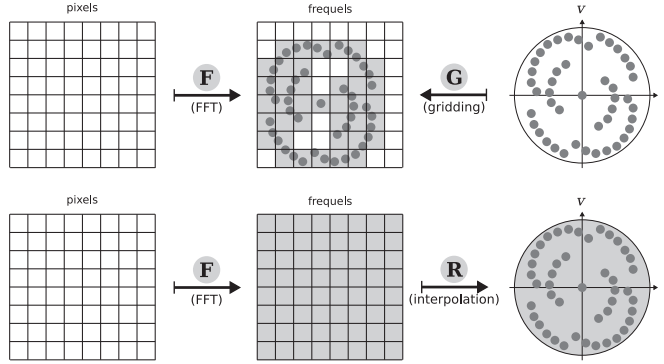


Figure 2.11: Schematic representation of mapping spatial frequencies into a discretized space. The upper panel displays regridding of the data (i.e. interpolation of the data with the frequel space), the bottom panel displays the Fourier interpolation (i.e. interpolation of the model with the data). Image taken from Thiébaud (2009).

where “argmin” means that the left side of the equation is equal to the value of \mathbf{x} that minimizes the right side of the equation, and $f_{ML}(\mathbf{x})$ is equivalent to:

$$f_{ML}(\mathbf{x}) = [\mathbf{d} - \mathbf{M} \cdot \mathbf{x}]^T \cdot \mathbf{W}_{err} \cdot [\mathbf{d} - \mathbf{M} \cdot \mathbf{x}] \quad (2.22)$$

where \mathbf{W}_{err} is the inverse of the covariance matrix of the errors \mathbf{e} . The minimum of f_{ML} can be found by solving the following “normal equation”:

$$\mathbf{M}^T \cdot \mathbf{W}_{err} \cdot \mathbf{M} \cdot \mathbf{x}_{ML} = \mathbf{M}^T \cdot \mathbf{W}_{err} \cdot \mathbf{d} \quad (2.23)$$

Nevertheless, since the $u - v$ coverage of the data is sparse, the solution of Eq. 2.23 is not unique, having many solutions that could fit the observed data. A simple way to find a solution to Eq. 2.23 is to assume that the matrix $\mathbf{M}^T \cdot \mathbf{W}_{err} \cdot \mathbf{M}$ is positive and semi-definite. Therefore, a valid value of \mathbf{x}_{ML} is:

$$\mathbf{x}_{ML} = \mathbf{x}_{dirty} = [\mathbf{M}^T \cdot \mathbf{W}_{err} \cdot \mathbf{M}]^\dagger \cdot \mathbf{M}^T \cdot \mathbf{W}_{err} \cdot \mathbf{d} \quad (2.24)$$

This solution is known as the *dirty map*. In practical terms, the *dirty map* corresponds to a Fourier inversion of the mapped data into the frequel space, where the missing frequencies are equivalent to zeros. This *dirty map*, or dirty image, corresponds to the real brightness distribution of the source convolved with the 2D transfer function of the system (see Fig. 2.12). Although, the *dirty map* is one of the solutions to the image reconstruction problem it does not fully minimize the difference between the image model and the data. Several techniques to find a more optimized solution have been developed. In the case of Radio interferometry, since the intrinsic observables are the amplitude and phases of the visibilities, a deconvolution-like process is widely used. The most known algorithm used in Radio astronomy for image reconstruction is CLEAN (Högbom, 1974;

Schwarz, 1978). Alternatively, in optical interferometry, the lack of all the phase information and the use of squared visibilities, requires the use of a Bayesian approach to perform the image reconstruction.

CLEAN

2

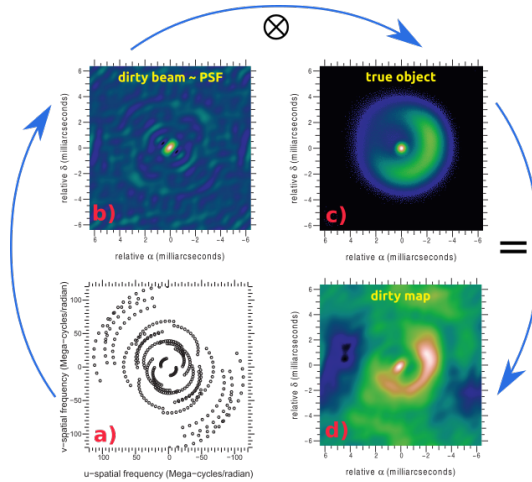


Figure 2.12: The panels display: (a) a $u-v$ coverage; (b) the *dirty beam* or the optical transfer function of the interferometer; (c) the real brightness distribution of the object; (d) the *dirty map*, which is the convolution of the dirty beam and the brightness distribution of the target. The target corresponds to the simulated data used for the Optical Interferometry Beauty Contest 2014 (see Lawson et al., 2004), and represents a model of LkHa 101. The $u-v$ coverage displayed in panel a corresponds to a simulation of the spatial frequencies sampled by the Navy Prototype Optical Interferometer (NPOI). The $u-v$ coverage was simulated with the data reduction suite OYSTER by C. A. Hummel. Image taken from Thiébaud (2013).

THE CLEAN algorithm begins with the *dirty map*. According to Frey and Mosoni (2009), this algorithm considers that the brightness distribution can be represented as a collection of point-like sources, and that there are no other elements in the field-of-view than the target of interest. The point-like sources that represent the brightness distribution of the source are estimated from the dirty map, removed from it, and stored in a new map. The estimation of the point-like sources is performed by iterative subtractions of the dirty beam from the maximum (or to some fraction of the peak; $\Delta_{max} = 5\%$) of the dirty map. When the maximum and minimum of the residual map have a similar value the iterative process stops. Finally, the new map with the point-like sources is convolved with a gaussian-like beam of the size of the main lobe of the dirty beam, and added to the residual map. Some of the handicaps of this technique are that:

(a) The convolution of the CLEANed image with a Gaussian function, whose FWHM is the same of the dirty beam, filters all the information beyond the diffraction limit. This smoothing process could modify the amplitude of the visibilities. Therefore, the fidelity of the reconstructed image is not longer maximized, particularly at the spatial

frequencies close to the diffraction limit.

(b) CLEAN does not use naturally the uncertainties of the data. Therefore, there is not a natural method to weight the SNR data, specially for data sets that include several instruments. Figure 2.13 displays an example of a dirty beam, dirty map, clean beam and clean map of a binary star.

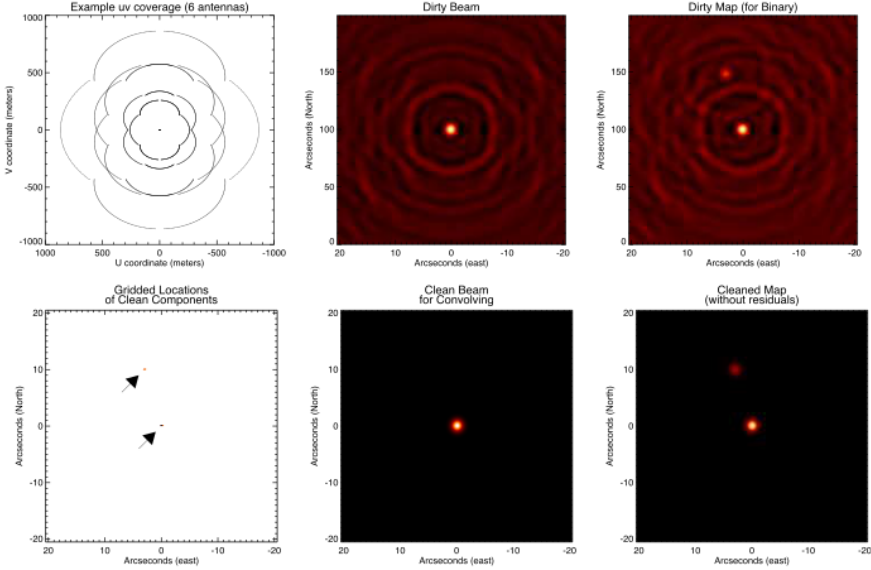


Figure 2.13: The image displays an example of a dirty beam, a dirty image of a binary source, as well as their corresponding $u-v$ coverage (upper panels). In the bottom panels, a representation of the binary source in the discrete (image) plane is displayed, together with the clean beam and CLEANed image. Image adapted from [Monnier and Allen \(2013\)](#)

BAYESIAN IMAGE RECONSTRUCTION

GIVEN the problem of multiple solutions of \mathbf{x}_{ML} , there is a necessity to use a given criteria to restrict the space of parameters to reconstruct a valid brightness distribution for the observed object. Therefore, the use of a Bayesian approach is used. For instance, \mathbf{x}_{ML} is represented as follows:

$$\mathbf{x}_{ML} = \operatorname{argmax} \Pr(\mathbf{x}|\mathbf{d}, \mathbf{m}) \quad (2.25)$$

where “argmax” means that the left side of the equation is equal to the value of \mathbf{x} that maximizes the right side of the equation, and $\Pr(\mathbf{x}|\mathbf{d}, \mathbf{m})$ is:

$$\Pr(\mathbf{x}|\mathbf{d}, \mathbf{m}) = \frac{\Pr(\mathbf{x}|\mathbf{m})\Pr(\mathbf{d}|\mathbf{x}, \mathbf{m})}{\Pr(\mathbf{d}|\mathbf{m})} \quad (2.26)$$

Here, $\Pr(\mathbf{x}|\mathbf{d}, \mathbf{m})$ corresponds to the “a posteriori” probability to find the intrinsic brightness distribution of the source (i.e. the image parameters) given the data \mathbf{d} and the

model \mathbf{m} . $\Pr(\mathbf{x}|\mathbf{m})$ is the probability of the image parameters given the “a priori” model of the true brightness distribution. $\Pr(\mathbf{x}|\mathbf{m})$ is assumed to be proportional to $e^{-\mu R(\mathbf{x})}$, where μ is the weight of the regularization and $R(\mathbf{x})$ is the regularization function. $\Pr(\mathbf{d}|\mathbf{x}, \mathbf{m})$ represents the likelihood of the data given the model image (i.e. the standard χ^2 function $e^{-1/2\chi^2(\mathbf{x})}$). Taking the negative log-probabilities to Eq. 2.25, we have:

$$\begin{aligned}\mathbf{x}_{ML} &= \operatorname{argmin} [-\ln [(\Pr(\mathbf{d}|\mathbf{x}, \mathbf{m})) + (\Pr(\mathbf{x}|\mathbf{m}))]] \\ \mathbf{x}_{ML} &= \operatorname{argmin} \left[-\ln \left[e^{-1/2\chi^2(\mathbf{x})} + e^{-\mu R(\mathbf{x})} \right] \right] \\ \mathbf{x}_{ML} &= \operatorname{argmin} [1/2\chi^2(\mathbf{x}) + \mu R(\mathbf{x})]\end{aligned}\quad (2.27)$$

Therefore, in Eq. 2.27, we have a *regularized maximum likelihood*. There are many regularizers $R(\mathbf{x})$. Some of the most widely used ones, based on the pixel-flux level, are named in Table 2.2. Among the regularizers, entropy is a very interesting one. This quantity ensures that the information contained in the image is the minimum possible (Baron and Young, 2008). Entropy allows to quantify the complexity of the image and find the “most uniform image” based only on the quality of the data. This regularizer can deal with data having different errorbars, and the reconstructed image is just a straight-forward inversion between the image and the $u - v$ plane. Thus Maximum Entropy methods allow to reconstruct images with *super-resolution* beyond the diffraction limit. This is simply because the image reconstruction process depends only on the optimization of the entropy functional and not only the resolution of the sampled longest baselines (Monnier and Allen, 2013).

There are several methods to find \mathbf{x}_{ML} . Two of the most important ones are the gradient descent method and the Monte Carlo Markov chain method. The **Gradient descent** is an optimization algorithm that takes steps proportional to the negative of a gradient function with respect to the image pixels. This method is fast; however, it may fall on local minima that can lead to a misleading solution in the image reconstruction process (see Baron and Young, 2008; Thiébaud and Giovannelli, 2010). On the other hand, the **Monte Carlo Markov Chain** is based on a random process which determines flux elements in a pixel grid (i.e. a Markov chain). The algorithm stops when the desired distribution of pixel flux fits its equilibrium distribution. This method uses a comparison between models like “nested sampling” or “parallel tempering” to check whether the convergence criteria have been reached (see Baron and Kloppenborg, 2010; Ireland et al., 2006). The great advantage of this method is that it could find a global minimum, at the cost of being slower than the gradient descent method.

To illustrate the role of regularizers in the image reconstruction process, Figure 2.14 displays two reconstructed images using the aperture masking data reported by Monnier et al. (1999) on the red super-giant VY CMa. These aperture masking data were taken with the Keck I telescope using a *21-holes* non redundant mask at $1.65 \mu\text{m}$. The reconstructed images were obtained using two different regularizers: (a) Gull-Skilling entropy (i.e. MEM) and (b) a quadratic regularization. The field-of-view of the images is of 600 mas with a pixel scale of 6 mas/pixel. The entropy image converged after 106 iterations

to a $\chi^2=1.009$; while the quadratic image only reached a $\chi^2=1.610$ after 2000 iterations. It is easily observed that the main features are similar in both images up to a contour level of 5% of the peak. However, for lower contours the distribution appears to be quite different, being the reconstructed image with a quadratic regularizer noisier. Comparing panel *c*) of Fig. 2.14 with panel *a*) of Fig. 2 in Monnier et al. (1999), both images are quite similar, being the reconstructed entropy image the one that better reproduced the real brightness distribution of the source.

Table 2.2: Regularizers for image reconstruction

| Name | Function | Reference |
|--------------------------|----------------------------------------------------|------------------------------------------------|
| Maximum Entropy | $R(\mathbf{x}) = -\sum_i x_i \log \frac{x_i}{m_i}$ | Burch et al. (1983); Skilling and Bryan (1984) |
| Burg Entropy | $R(\mathbf{x}) = \sum_i \log x_i$ | Narayan and Nityananda (1986) |
| Quadratic regularization | $R(\mathbf{x}) = \sum_i x_i^2$ | Tikhonov and Arsenin (1977) |
| Total Variation | $R(\mathbf{x}) = \sum_i \nabla(\mathbf{x}) _i$ | Rudin et al. (1992) |

Note: f_i is the positive fraction of pixel i , m_i is an image prior given by the user.

IMAGE RECONSTRUCTION SOFTWARE

IMAGE reconstruction software in optical interferometry is still an open field of research. Since 2004 the Optical Interferometry community, supported by the International Astronomical Union, has performed a bi-annual contest termed “The Beauty Contest”. Its objective is to test algorithms and techniques to perform image reconstruction in optical interferometry (Lawson et al., 2004). Here, I present some of the software packages used by the groups participating in the Beauty Contest.

BSMEM:⁶ This code uses a Bispectrum Maximum Entropy Method to reconstruct images. It was developed by the Cambridge optical interferometry group. BSMEM uses a gradient descent method to maximize the inference of an image (Buscher, 1994). This software accepts two types of regularizers: Gull-Skilling entropy and Quadratic regularization. The input files of the software are standard OIFITS files. The likelihood of BSMEM corresponds to a standard χ^2 , which minimizes residuals of the powerspectra + bispectra, $(J_n^{\text{pow}}) + (J_n^{\text{Bis}})$, obtained after subtracting the measured values from the model. This can be expressed in the following way (Baron and Young, 2008):

$$\chi_D^2 = \sum_{n=1}^{N_{\text{pow}}} J_n^{\text{pow}} + \sum_{n=1}^{N_{\text{bis}}} J_n^{\text{Bis}} \quad (2.28)$$

where the powerspectrum and the bispectrum are defined in the following form:

$$J_n^{\text{pow}} = \left(\frac{P_n - P_n^{\text{data}}}{\sigma_{P_n}} \right)^2 \quad (2.29)$$

⁶Available at: <http://www.mrao.cam.ac.uk/research/optical-interferometry/bsmem-software/>

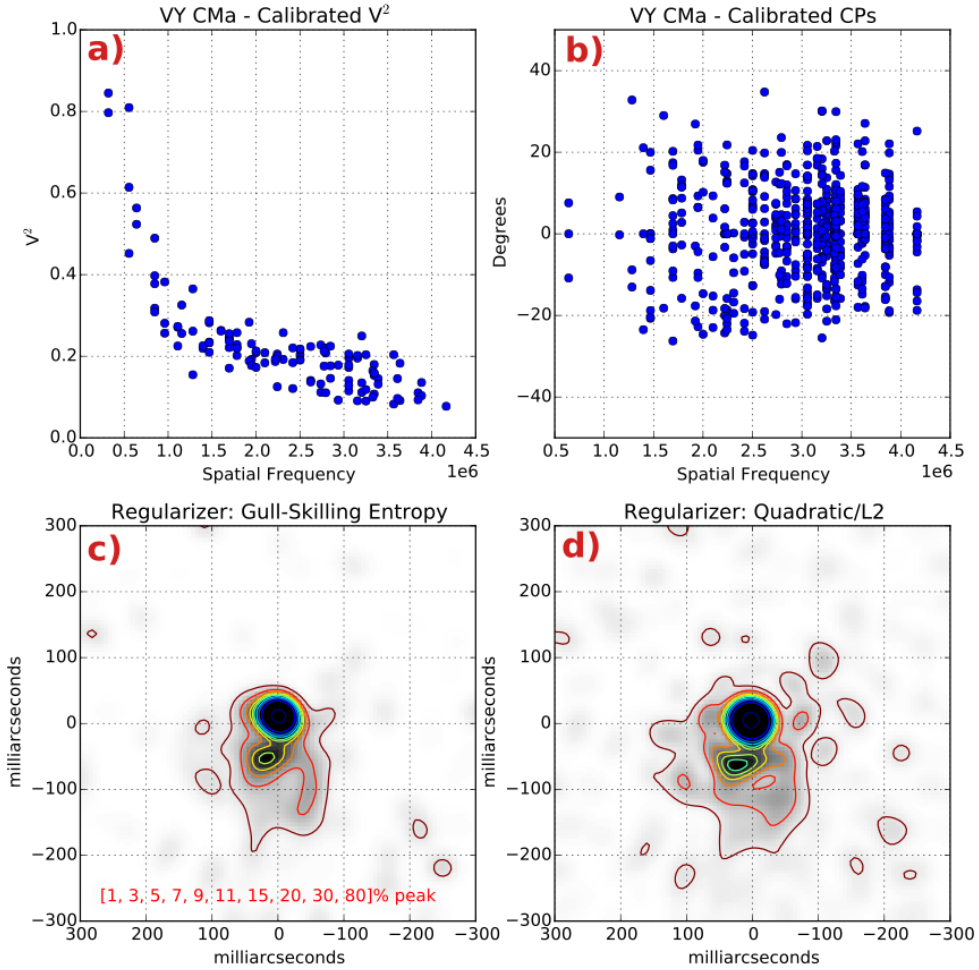


Figure 2.14: The image displays a comparison of reconstructed images using different regularizers. Panel *a*) displays the calibrated V^2 of the aperture masking data on VY CMa taken at $1.65 \mu\text{M}$. Panel *b*) displays the calibrated closure phases. Panel *c*) displays a reconstructed image using Gull-Skilling entropy. Panel *d*) displays a reconstructed image using a quadratic regularizer. Contours for both panels *c* and *d* are label on panel *c*.

$$J_n^{\text{Bis}} = \left(\frac{\Re \left[(B_n - B_n^{\text{data}}) \frac{B_d^{\text{data}*}}{|B_d^{\text{data}}|} \right]}{\sigma_n^{\text{rad}}} \right)^2 + \left(\frac{\Im \left[(B_n - B_n^{\text{data}}) \frac{B_d^{\text{data}*}}{|B_d^{\text{data}}|} \right]}{\sigma_n^{\text{tan}}} \right)^2 \quad (2.30)$$

with:

$$\sigma_n^{\text{rad}^2} = \frac{1 + e^{-\sigma_{C_n}^2}}{2} T_n^2 + \frac{1 + e^{-\sigma_{T_n}^2}}{2} \sigma_{T_n}^2 \quad (2.31)$$

$$\sigma_n^{\text{tan}^2} = \frac{1 - e^{-\sigma_{C_n}^2}}{2} T_n^2 + \frac{1 - e^{-\sigma_{T_n}^2}}{2} \sigma_{T_n}^2 \quad (2.32)$$

where P_n are the modeled powerpectra data, P_n^{data} are the sampled values of the powerspectrum, and σ_{P_n} are their uncertainties. Analogously, B_n are the modeled bispectra, and B_n^{data} are the measured bispectrum data. $B_d^{\text{data}*}$ and $|B_d^{\text{data}}|$ are the complex conjugates of the bispectrum data and their absolute values, respectively. It is important to highlight that for the bispectra a standard χ^2 is not used. This is because a Gaussian statistics of the noise is assumed and also the amplitude and phase of the complex data are assumed to be independent variables (Pauls et al., 2005). Therefore, a quadratic convex approximation of the true likelihood is assumed (i.e. a noise ellipse is a good representation of the bispectra errors). Therefore, $\sigma_n^{\text{rad}^2}$ and $\sigma_n^{\text{tan}^2}$ are the radial and tangential components of the noise ellipse. C_n and T_n correspond to the closure phase and triple amplitudes measurements, respectively.

Along the following chapters of this thesis, we have used BSMEM extensively to reconstruct images of massive stars at different astrophysical scenarios. In fact, the optical interferometry group of the Instituto de Astrofísica de Andalucía participated in the “2014 Beauty Contest”, using BSMEM to reconstruct PIONIER/VLTI images of the surface of two giant-stars: VY-CMa and R Car. As a result of our work, we were selected as the winners of the 6th edition of this international competition (see Monnier et al., 2014). Figure 2.15 displays the reconstructed images made by our group for the Beauty Contest. In the following lines, the main features of the images of the targets are described.

VY CMa:

- It shows an over-resolved dust-shell from which the fraction of emission in the shell compared to the star can be computed.
- The photosphere is elongated along East-West direction (it could be due to optical depth effects from foreground dust, circumstellar molecular emission, and/or temperature variations across photosphere).
- Two bright spots are on the eastern limb of star.

- While the fraction of light in the shell depends on the wavelength, the features relating to the star itself do not appear strongly chromatic.
- The H band diameter is approximately the same size as the near-continuum K band size reported by VLTI/AMBER (~ 11.3 mas).

R Car:

- It shows prominent circumstellar emission shells.
- The shells are significantly stronger in the edge channels of H band, hardly visible in the center channel.
- The photosphere is mostly circular but with two main spots near the center. The two spots are close together and so could be really one asymmetric, elongated spot.

MiRA:⁷ This software is a Multi-aperture Image Reconstruction Algorithm. The algorithm is designed to reconstruct images even with poor $u - v$ coverage, or with data without closure phase information (Thiébaud, 2008). MiRA uses a Fourier interpolation to sample the observed visibilities into the frequel space. This setup allows the code to be efficient over a large data set. One of the advantages of MiRA is the large number of regularizers implemented in this software. MiRA uses a limited variable memory method (Thiébaud, 2002) to look for the best image. It is based on an optimization over a small sub-space of search direction, which are determined by the penalization function. To ensure that the recovered image is normalized and positive, MiRA implements a change of variable in the brightness distribution, \mathbf{x} , becoming:

$$x_j = \frac{x'_j}{\sum_k x'_k} \quad (2.33)$$

where $\mathbf{x}' \in \mathbb{R}^n$. MiRA is not designed to deal with the specific degeneracy of the bispectrum; it can account for any kind of data to reconstruct the image. This is the reason why it is able to reconstruct images without phase information (with 180° orientation ambiguity).

MACIM:⁸ This software is a MARKov Chain IMager that performs a global optimization process of the image model probability (Ireland et al., 2006). MACIM uses a maximum-entropy regularizer, as well as a dark interaction energy regularizer. This second one consists of the sum of all pixel boundaries with zero flux on either side of the boundary. Therefore, it favors large regions of dark spaces with interwoven bright regions. As a consequence, this regularizer is particularly useful to map binary or multiple systems. The

⁷Available at: <http://cral.univ-lyon1.fr/labo/perso/eric.thiebaud/?Software/MiRA>

⁸Available at: <http://www.mso.anu.edu.au/~mireland/macim.html>

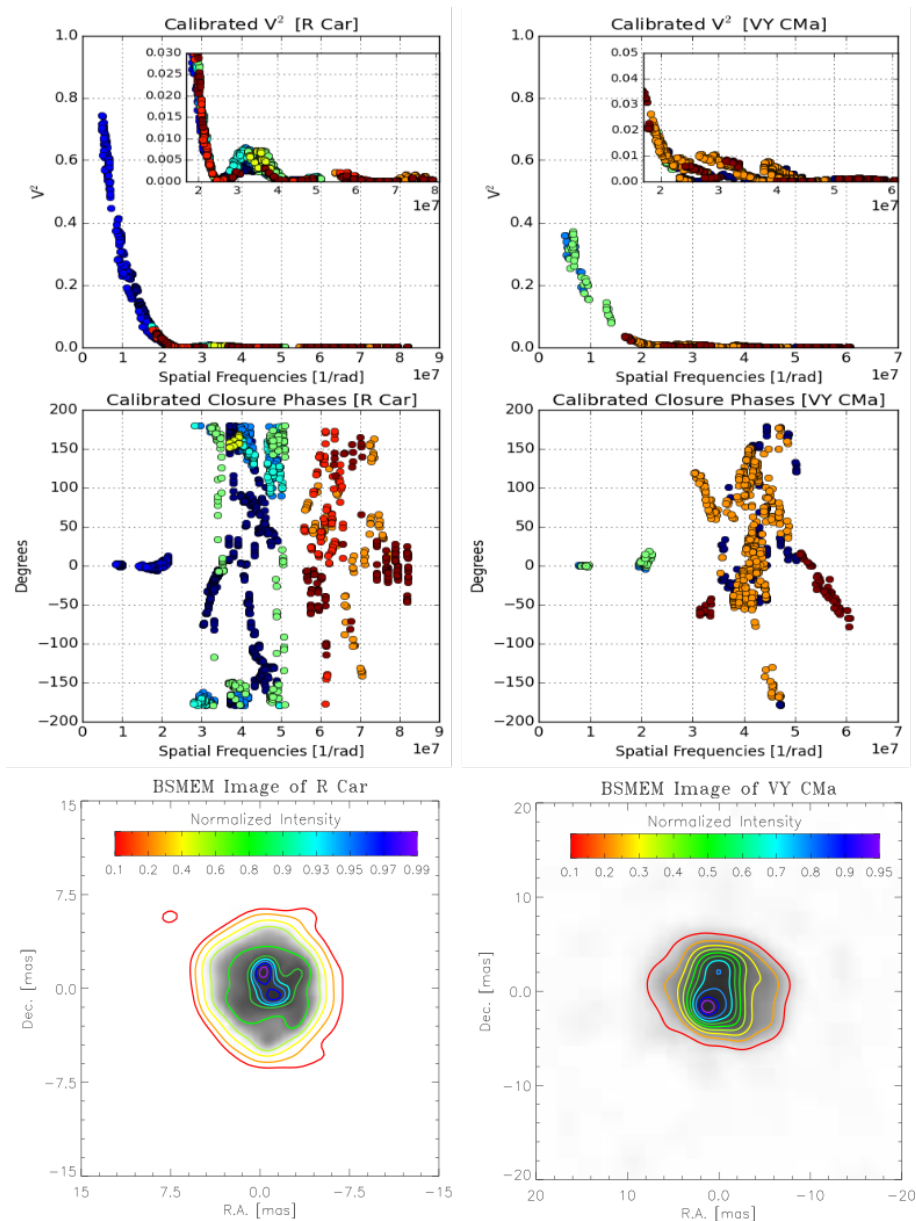


Figure 2.15: The figure displays the received interferometric observables and the reconstructed images that won the “2014 Interferometric Image Reconstruction Beauty Contest” using PIONIER/VLTI data. The *right* column corresponds to the data and image of VY CMa, the FWHM of the convolved beam used for in the image reconstruction is of 1.7 mas. The *left* column displays the R Car data and image, the full width at half maximum (FWHM) of the convolved beam for this source is of 1.3 mas. Both panels has a pixel scale of 0.3 mas/pixel. The different colors in the observables correspond to different sub-sets of observations. The values of the different contours in the BSMEM images are displayed on the image.

handicap of this algorithm is that the convergence can be very slow, depending on the initial parameters.

Additionally to the mentioned software, there are some other packages in the community to perform image reconstruction. To obtain more information see [Monnier et al. \(2014\)](#), where a list of them is given, as well as examples of reconstructed images. As a new approach to tackle the image reconstruction problem, [Schutz et al. \(2014, 2015\)](#) presented a new code called PAINTER (Polychromatic opti**AI** INTERferometric Reconstruction software). This software is a spatial-spectral (3D) image reconstruction algorithm that uses the powerspectra, the bispectra, and the differential phases to perform a polychromatic image reconstruction.

3

THE FORMATION OF MASSIVE STARS

THE CASE OF NGC 3603 IRS9A*

*Whenever we proceed from the known into the unknown
we may hope to understand, but we may have to learn
at the same time a new meaning of the word "understanding."*

Werner Heisenberg

This chapter is dedicated to the description of the initial conditions of the formation of massive stars. Despite the theoretical and observational advances in the last decades to study the first stages of the high-mass stars lives, there is still an open controversy about how these stars are formed. Currently, the two main competing theories are: (i) monolithic collapse and (ii) competitive accretion. Both theories suggest that massive stars gather mass during their initial phases via accreting disk-like structures. However, those disks have remained elusive for the most massive young objects. This is mainly because of the observational challenges due to the large distances at which they are located, their rareness compared to their low-mass counterparts, and the high interstellar extinction of their dusty parental clouds. Therefore, the study of each young massive stellar object matters. In this work, the case of NGC 3603 IRS 9A, a young massive stellar object still surrounded by an envelope of molecular gas is presented. Previous mid-infrared (MIR) observations with long-baseline interferometry have provided evidence for a disk of 50 mas diameter at its core. Here, these observations are expanded to near-infrared wavelengths. This study analyses new Sparse Aperture Masking data taken with the near-infrared camera of the Very Large Telescope at K_s and L' wavelengths in addition to archival CRIRES*

Parts of this chapter have been submitted to Astronomy & Astrophysics, [Sanchez-Bermudez et al. \(2014b\)](#).

spectra of the H_2 and $B\gamma$ lines. The calibrated V^2 trends of the K_s and L' bands suggest the presence of a partially resolved compact object of ~ 30 mas at the core of IRS 9A, and the presence of an (over-resolved) extended structure. The spectroastrometric signal, obtained from the CRIFRES spectra, of the H_2 line shows that this spectral feature arises from the large scale extended emission (~ 300 mas) of IRS 9A, while the $B\gamma$ line appears to be formed at the core of the object (~ 20 mas). To have a complete understanding of the IRS 9A morphology, steady state radiative transfer models are performed to fit the observed V^2 and SED. Our best model supports the existence of a compact disk-like structure at the core of IRS 9A surrounded by an envelope with bipolar cavities. However, our model still presents inconsistencies between SED modelling and the interferometric data, which may be in part attributed to shortcomings of the data, but probably also implies a more complex morphology of the target than what was assumed in our models.

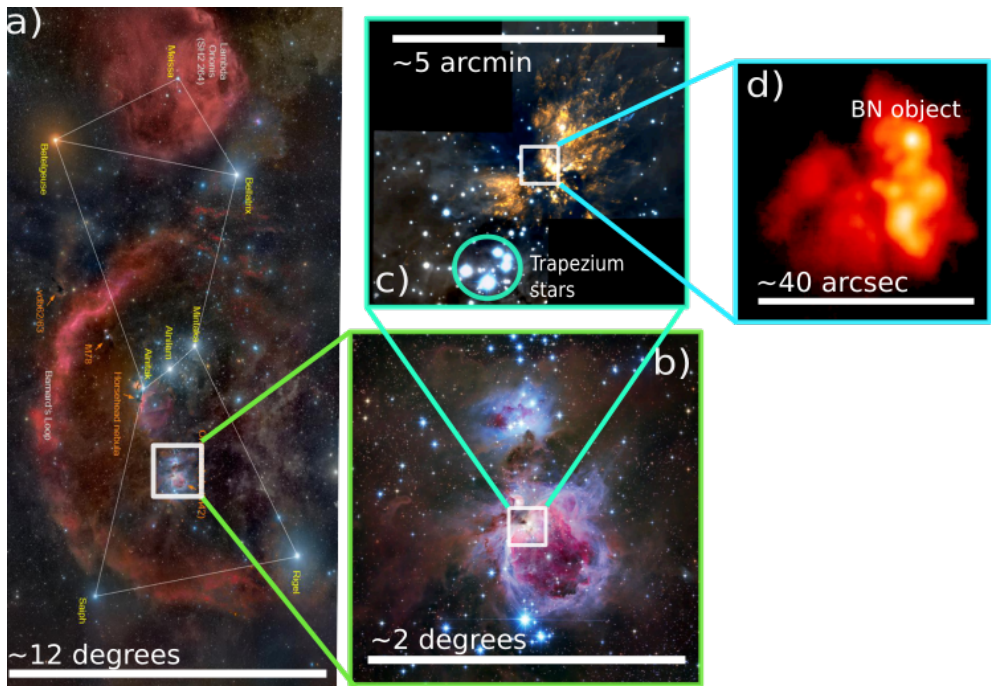


Figure 3.1: Star formation in Orion. The picture in panel *a* shows the giant molecular cloud of Orion, one of the best-known regions of star formation in the Galaxy. Different angular scales are displayed in the different sub-panels. Panel *b* presents a color composite image of the Orion Nebula (M42) taken with the Spitzer Space Telescope. Panel *c* presents the BN/KL region, and in which star formation still occurs nowadays. The image was taken with the Gemini South multi-conjugate adaptive optics system (GeMS), and was adapted from [Bally et al. \(2015\)](#). The “Trapezium” stars (a massive hierarchical system) are labeled. Panel *d* displays a mid-infrared image at $20 \mu\text{m}$ of the so-called Becklin-Neugebauer object, an intermediate-mass protostar, together with other infrared cores where star formation is happening. The image was adapted from [Gezari et al. \(1998\)](#).

3.1. INTRODUCTION: HOW ARE STARS FORMED?

3.1.1. BASIC CONSIDERATIONS

STAR formation takes part in the interiors of (giant) molecular clouds (MCs), which possess a clumpy structure at all spatial scales. The main sub-structure of these clouds consists of: (i) clumps, which are the precursors of stellar clusters; (ii) cores (filaments), the building blocks of individual (or multiple) stars. Table 3.1 displays the typical physical conditions for massive molecular clouds, clumps and cores. Figure 3.1 shows, as an example, the giant molecular cloud in Orion and its structure at different spatial scales, where star formation occurs.

Table 3.1: Physical properties of giant molecular clouds and its fractal substructures.

| Parameter | Giant Molecular Cloud | Molecular Cloud | Clump | Core |
|-----------------------------------------|-----------------------|-----------------|-----------------|------------|
| Size(pc) | 10-60 | 2-20 | 0.1-2 | ≤ 0.1 |
| Density ($n(\text{H}_2)/\text{cm}^3$) | 100-500 | 10^2 - 10^4 | 10^3 - 10^5 | $>10^5$ |
| Mass (M_\odot) | 10^4 - 10^6 | 10^2 - 10^4 | 10 - 10^3 | 0.1-10 |
| Temperature (K) | 7-15 | 10-30 | 10-30 | 7-15 |

Adapted from Mac Low and Klessen (2004).

The formation of stars begins when MCs **compress** to form protostellar cores through gravo-turbulent fragmentation of the cloud (Mac Low and Klessen, 2004). Once the molecular cores are formed, and the cores become self-gravitating, gravity plays an important role in **collapsing** the core, thus forming a star. The “free-fall” time, t_{ff} , required to collapse the gas depends on the density, ρ , of the core in the following form (Zinnecker and Yorke, 2007):

$$t_{ff} = 2.1 \times 10^5 \text{ year} \left[\frac{\rho}{10^{-19} \text{ g cm}^{-3}} \right]^{-1/2}, \quad (3.1)$$

The required mass necessary by the core to collapse is known as the “Jeans mass”, M_{Jeans} , and depends on the temperature of the gas and the density of the core. It is calculated with the following expression:

$$M_{Jeans} = 1.1 M_\odot \left[\frac{T_{gas}}{10 \text{ K}} \right]^{3/2} \left[\frac{\rho}{10^{-19} \text{ g cm}^{-3}} \right]^{-1/2} \quad (3.2)$$

where T_{gas} is the temperature of the gas in the core. After the collapsing phase, the **accretion** of material continues towards the forming star as it evolves, allowing the core to grow in mass. At the same time, the core contracts on the Kelvin-Helmholtz timescale:

$$\tau_{KH} \sim GM_*^2 / R_* L_* \quad (3.3)$$

where G is the gravitational constant, M_* , R_* , and L_* are the mass, radius and the luminosity of the forming star, respectively. The Kelvin-Helmholtz time is the temporal scale necessary, of sufficiently high densities and temperatures, for fusing Hydrogen in the nuclei of stars (Zinnecker and Yorke, 2007). Figure 3.2 displays the Kelvin-Helmholtz timescale for zero-age main-sequence¹ (ZAMS) stars as a function of the stellar mass. The details of the accretion process onto stars is one of the main questions of contemporary astrophysics. According to Zinnecker and Yorke (2007), this problem can be separated into different parts: (i) the evolution of the central core, (ii) the details of transporting material from the disk to the core, (iii) transporting material inward within the disk, and (iv) accretion onto the disk. In the case of massive stars, accretion of material to the central object has to overcome large radiative pressure from the core. How the initial cloud undergoes the collapse and accretion phases is particularly challenging to observe in massive stars because of the extinction produced by the large amount of material around them, and their rapid evolution compared to their lower mass counterparts. The lack of observational constraints means that there still exist several competing theories that aim at explaining the formation of massive stars.

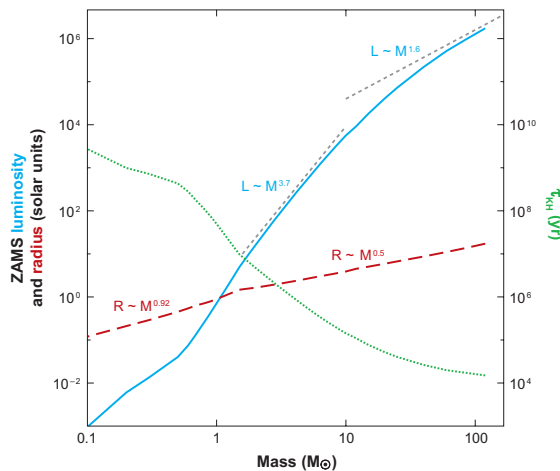


Figure 3.2: Kelvin-Helmholtz timescale as function of the stellar mass. The luminosity and radius of the stellar source as function of the mass is also displayed. Taken from Zinnecker and Yorke (2007).

3.1.2. MODELS OF MASSIVE STAR FORMATION

THERE are two contemporary models that aim at explaining high-mass star formation: **core collapse** (or monolithic collapse) and **competitive accretion**. The main difference between them is the way in which massive stars gather mass during their formation. On the one hand, core collapse (Krumholz, 2006; Krumholz et al., 2007a,b; Mc-

¹ZAMS stars are stellar sources that just began the hydrogen-burning phase in their interiors.

Kee and Tan, 2002) suggests that the total mass of each forming high-mass star is determined since the beginning of the collapsing phase. More specifically, it is constrained by the total mass of the pre-stellar core. Therefore, the resultant spatial and phase space distribution of the newly formed stars and cores should be the same (see e.g., Alves et al., 2007). Krumholz et al. (2007a,b) determined through radiative transfer simulations that the radiation feedback from the release of potential energy of the collapsing gas prevents the fragmentation of the cloud to scales comparable to the Jeans mass ($\sim 0.5 M_{\odot}$). In fact, this model suggests that fragmentation stops at scales on the order of ~ 0.01 - 0.1 pc, forming the pre-stellar massive cores from which massive stars are born. The subsequent evolution of these cores proceeds through the accretion of material via massive disks with sizes on the order of ~ 1000 astronomical units (AU). Yorke and Sonnhalter (2002) performed hydrodynamical simulations of isolated high-mass cores between 30 - $120 M_{\odot}$. These authors found that in the case of a core of $120 M_{\odot}$, a final bound stellar system (or an individual star) of around $43 M_{\odot}$ could be formed according to their simulations. Krumholz et al. (2005) reported that collapsing 100 and $200 M_{\odot}$ cores could form stars of with $M \geq 25 M_{\odot}$. Figure 3.3 shows an snapshot of the Krumholz et al. (2007a) simulations, assuming core-collapse as the formation mechanism.

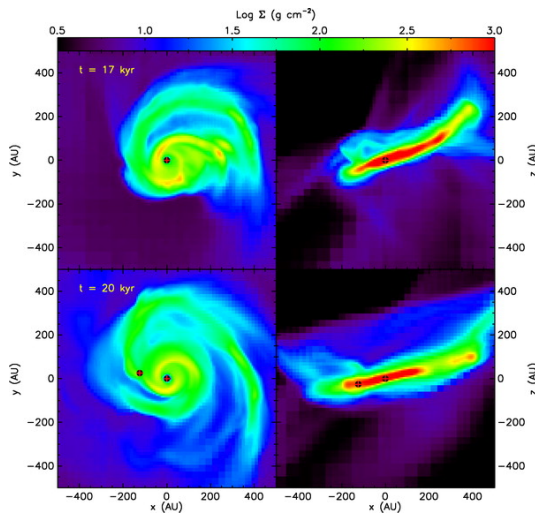


Figure 3.3: The picture shows two moments (at $T=17$ and 20 kyr) in the simulation carried out by Krumholz et al. (2007a), in which massive star formation occurs via monolithic collapse. One of the main results of these simulations is that most of the material in the initial massive core forms one or several stellar objects. Fragmentation and subsequent accretion occur mostly in a self-shielding disk (as it is appreciated in the picture). The *left* panels display the face-on accretion disk and the forming sources, while the *right* panels show the same system viewed edge-on. The color scale indicates the surface density of the system. Black dots with red crosses mark the protostars.

On the other hand, competitive accretion (Bonnell and Bate, 2006; Bonnell et al., 2001, 2004; Smith et al., 2009) is based on the inefficiency of the cloud fragmentation

in a turbulent medium. This model predicts that massive stars are formed from pre-stellar cores with masses around the Jeans mass and subsequently accrete material from their environment. In competitive accretion, the total reservoir of gas available in the cloud affects the massive star formation process. The pre-stellar cores located close to the minimum of the gravitational potential tend to accrete more material, forming massive stars. In contrast, pre-stellar cores located in low-density regions in the cloud form low-mass stars (see Fig. 3.4). This model does not only predict a mechanism to form massive stars, but a complete initial mass function (IMF) for an entire cluster. This scenario also predicts the formation of accretion disks at early stages of forming high-mass stars. However, due to the highly interacting medium in which massive stars are formed, these disks could be truncated or destroyed. In fact, [Moeckel and Bally \(2007\)](#) suggest that interactions with nearby stars assist the capture of companions, thus explaining the hierarchical systems observed.

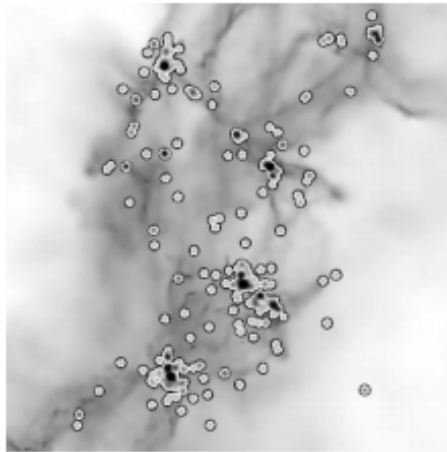


Figure 3.4: The panel displays a snapshot of a simulation by [Bonnell et al. \(2004\)](#) in which the fragmentation of a molecular cloud is observed. Black dots represent massive stars, forming at local minima of the gravitational potential. White dots correspond to low-mass stars. The final mass distribution resulting from this simulation is consistent with a Salpeter Initial Mass Function. The filamentary structure of the cloud is also appreciated.

One important discrimination between the different massive star formation scenarios is the degree of low/intermediate mass components that are formed together with high-mass stars. In the case of monolithic collapse, the massive cores are not prone to a high degree of fragmentation. Therefore, only an insignificant fraction of the cores' mass is converted into low-mass stars. In contrast, for competitive accretion, the cores are highly fragmented, which result in the formation of a large population of coeval low-mass stars (see [Rivilla et al., 2013a,b](#)). Another mechanism of massive star formation invokes stellar collisions and mergers. However, such events are rare and only probable in the centers of rich young clusters.

3.1.3. DISKS AND ENVELOPES IN MASSIVE YOUNG STELLAR OBJECTS

BOTH models predict the formation of disks, so we expect them to be a generic feature of massive young stellar objects. It is therefore imperative to understand the physics of these structures and many fundamental questions are still open (e.g. sizes, accretion rates, densities, ages). This is mainly because of the lack of observational evidence of such disks due to the high extinction that affects MYSOs and the necessity of high-angular resolution. One of the most important questions is the role of the radiation pressure of the luminous central stars ($L \sim 10^4 - 10^5 L_\odot$) on the physics of the accretion disks. Massive stars have short Kelvin-Helmholtz times compared to the accretion time-scale. Figure 3.5 shows the accretion time-scale versus the mass of the forming stars, assuming the Bondi-Hoyle formalism described in [Bonnell and Bate \(2006\)](#). As it is appreciated, when the accretion time-scale is compared with the Kelvin-Helmholtz times of Fig. 3.2, the later ones are lower for the same stellar mass. For example, for a $50 M_\odot$ star its Kelvin-Helmholtz time is 6×10^4 years, while the accretion time-scale is of the order of 10^5 years. This constraint is more evident as the mass increases. The main consequence of this scenario is that, by the time the central star is fusing Hydrogen, it is still accreting material. This increases the radiative output of the central star and thus disrupts the way in which accretion occurs and imposes strong conditions to the formation of high-mass stars. For example, Bondi-Hoyle accretion simulations predict that radiation pressure could stop accretion for massive stars $\geq 10 M_\odot$ ([Edgar and Clarke, 2004](#)). These results highlight the necessity to have proto-stellar disks to shield the accreting material from the radiation pressure to form the most massive stars, as predicted by the massive star formation theories.

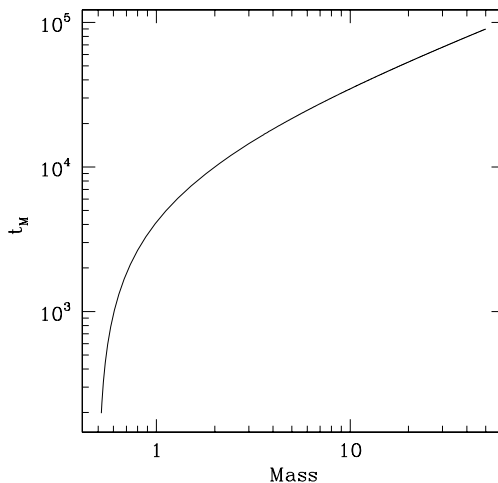


Figure 3.5: Accretion time-scale as function of the stellar mass. The initial conditions included a Jeans mass of $0.5 M_\odot$ and a density of the dust of $\rho = 10^{17} \text{ g/cm}^3$ (adapted from [Bonnell and Bate, 2006](#)).

During the last decade, important progress has been made, not only in the study of massive proto-stellar disks, but also of the whole morphology of MYSOs. From the theoretical point of view, many studies have been conducted to explain the different properties of disks in MYSOs, most of them in the context of core collapse. For example, [Vaidya et al. \(2009\)](#) performed steady state models of thin disks around MYSOs to investigate the role of accretion. Additionally, [Krumholz et al. \(2009\)](#) performed 3D simulations of forming massive stars showing the presence of rotational structures (i.e. accretion disks) with high accretion rates ($\sim 10^{-4} M_{\odot}/\text{yr}$). These simulations also suggest that gravitational and Rayleigh-Taylor instabilities in the disk-like structures overcome the radiation pressure of the star and lead to the formation of companions. [Seifried et al. \(2011, 2012\)](#) presented hydrodynamical simulations of collapsing massive cores to explain the role of magnetic fields on the stability of massive disks, concluding that magnetic pressure actively contributes to the stability of the disks. Additionally, [Kuiper et al. \(2014\)](#) determined, through hydrodynamical simulations, that the accretion time of the disk is strongly correlated with the time at which protostellar outflows are present.

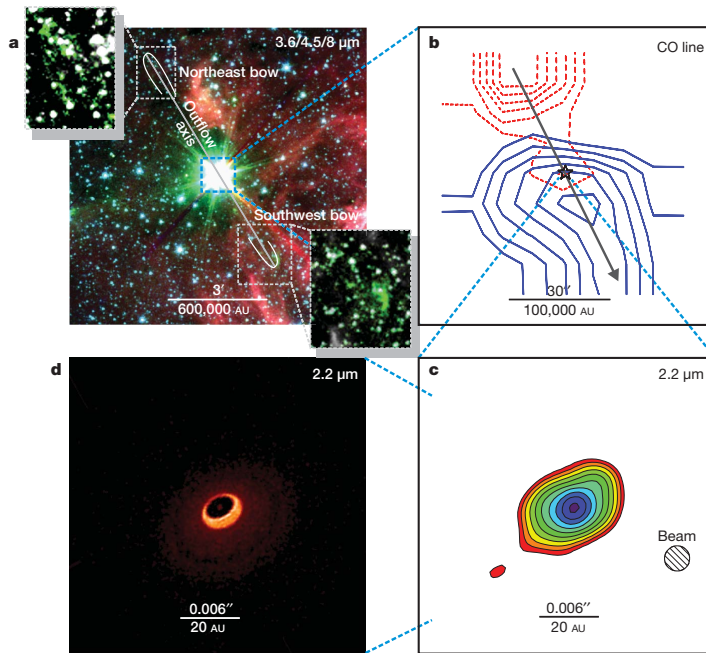


Figure 3.6: Diagram of the disk-outflow system of IRAS 13481-6124, taken from [Kraus et al. \(2010\)](#). An image from the Spitzer Space Telescope is shown in panel *a*. The two bow shocks observed in opposite direction from the central target are highlighted. Figure *b* displays in contours the outflows of the system as observed through the CO(3-2) emission line with APEX. Panel *c* shows the reconstructed image of the central disk (perpendicular to the outflows) from the AMBER/VLTI data. Panel *d* displays the best-fit model of a disk to the interferometric AMBER data.

Significant observational progress was triggered by the advent of adaptive optics (AO) at 8-10m class telescopes, infrared interferometry, as well as by the improved sensitivity and angular resolution of millimeter interferometers. For example, radio interferometric observations have found evidence of molecular outflows and jets launched at the core of the MYSOs (e.g., [Beuther et al., 2002](#); [Beuther and Shepherd, 2005](#)), as well as evidence of disk-like structures perpendicular to such outflows (e.g., [Beltrán et al., 2005](#)), thus providing us with a picture consistent with the predicted circumstellar disks. Recently, [Boley et al. \(2013\)](#) performed a survey of disks around a sample of 24 intermediate and high-mass stellar objects at MIR wavelengths with MIDI at the Very Large Telescope Interferometer. Almost all the observed massive stars of their sample presented elongated structures at scales ≤ 100 AU, which could be associated to disks and/or outflows. Additional examples at mid-infrared wavelengths include the work of [de Wit et al. \(2011\)](#) on the MYSO CRL 2136 and [Grellmann et al. \(2011\)](#) on NGC 2264 IRS 1*. We point out that the work of [de Wit et al. \(2007\)](#) is one of the first attempts to perform a simultaneous model fitting to the spectral energy distribution (SED) of W33A and its mid-infrared interferometric visibilities.

At near-infrared wavelengths, perhaps the most representative case study of disks in MYSOs was performed by [Kraus et al. \(2010\)](#). These authors resolved a hot, compact disk around the MYSO IRAS 13481-6124 ($M \sim 20 M_{\odot}$), with AMBER/VLTI interferometric observations. The observed structure exhibits a projected elongated shape of 13×19 AU with a dust-free inner gap of 9.5 AU, matching the expected location of the dust sublimation radius for this object. More recently, [Sánchez-Monge et al. \(2013\)](#) reported the detection of an edge-on disk on Keplerian rotation around a central B-star of $18 M_{\odot}$ in the G35.20-0.74N high-mass star forming region. They used observations with the Atacama Large Millimeter Array (ALMA) of hot-core tracers like CH_3CN or CH_3OH . The discovered disk has an approximate radius of 2500 AU and a mass of $3 M_{\odot}$.

Apart from the mentioned examples of observations (or models) of the morphology of MYSOs, there have been several studies to characterize MYSOs from their spectra. Here, two methods are discussed briefly: (i) the characterization of their SED and (ii) the analysis of the flux centroid of absorption or emission lines through spectroastrometry. The work of [Robitaille et al. \(2006\)](#) can serve as a good example of the first method. These authors performed a grid of $\sim 10^5$ SED models of YSOs up to masses of $50 M_{\odot}$. Their models include disks, envelopes and cavities to reproduce the observed SEDs. However, in spite of the large number of models created, this work still presents some limitations and uses simplifications in the geometry of the MYSOs' morphology. For example, it avoids disks inhomogeneities and/or binarity. Spectroastrometric studies include the work of [Wheelwright et al. \(2012\)](#) on the Be star HD 327083, in which these authors compare the spectroastrometric information obtained with CRIFES and the interferometric observables of AMBER to characterize the circumstellar disk around a binary system (see also [Wheelwright et al., 2010](#)).

3.2. THE MYSO NGC3603 IRS 9A*

IN this work, we explore the morphology of the MYSO NGC 3603 IRS 9A* (abbreviated hereafter as IRS 9A) with near-infrared interferometric observations and long-slit spectra. The target, which is located in the giant HII region NGC 3603 at a distance of 7 ± 1 kpc, is a MYSO with an estimated mass of $\sim 40 M_{\odot}$ (Nürnberg, 2003). Due to its location in NGC 3603, the natal cloud of this luminous source ($\sim 2.3 \times 10^5 L_{\odot}$) has been partially eroded by the stellar radiation of a massive cluster of O and B stars located at a projected distance of 2.5 pc to the North-West from the source, thus making it observable at infrared wavelengths. However, its spectral index ($\alpha_{2.2-10\mu m}=1.37$) suggests that the source is still surrounded by considerable circumstellar material. In fact, the observed excess of mid-infrared (MIR) emission observed and its positive spectral index resemble the properties of low-mass class I young stellar objects (Lada, 1987; Whitney et al., 2003). This hypothesis of a partially wind-stripped young object offers the intriguing possibility to peer behind the veil at a MYSO during one of its early evolutionary stages.

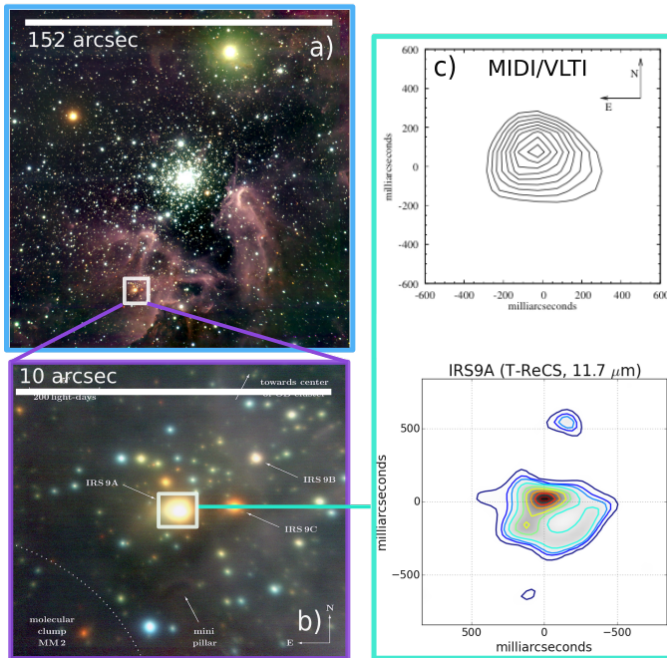


Figure 3.7: The figure displays in panel *a* the giant HII region NGC 3603, a well-known region in the Galaxy where massive star formation occurs. Panel *a* corresponds to a combined image of three different filters: J_s , H , and K_s taken with the ISAAC camera of the VLT (Credits: European Southern Observatory). Panel *b* displays a zoom onto the region where IRS 9A is located. This image corresponds to a JHK composite image taken with NACO/VLT (adapted from Nürnberg (2008)). Panel *c* displays the BSMEM reconstructed image resulted from the T-ReCS/Gemini interferometric data, and the deconvolved MIDI/VLTI data described in Vehoff et al. (2010).

Previous MIR high angular resolution observations of the morphology of IRS 9A identified at least two components associated with a warm-inner disk-like structure and a cold elongated envelope with temperatures of ~ 1000 and ~ 140 K, respectively (Vehoff et al., 2010). On the one hand, the envelope, resolved with MIR SAM observations, using the T-ReCS IR camera on Gemini South, exhibits an angular size of 330×280 mas. On the other hand, observations with the ESO MIDI instrument, attached to the VLTI, implied an angular extension of ≤ 50 mas for the compact structure.

In our analysis, we make use of SAM data taken with the ESO NIR facility NACO, at the ESO VLT, to study the morphology at the central region of IRS 9A. These data are complemented with NIR long-slit spectroscopic observations with CRIFES/VLT from the ESO archive. We also re-analyze the existing MIDI/VLTI and T-ReCS/Gemini data including them in our analysis. The layout of this chapter is as follows: Section 3.3 describes the observations and data reduction; our analysis and results for the different used techniques, as well as our models, are presented in Section 3.4; in Section 3.5, we discuss our results; finally, in Section 3.6 we present our conclusions.

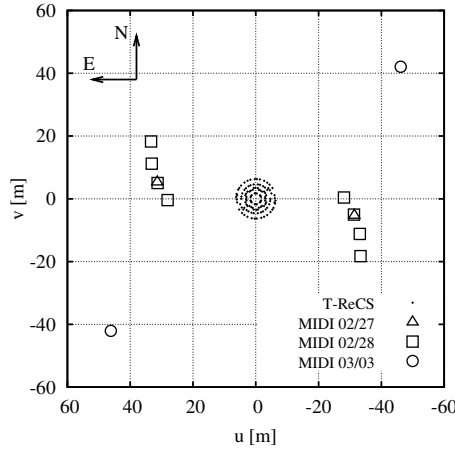


Figure 3.8: u - v coverage of the mid-infrared interferometric data taken with T-ReCS/Gemini and MIDI/VLTI presented in Vehoff et al. (2010). Notice how the coverage of T-ReCS is circular and homogeneous for the sampled spatial frequencies. In contrast, the coverage of MIDI/VLTI is non-uniform.

3.3. OBSERVATIONS AND DATA REDUCTION

3.3.1. SPARSE APERTURE MASKING DATA.

WE performed Adaptive Optics observations of IRS 9A with NACO in its aperture masking mode using the K_s ($2.2\mu m$), L' ($3.8\mu m$) and M' ($4.7\mu m$) bandpasses on March 12th, 2012² (UTC), combined with the S27/L27 cameras ($0.027''/\text{pixel}$) and the

²ESO programme: 088.C-0093(A).

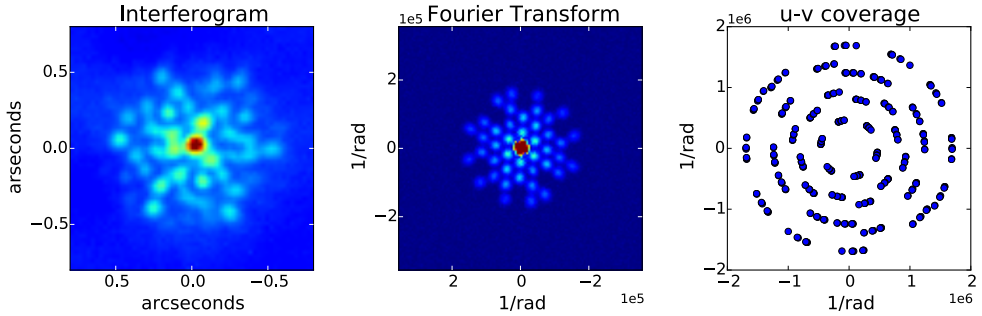


Figure 3.9: **Left:** IRS 9A Averaged interferogram in the image plane observed in a data cube. **Center:** Fourier Transform of the averaged interferogram. **Right:** u-v coverage of our SAM observations.

7holes mask. This mask and configuration are appropriate to be used with targets in the magnitude range of IRS 9A. The relatively uniform $u - v$ coverage afforded by this mask yielded a synthesized beam with angular resolution (θ) at each band of 35, 60, and 80 mas for the K_s , L' and M' filters, respectively.

Observations were taken using repeated standard calibrator-science target sequences over a period of ~ 2 hours per filter (see Table 3.2). Each observation on target and calibrator was composed of four dither positions. Due to the elevated noise and the presence of vertical stripes in the upper half of the NACO detector at the time of the observations, the dither positions were performed following a squared box in the lower half of the detector. The repeated observation helped to improve our $u - v$ coverage through Earth rotation synthesis (see Fig 3.9). All SAM data were initially sky subtracted, flat fielded, and bad pixel corrected. For each different position, the sky frames were constructed via separate observations of an empty field close to the target. The sky subtraction did not result in a fully flat background as expected: on the contrary, patterns were found to remain on the images in the L' -filter. The size of these patterns was larger than the size of the interferogram. Because fringes are encoded at high spatial frequency, we assumed that the effects of these residuals were not significant. Additionally, due to high airmass and variable seeing, the NACO/SAM M' -filter observations had low photon counts on target and no interferograms were distinguishable for almost all the recorded data. Therefore M' -data were discarded from our analysis.

In order to improve the SNR, a frame-selection algorithm rejected approximately 50% of the recorded images based on two flux criteria: (i) the total counts on a circular mask of the size of the interferogram, and (ii) the counts at the peak of the interferogram. The final frames were cropped and stored in cubes of 128×128 pixels centered on the source peak pixel. Point-source reference stars located not further than 2° from IRS 9A were observed to calibrate the telescope-atmosphere transfer function. Table 3.2 lists the data sets recorded for both target and calibrators at each observed filter. Figure 3.9 shows, as an example, the L' -filter data giving the average interference pattern over a

data cube, the power spectrum, and the final $u-v$ coverage built through Earth-rotation aperture synthesis.

Table 3.2: Observing log of VLT/NACO-SAM imaging observations taken on March 12th, 2012.

| Time (UT) | Source | Filter | NDIT ^a | DIT ^b | Camera |
|-----------|-----------------------|--------|-------------------|------------------|--------|
| 05h 05m | IRS 9A | K_s | 8.0 | 10.0 | S27 |
| 05h 20m | HD 98194 ^c | K_s | 8.0 | 10.0 | S27 |
| 05h 32m | IRS 9A | K_s | 8.0 | 10.0 | S27 |
| 05h 46m | HD 98133 ^c | K_s | 8.0 | 10.0 | S27 |
| 06h 00m | IRS 9A | K_s | 8.0 | 10.0 | S27 |
| 06h 15m | HD 98194 ^c | K_s | 8.0 | 10.0 | S27 |
| 06h 27m | IRS 9A | K_s | 8.0 | 10.0 | S27 |
| 06h 39m | HD 98133 ^c | K_s | 8.0 | 10.0 | S27 |
| 07h 10m | IRS 9A | L' | 126 | 0.5 | L27 |
| 07h 22m | HD 97398 ^c | L' | 126 | 0.5 | L27 |
| 07h 30m | IRS 9A | L' | 126 | 0.5 | L27 |
| 07h 41m | HD 98133 ^c | L' | 126 | 0.5 | L27 |
| 07h 50m | IRS 9A | L' | 126 | 0.5 | L27 |
| 08h 02m | HD 97398 ^c | L' | 126 | 0.5 | L27 |
| 08h 13m | IRS 9A | L' | 126 | 0.5 | L27 |
| 08h 27m | HD 98133 ^c | L' | 126 | 0.5 | L27 |

^a Number of exposures.

^b Detector integration time in seconds. The total integration time of each observation amounts to $N \times \text{DIT} \times \text{NDIT}$.

^c Stars used as calibrators of the sparse aperture masking data.

To reduce the raw data to calibrated squared visibilities and closure phases, an analysis pipeline written in IDL, originally developed at Sydney University, was employed. This code constructs a sampling template (specific to the given configuration of mask and filter) to extract complex visibilities from the Fourier transform domain. Raw interferometric observables are obtained as an average over the data cube for all baselines sampled by the mask. Finally, the calibrated amplitudes are obtained through the ratio between raw V^2 on source and calibrator, while calibrated CPs are obtained by subtracting the CPs of the calibrator from the ones on the target. A more detailed description of the SAM technique can be found in [Tuthill et al. \(2010, 2000\)](#). Additionally, our data were also reduced with the YORICK pipeline for aperture masking (SAMP; [Lacour et al., 2011](#)) developed at Paris Observatory. Similar results were obtained using both codes.

To test the level of confidence of both the CPs and the V^2 of our calibrators, we performed a cross-calibration between the different PSF reference stars to determine the response of the interferometric observables and identify systematics. We performed an

auto-calibration test for pairs of calibrators taken in the same quadrant of the detector to minimize the difference in the pixel gain of the interferogram and, hence, reduce the variability in the V^2 level. Our tests confirm that the CPs of the calibrator have individual standard deviations $\sigma_{CPs} \sim 2^\circ$.

Figure 3.10 presents the calibrated V^2 and CPs of our IRS 9A K_s and L' observations. The interferometric observables depict a partially resolved target with point-like symmetry for all the different sampled position angles. The V^2 levels vary between ~ 0.4 - 0.8 and ~ 0.2 - 0.7 for L' and K_s , respectively. CPs vary within about -10° and 10° for the two filters.

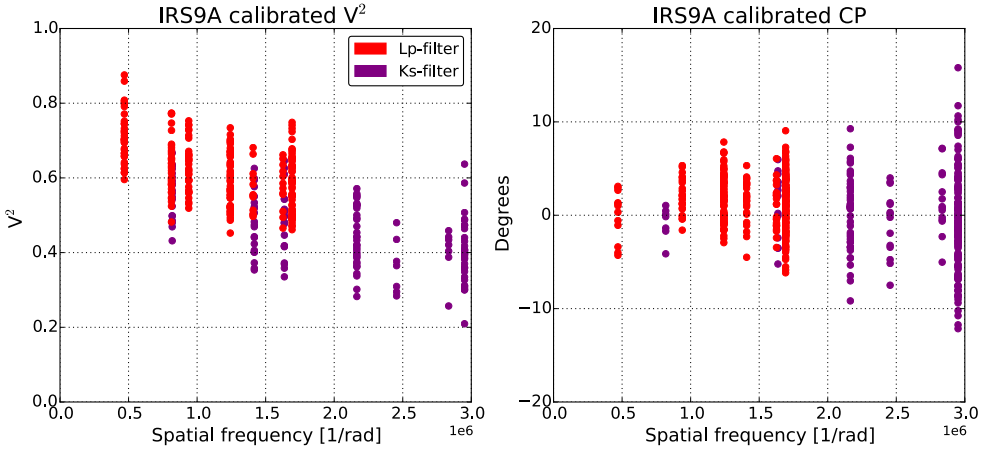


Figure 3.10: Calibrated squared visibilities (left) and closure phases (right) of IRS9A. The V^2 values imply the presence of a partially resolved structure while the CPs are consistent with inversion symmetry of the target.

3.3.2. CRIRES DATA

THE source was observed with the CRIRES spectrograph (Käufl et al., 2004) as part of the 080.C-0873(A) observing programme. We obtained these data from the ESO archive. Observations were taken using a grating of 31.6 lines/mm centered on two near-IR emission lines: H_2 ($2.121 \mu\text{m}$) and Br_γ ($2.166 \mu\text{m}$). The slit length was of $\sim 40''$ with a plate scale of $0.086''/\text{pixel}$. The covered dispersion ranges were: 2.108 - 2.150 and 2.161 - $2.200 \mu\text{m}$ for H_2 and Br_γ , respectively. These observations were conducted using a long-slit with a width of $0.6''$, and a resolving power of $R \sim 33000$ or 9 km/s . The CRIRES observations were not AO-assisted. To obtain information of the emission lines at different orientations of the target, three position angles (0° , 90° and 128°) were covered by the slit for each one of the observed lines. The exposure time was 60 seconds for both observed lines. Two nodding positions interwoven with sky observations were taken at each slit position.

The data reduction was performed using IRAF and proprietary IDL routines. First,

the 2D spectrum was corrected for the flat-field, bad pixels and sky contamination. No strong telluric OH lines were observed at positions threatening to contaminate astrophysically useful lines in the spectra. However, in order to avoid spurious signals in our data resulting from OH lines, we subtracted the sky observations from the science spectra. After the previous correction, the two nodding positions were aligned along the spatial axis and combined into a single spectrum. To correct for blending along the dispersion axis, a 2nd-degree polynomial was fit to the stellar continuum spectrum, which was then subtracted from the science spectra frames. Figure 3.13 displays the integrated H₂ and Br_γ emission lines using an aperture of twice the FWHM of the continuum emission, after processing as described.

3.4. ANALYSIS AND RESULTS

3.4.1. THE CORE OF IRS 9A

TO obtain an estimate of the physical size of the circumstellar structure around the core of IRS 9A, we first fit a geometrical model of a uniform disk to the V^2 functions from our SAM data. Since we do not completely resolve the compact structure, we omitted the effect of the inclination in the model at this stage. The angular size of the disk obtained with our model is, therefore, an upper limit of the real angular size of the target. The model of a uniform disk in the Fourier space is given by the following expression:

$$V(u, v)^2 = \left[\frac{A_1}{A_1 + A_2} \right] \left[2 \frac{J_1(\pi\theta r)}{\pi\theta r} \right]^2, \quad (3.4)$$

where J_1 is a first order Bessel function, θ is the diameter of the disk in radians, and r corresponds to the measured spatial frequencies. The coefficient A_1 corresponds to the squared correlated flux at zero baseline for the disk, and A_2 to the squared uncorrelated flux, where $A_1 + A_2 = 1$. To optimize the model fit, we used a Levenberg-Marquart algorithm implemented at the IDL *MPFIT* package (Markwardt, 2009). Figure 3.11 displays the best-fit model obtained for both filters, while Table 3.3 gives values of the best-fit parameters and their uncertainties. The fact that A_1 does not reach unity in both bands provides evidence for over-resolved extended flux. Nürnberger (2008) presented the L' -band large scale structure of the circumstellar environment around IRS 9A. That work presented an East-West elongated emission around IRS 9A with an angular size of around ~ 1.0 - $1.5''$ (or $\sim 7 \times 10^3$ - 10×10^3 AU at a distance of 7kpc). The angular extension of that diffuse emission is larger than the angular resolution of our shortest baseline ($\theta = 0.5''$), thus, this can explain the origin of the over-resolved flux observed at our NACO/SAM data at L' . In the case of K_s , the presence of circumstellar matter or a halo of scattered light could also explain the over-resolved flux observed in our interferometric data. This finding will be addressed in subsequent sections.

Additionally to the geometrical model, we performed image reconstruction with the calibrated data sets. The maximum entropy code BSMEM was used for this purpose

(Buscher, 1994). We used a uniform disk prior to perform the reconstruction. The initial model setup included a disk with a diameter of 50 and 100 mas for K_S and L' , respectively. The final images were obtained after 13 and 40 iterations. Fig. 3.12 displays the reconstructed images. As it was expected, IRS 9A appears quite compact, however a slight elongation is seen in East-West direction in the K_S -filter. On the other hand, at L' , the source looks quite symmetrical. It is important to mention that maximum-entropy (MEM) images have usually a super-resolution beyond the diffraction limit, since the reconstruction depends only on the entropy statistics (for a more detailed description see Monnier, 2003; Monnier and Allen, 2013). The images presented in Fig 3.12 are just the result of the reconstruction and have not been subsequently convolved with any beam to make more evident that the source does not resemble a point-like object (although it is not completely resolved).

Table 3.3: Parameters of best-fit uniform-disk model to the V^2 data.

| Filter | Parameter | Value | σ^a |
|--------|----------------------|-------|------------|
| K_S | A_1^b | 0.56 | 0.02 |
| | D [mas] ^c | 27.5 | 2.2 |
| L' | A_1^b | 0.67 | 0.02 |
| | D [mas] ^c | 34.2 | 4.5 |

^a $1-\sigma$ errors of the best-fit parameters assuming a reduced χ^2 of one.

^b V^2 value at zero-baseline.

^c Diameter of the fitted disk model in units of milliarcseconds.

3.4.2. H₂ AND Br γ SPECTROASTROMETRIC SIGNALS

To determine and characterize the region from which H₂ and Br γ emission lines arise, we extracted the spectroastrometric (SA) signal from both lines using custom routines written in the Interactive Data Language (IDL). This procedure tracks the centroid of the stellar continuum and of the emission line as a function of wavelength, with an astrometric precision of the order of few milliarcseconds (see Whelan and Garcia, 2008). The SA signal was measured on the non-continuum-subtracted data, and recovered by applying a Gaussian fitting to the intensity profile of the observed lines along the spatial axis for each one of the dispersion axis bins.

To eliminate the draw-back shift of the SA signal caused by the superposition of the stellar continuum at the emission line position, we corrected our signal as follows (see Pontoppidan et al., 2008; Whelan and Garcia, 2008):

1) The flux of the line ($F_{\lambda(\text{line})}$) was weighted by the sum of the flux of the line and continuum ($F_{\lambda(\text{continuum})}$) according to the following expression:

$$w_f = \left[1 + \frac{F_{\lambda(\text{continuum})}}{F_{\lambda(\text{line})}} \right] \quad (3.5)$$

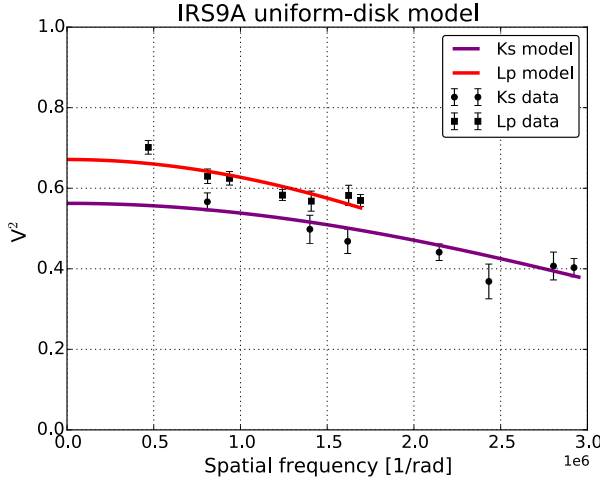


Figure 3.11: Uniform disk model. The mean weighted V^2 data points are represented by black circles and squares for the Ks and L' filters, respectively. The red and purple lines represent the best-fit model for the V^2 in L' and Ks , respectively.

2) We computed w_f using the average value of $F_{\lambda(line)}$ and $F_{\lambda(continuum)}$. The differences in the centroid position between line and continuum were then multiplied by the computed flux weight, w_f .

Figure 3.13 displays the SA signal of the different position angles for both H_2 and $Br\gamma$ lines. The SA signals, displayed on the histograms, are averaged over three and five bins for H_2 and $Br\gamma$, respectively. All the signals are corrected for the continuum effect, using an average $F_{\lambda(continuum)}/F_{\lambda(line)}$ of ~ 0.5 and ~ 0.9 for the $Br\gamma$ and H_2 , respectively.

On the one hand, the $Br\gamma$ emission line appears to be formed at the core of IRS 9A with maximum offsets from the continuum of around ~ 20 mas. On the other hand, in the H_2 line, the SA signal presents maximum offsets of the order of ~ 150 - 300 mas, depending of the position angle of the slit. The sizes of the SA signatures are consistent with the structures observed in our SAM data. This suggests that the central region of IRS 9A has a compact structure that contains ionized material, and a more extended surrounding envelope composed of molecular hydrogen.

The maximum shift in the H_2 SA signal at $PA=0^\circ$ is blue-shifted from the line's systemic velocity while the maxima of the shifts in the H_2 SA signal at $PA=90^\circ$ and $PA=128^\circ$ coincide with the line's systemic velocity. Since the width of the line profile goes from -10 to 10 km/s, and the spectral resolution of CRIRES is of 9 km/s, the observed line profile just resembles the response function of the spectrograph. There are two main mechanisms that give rise to the infrared emission of the observed transition, $v=1-0$ S(1), in H_2 : collisional excitation (e.g., Smith, 1995) and ultra-violet resonant-fluorescence (e.g., Black and van Dishoeck, 1987). However, to disentangle which mechanism is responsible for the observed emission line, a test of the flux ratio between the H_2 line at $2.12\mu\text{m}$

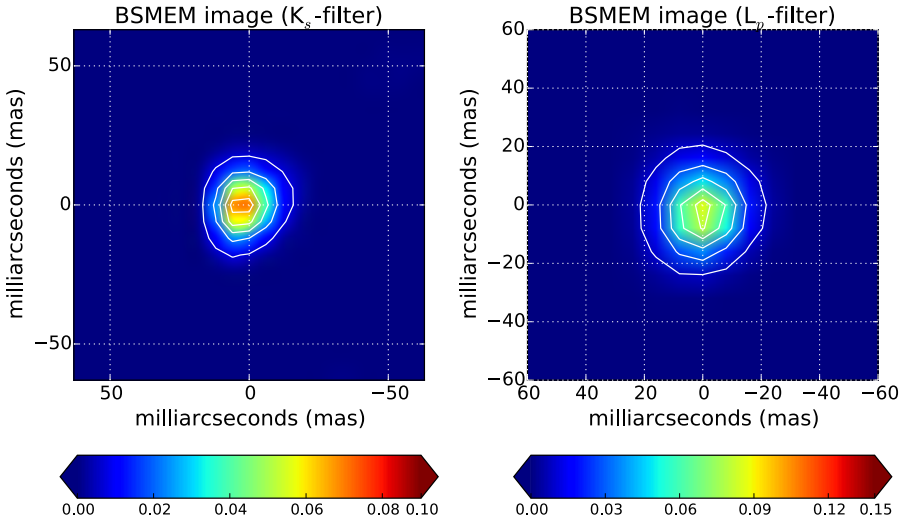


Figure 3.12: Reconstructed images of IRS 9A from the NACO/SAM data using BSMEM. The *left* panel shows the image for K_s and the *right* panel the image for L' . The total flux of the images is normalized to unity. Each panel has overlaid black contours that correspond to 10, 30, 50, 70 and 90% of the peak flux.

and the H_2 line at $2.24\mu\text{m}$ ($v=2-1$ S(1)) is required (high ratios between those lines implies that the origin of the emission is due to shocked gas and low ratios that the emission is caused by fluorescence; see e.g., [Wolfire and Konigl, 1991](#)). Such a study is beyond the scope of this work.

$\text{Br}\gamma$ SA signals at position angles of 90° and 128° exhibit an inverted double peaked profile, with one of the peaks blue-shifted and the other red-shifted. Velocities at the peaks for both position angles are of about -30 and 30 km/s, respectively. The characteristic SA signature of a disk-like structure presents a double peak profile with directions of the peaks reversed to the other (see e.g., [Blanco Cárdenas et al., 2014](#); [Brown et al., 2013](#); [Pontoppidan et al., 2011](#)). Therefore, the observed SA profiles cannot arise from a standard disk-like structure in Keplerian rotation. On the contrary, this type of SA signature appears to be formed in more complex systems with asymmetries or several components within it. Another intriguing possibility is that the observed $\text{Br}\gamma$ SA signal could be explained by the presence of a binary system. [Bailey \(1998\)](#) presented the characterization of several pre-main sequence binaries that exhibit similar SA signals to IRS 9A, finding double-peak profiles created by the binaries that variate depending on the observed PA; with the maximum shift seen at the position angle of the line connecting the components of the binary. Therefore, binarity of the central source may explain the lack of a clear double-peak profile at $\text{PA}=0^\circ$. In this scenario, the observed SA signal could be explained by the combined effect of two lines, each one produced by one stellar component, in which one of them exhibits a narrow profile and the other one a broader

line-width (see the case of KK Oph in Bailey, 1998).

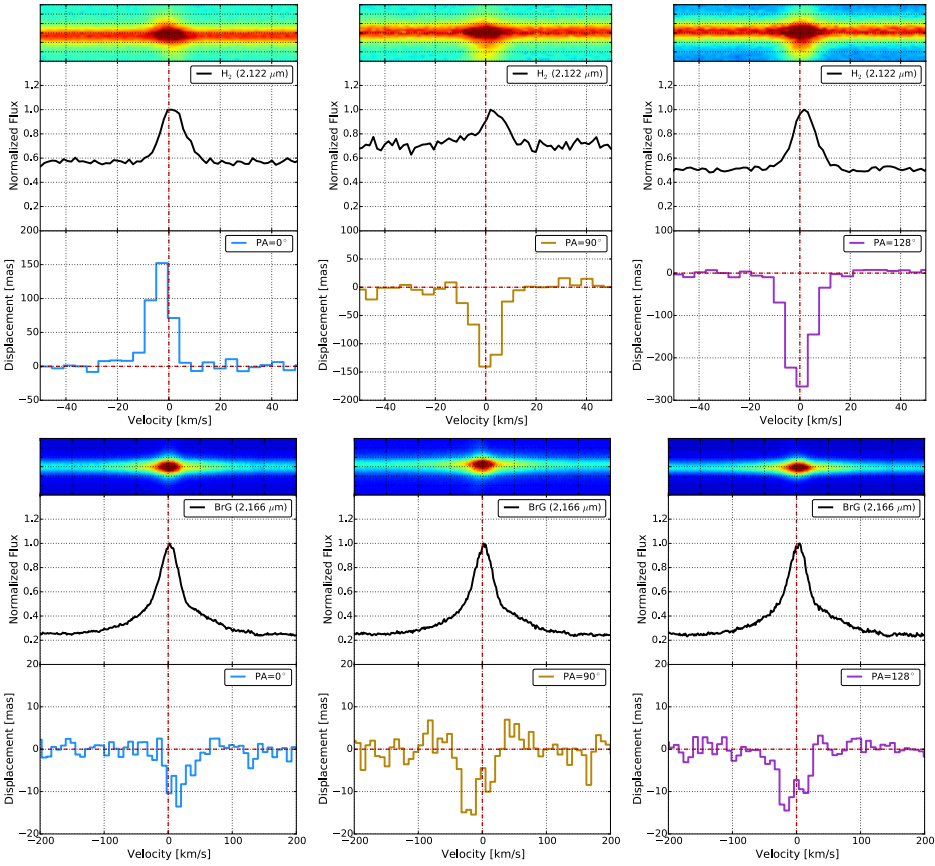


Figure 3.13: Spectroastrometric signals of the H_2 and $Br\gamma$ lines of IRS 9A. The H_2 emission line appears to originate from the large-scale structure of IRS 9A while the $Br\gamma$ line is formed at the core of IRS 9A. The spectroastrometric signal of the line displayed is weighted with w_f . The mean ratio $F_{\lambda(\text{continuum})}/F_{\lambda(\text{line})}$ is of ~ 0.9 and ~ 0.5 for the H_2 and the $Br\gamma$ line, respectively. The 2D spectral lines are also displayed in colors.

A simple way to determine whether the $Br\gamma$ SA signal is formed by a distribution of material in a common orbital plane (e.g., disk or binary) consists in representing two SA signals observed at different position angles in a x-y 2D plot. If the resulting trend of the astrometric offsets in the x-y plot can be approximated by a linear function, then the material (from which the SA signal is formed) is coplanar, as expected for an orbital plane (Bailey, 1998; Takami et al., 2003). Figure 3.14 displays three panels with the x-y maps produced with the observed position angles. As can be seen, neither the x-y plot created with the SA signals on position angles 90° and 0° , nor the plot with position angles 128° and 0° yields a linear distribution.

In contrast, the x-y panel with position angles 128° and 90° fits a straight line. The

line overplotted in panel three of Figure 3.14 represents a best-fit approximation to a function of the form $y=mx+b$ with $m=0.98$ and $b=1.02$. This finding supports the hypothesis that some component of the ionized gas at the core of IRS 9A share a common orbital plane with a position angle in the plane of the sky of $\sim 150^\circ$ East of North. However, additional material is located at different orientations, suggesting that the observed SA signals represent the contribution of several morphological components of IRS 9A. Furthermore, our findings can be compared to the ones obtained by Bailey (1998) for the Herbig Ae/Be star Z CMA. This object shows at least two components with different orbital planes, a binary+disk system with perpendicular outflows, in its 2D spectroastrometric plots, suggesting that IRS 9A and Z CMA may have a similar morphology. As observed in each panel of Fig. 3.14, the maximum displacements of the Br γ centroids are ≤ 20 mas for all the position angles sampled.

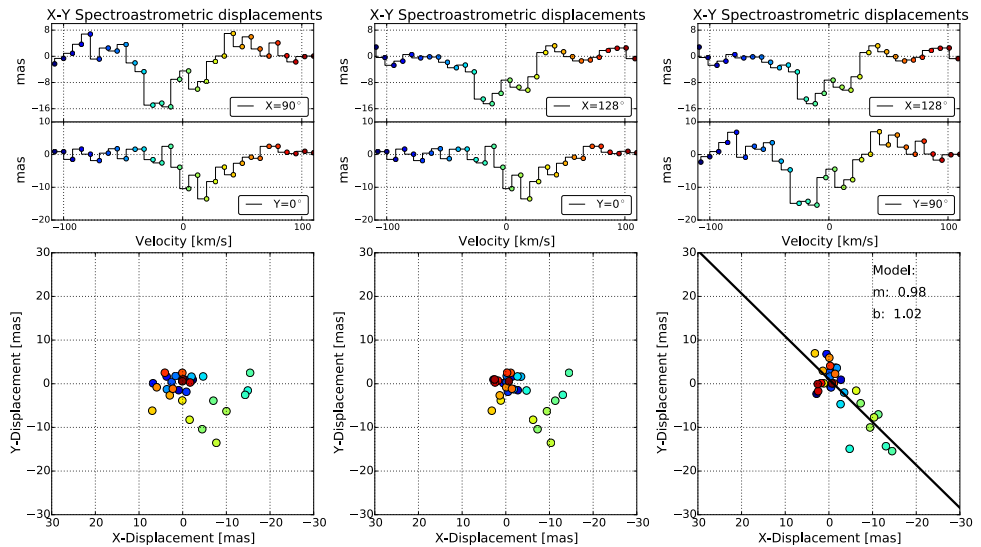


Figure 3.14: 2D plots of the Br γ SA signals. Each panel in the columns represents the flux centroid displacements at two given position angles, as indicated at the top SA signals. Each spectral bin is represented by different colors. The black line in the right panel indicates the best-fit solution to a linear distribution for the given spectroastrometric signals.

3.4.3. RADIATIVE TRANSFER MODEL OF IRS 9A

TO determine the physical conditions that best reproduce all the observational information of IRS 9A, we linked the observed V^2 of our SAM data with the MIR observations from the literature, and the object's SED through a multi-wavelength radiative transfer simulation. We considered a physical scenario that includes similar properties to the Class I YSO described by Whitney et al. (2003). The structure of the model consists of a compact flared disk around the central source of radiation surrounded by an outer

elongated envelope, with the envelope having two bipolar cavities probably created by jets and outflows launched at the core of IRS 9A (see Fig. 3.15). A similar morphology was modeled previously by [Vehoff et al. \(2010\)](#). However, we have found that some changes in the parameters should be introduced to fit the new NACO/SAM data. The 3D density distribution of the disk in spherical coordinates, $\rho_{disk}(R, z, \phi)$, follows a power law described by the expression:

$$\rho_{disk}(R, z, \phi) = \rho_0^{disk} \left[\frac{R}{100 \text{ AU}} \right]^{\beta+1} \exp \left[-1/2 \left(\frac{z}{h(R)} \right)^2 \right] \quad (3.6)$$

where ρ_0 is the scale factor of the density, R is the disk radius and β the scale height power-law exponent. The scale height function is given by: $h(R) = h_0(R/R_0)^\beta$. The envelope density distribution corresponds to an elongated structure of infalling material according to [Ulrich \(1976\)](#). It has the following form:

$$\rho_{env}(R, z, \phi) = \frac{\dot{M}_{envelope}}{4\pi(GM_*r_0)^{1/2}} \left[\frac{r}{r_0} \right]^{-3/2} \left[1 + \frac{\mu}{\mu_0} \right]^{-1/2} \left[\frac{\mu}{\mu_0} + \frac{2\mu_0^2 r_0}{r} \right]^{-1} \quad (3.7)$$

where r is the radius of the envelope, r_0 is the normalization radius of the envelope, and \dot{M} is the rate of mass infall. The factors μ_0 and μ are related by the equation for the streamline: $\mu_0^3 + \mu_0(r/r_0 - 1) - \mu(r/r_0) = 0$. The density distribution in the envelope cavity was considered to be uniform. It is important to highlight that our simulation does not consider binarity and/or irregularities in the disk at the core of IRS 9A; such details lie beyond the scope of this work.

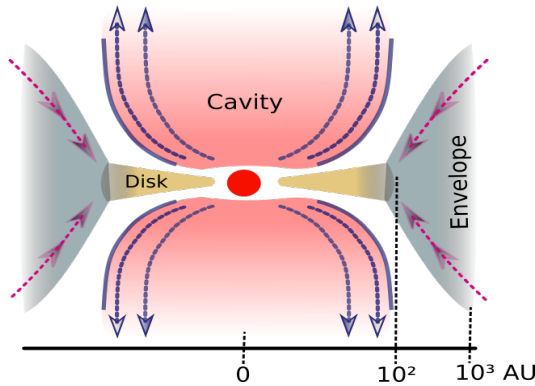


Figure 3.15: The schematics presents the model of the IRS 9A morphology adopted to perform our radiative transfer simulations. The model includes an inner disk surrounded by an envelope with bipolar cavities. The purple lines in the cavities indicates the direction of the radiation escaping from the core, while the pink lines in the envelope represents the infall of material from the envelope through the disk. The typical scales of the different components are shown.

To perform the radiative transfer simulation, we used the *Hyperion* software ([Robinaille, 2011](#)). This code carries out 3D dust continuum radiative transfer simulations

while creating SEDs and images at the required wavelengths. Our *Hyperion* simulations used the density distributions of the previously mentioned structures to determine their temperature and flux maps. The code uses a modified random walk (MRW) approximation to propagate the photons in the thickest regions of the simulations. The model assumes a modified MRN grain-size distribution (Mathis et al., 1977) as determined by Kim et al. (1994). The chemical composition of the dust includes astronomical silicates, graphite and carbon. The simulated models also include the scattering of the dust with a full numerical approximation to the Stokes parameters in the ray tracing process. The gas-to-dust ratio of 100:1, a foreground extinction of $A_V=4.5$ (the extinction law used is described in Robitaille et al., 2007), and a distance of 7 kpc were used for all simulations (Nürnberg, 2003).

From the radiative transfer simulations, we obtained synthetic images of the morphology of IRS 9A for the K_s and L' bands observed with NACO/SAM (see Sec. 3.4.1), for the N -band ($11.7 \mu\text{m}$) observed with T-ReCS, and for the MIDI/VLTI ($8\text{-}13 \mu\text{m}$) data described in Vehoff et al. (2010). Subsequently, the V^2 were extracted from those images, at the sampled spatial frequencies by the observations, using proprietary IDL routines. We also obtained synthetic SEDs in the range of $1\text{-}500 \mu\text{m}$. For all images, the total flux was normalized according to the largest angular size at the spatial frequencies sampled for each one of the instruments that was used.

Table 3.4: Radiative transfer models of IRS 9A.

| Parameter | Robitaille's tool (No. 3006825) ^a | Vehoff+2010 (No. 3012790) ^a | Best V^2 model (this work) |
|---------------------------------------------------|-------------------------------------------------|-------------------------------------------|---------------------------------|
| Total luminosity (L_\odot) | 1.0×10^5 | 9.2×10^4 | 8.0×10^4 |
| Stellar mass (M_\odot) | 27.2 | 25.4 | 30.0 |
| Stellar temperature (K) | 39000 | 38500 | 38000 |
| Disk mass ^b (M_\odot) | 1.8×10^{-1} | 5.0×10^{-1} | 5.0×10^{-1} |
| Disk outer radius (AU) | 91.0 | 94.0 | 80.0 |
| Disk inner radius (AU) | 28.0 | 25.0 | 10.0 |
| Disk flaring power - β - | 1.1 | 1.2 | 1.2 |
| Disk scale height at 100 AU - h - | 8.9 | 8.8 | 8.0 |
| Envelope outer radius (AU) | 1.0×10^5 | 1.0×10^5 | 7×10^3 |
| Envelope cavity angle (deg.) ^c | 31.0 | 29.0 | 30.0 |
| Bipolar cavity density (g/cm^3) | 7.7×10^{-21} | 9.9×10^{-21} | 1.0×10^{-20} |
| Inclination (deg) ^d | 87.0 | 85.0 | 60.0 |

^a Number of the model from Robitaille's database.

^b Total mass (dust+gas).

^c Half-opening angle of a conical cavity in the envelope.

^d Inclination angle of the disk-envelope from the line of sight: 0° means that the disk and envelope are seeing face-on, 90° means that the disk and envelope are seeing edge-on.

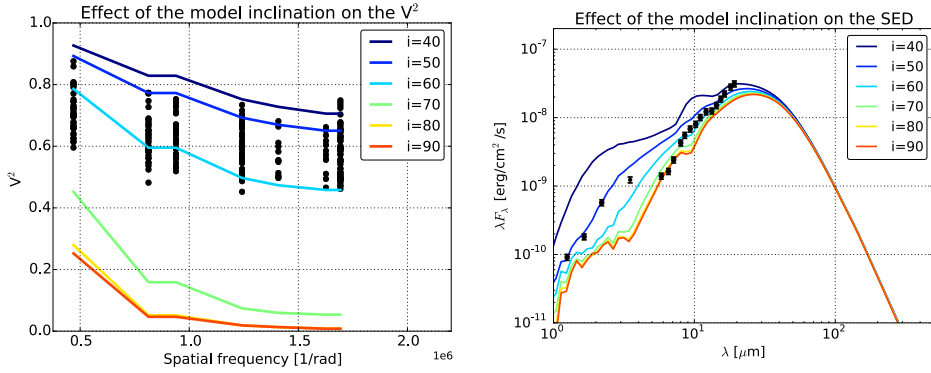


Figure 3.16: Effect of the change in the inclination angle, i , of the model on the simulated V^2 and SED. On the *left* panel, the effect of modifying i on the NACO/SAM L' -filter is observed. On the *right* panel, the effect of changing i over the SED is displayed. The different colors correspond to different values of i , while the black dots represent the data in both panels.

THE PARAMETER SPACE

TO constrain the parameters of our model, we used as starting point the disk-envelope system presented by [Vehoff et al. \(2010\)](#). However, we observed that the new SAM data were not fit by this model. Therefore, some modifications were necessary to reproduce the observed visibilities. We are aware that our initial assumptions cannot cover the full range of the parameter space. The model presented is, in consequence, the best-fit approximation given the assumed components and limitations to the explored parameter space. Future improvements require the use of a more complete systematic χ_2 minimization (e.g., via least squares fitting) to both the SED and V^2 , besides the determination of the appropriate SED at scales of the object's morphology. The model parameters were estimated as follows:

a) The central source (T_{eff}, L_, M_*):* As established in [Vehoff et al. \(2010\)](#), the model assumes the typical stellar parameters of an O-star on the main-sequence (see e.g., [Martins et al., 2005](#)). The effective temperature was thus set to $T_{eff} = 38000$ K, the luminosity to $L_* = 1.0 \times 10^5 L_\odot$, and the mass to $M = 30 M_\odot$. Variations of the luminosity were performed in steps of $1 \times 10^4 L_\odot$. The final value was established on $8 \times 10^4 L_\odot$, to ensure a good fitting to the SED.

b) The disk ($R_{in}, R_{out}, m_{disk}, \beta, h_0$): The inner radius of the disk was obtained from variations of the value given by [Vehoff et al. \(2010\)](#). The covered values went from 10 to 25 mas in increments of 5 mas. The value that best reproduce the observed V^2 is $R_{in} = 10$ mas. This value is in agreement with the sublimation radius of the dust (for a sublimation temperature $T_{sub} = 1500$ K) according to [Monnier and Millan-Gabet \(2002\)](#):

$$R_{sub,disk} = 1.1 \sqrt{Q_R} \left[\frac{L_*}{1000 L_\odot} \right]^{1/2} \left[\frac{T_{sub}}{1500 K} \right]^{-2} \text{ AU} \quad (3.8)$$

Considering a ratio of the dust absorption efficiencies $Q_R=1$, the inner radius was thus estimated as: $R_{in}=R_{sub,disk}=10$ AU. On the other hand, the initial value of the outer radius was initially set to $R_{out}=100$ AU, since this was the value derived from the geometrical model ($R \sim 14$ mas ~ 98 AU) described in section 3.4.1. Variations of R_{out} were performed in steps of 10 AU from 40 to 100 AU. We observed that changes in this range do not have a strong impact in the simulated SED, and that they only introduced slight changes in the simulated V^2 within the scatter of the observed V^2 . Therefore, we adopted an average value of $R_{out}=80$ AU. For the mass of the disk and the flaring exponent, β , we used the same values as Vehoff et al. (2010), thus $m_{disk}=5 \times 10^{-3} M_{\odot}$ and $\beta=1.2$, respectively. To determine the scale height, h_0 , at 100 AU, we performed several tests with values of h_0 between 3-10 AU, with steps of 1 AU, finding that the value that best reproduces the visibilities is $h_0=8$ AU, very close to the value previously reported by Vehoff et al. (2010).

c) Envelope and cavities ($\phi, \rho_{cav}, R_{out,cav}$): The parameters of the envelope and cavities were adopted from Vehoff et al. (2010). The value of the opening angle of the cavity (ϕ) was fixed to 30° , and the density (ρ_{cav}) to 1×10^{-20} g/cm³. For the envelope, we adopted a normalization radius of 100 AU, and an outer radius of 7×10^3 AU (1"). The scale of the outer radius was inferred from the extension observed at MIR wavelengths which exhibit an angular scale of around 1". Tests with larger $R_{out,cav}$, like the value reported by Vehoff et al. (2010), produced visibilities systematically below the observed levels, and were therefore discarded.

d) Orientation (i, ϕ): From Nürnbergger (2008) we expect that the cavity opening axis of the disk-envelope system is oriented East-West, with a position angle, ϕ , in the plane of the sky of $\sim 70^\circ$ East of North. On the other hand, from our simulations, we noticed that the inclination angle of the disk to the line of sight, i , was a critical parameter to model the SED and V^2 . Figure 3.16 displays, as an example, the effect of the inclination in the simulated V^2 for the L' -filter and SED for different values of i between 40° and 90° in steps of 10° . From these results, we adopted an inclination angle of $i=60^\circ$ for our radiative transfer simulations.

Figure 3.17 presents a comparison of the fitting to the V^2 of our best-fit model with (i) the model of the MIR morphology of IRS 9A presented by Vehoff et al. (2010), and with (ii) the best-fit model of the IRS 9A SED obtained with Robitaille's online fitting tool³ (Robitaille et al., 2007). Vehoff's model was also obtained from the Robitaille's tool, but it does not correspond to the best-fit model delivered by the online database for the used data, although it provides a reasonable fit to the MIR visibilities. We included both models in Fig 3.17 for completeness. It is important to remark that the model of Vehoff et al. (2010) analyzed here has a maximum angular size at zero spacing of $\sim 2''$. Caution is recommended when comparing to Fig. 6 of Vehoff et al. (2010), since these authors limited the maximum size to 0.85", leading to bias in the visibilities of the shortest baselines. Table 3.4 displays the parameters of each model. Figure 3.18 displays the SED of IRS 9A for

³<http://caravan.astro.wisc.edu/protostars/>

each of the models plotted over the observational data. The NIR photometry was taken from [Nürnberg \(2003\)](#) and the MIR one from [Vehoff et al. \(2010\)](#). Fig. 3.19 displays an RGB image, composed with our models at 2.2, 3.8 and 11.7 μm .

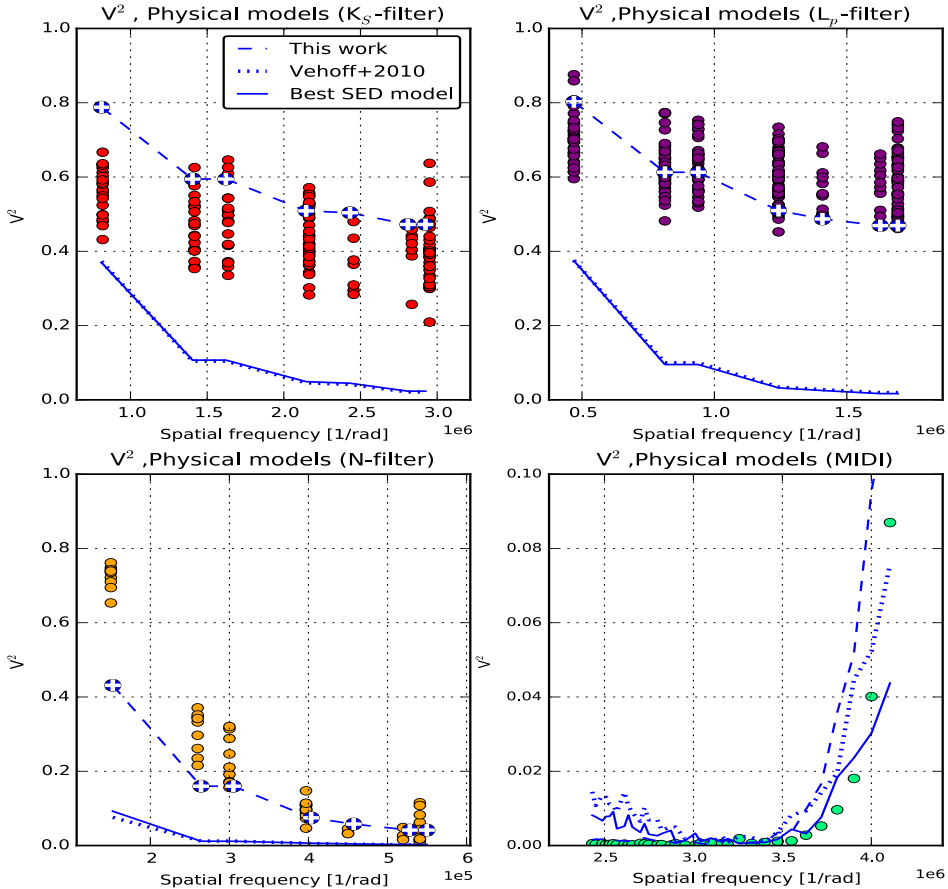


Figure 3.17: Models of IRS 9A giving predicted V^2 at NIR and MIR wavelengths. The model signals are displayed with varying linetypes (see key), while the data corresponding to each waveband are displayed with dots of different colors.

3.5. DISCUSSION

As shown in Fig. 3.17, the model presented by [Vehoff et al. \(2010\)](#) based on the MIR data does not reproduce the observed V^2 signals extracted from the new NIR SAM observations. In fact, that model is shifted systematically towards lower V^2 values at the three K_s , L' and N bands. Similar V^2 misfits are observed for the model obtained with Robitaille's online tool. To perform a more quantitative comparison between the differ-

ent models, we computed the root mean squared error (RMSError)⁴ for each V^2 data set and SED. Table 3.5 displays the obtained RMSError for the different models and data sets. Note how the model presented in this work exhibits considerably lower residuals than the other two models for the NACO/SAM and T-ReCS data. However, the residuals of our model are similar to the ones presented by the other two models for the MIDI data.

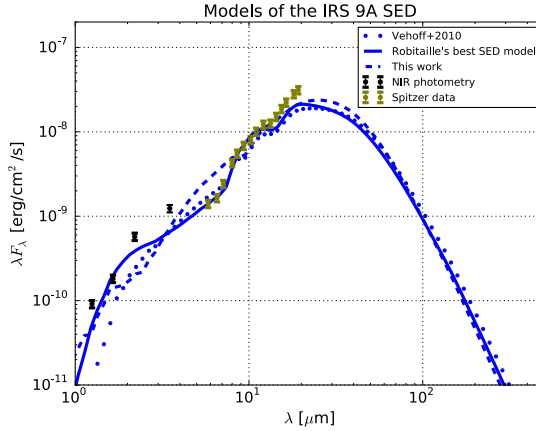


Figure 3.18: Comparison between the various different “best-fit” (see text) models to the IRS 9A SED. The photometry data are displayed in black and green. The different models are shown in blue (see the caption inside the plot). The SED models are displayed assuming an aperture of 3” at a distance of 7.0 kpc and $A_V=4.5$.

Table 3.5: Comparison of the root mean square error (RMSError) between the different models of IRS 9A.

| Data set | Robitaille’s tool (No. 3006825) | Vehoff+2010 (No. 3012790) | Best V^2 model (this work) |
|------------------------|------------------------------------|------------------------------|---------------------------------|
| NACO/SAM K_S -filter | 6.5 | 6.6 | 3.0 |
| NACO/SAM L' -filter | 25.2 | 25.4 | 5.0 |
| T-ReCS data | 20.4 | 20.0 | 9.8 |
| MIDI data | 5.2 | 3.0 | 4.0 |
| SED | 2.29 | 2.98 | 3.4 |

From Fig. 3.18 it is appreciated that, despite this poor performance when confronted with the interferometric data, good fits to the SED are exhibited by both Robitaille and Vehoff models. In fact, our model presents the highest residuals. Nevertheless, this result is not unexpected since SED fitting alone often offers highly degenerated outcomes:

⁴ $RMSError = \sqrt{\frac{\sum_i ((d_i - m_i) / \sigma_i)^2}{n}}$, where d_i corresponds to the sampled data point i ; m_i is the corresponding model point; σ_i is the standard deviation of the data; n is the total number of the sampled points.

strong constraints are only provided when SEDs are used in concert with spatial information identifying the origin of the emission. For example, even simple single envelope Robitaille models are sufficient to reproduce the observed SED, although none reproduce simultaneously the observed V^2 . Furthermore, the apertures used to extract the SED measurements are considerably larger ($3''$) than the angular size of IRS 9A. Therefore, some measurements may be contaminated by flux from nearby sources in the field (see e.g., Fig 2 in Nürnbergger, 2008, in which additional sources are observed around IRS 9A in a radius of $\sim 5''$). This underlines the importance of obtaining SED data at adequate angular resolution, as well as of multi-wavelength interferometric observations combined with SED modelling to construct a reliable physical framework of the MYSOs morphology.

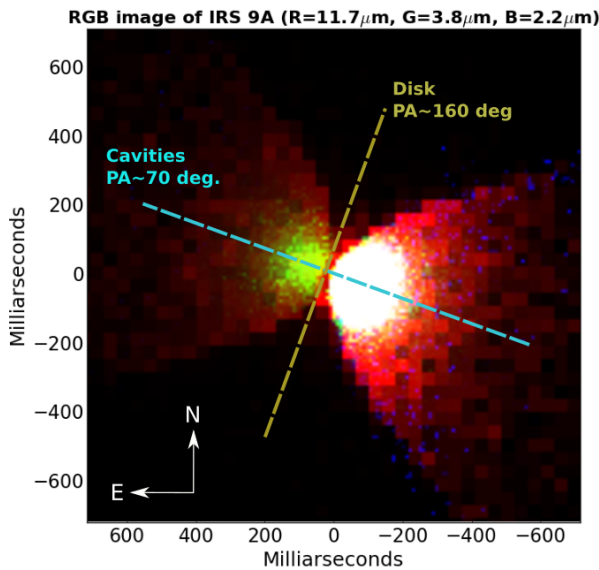


Figure 3.19: Composed RGB map with our model images. Note how the emission arise from the cavities dominating the IR. The red, green, and blue filters correspond to the images of the models at $11.7 \mu\text{m}$, $3.8 \mu\text{m}$, and $2.2 \mu\text{m}$, respectively.

In contrast to previous works, we have produced a model of IRS 9A reproducing all observable data including V^2 signals at NIR and MIR wavelengths (although some deviations are present at the shortest baselines of the K_s and L' filters and in the largest baselines of the MIDI data). Our model reproduces the longest baseline visibilities from the T-ReCS data, but underfits V^2 at the shortest T-ReCS baselines. It is important to highlight that, in contrast to the other filters, the N-band T-ReCS data sample the largest scale of the IRS 9A morphology. Therefore, we infer that our model faithfully reproduces the IRS 9A morphology up to scales $\leq 1''$ (7000 AU), but significantly differs from the V^2 data, corresponding to angular scales between $1''$ - $1.6''$ (7000-11000 AU). In fact, from the

reconstructed T-ReCS/SAM image presented in [Vehoff et al. \(2010\)](#), it is noticeable that the morphology of IRS 9A at larger scales is irregular and more complex than our modelling.

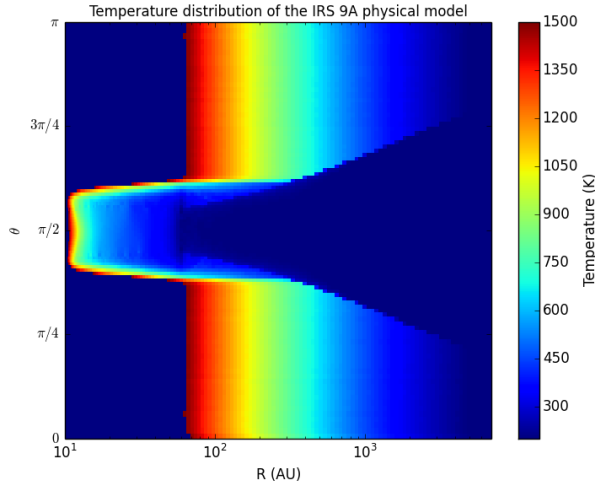


Figure 3.20: Radial cut of the temperature distribution of the dust around IRS 9A. The picture displays the temperature profile of the disk and the envelope obtained with our best radiative transfer model. The axis is given in spherical coordinates (r, θ) and the colors represent different temperature values of the dust.

Figure 3.20 displays a radial slice through the temperature distribution of our best model. It is observed that the disk atmosphere has a temperature close to the dust sublimation limit ($T \sim 1500$ K) while the mid-plane regions of the disk have an average temperature around $T \sim 600$ K. Our simulation also suggests that regions closer than 2 mas (10 AU) to the central source are dust-free because processes as the stellar radiation and/or self-heating of the disk sublimate the dust at these scales (see e.g., [Vaidya et al., 2009](#)).

As concerns to the origin of the emission observed in the IRS 9A SED, Figure 3.21 shows the thermal and scattering contributions from the best-fit physical model. This plot indicates that scattered photons from the stellar source are the most important source of radiation at the K_s -filter, and that they also contribute to the emission observed at the L' -filter, while thermal emission from the dust dominates the mid- and far-infrared.

3.6. CONCLUSIONS

a) The analytical model of a Class I YSO described by [Whitney et al. \(2003\)](#) appears to be a relatively good approximation of the morphology of IRS 9A. This source appears to be an embedded object surrounded by a thick envelope which dominates the spectral energy distribution, and with a flat plausibly disk-like structure at its center. This result supports contemporary thinking in star formation, which suggest that massive stars gain mass

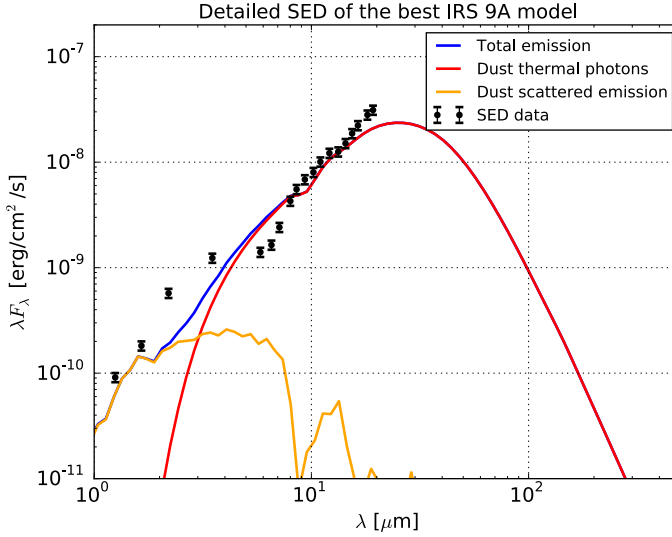


Figure 3.21: Spectral energy distribution of the best-fit radiative transfer model (blue line). The thermal and scattering contributions are displayed separately in red and yellow linetype respectively.

via accretion disks that shield part of the infalling material from the strong radiation pressure.

b) From our NACO/SAM data, we have confirmed the presence of a compact, possibly disk-like, structure with an angular size ≤ 30 mas. From our radiative transfer simulations, we have found that this structure is responsible for most of the NIR flux distribution of the IRS 9A SED.

c) From our best-fit radiative transfer model, we have found that the large scale MIR emission is dominated by the heated dust within the envelope cavity. This is particularly supported by the observed morphology at $11.7 \mu\text{m}$ with T-ReCS. The model envelope has an angular size of $\sim 1''$. Due to the high luminosity of the central source, the hot inner regions of the envelope also emit at NIR wavelengths.

d) The morphology of the best-fit physical model in the L' -filter is consistent with the shape observed in full-pupil NACO imaging presented by Nürnberg (2008). This hot extended emission from the envelope is apparently also responsible of the over-resolved emission observed in the K_s and L' squared visibility signals.

e) Our best physical model suggests that the system of disk+envelope is inclined $\sim 60^\circ$ out of the plane of the sky, where 0° corresponds to a face-on orientation of the disk. Moreover, from our simulations, we find that smaller inclination angles generate a large bump at near-IR wavelengths and V^2 close to unity. Higher inclinations, as suggested in prior literature models, produce low V^2 (failing to reproduce the data).

f) From the Bry spectroastrometric signal, we have found that the core of IRS9A is

complex. A common orbital plane obtained from the 2D plot of position angles 90° and 128° is consistent with the orientation of the disk in the plane of the sky. However, it is clear that additional ionized gas at different position angles is present. These findings can be explained by a contribution of flux arising from the envelope to the flux centroid, at regions where the envelope mixes with the disk (10 mas; ~ 60 AU); and by the material located in the envelope cavities. Additional components and/or streamers are also plausible explanations. New spectroastrometric observations and/or interferometric observations with GRAVITY/VLTI and/or MATISSE/VLTI, combined with radiative transfer emission line models, may be useful in confirming this hypothesis and/or search for the presence of additional stellar companions at the core of IRS 9A.

g) A complete self-consistent physical scenario describing IRS 9A complex morphology is challenging, in particular fitting both the spectral energy distribution and both small/large spatial structures. However, systems such as this one represent important and rare test cases with which to confront theoretical models. In this work, we have demonstrated that a multi-wavelength approach is necessary to unveil the physical and geometrical properties of the MYSOs. Our results indicate that optical interferometry and spectroastrometry are important observing techniques to map the morphological properties at the core of MYSOs, where important physical phenomena occur. Our work also shows that the accuracy of the available SED measurements, the angular resolution of interferometers, and complexity in the source are important obstacles for arriving at fully consistent models of MYSOs.

h) Future work will require more data with these techniques to refine the existing models. Moreover, additional data at longer wavelengths (e.g. observations with ALMA) are also necessary to constrain better the Rayleigh-Jeans part of the SED, and to obtain more accurate information of the size and density of the envelope. Similar analysis should be extended to other MYSOs to systematically study their properties, driving further incisive testing of massive star formation scenarios.

4

MULTIPLICITY IN MASSIVE STARS

THE CASE OF HERSCHEL 36 AND HD 150 136

The fact that we live at the bottom of a deep gravity well, on the surface of a gas covered planet going around a nuclear fireball 90 million miles away and think this to be normal is obviously some indication of how skewed our perspective tends to be.

Douglas Adams

One of the main observational properties of massive stars is that they usually belong to multiple systems. Recent findings suggest that around 90% of O-stars possess at least one massive stellar companion. In fact, it may well be that almost all massive stars are born as triples or higher multiples, but their large distances require very high angular resolution, combined with a high dynamic range, to directly detect the companions at milliarcsecond scales. This chapter is dedicated to study multiplicity in massive stars using optical long-baseline interferometry. For this purpose we have analyzed the triple nature of two peculiar systems: Herschel 36 and HD 150 136.

On the one hand, HD 150 136 is the nearest system to Earth with a total mass $> 100 M_{\odot}$, and it provides a unique opportunity to study an extremely massive system. Moreover, one of the components of this system was classified as an O3 V star. Therefore, it means that this target is very young (age $\sim 2Ma$). This thus allows us to study not only a very massive system, but also a very young one.

Parts of this chapter have been published in *Astronomy & Astrophysics* **554**, L4 (2013), and **572**, L1 (2014), [Sanchez-Bermudez et al. \(2014a, 2013\)](#).

On the other hand, Herschel 36 is a young massive system located at 1.3 kpc. It has a combined smallest predicted mass of $45 M_{\odot}$. This system is located at the center of the M8 nebula, and is responsible for ionizing most of its gas, in a similar fashion as θ^1 Ori C ionizes most of the gas of the Orion nebula. The spectroscopic information of this system suggests that in addition to the tight spectroscopic binary, there is an additional component, rotating in a wider orbit. This outer component appears to be the most massive one, suggesting a different mechanism than other triple hierarchical systems.

Both systems were analyzed using multi-epoch spectroscopic data, from which their triple nature was inferred. Nevertheless, their widely separated third components have never been observed directly. This work performed optical long-baseline interferometric observations of both targets at near-infrared wavelengths with AMBER/VLTI to obtain astrometric and photometric measurements of the spectroscopic binaries and their putative tertiary components.

The observed squared visibilities and closure phases show the typical cosine signature of a resolved binary (an unresolved spectroscopic binary + single component), confirming the triple hierarchical nature of the systems. The interferometric observables were fit using proprietary IDL routines and the code LitPro to obtain the brightness ratios and position angles of the components in the plane of the sky. BSMEM was used to image the systems, and, finally, an estimate of the orbit was obtained.

4.1. INTRODUCTION

THE chemical composition of the universe cannot be understood without considering the formation and evolution of high-mass stars. On average, massive stars in every stage of their life cycles dominate the stellar feedback to the interstellar medium in our Galaxy. They may both trigger and disrupt star formation, mainly by the supernova explosions that put an end to their lives. Additionally, part of the chemical enrichment of the interstellar medium is produced by their strong stellar winds. However, in spite of their importance, our knowledge about these objects and their evolution is still fragmentary (see Chapter 3). This is principally because they spend a significant part of their main-sequence life-time while still embedded in their natal clouds ($\sim 20\%$), where the high extinction makes it difficult to observe their initial phases, they evolve rapidly (\sim Ma), are rare, and typically located at large distances (≥ 1 kpc) (Zinnecker and Yorke, 2007).

One of the most important observational clues to understand the formation of massive stars is multiplicity. A way to measure the degree of multiplicity in a system is by using the companion star fraction (csf). This quantity is defined as $\text{csf} = (B + 2T + 3Q + \dots) / (S + B + T + Q + \dots)$, where S are single stars, B are binary systems, and so on up to account for all the companions that form a tied system (Reipurth and Zinnecker, 1993). To highlight the importance of multiplicity in massive stars, as an example one could see that the csf is at least three times larger in the Orion Trapezium system than in the lower mass

stars that belong to the Orion Nebula (Zinnecker and Yorke, 2007). Additionally, studies to determine the proportion of spectroscopic binaries among massive stars suggest that, depending on the region (cluster), the fraction of multiple systems ranges between 20 and 60 % approximately. (e.g., Sana and Evans, 2011). As an example, Table 4.1 displays the spectroscopic binary fraction for O stars in a sample of nearby clusters with a mean spectroscopic binary fraction of 0.44. These results demonstrate that multiple companions in massive stars are important to characterize these objects, and that neglecting this property might lead to a misleading characterization of their physical properties.

Sana and Evans (2011) describe some of the main physical processes that show a strong dependency on multiplicity. Among them are: (a) the difference of evolutionary paths followed by single objects and multiple systems (see e.g., Crowther et al., 2010; de Mink et al., 2009; Langer et al., 2008; Sana et al., 2012); (b) the effect of wind collisions and the intrinsic X-ray luminosities of high-mass stars (Sana et al., 2006); (c) the role of winds in evolved binaries for the creation of dust (Tuthill et al., 2008); (d) variations in the apparent strength of the massive stars spectrum (Struve-Sahade effect; Linder et al., 2007) and; (e) the stellar velocity dispersion of clusters (Gieles et al., 2010)

Table 4.1: Spectroscopic binary fraction of massive stars in nearby clusters (adapted from Sana and Evans, 2011).

| Cluster | No. of O stars | Binary Fraction | Reference |
|----------|----------------|-----------------|-----------------------|
| NGC 6611 | 9 | 0.44 | Sana et al. (2009) |
| NGC 6231 | 16 | 0.63 | Sana et al. (2008) |
| IC 2944 | 14 | 0.53 | Sana et al. (2011) |
| IC 1805 | 8 | 0.38 | Hillwig et al. (2006) |
| IC 1848 | 5 | 0.40 | Mahy et al. (2009) |
| NGC 2244 | 6 | 0.17 | Penny et al. (1993) |
| Tr 14 | 6 | 0.00 | García et al. (1998) |

4.1.1.1. FORMATION MECHANISMS OF MASSIVE MULTIPLE SYSTEMS

ACCORDING to Zinnecker and Yorke (2007) some of the possible mechanisms to form high-mass multiple systems are:

a) Disk or filament fragmentation in a similar fashion as low-mass T Tauri stars (Bonnell and Bastien, 1992; Monin et al., 2007).

b) Formation of tight “twin” binaries with an orbital separation smaller than a typical Jeans length through the accretion of wider low-mass systems, allowing these low-mass components to accrete more mass and eventually become massive systems (Bonnell, 2005; Maeder and Behrend, 2002).

c) The formation of massive multiples through failed mergers and stellar collisions in early dynamical interactions (Bonnell, 2005; Zinnecker and Bate, 2002). This scenario would favor the formation of tight eccentric massive binaries.

d) The formation of multiple systems through disk-assisted capture (Bally and Zinnecker, 2005). This models suggests that early interactions among accretions disks in young massive stellar objects could assist binary companions. This mechanism is favored in the competitive accretion scenario of massive star formation (see Sec. 3.1.2).

Nevertheless, to discern which of the aforementioned models is correct (or a favored one), the analysis of the properties (period distributions, mass ratios, orbital eccentricities, etc.) of multiple systems is required. However, this is not an easy task, particularly because of the large parameter range that should be scanned. For example, the separation of components in multiple systems varies from 0.1 AU up to 10^4 AU, which corresponds to angular separations between 0.1 mas and $10''$ at a distance of 1 kpc. Additionally, the dynamic range necessary to observe multiple components is another important factor to take into account. For example, to observe O stars with O or B companions requires contrast ratios between 0.1 to 1. Nevertheless, to observe solar-type companions around O stars would require contrast ratios of 10^4 - 10^5 . To observe multiples with such contrast ratios is as difficult as observing planets around low-mass stars. Therefore, this indicates that several high-angular resolution and high-dynamic range techniques are necessary to cover the entire parameter space.

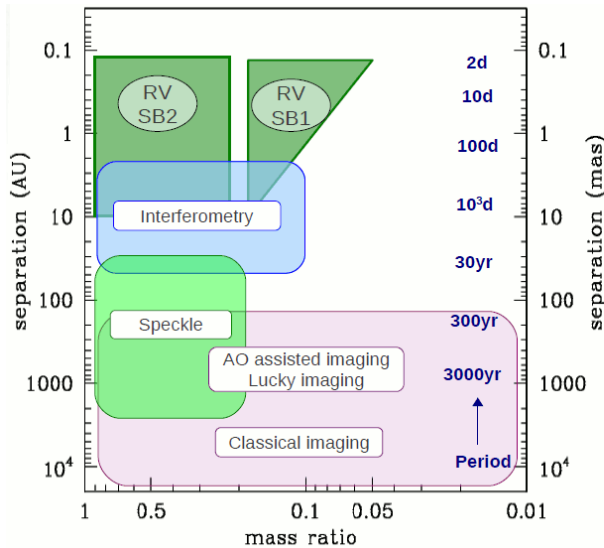


Figure 4.1: Scheme of the parameter space to search for multiple companions in high-mass multiple systems. The different high-angular resolution techniques used to map different parts of the range of separations and mass/brightness ratios are given. The values for the spatial scale are given, assuming that the targets are placed at 1 kpc from the solar system. Adapted from Sana and Evans (2011).

4.1.2. HIGH-ANGULAR RESOLUTION TECHNIQUES TO STUDY MASSIVE MULTIPLE SYSTEMS

THERE are several observing techniques that can be used to study multiplicity in massive stars. However, each one of them can only sample a specific part of the parameter space spanned by separation and brightness ratios. Figure 4.1 displays a schematic of the different observing techniques that might be used to observe stellar companions around high-mass stars. For very compact systems with separations between 0.1 and 10 mas, only spectroscopy provides the necessary resolution to observe these systems. It is interesting to note that spectroscopy does not allow us to observe systems whose orbital planes lie close to the plane of the sky. This thus create an observational bias to account for the total degree of multiplicity at these range of angular separations.

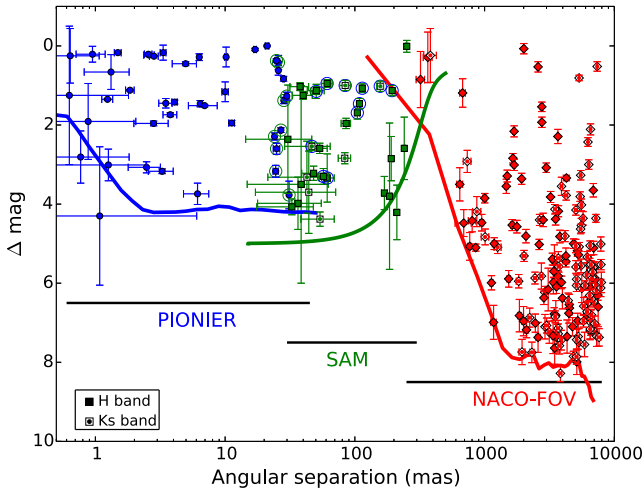


Figure 4.2: The image displays a plot of the detected multiple systems with the SMASH survey performed by Sana et al. (2014). The different observed targets are identified with different colors, depending on the instrument used. The solid lines indicate the mean sensitivity of the used instruments, and the large open circles mark targets detected with both NACO/SAM and PIONIER/VLTI.

In contrast, interferometry, both in the form of optical long-baseline interferometry and Sparse Aperture Masking, provides a unique tool to observe compact systems with angular separations between 2 and 60 mas. Nevertheless, interferometric observations are limited to bright sources only. In the case of the VLTI, the limiting magnitude for the observation of multiple stars ranges from 5 to 7, depending on whether the ATs or the UTs are used, respectively. Very long baseline optical interferometry did not play any major role for large multiplicity surveys until very recently. This was mainly because of the large amount of time required to take the data and the observational cost of using several of the major telescopes in the world at the same time. However, refinements in the acquisition of the data, and the arrival of new instruments (e.g., PIONIER/VLTI) have

opened the door to perform large interferometric observations of massive multiple systems. For multiple systems with angular separations between components larger than 60 mas, techniques such as speckle, adaptive optics, or even seeing limited imaging are used.

The most complete survey to determine multiplicity in massive stars was performed recently by Sana et al. (2014) (although this is the most complete study on multiplicity, we also refer the readers to the works of Maíz Apellániz, 2010; Mason et al., 2009; Sota et al., 2014). These authors studied 117 O stars with SAM NACO/VLT and 162 O stars with PIONIER/VLTI. Thus, they covered angular scales between 1-45 and 30-250 mas, in combination with dynamic ranges of $\Delta H < 4$ and $\Delta H < 5$, respectively. 96 of the targets were observed with the two techniques, thus fully covering the mentioned range of angular scales. For this main sample of 96 stars, Sana et al. (2014) found that 53 % of them have at least one companion within 200 mas. When including the information from AO observations of these targets, these authors found that the fraction of systems with at least one component increased to 76%. Finally, if spectroscopic information was added (i.e. the number of spectroscopic binaries among the main-sample), the fraction of multiple systems reached around 90%. Moreover, around 30% of the observed targets belong to hierarchical triple systems. Figure 4.2 displays a plot of the detected companions in the survey of Sana et al. (2014).

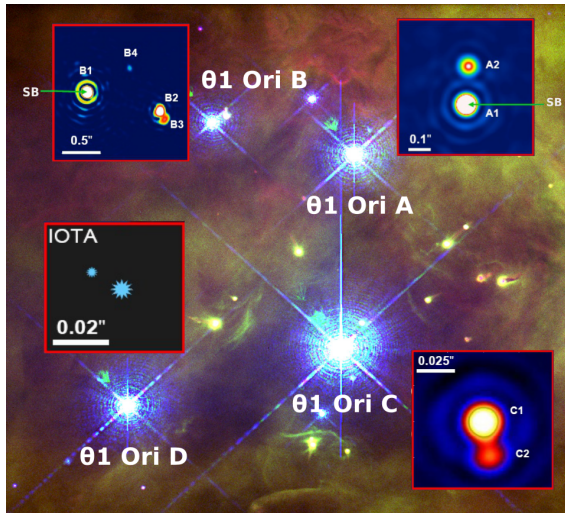


Figure 4.3: The image displays the Trapezium system located at the center of the Orion nebula. The four main components are observed: θ^1 Ori A, B, C and D. Each one of the sub-panels displays the multiple components that form each one of the main four sources. As it is observed, each one of the targets exhibits several hierarchical components, covering a wide range of angular scales. Some of them have been only detected with spectroscopy, while others have been imaged with optical interferometry and AO data. Image adapted from the one created by Thomas Preibisch (available at: <http://www.usm.uni-muenchen.de/people/preibisch/multiplicity.pdf>).

It is important to mention that, although the fraction of multiple systems is quite large, about 5% of the known O stars do not belong to any cluster and do not have any known companions. These stars are known as field stars. Some of them move with high velocities and are known as “runaway stars”. (see e.g., [de Wit et al., 2004](#); [Kroupa, 2000](#)). Some theories about the origin of these stars invoke dynamical three-body encounters at their early stages. This indicate that “runaway” stars might have an origin in multiple systems (e.g., binary and triple multiples). During these early dynamical interactions, the potential kinetic energy are exchanged, modifying the orbital motion and ejecting one (or several) components with high proper motions of around $\sim 50\text{-}100$ km/s ([Gies, 1987](#); [Poveda et al., 1967](#)); these are the typical velocities observed in “runaway stars”.

In addition to the study of multiplicity in large surveys, there are individual objects that must be analyzed in more detail because of their complexity or special importance. An example for such a system is the Trapezium (see e.g., [Schertl et al., 2003](#)), a high-order multiple that is responsible for the ionization of most of the material in the Orion nebula. High-order systems, like this one, are thought to be created by merging few sub-clusters (created due to gravo-turbulent fragmentation of the natal molecular cloud), in which there is at least one massive star. Thus, the study high-order systems provides important clues for massive star formation scenarios. Figure 4.3 displays an image of the Trapezium, with its main four components labeled. As the figure shows, each one of the four main targets is a binary or even a high-order multiple. The true degree of multiplicity in the trapezium system has been revealed only with the use of high-angular resolution techniques, in particular optical interferometry and spectroscopy. In this work, we describe interferometric observations of the similarly interesting (albeit somewhat less complex) multiple systems HD 150 136 and Herschel 36.

In this chapter, we report new long-baseline interferometric measurements of Herschel 36 and HD 150 136 with the instrument AMBER at the ESO Very Large Telescope Interferometer. The objective of this work was to resolve the outer component from the spectroscopic binary in both systems and the specific objectives were the following: (i) to provide accurate astrometric measurements of their separation, (ii) to measure their brightness ratio, and (iii) to give an estimate of their orbits.

4.2. HERSCHEL 36

Herschel 36 is a young massive system located at 1.3 kpc ([Arias et al., 2006](#)) in the Hour-glass high-mass star-forming region in the central part of the M8 nebula. This object is responsible for most of the gas ionization in the region. [Arias et al. \(2010\)](#) concluded that Herschel 36 is composed of at least three main components: two of them are the stars¹ *Ab1* (O9 V) and *Ab2* (B0.5 V), which form a close binary (system *Ab*) with a period of 1.54 days; the third one is component *Aa* (O7.5 V), which is the most luminous star of

¹The adopted nomenclature is consistent with the denominations of the stellar components of Herschel 36 according to the Washington Double Star Catalog (WDS). [Arias et al. \(2010\)](#) used *A*, *B1*, and *B2* for components *Aa*, *Ab1*, and *Ab2*, respectively.

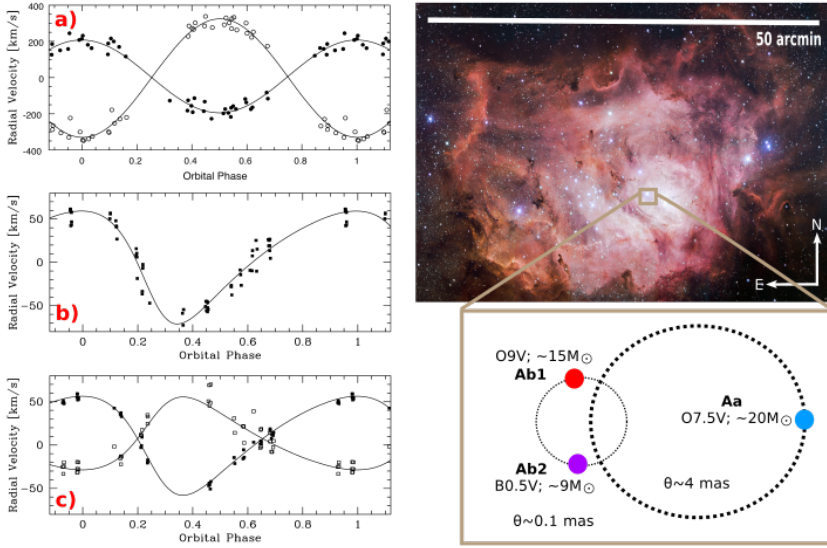


Figure 4.4: The image displays on the *left* three panels with: a) the radial velocity curves of the spectroscopic binary *Ab*. The open dots correspond to the measurements of *Ab1*, and the dark dots correspond to *Ab2*; b) the velocity curve of the putative outer component *Aa*; c) the velocity curve of the systemic velocity of system *Ab* (open squares); and the velocity curve of *Aa* (dark squares). Panels a), b) and c) were adapted from Arias et al. (2010). On the *right* the image displays an schematics of the expected configuration of Herschel 36.

the system and dominates its ionizing flux. These authors also reported strong variations in the line profile, shape, and radial velocity of the known components of Herschel 36, which indicate that component *Aa* and system *Ab* are gravitationally tied up in a wider orbit with a period of approximately 500 days and a projected semi-major axis of 3.5 mas between components *Aa* and *Ab*. The smallest spectroscopic predicted mass of the system *Aa+Ab* is of $19.2+26.0=45.2 M_{\odot}$ (see Fig. 4.4). **This system is intriguing because the combined luminosity of its putative three components agree with the expected theoretical luminosity of three ZAMS stars (Arias et al., 2010). This evolutionary stage is very difficult to observe since it only lasts shorter than 1 Ma in stars of such high mass.** Moreover, in addition to the *Aa + Ab* components, there is a fourth star located at $0.25''$ (Herschel 36 SE; Goto et al., 2006) and other stars several arcseconds away that may also be gravitationally bound to Herschel 36. Because of its location, multiplicity, and role in the nebula, this system has therefore been compared to θ^1 Ori C (Kraus et al., 2009) in the Orion Trapezium. The complete characterization of Herschel 36 may provide new links between the observed properties and the evolutionary models of massive stars. For example, the fact that component *Aa* is the most massive one, and not one of the components of the spectroscopic binary, may imply that the formation of this system was due to early dynamical interactions.

4.3. HERSCHEL 36: OBSERVATIONS AND DATA REDUCTION

A single 1 hr observation of Herschel 36 was obtained with AMBER (Petrov et al., 2007) in its low-resolution mode (LR-HK), using the VLT unit telescopes (UTs) 1, 2, and 4 on April 17, 2014 (JD2456764.8)². The triplet used for our observations has a longest baseline length of 130 m and a shortest baseline length of 57 m. The synthesized beam ($\theta = \lambda_{min}/2B_{max}$) for the total JHK bandpass is 3.65×0.93 mas with a position angle of 123° east of north. The instrumental setup allowed us to obtain measurements in the *J*, *H*, and *K* bands with a spectral resolution of $R = \lambda/\Delta\lambda \sim 35$. A standard calibrator – science target – calibrator observing sequence was used. The chosen calibrator, HD 165920 (selected with SearchCal; Bonneau et al., 2006, 2011), has a diameter of 0.289 mas and is separated by 1.95° from Herschel 36. It is a K1 IV-V star with magnitudes of $J=6.55$, $H=6.13$, and $K = 6.03$, similar to the corresponding magnitudes of the target. The airmass reported for the calibrator and target was ~ 1.04 . Figure 4.5 shows the *u-v* coverage of our observations.

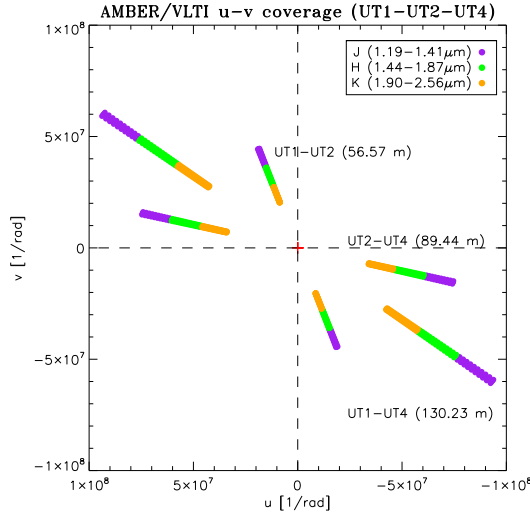


Figure 4.5: *u-v* coverage of our AMBER/VLTI observations of Herschel 36. The different bandpasses are displayed in different colors. The length of each baseline is also shown.

For the AMBER data reduction we used the software *amdlb v3*³ (Chelli et al., 2009; Tatulli et al., 2007). To eliminate frames that were deteriorated by variable atmospheric conditions (seeing varied between 0.6 to 1.0 at the time of our observations) and/or technical problems (e.g., shifts in the path delay, piston), we performed a three-step frame

²Based on observations collected at the European Organization for Astronomical Research in the Southern Hemisphere, Chile, within observing programme 091.D-0611(A). Within the same observational programme, the ESO archive contains additional observations of Herschel 36 taken on April 2013. However, these data are not usable for scientific purposes because of technical problems with the fringe tracker FINITO.

³http://www.jmmc.fr/data_processing_amber.htm

selection based on the following criteria: (i) first, we selected the frames with a baseline flux higher than ten times the noise, (ii) second, from this selection, we chose the frames with an estimated piston smaller than $15 \mu\text{m}$, and, finally, (iii) we selected the 50% of the frames with the highest signal-to-noise ratio. The two sets of calibrator observations exhibit a similar V^2 response within 5% accuracy on the UT2-UT4 and UT1-UT4 baselines. However, the squared-visibility (V^2) response of the UT1-UT2 baseline had a larger discrepancy. Additionally, the first set of calibrator observations presented low-photon counts. Therefore, we decided to only use the second set of calibrator observations to normalize our science target visibilities. The calibrated V^2 and closure phases are displayed in Fig. 4.6 for H and K bands.

4

4.4. HERSCHEL 36: ANALYSIS AND RESULTS

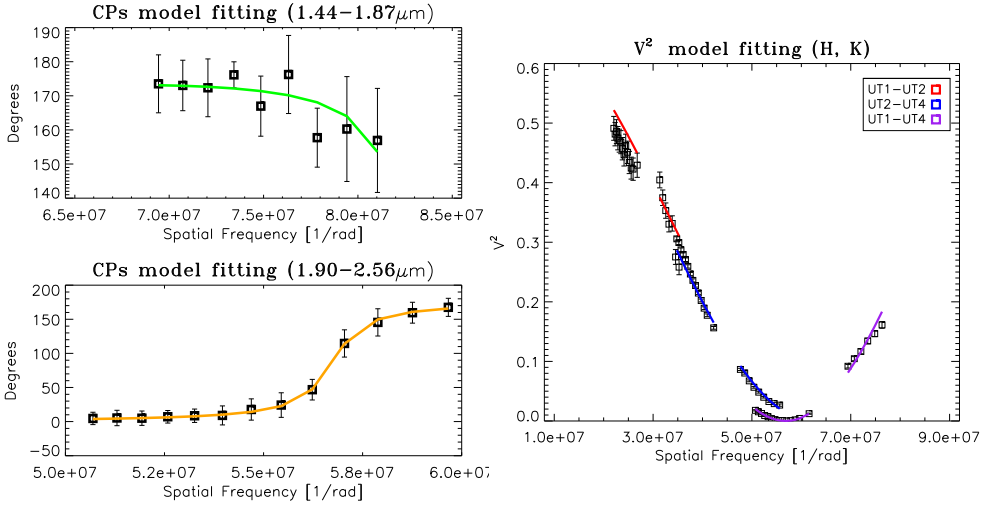


Figure 4.6: *Left:* Measured CPs of Herschel36. The best-fit models are represented in green and orange lines for the H and K band. *Right:* Herschel 36 V^2 model fitting. The panel displays the V^2 for the H and K filters in black and the best-fit solution at different colors for each one of the baselines.

WE used the orbital elements calculated in Arias et al. (2010) from the spectroscopic data of Herschel 36 to estimate the apastron of component Aa and system Ab . According to the ellipse equation, the distance to the apastron is $p = a(1 + e)$, where a is the semi-major axis and e the eccentricity of the system. Using the semi-major axis, inclination, and eccentricity from Table 3 of Arias et al. (2010), we estimated p_{Aa+Ab} for the system $Aa+Ab$:

$$p_{Aa+Ab} = (a_{Aa} + a_{Ab}) \sin(i_{Aa}) (1 + e_{Aa+Ab}) = 8.12 \times 10^8 \text{ km}. \quad (4.1)$$

For the close binary Ab , we used the values from Table 2 of Arias et al. (2010) to com-

pute p_{Ab} :

$$p_{Ab} = (a_{Ab1} + a_{Ab2}) \sin(i_{Aa})(1 + e_{Ab1+Ab2}) = 1.12 \times 10^7 \text{ km}. \quad (4.2)$$

The values of p_{Aa+Ab} and p_{Ab} at the distance of Herschel 36 thus correspond to 4 mas and 0.06 mas. In contrast to p_{Aa+Ab} , the apastron of system Ab indicates that it is below the VLTI angular resolution limit at the observed frequencies. Therefore, we fitted the calibrated V^2 and CPs with a model of a binary, composed of two unresolved sources (system Ab plus component Aa). We used the software LITpro to obtain the best-fit model parameters (Tallon-Bosc et al., 2008). We emphasize that both V^2 and CPs exhibit a clear cosine signature, which is typical of a binary source.

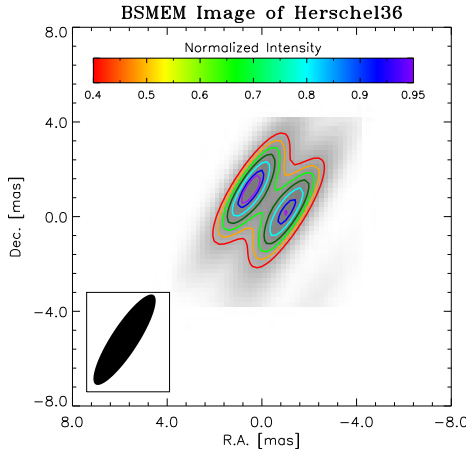


Figure 4.7: BSMEM image of Herschel36. Contours represent 40, 50, 60, 70, 80, 90, and 95% of the peak's intensity. The interferometric beam ($\theta = \lambda_{min}/2B_{max}$) for the data in H and K bands is of 4.50×1.14 mas with a position angle of 123° east of north. The northern component is the star Aa .

The quality of the J -band data was too low to be used in our model fitting, these data even introduced systematic residuals in the model fitting. Hence, we decided to exclude them from our analysis. This is expected because calibrating short wavelengths, such as the J band, is a difficult task in optical interferometry. It usually requires the highest performance of the instrument and good atmospheric conditions. Unfortunately, there were seeing variations, unstable fringe lock, and low SNR of the fringe-tracking during our observations.

To circumvent these difficulties, we restricted the model fit to the data of the H and K filters. Moreover, since CPs are free of telescope-dependent phase errors induced by atmosphere and telescope vibration, they are usually more resistant to these systematic errors than the V^2 . Our analysis, showed that the V^2 at zero baseline of the H and K bands do not reach unity. This means that an additional constant term had to be added to our

binary model to achieve a good fit to the data. This over-resolved flux can be explained by an additional stellar component or extended emission (e.g., scattering halo) in the field of view (~ 60 mas) at a larger angular distance than the one sampled by the shortest baseline (~ 10 mas). To investigate these possible scenarios in more detail, additional interferometric observations with shortest baselines are required. The geometrical model of the V^2 and CPs was thus fitted to the H and K filters together and to each band independently. The best-fit model parameters are reported in Table 4.2. The model in Fourier space, and the data are displayed in Fig. 4.6. Any systematic differences between model and data are within $2\text{-}\sigma$ of the data uncertainties.

Our model shows an average angular separation of 1.81 ± 0.03 mas between component Aa and system Ab . Assuming that component Aa is located at the center of the frame of reference, system Ab is located at an average projected position angle of $222^\circ \pm 10.5^\circ$ east of north. The best-fit flux ratio corresponds to $f_{Ab}/f_{Aa} = 0.95 \pm 0.12$. The $1 - \sigma$ uncertainties were estimated from the standard deviations of the best-fit values of the fitting to the individual and the combined bands.

Table 4.2: Best-fit of a binary model (system $Aa + Ab$) of Herschel 36 to the V^2 and CPs.

| Parameter | Combined | H | K | $1\text{-}\sigma^f$ |
|------------------------------|----------|-------|-------|---------------------|
| $f_{\text{over-resolved}}^a$ | 0.17 | 0.18 | 0.17 | 0.095 |
| f_{Aa}^b | 0.42 | 0.42 | 0.43 | 0.12 |
| f_{Ab}^c | 0.41 | 0.40 | 0.40 | 0.12 |
| d [mas] ^d | 1.82 | 1.80 | 1.81 | 0.03 |
| Φ [deg] ^e | 234.0 | 214.8 | 217.0 | 10.5 |

^a Fraction of total over-resolved flux.

^b Fraction of total flux contained in Aa .

^c Fraction of total flux contained in the inner system ($Ab1+Ab2$).

^d Angular separation between Aa and system Ab in milliarcseconds.

^e Angle between Aa and system Ab projected on the sky measured east of north.

^f $1\text{-}\sigma$ errors computed from the standard deviation of the best-fit models.

Image reconstruction was performed with the package BSMEM (Buscher, 1994; Lawson et al., 2004). This code uses a maximum-entropy algorithm to recover the real brightness distribution of the sources. To improve the quality of the image and reduce the side-lobes, we used the CPs and V^2 of both the H and K filters at the same time for the image reconstruction. The best produced image was created after 54 iterations. The best image has a χ^2 of 2.16 between the data and the final model. This image is displayed in Fig. 4.7 and is consistent with the best-fit geometrical model applied to the V^2 and CPs. Because f_{Aa}/f_{Ab} is almost one, the photometric center is between the two components.

4.5. HERSCHEL 36: DISCUSSION AND CONCLUSION

WE separated for the first time component Aa of Herschel 36 from the spectroscopic binary, the system Ab . Our results agree excellently well with those obtained by Arias et al. (2010). The recent statistical analysis of the brightness ratio distribution in massive multiples reported by Sana and Evans (2011) showed that close binaries typically consist of components with equal masses, while larger differences in masses can be found between components orbiting at larger angular separation. These results imply that companions at intermediate (100-1000 mas; 100-1000 AU at 1 kpc) or large spatial scales ($\geq 1''$; ≥ 1000 AU at 1 kpc) might be formed in a process independent of the processes of close spectroscopic binaries (e.g., from a different fragmented core and/or dynamical interactions; Bonnell et al., 2004).

Coplanarity of the orbits in massive multiple systems typically indicates that they were formed by a single collapse event. Hence, a complete characterization of the orbital parameters in this type of systems is mandatory for establishing useful constraints to stellar evolutionary models. In this respect, Herschel 36 is an important laboratory for determining coplanarity in massive multiples. According to Arias et al. (2010), the inclinations between the orbital planes of system Ab and Aa are related by the following relation: $\sin i_{Aa} = 1.03 \sin i_{Ab}$. This result restricts the inclination angles to two possibilities: $i_{Ab} \approx i_{Aa}$ or $i_{Ab} \approx 180^\circ - i_{Aa}$.

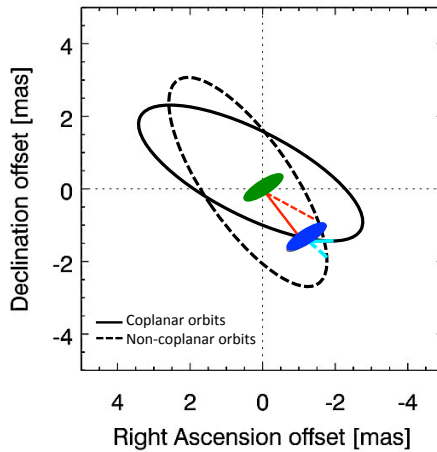


Figure 4.8: Orbital motion of Ab around Aa . The size of the blue and green ellipses corresponds to the uncertainty of the astrometric position of Ab and Aa , respectively. The *black solid ellipse* corresponds to the orbital solution where both orbits are coplanar. The *black dotted ellipse* corresponds to the non-coplanar case. The red lines represent the periapsis, and the light-blue lines the distance from system Ab to the projected ellipses of the orbits.

To explore this hypothesis, we obtained a first-order approximation of the absolute orbital parameters. To determine a complete solution of the outer orbit of Herschel 36 requires some knowledge about the orbital inclination, which can only be derived ac-

curately if at least three astrometric observations are available; unfortunately, we only have one. Therefore, some assumptions need to be made to provide an estimate of the complete orbit. We used the estimate of the inclination angles for the coplanar and non-coplanar cases ($i_{Aa} \sim i_{Ab} \sim 70^\circ$ and $i_{Aa} \sim 70^\circ$, $i_{Ab} \sim 110^\circ$, respectively) and the estimate of the masses made by Arias et al. (2010), in addition to our estimation of p_{Aa+Ab} to perform our simulations.

With these assumptions, we left the angle of the ascending node (Ω) as a free parameter in our orbital simulations. The angle of the ascending node resulted in $243^\circ \pm 12$ for the coplanar and $214^\circ \pm 50$ for the non-coplanar case. Fig. 4.8 displays the orbital solutions. The large uncertainty in Ω can be explained as a result of the change in the goodness of the fit due to the measurement offset from the orbit and the projection of the ellipse onto the line that connects the measurement and model position. Fig. 4.8 shows that components Aa and Ab of Herschel 36 appear to be very close to their periastron passage. Using the ephemeris of Arias et al. (2010), we estimated the periastron passage for a period of 500 days of component Aa at the Julian date $T_0 = 2456779.5 \pm 8$, which is very close to the date of our AMBER observations. The small angular separation measured with our AMBER observations (~ 2 mas) compared with our apastron estimation agrees with this prediction.

Herschel 36 thus belongs to the increasing number of O stars that form hierarchical multiple systems, which can provide important information about the high-mass star formation scenarios. To determine whether its orbits are coplanar or not, future astrometric NIR observations with the high angular interferometric resolution of AMBER and/or with the four-beam combiner PIONIER/VLTI in combination with a follow-up program of the spectroscopic solution are required.

4.6. HD 150 136

HD 150 136, in the open cluster NGC 6193, is a very massive system, with an estimated mass above $100 M_\odot$. Niemela and Gamen (2005) found that the brightest component of HD 150 136 is of spectral type O3. At a distance of 1.30 ± 0.12 kpc (Herbst and Havlen, 1977) it is the closest star of this kind to the solar system. In a detailed spectroscopic study Mahy et al. (2012) found a third massive component in HD 150 136, that was already tentatively predicted by Niemela and Gamen (2005). Mahy et al. (2012) reported that the tightly bound inner system is composed of a primary (P) of spectral type O3V((f*))–3.5V(f+) and a secondary (S) of O5.5–6V with eccentricity $e = 0$, inclination $i = 49^\circ \pm 5^\circ$ and an orbital period of 2.67 days. The tertiary (T) was reported to be of spectral type O6.5–7V, and in orbit around the *inner system* with a period of 3000 to 5500 days. During the refereeing process of our results, Sana et al. (2013) determined the first solution of the orbit between T and the *inner system* using independent interferometric and spectroscopic data. They resolved T with a projected angular separation of ~ 9 milliarcseconds (mas) at a position angle of 236° N \rightarrow E with a period of 8.2 years and a eccentricity (e) of 0.73. The dynamical masses of HD 150 136, found by those authors,

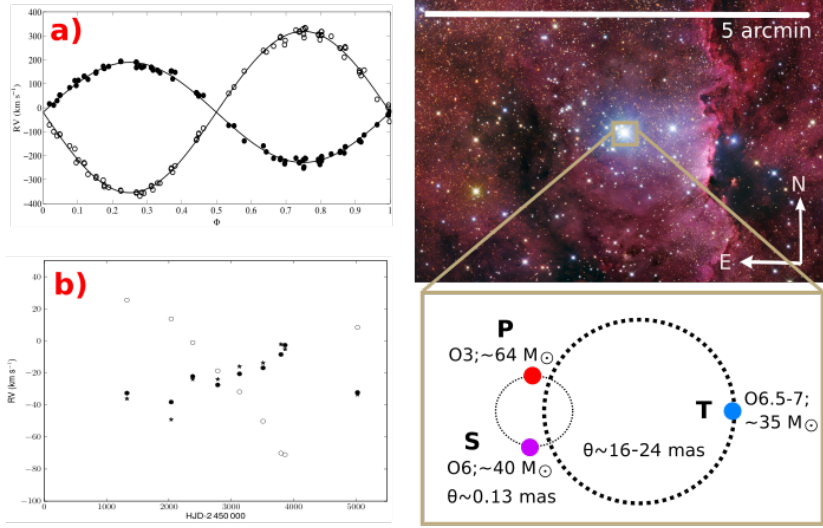


Figure 4.9: The image displays on the *left* two panels with: a) the radial velocity curves of the spectroscopic binary. The open dots correspond to the measurements of *S*, and the dark dots correspond to measurements of *P*; b) The velocity curve of the systemic velocity of system *P*+*S* (filled circles and stars) and the velocity curve of *T* (open circles). Panels a) and b) were adapted from Mahy et al. (2012). On the *right* the image displays an schematics of the expected configuration of HD 150 136.

agree with the previous predictions of Mahy et al. (2012) with 63 ± 10 , 40 ± 6 and 33 ± 12 M_{\odot} for *P*, *S* and *T*, respectively (see Fig 4.9).

The flux ratio between the *inner system* and *T* observed from the *H*-band interferometric measurements supports the previous estimation of spectral types and evolutionary stages (main-sequence stars) suggested by Mahy et al. (2012). In order to unveil the link of the observed multiplicity and the evolutionary models of massive stars, a continuing interferometric and spectroscopic monitoring is mandatory.

4.7. HD 150 136: OBSERVATIONS AND DATA REDUCTION

A single snapshot observation of HD 150 136 was obtained with AMBER in its Low Resolution Mode (LR-HK), using the VLT unit telescopes (UTs) 1, 3, and 4 on March 4th, 2013 (JD 2456355.9). The triplet used for our observations has a maximum baseline length of 130 m and a minimum baseline length of 63 m. The synthesized beam obtained with this configuration has 3.59×1.43 milliarcseconds (mas) with a position angle of 314.9° . The instrumental setup allowed us to obtain measurements in the *J*-, *H*-, and *K*-bands with a spectral resolution of $R = \lambda/\Delta\lambda \approx 35$. A standard calibrator – science target – calibrator observing sequence was used. The chosen calibrator, HD 149 835, is separated by 1.47° deg from HD 150 136. It is a K0III star with magnitude of *J* = 5.5, *H* = 5.1, and *K* = 4.9, similar to the corresponding magnitudes of the target (see Table

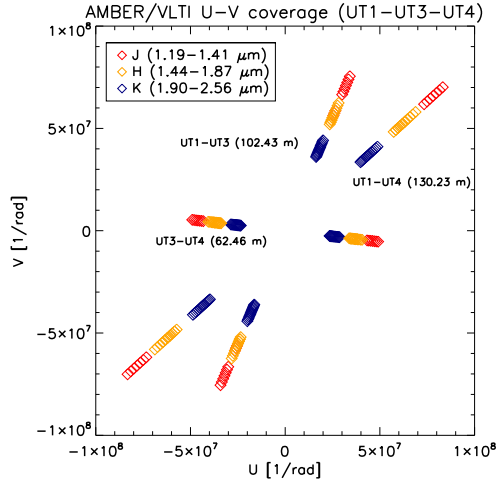


Figure 4.10: $u - v$ coverage of our AMBER/VLTI observations of HD 150 136. The baselines length is displayed in the plot.

4.4). The airmass reported for the calibrator is 1.19, and 1.15 for the target, respectively. Fig. 4.10 shows the $u - v$ coverage of our observations.

As well as with Herschel 36, we used the *amdl*lib3 data reduction software to analyze the AMBER data. In order to eliminate frames which were deteriorated by variable atmospheric conditions and/or technical problems (e.g., shifts in the path delay), we selected only the 20% of frames with the highest signal-to-noise ratio. The two sets of calibrator observations exhibit similar V^2 response within 5% accuracy. Hence, we interpolated a linear fit to the calibrator visibilities for the epoch of the science target to normalize our visibilities. The obtained calibrated squared visibilities at K -band and closure phases are displayed in Fig. 4.11.

4.8. HD 150 136: ANALYSIS

WE note that the apparent separation between P and S in the *inner system* of HD 150 136 is about 0.1 mas (Mahy et al., 2012), and thus more than one order of magnitude smaller than what can be resolved with VLTI in the NIR. Therefore, to fit the calibrated measurements we chose the model of a binary, composed of two unresolved sources (*inner system* plus tertiary companion, T). The model fitting was done with the LITpro software to obtain the best-fit model parameters.

When fitting the CPs and V^2 of all bands simultaneously, we noted significant systematic residuals at the shorter wavelengths: the V^2 values were consistently too low for all baselines in J and showed some systematic errors for the shortest baseline (UT1-UT3) in H . Since the photon count of the target was unexpectedly low in J and H , we

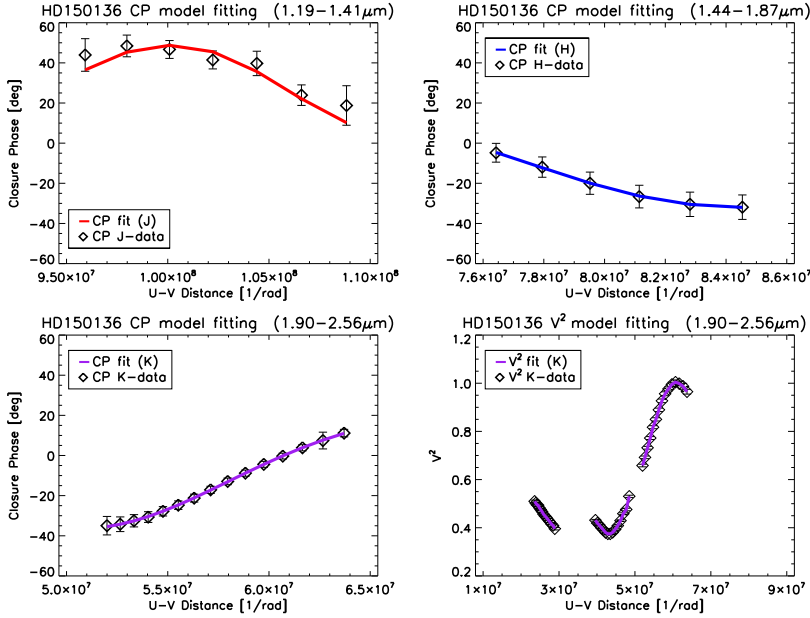


Figure 4.11: CP and V^2 Model fitting. Data are shown in black diamonds and the best obtained model in colored lines.

suspect some technical problems were present in the observations, but could not identify the exact cause. Hence, to circumvent the systematics observed in the V^2 from the unsatisfactory calibration in J - and H -band, we chose to restrict the model fit only to the CP data of the three bands. Since CP data by definition eliminate with high reliability most of the atmospheric effects, they are, usually, much more robust to systematic errors than V^2 , which are strongly affected by weather conditions (e.g. strong variable seeing). Therefore, the use of CP to our model fitting provides a good estimator of the real brightness distribution of the source. The model was fitted to the combined CPs from all bands and to the CPs from each band individually. The resulting fits for the individual bands are shown in Fig. 4.11. Any biases are small with respect to the dynamic range of the data.

The best-fit parameters are listed in Table 4.3. We find an angular separation of 7.27 ± 0.05 mas of T from the *inner system*, a Position angle on the sky of $209 \pm 2^\circ$ East of North, and a flux ratio of $f_T / f_{inner} = 0.25 \pm 0.03$. The 1σ uncertainties were estimated from the standard deviations of the best-fit values from the fits to the individual bands. We should note that in the case we extend the model fit to both the V^2 amplitudes and the CPs for the three individual bands, the resulting fits agree within the 1σ uncertainties with the CP-only fits. This gives extra support to our results. For illustrative purposes, we show in Fig. 4.11 the fit to the K -band V^2 data of the reported model.

Image reconstruction from the interferometric data was performed with the BSMEM

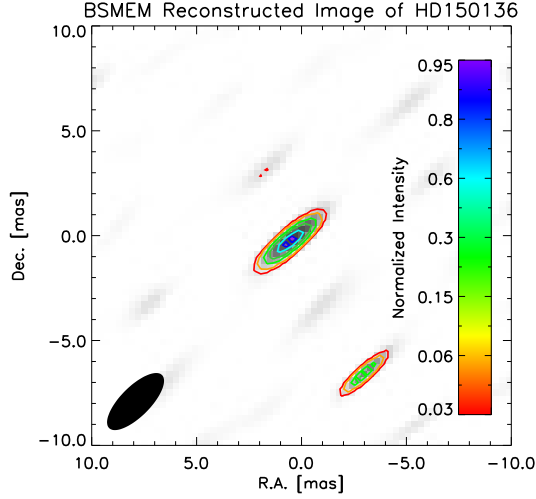


Figure 4.12: BSMEM reconstructed image of HD 150 136. The total flux is normalized, contours represent 3, 7, 15, 30, 60, 80 and 95% of the maximum. The black ellipse at the bottom-left represents the synthesized beam of our interferometer.

package. For the image reconstruction we decide to include all CP and V^2 of the three observed wavelengths in order to improve the quality of the image and reduce the side-lobes. The best reconstructed image was created after 45 iterations. It is displayed in Fig. 4.12 and it is consistent with the parameters obtained from the model fitting.

4.9. HD 150 136: RESULTS AND DISCUSSION

THE measured flux ratio between the tertiary and the inner system agrees well with the flux ratio that results from the V magnitudes computed for the three components by Mahy et al. (2012): $f_{theor,T/inner} = 0.19 \pm 0.08$, and with the H -band astrometric measurements by Sana et al. (2013): $f_{PIONIER,T/inner} = 0.24 \pm 0.02$. For a more detailed analysis of the source brightness, we used the Bayesian code CHORIZOS (Maíz-Apellániz, 2004) to obtain the extinction for HD 150 136 using as input the Strömgren + NIR photometry in Table 4.4. More specifically, we used the Milky Way SED grid of Maíz Apellániz (2013a) and the new family of extinction laws described in Maíz Apellániz (2013b). The results of the fit are a monochromatic color excess $E(4405 - 5495) = 0.431 \pm 0.009$ and an extinction law with $R_{5495} = 4.12 \pm 0.13$. The somewhat large value of R_{5495} is typical of stars in H II regions such as HD 150 136 and the value of $E(4405 - 5495)$ is within the expected range for a star of its Galactic coordinates and distance. The above values correspond to $A_J = 0.560 \pm 0.021$, $A_H = 0.360 \pm 0.013$ and $A_K = 0.230 \pm 0.009$. Note, however, that the largest residual of the fit comes from the K -band photometry, suggest-

Table 4.3: Best-fit parameters of a binary model (inner system plus tertiary) for HD 150 136 to the closure phases to all bands combined and to each band individually.

| Parameter | Combined | <i>J</i> | <i>H</i> | <i>K</i> |
|---------------------------|----------|----------|----------|----------|
| f_{inner}^a | 0.80 | 0.78 | 0.80 | 0.82 |
| f_T^b | 0.20 | 0.22 | 0.20 | 0.18 |
| d [mas] ^c | 7.27 | 7.27 | 7.19 | 7.19 |
| Φ [deg] ^d | 209.0 | 210.2 | 206.7 | 210.7 |

^a Fraction of total flux contained in the inner system ($P+S$).

^b Fraction of total flux contained in the tertiary (T).

^c Angular separation between inner system and T in milliarcseconds.

^d Projected angle of the system on the sky.

ing a small excess in the observed spectrum of the order of 0.03 magnitudes. We also verified that the existing Tycho-2 photometry agrees with the model SED derived from CHORIZOS.

Table 4.4: Strömgren and NIR Photometry of HD 150 136.

| Strömgren Photometry ^a | | NIR Photometry ^b | |
|-----------------------------------|--------------------|-----------------------------|------------------|
| V | 5.647 ± 0.001 | J | 5.15 ± 0.037 |
| $b - y$ | 0.192 ± 0.009 | H | 5.09 ± 0.018 |
| m_1 | -0.043 ± 0.011 | K | 4.99 ± 0.018 |
| c_1 | -0.114 ± 0.002 | | |

^a Values taken from [Grønbech and Olsen \(1976\)](#).

^b J -band values obtained from [Clarke et al. \(2005\)](#) and H - and K -band values from the 2MASS catalog ([Skrutskie et al., 2006](#)).

The age of the HD 150 136 system cannot be too young (~ 0.1 Ma) because the system has clearly emerged from the embedded phase. On the other hand, it cannot be too old (~ 2 Ma or older) because in that case the more massive component would have evolved to a later spectral type than O3 V. Therefore, the age must be close to 1 Ma. Using the corresponding Geneva isochrone without rotation ([Lejeune and Schaerer, 2001](#)) and assuming T_{eff} of 44 500 K, 39 000 K, and 37 000 K for P , S , and T , respectively, we derive a flux ratio $T/(P+S)$ in the K band of 0.22, which is within one sigma of our value. Such a triple system should have a combined absolute magnitude in the K band of -5.04 (as derived from the assumed isochrone and temperatures). On the other hand, after correcting for a distance of 1.3 kpc and the extinction derived above, a measured K magnitude of 4.991 results in an absolute magnitude $M_K = -5.81$, significantly brighter than expected. If, however, we assume an age of 1.8 Ma the total expected magnitude of the system would increase by more than a magnitude. Hence, one possibility is that the sys-

tem is several hundred thousand years older than 1 Ma.

From the flux ratio between the *inner system* and *T* obtained at each filter as well as the described photometric analysis, we obtained the following absolute magnitudes for *T*: $M_{T,J} = -4.34 \pm 0.23$, $M_{T,H} = -4.09 \pm 0.21$ and $M_{T,K} = -3.93 \pm 0.21$. These values are in agreement (within 1σ confidence) with the colors of an O6.5-O7 main-sequence star according to the calibration of O-type stars developed by Martins et al. (2005). Consistently, the *J*-, *H*- and *K*- absolute magnitudes of the *inner system* ($M_{inner,J} = -5.71 \pm 0.23$, $M_{inner,H} = -5.60 \pm 0.21$ and $M_{inner,K} = -5.59 \pm 0.21$) are also (within 1σ accuracy) in agreement with a combined pair of O3+O5.5 stars ($M_{theor,J} = -5.63$, $M_{theor,H} = -5.52$ and $M_{theor,K} = -5.42$ Martins et al., 2005), as it was expected. Such a photometric analysis, only feasible with our multi-wavelength interferometric observations, clearly provide us consistent information on the nature of HD 150 136.

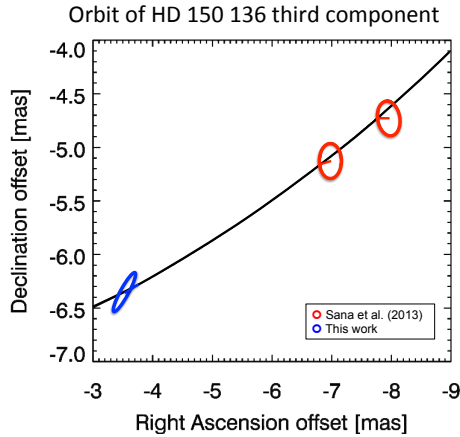


Figure 4.13: Orbital motion of *T* around the *inner system*. The coordinate system is centered on the *P + S* position, the red ellipses correspond to the astrometric positions of Sana et al. (2013) and the blue one to our AMBER data. The size of the ellipse is equivalent to 1σ uncertainty and the straight blue and red lines indicate the offsets of the measured astrometric positions from the best orbital fit. The continuous black line represents the best fit to the orbital motion.

Additionally, we find an angular separation of *T* from the *inner system* of 7.22 ± 0.22 mas and a position angle of $209 \pm 2^\circ$ N→E. Those measurements are consistent with the results obtained by Sana et al. (2013). Nevertheless, in order to improve the knowledge of *T* orbital motion, we performed a model fitting of the period and epoch (keeping the rest of the orbital parameters fixed) of *T* towards the *inner system*. For this purpose we combined our new interferometric measurement with the radial velocities and the two astrometric epochs of Sana et al. (2013). Our best fit retrieves a change in the orbital period from 3008 to 2770 days and a modification in the epoch (periastron passage) from 2451241 to 2451614. A preliminary analysis of our spectroscopic data from monitoring

HD 150 136 within the *OWN Survey project* (Barbá et al., 2010) from April 2005 to July 2012, and the recent published spectral analysis of Sana et al. (2013) indicates that *T* may indeed be approaching the periastron of its orbit within the next two years. Interferometric measurements at such position will help us to derive, without ambiguity, the semi-minor axis of the orbit and to constrain with high precision the other orbital parameters. Figure 4.13 displays the best fit of our interferometric data in addition to the previous measurements.

HD 150 136 is one more example of O stars that belong to multiple systems with gravitational bound components at different spatial scales. The fact that massive stars are born in multiple systems have strong implications on their star formation scenarios. Thus, the orbital motion of component *T* around the HD 150 136 *inner system* deserves a complete study in order to test the coplanarity of the orbits in this massive multiple, which can provide us with important clues about its formation. The currently favored theoretical models for the formation of high-mass stars are: (i) the collapse of a massive monolithic protostellar core (Krumholz et al., 2009) and (ii) competitive accretion in clusters (Bonnell and Bate, 2006). On average, the components of a massive multiple that forms through collapse of a monolithic cloud are expected to have coplanar orbits, while the formation of massive stars from clouds with hierarchical sub-structure (or posterior formation of multiples from dynamical encounters) will favor the creation of systems with more randomly distributed orbits. High resolution spectroscopy will have to be combined with astrometry from the high angular resolution (~ 2 mas) of AMBER NIR interferometry to acquire the necessary data for such future work.

5

MASSIVE STARS AT THE GALACTIC CENTER

THE BOW SHOCKS IN THE MINI-SPIRAL

Astronomy? Impossible to understand and madness to investigate.

Sophocles

There exists an enigmatic population of massive stars in the central parsec of the Galactic center that were formed a few million years ago. A fraction of these stars has been found to orbit the supermassive black hole, Sgr A, in a projected clockwise disk-like structure, which suggests that they were formed in a formerly existing dense disk around Sgr A*. This chapter is focused on the study of a subgroup of these objects, the extended, near-infrared bright sources IRS 1W, IRS 5, IRS 10W, and IRS 21, that have been suggested to be young, massive stars that form bow shocks through their interaction with the interstellar medium. Their nature has impeded accurate determinations of their orbital parameters. We aim at establishing their nature and kinematics to test whether they form part of the clockwise disk.*

We performed NIR multiwavelength imaging with NACO/VLT using direct adaptive optics and AO-assisted SAM. We introduce a new method for self-calibration of the SAM point spread function in dense stellar fields. The emission mechanism, morphology, and kinematics of the targets were examined via 3D models, combined with existing models of the

Parts of this chapter have been published in *Astronomy & Astrophysics* **567**, A21 (2014); [Sanchez-Bermudez et al. \(2014c\)](#).

gas flow in the central parsec. We confirm previous findings that IRS 21, IRS 1W, and IRS 5 are bow-shocks created by the interaction between mass-losing stars and the interstellar gas. The nature of IRS 10W remains unclear. Our modeling shows that the bow-shock emission is caused by thermal emission, while the scattering of stellar light does not play any significant role. IRS 1W shows a morphology that is consistent with a bow shock produced by an anisotropic stellar wind within a locally inhomogeneous ISM density. Our best-fit models provide estimates of the local proper motion of the ISM in the Northern Arm that agree with previously published models that were based on radio interferometry and NIR spectroscopy. Assuming that all of the sources are gravitationally tied to Sagittarius A*, their orbital planes were obtained via a Monte Carlo simulation.

Our targets appear to be Wolf-Rayet stars associated to the last starburst at the GC. Our orbital analysis suggests that they are not part of any of the previously suggested coherent stellar structures, in particular the clockwise disk. We thus add more evidence to recent findings that a large proportion of the massive stars show apparently random orbital orientations, suggesting either that not all of them were formed in the clockwise disk, or that their orbits were randomized rapidly after formation in the disk.

5

5.1. INTRODUCTION

THE Galactic center (GC) is an excellent laboratory to test the physics of some of the densest regions of galaxies. Located at a distance of 8 kpc from the Solar system, the GC harbors the closest supermassive black hole, named Sgr A*, with an estimated mass of around $M_{\text{SgrA}^*} \sim 4 \times 10^6 M_{\odot}$ (Genzel et al., 1996; Ghez et al., 1998; Schödel et al., 2003, 2002). Observations performed at radio wavelengths with the Very Large Baseline Array suggest that the size of the radio counterpart of SgrA* corresponds to 3-10 light minutes (Doeleman et al., 2001, 1008; Rogers et al., 1994). Since the GC is 10^5 times closer than other galactic nuclei, it provides a unique opportunity to test the interactions of a super massive black-hole with its environment.

The currently detectable stars in the central parsec of the Milky Way, which constitute on the order of 10% of the estimated total amount of stars in that region, can be roughly classified into three groups: (a) late type red giants and super-giants; (b) asymptotic giant branch (AGB) stars and; (c) hot-early young type stars. It is very difficult to explain the existence of the young stars in the central parsec via standard star formation through cloud collapse, as in other parts of the Galaxy (Genzel et al., 2010; Lu et al., 2009; Najarro et al., 1994). For a gas cloud to collapse in the presence of tidal shear from the super-massive black hole, the gas cloud should have to be denser than the “Roche” density (Genzel et al., 2010):

$$n_{\text{Roche}}(R) \sim 6 \times 10^{10} \left(\frac{R}{0.1 \text{ pc}} \right) \text{ cm}^{-3} \quad (5.1)$$

where R is the size of the cloud. Therefore, for a cloud of 0.1 pc in size, a density of $\sim 10^{10} \text{ cm}^{-3}$ is required. Nevertheless, the currently observed densities of the gas in

the GC region (10^5 - 10^6 cm^{-3} ; [Christopher and Scoville, 2003](#)) are many orders of magnitude lower than the one necessary to overcome the tidal disruption produced by the gravitational field of the SgrA* ([Alexander, 2005](#); [Ghez et al., 2005](#)).

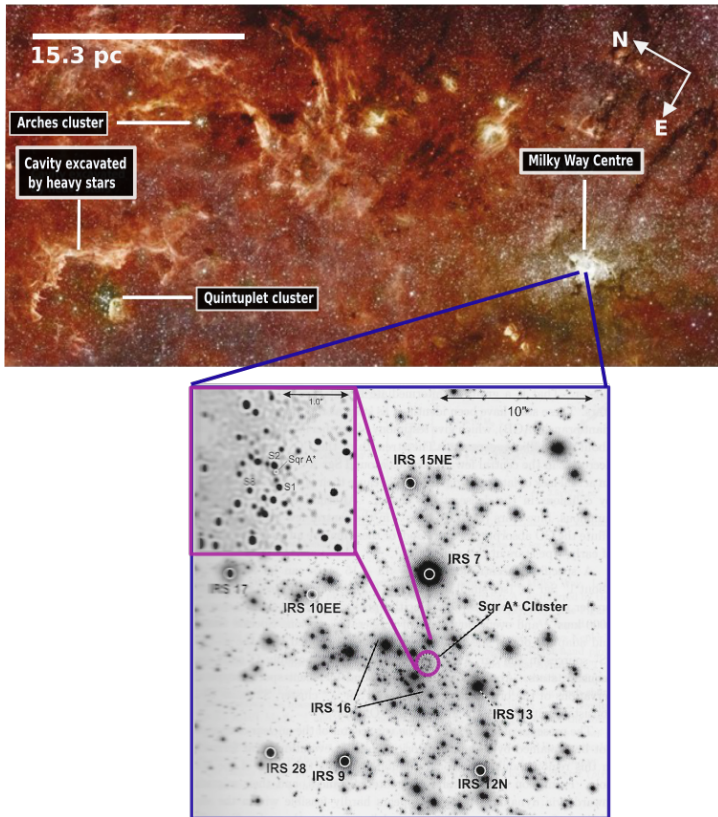


Figure 5.1: The *upper* panel displays the GC on large scales. Three of the clusters with some of the most massive stars in the Milky Way are labeled: a) The Arches cluster; b) the Quintuplet cluster; c) the Nuclear stellar cluster. Image composite with Hubble Space Telescope and Spitzer observations. Credits: NASA, ESA, D.Q.Wang, JPL, S. Stolovy. The *lower* panel displays a zoom onto the central parsec of the GC. Some of the massive stars are labeled. An additional zoom onto the close environment of SgrA* is also displayed. Image taken from [Eckart et al. \(2005\)](#).

Also, the tidal field of Sgr A* would rapidly disrupt any molecular gas cloud with a density as normally observed in the Milky Way when it enters the central parsecs. Nevertheless, there are around 177 identified massive stars in the central parsec of the galactic center ([Bartko et al., 2010](#)). They correspond to dwarf and giant main-sequence O, B and Wolf-Rayet stars, having ages on the order of $\sim 6 \pm 2$ Ma ([Lu et al., 2013](#); [Paumard et al., 2006](#)). This observational evidence marks the GC as one of the places with the richest concentration of massive stars in the Galaxy. For a complete description of the different scenarios that could have led to the formation of massive stars in the GC see the review

of Genzel et al. (2010). There are still many open questions related to the different possible formation scenarios of the young stars near Sgr A*. These are being investigated in many ongoing observational and theoretical studies.

Some of these young stars appear to orbit the black hole in a disk-like structure that rotates in a clockwise direction (referred to as clockwise system, CWS, in the following). This is one of the observations that favors the hypothesis for their formation *in situ* in a formerly existing gas disk around Sagittarius A* (Bartko et al., 2009; Levin and Beloborodov, 2003; Lu et al., 2009; Paumard et al., 2006). Considerable open questions in this picture remain, however, in particular, concerning the nature of the young stars that are not part of the CWS (see, e.g., discussion in Genzel et al., 2010): Is the second postulated system of a counterclockwise streamer or disk (CCWS) real? Is the CWS strongly warped? Can the current kinematical configuration of the young, massive stars be reached when one assumes that all of them are on the CWS? It is therefore of great interest to obtain as much information as possible about the orbital parameters of all young, massive stars

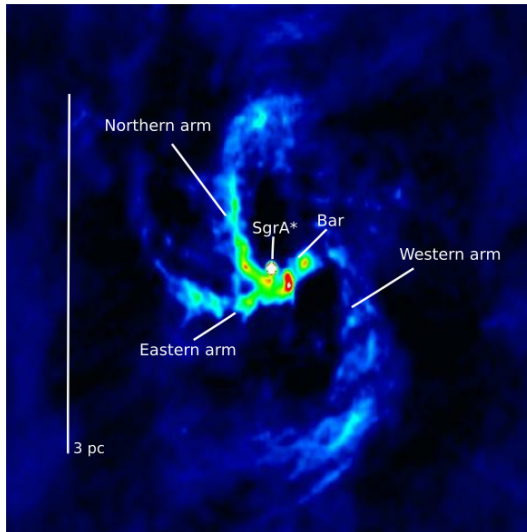


Figure 5.2: Radio continuum emission at 3.6 cm from the inner few parsecs of our Galaxy. The different features of the mini-spiral are labeled. The bright point source in the center is Sagittarius A*. Image taken from the NRAO image gallery (Credits to: Roberts, D.A., Yusef-Zadeh, F., Goss, W.M).

Among the observed massive stars, there are some that interact with streamers of gas and dust, named Sagittarius A West, at the central parsecs of the GC. The study of these stars is the subject of the present chapter. Sagittarius A West, the so-called mini-spiral, is a prominent feature of the interstellar medium (ISM) in the inner ~ 2 pc of the Milky Way (Ekers et al., 1983; Lo and Claussen, 1983). It is made up of three streamers of ionized gas, termed the Northern, Western, and Eastern arms. Figure 5.2 displays an image of the

central 3 pc of the Milky Way taken at 3.6 cm with the Very Large Array. In this image the different parts of the mini-spiral are observed. Studies of the radial velocities and proper motions of the gas in the mini-spiral have shown that their dynamics can generally be described by three bundles of quasi-Keplerian orbits in the combined potential of the central stellar cluster of the Milky Way plus a supermassive black hole (e.g., [Paumard et al., 2004](#); [Vollmer and Duschl, 2000](#); [Zhao et al., 2009](#)).

It is generally thought that the gas in the mini-spiral is ionized by the radiation of the massive stars within 0.5 pc of the supermassive black hole, Sagittarius A* ([Bartko et al., 2010](#); [Lu et al., 2013](#); [Paumard et al., 2006](#)). Some bow shocks show evidence of interactions between stellar winds from the young massive stars and the ISM in the mini-spiral ([Buchholz et al., 2011](#); [Clénet et al., 2004](#); [Geballe et al., 2006](#); [Mužić et al., 2007](#); [Tanner et al., 2005](#)). Some of these bow shocks are among the brightest near- to mid-infrared sources in the central parsec of the Galactic center and have been known for decades ([Becklin and Neugebauer, 1975](#); [Rieke and Low, 1973](#)) before their nature was finally revealed through radiative transfer modeling and, in particular, high angular resolution imaging ([Tanner et al., 2002, 2005](#)).

[Tanner et al. \(2005\)](#) analyzed high angular resolution NIR observations of the sources IRS 1W, 5, 10W, and 21 and modeled their bow shocks. From the large measured stand-off distances of the bow shocks' apices the authors concluded that the central sources must be Wolf-Rayet stars and thus were created in the above-mentioned star formation event. Because of the highly embedded nature of the sources, no spectroscopic confirmation of this classification could be obtained so far, with the exception of a tentative identification of IRS 1W as a Be star by [Paumard et al. \(2006\)](#). The lack of suitable spectra means that the line-of-sight velocities of the bow-shock stars are unknown and cannot be used to estimate their orbital parameters.

Nevertheless, bow-shock (BS) sources are of great interest because they allow us, in principle, to infer all six of their phase space parameters, and thus one more (the line-of-sight distance) than in the case of other young stars. Their 2D positions and proper motions can be inferred from imaging. Their line-of-sight (LOS) velocities and distances can be inferred from their interaction with the mini-spiral and from the resulting shape of the bow shocks in combination with models of the gas flow in the mini-spiral (e.g., [Paumard et al., 2004](#); [Vollmer and Duschl, 2000](#); [Zhao et al., 2009](#)). In this way, [Tanner et al. \(2005\)](#) were able to show that the kinematic properties of IRS 1W and 10W, as determined from their measurements, are consistent with the hypothesis that these stars belong to the CWS. However, they did not have the necessary proper motion measurements to perform this kind of analysis on IRS 5. For IRS 21, [Tanner et al. \(2005\)](#) were unable to resolve its bow-shock and concluded that it was seen face-on (see also [Tanner et al., 2002](#)). [Buchholz et al. \(2011\)](#), however, were recently able to resolve the bow-shock structure of IRS 21 through deconvolution of high-quality adaptive optics data and could thus discard the face-on hypothesis.

Here we continue the investigation of the bow-shock sources IRS 1W, 5, 21, and 10W

by Tanner et al. (2005). We use our own multiwavelength AO assisted imaging as well as AO-assisted SAM (see, e.g., Tuthill et al., 2006) to investigate the structure of the sources, which we then fit with fully three-dimensional models. The results from the modeling are then combined with new, more accurate proper motion measurements and with models of the mini-spiral flow to investigate the kinematics of the bow-shock stars.

The chapter layout is the following: Section 5.2 describes the acquisition and reduction of the data. The calibration process and image reconstruction of our SAM observations is described in particular detail because we describe a novel way of self-calibrating SAM data in a dense stellar field. This procedure can be of general interest for SAM observations of targets in dense stellar fields. Section 5.3 describes the results of the proper motion measurements. Section 5.4 describes the mathematical model used in determining the shape and emission of the bow shocks and the corresponding fitting procedure. Section 5.5 describes the local kinematics of the Northern Arm at the position of the bow shocks and the procedure of determining the probability density function of the source orbital planes. Finally, in Sect. 5.6 we discuss our results and present our conclusions.

5.2. OBSERVATIONS AND DATA REDUCTION

5.2.1. AO IMAGING

WE used AO-assisted imaging observations of the central parsec of the GC using VLT/NACO to measure the proper motions of the bow-shock sources and to infer their structure. Table 5.1 summarizes the observations. The bright supergiant IRS 7, located about 5.5" north of Sgr A*, was used to close the loop of the AO. IRS 7 is a variable source (Ott et al., 1999). The most recently published values for its flux are $K_s = 7.69 \pm 0.06$ in April 2006 and $K_s = 6.96 \pm 0.04$ in March 2009 (see Schödel et al., 2013). All imaging data were sky subtracted, flat fielded, corrected for bad pixels, and then combined via a shift-and-add algorithm into final mosaics, as described, for instance, in Schödel et al. (2009). The saturated cores of bright stars were repaired in all images from epochs 2002 to 2008. The images from 2009 to 2011 did not need to be repaired since saturation was not a problem because of the short exposure times used for these observations. The data from 2010 and 2011 were taken with NACO's *cube mode*, which registers each individual exposure (see Girard et al., 2010). To improve the image quality of the latter data we applied a *lucky imaging* method and selected the 30% of the frames with the highest Strehl ratios.

To remove the seeing halos in the AO images, we extracted PSFs from the *H*- and K_s - band images that were obtained with the S13 camera of NACO and deconvolved the images with the Lucy-Richardson algorithm (Lucy, 1974). The deconvolved images were restored with a Gaussian beam of 2 pixels FWHM to create the final images to be used in our analysis.

Table 5.1: VLT/NACO imaging observations.

| Date | Filter | N ^a | DIT ^b [s] | Camera ^c |
|--------------------------|-------------|----------------|----------------------|---------------------|
| 03 May 2002 ^d | K_s | 60 | 20 | S27 |
| 10 May 2003 ^d | K_s | 2280 | 0.5 | S27 |
| 12 Jun 2004 ^d | $IB_{2.06}$ | 96 | 30 | S27 |
| 13 May 2005 ^d | K_s | 6180 | 0.5 | S27 |
| 29 Apr 2006 ^d | K_s | 896 | 2 | S27 |
| 28 May 2008 ^d | K_s | 104 | 10 | S27 |
| 31 Mar 2009 ^d | K_s | 1920 | 1 | S27 |
| 28 Sep 2010 ^d | K_s | 2016 | 1.0 | S27 |
| 17 May 2011 ^d | K_s | 143 | 2.0 | S27 |
| 03 May 2009 ^e | K_s | 109 | 3 | S13 |
| 21 Jul 2009 ^e | H | 138 | 10 | S13 |
| 03 Jun 2010 ^f | L' | 20 | 5 | L27 |
| 03 Jun 2010 ^f | $NB_{3.74}$ | 6 | 20 | L27 |
| 04 Jun 2010 ^f | L' | 20/30 | 5 | L27 |

^a Number of exposures.

^b Detector integration time. The total integration time of each observation amounts to $N \times \text{DIT}$.

^c The pixel scale of the NACO S27 camera is 0.027"/pixel, that of S13 is 0.013"/pixel.

^d Used for proper motion measurements.

^e Imaging observations used to investigate the structure of the bow shocks.

^f SAM observations used to investigate the structure of the bow shocks.

5.2.2. OBSERVATIONS WITH SPARSE APERTURE MASKING

OUR SAM observations of the GC central parsec were performed in the nights of 3/4 and 4/5 June 2010 with VLT/NACO. We used the L27 camera ($0.027''/\text{pixel}$) and chose two combinations of filters and mask: the L' broad-band filter ($\lambda_{\text{central}} = 3.80 \mu\text{m}$, $\Delta\lambda = 0.62 \mu\text{m}$) was combined with the $BB_9\text{holes}$ mask and the $NB_3.74$ narrow-band filter ($\lambda_{\text{central}} = 3.74 \mu\text{m}$, $\Delta\lambda = 0.02 \mu\text{m}$) with the 9_holes mask. The latter combination reduces bandwidth smearing, while the first combination leads to higher sensitivity. The observations were recorded using pupil tracking.

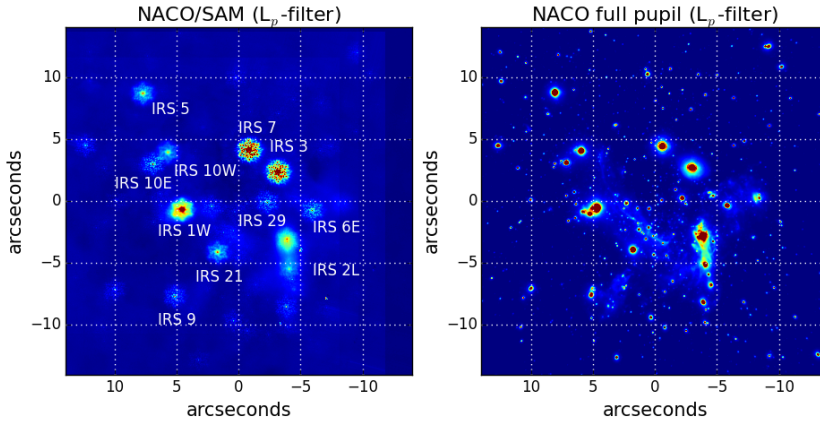


Figure 5.3: *Left*: Sparse aperture masking L' frame of the Galactic center. Prominent sources are labeled with their names. *Right*: The panel displays, for comparison, the central parsec observed with NACO in full pupil mode. Positions are given as distances from the center of the field of view.

The wide field of view ($27'' \times 27''$) of the L27 camera allowed us to observe all targets simultaneously. All SAM data were pre-processed according to standard imaging data reduction, that is, sky subtraction, flat-fielding, and bad-pixel correction.

Depending on the observational data sets, the sky was obtained by calculating either (i) the median of separate sky observations obtained on a dark cloud about $400''$ north and $700''$ west of Sagittarius A*, or (ii) via the median of the appropriately clipped values at each pixel from the dithered images on-target when no dedicated sky observations close in time were available. We note that sky subtraction did not result in a completely flat background as expected. Instead, patterns remained in the images, probably because of the rapid and variable atmospheric conditions. However, these patterns varied on scales of $\sim 2''$, that is, on scales larger than the size of the SAM PSFs. Their impact on the calibration of the SAM observations was therefore considered not significant. A reduced individual image frame (L' , $BB_9\text{holes}$) is shown in Fig. 5.3.

The so-called cube mode was used to save each single-detector integration time (DIT) frame. The advantage of this mode is that it allows selecting the best frames. In our case, frame selection was necessary because atmospheric conditions (and the AO

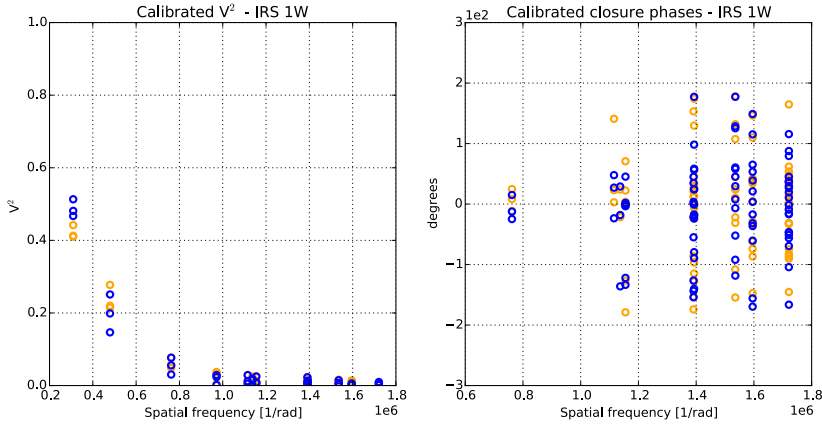


Figure 5.4: Calibrated squared visibilities and closure phases for the SAM observations of IRS 1W. Orange circles: calibration with the synthetic calibrator technique. Blue circles: calibration with IRS 7 as calibrator. The CPs values are plotted over the spatial frequency of one of the three baselines used to compute each one of them.

correction) were affected by highly variable seeing and the passage of clouds. About 80% of the frames were de-selected (using a simple flux criterion on the star IRS 7). The final set of data consists of a group of 13 cubes composed of 20–30 exposures with 5 s and 20 s DIT each for L' and $NB_3.74$ filters, respectively. Finally, the selected frames for each of the individual targets were stored into separate cubes of 128×128 pixels.

The standard observing technique for SAM requires closely interwoven observations between calibrator and target. The calibrator must be a nearby point-like source (within $\sim 1^\circ$ – 2°). We obtained observations of the calibrator sources HD 161718 and HD 162907. A dither pattern was used in which the source was located at the center of the four quadrants of the detector so that the sky could be extracted by a simple median superposition of the dithered target observations.

5.2.3. EXTRACTION AND CALIBRATION OF THE INTERFEROMETRIC OBSERVABLES FROM THE SAM DATA

FOR the subsequent processing of the SAM data we used an IDL pipeline developed at Sydney University (priv. comm., M. Ireland). This code constructs a matched filter for the given instrumental setup (pixel scale, observing wavelength, filter, aperture mask) and uses it to measure the squared visibilities, V^2 , for all interferometric baselines as well as the bispectra, which are the ensemble of the visibility products for all non-redundant baseline triangles. The arguments of these bispectra are the closure phases. The CPs provide information of the point-symmetry of the source and are free of telescope-dependent phase errors induced by atmosphere and telescope vibrations.

Finally, to eliminate the baseline-dependent errors, the calibrated V^2 were obtained by the ratio of the raw V^2 of the target and calibrator, while the calibrated CPs were obtained by subtracting the calibrator CPs from the CPs of the target.

We note that the $u-v$ coverage of the targets in our observation was not limited by the properties of the interferometric masks used, but was increased through Earth rotation synthesis by combining observations of the targets at different parallactic angles.

To accurately calibrate the SAM observations, it is generally recommended to frequently switch between the target and the calibrator while leaving all AO settings unchanged. But this was not possible for our observations because of the highly variable conditions (seeing, clouds) that made changes to the AO setting necessary, delayed calibrator observations, and led to unstable correction. We thus lacked of sufficient, adequate calibrator observations.

One of the possible solutions to overcome this problem was using the IRS 7 star as calibrator because it is contained in all our SAM frames. This source was already tested and used by [Tuthill et al. \(2006\)](#) as a calibrator for SAM observations. However, they performed their observations at shorter wavelengths than we did. IRS 7 is known to be surrounded by extended emission at MIR wavelengths ([Viehmann et al., 2006](#)), which may already show some contribution at the long NIR wavelengths used here. In addition, the images of IRS 7 may have been affected by local systematic variations of the background and do not properly reflect the variance of PSF and background for the entire FOV of our observations.

To overcome these problems we developed a technique that we called the synthetic calibrator. This method takes advantage of the many bright sources in a crowded FOV as is the case for the GC. The procedure is very similar to the iterative extraction of an empirical PSF from a crowded field that is implemented in PSF fitting algorithms such as *StarFinder* ([Diolaiti et al., 2000](#)). We used *StarFinder* to (i) select the brightest stars in the SAM images (excluding known, obviously extended sources such as IRS 1W) to construct a preliminary PSF by median superposition; (ii) clean the images from secondary sources with the help of the preliminary PSF and subtract large-scale variations of the background emission; and (iii) obtain a final PSF from the median superposition of the cleaned images of the reference stars. The final PSF, which corresponds to the interferogram of a point source, was normalized to a total flux of one. We used the sources IRS 7, IRS 3, IRS 29, and IRS 6E to construct the synthetic calibrator.

This technique provides a reliable way to minimize the contribution of all the potential systematic errors related to each one of the individual sources. Even more, the synthetic calibrator is robust, under certain constraints, to the use of slightly extended sources as inputs (like IRS 3). These restrictions require that the in-going sources have no strong closure phase information (i.e. the source is not asymmetric) and that their emission is dominated by the point-like source. We can observe, at first glance, in [Fig. 5.3](#) that the four sources used to build the synthetic calibrator fulfill the requested constraints and have a significantly crispier PSF than our science targets.

Table 5.2: Iterations and reduced χ^2 for BSMEM image reconstruction.

| Source | Iterations | χ^2 |
|---------|------------|----------|
| IRS 1W | 15 | 1.10 |
| IRS 5 | 15 | 1.86 |
| IRS 10W | 12 | 2.31 |
| IRS 21 | 20 | 1.82 |

We used the few valid calibrator observations to verify this technique by comparing the calibrated V^2 and CP values that were obtained with the synthetic calibrator and with a real calibrator. No systematic differences were found. We also compared the resulting calibrated V^2 and CP obtained with the synthetic calibrator and with IRS 7 as calibrator. Again, the values agreed within their uncertainties. This also confirms that IRS 7 is unresolved with the chosen SAM setup. Figure 5.4 shows a comparison of the calibrated V^2 and CPs using the synthetic calibrator technique and IRS 7 as calibrator for one of our sources. We decided to use the synthetic calibrator technique to calibrate the V^2 and CP of all our targets. Figure 5.4 illustrates the information that can be obtained from our SAM measurements: IRS 1W is completely resolved-out for baselines longer than 4 meters, which indicates that the source angular size is extended and larger than 120 milliarcsec; the closure phases differ significantly from zero, which excludes a point-symmetric structure for the source.

We note that the synthetic calibrator technique can only be used when several sufficiently bright sources are present within the FOV and when the PSF is not expected to vary significantly over the FOV. It may be ideal for observations of stars in dense clusters, where it can both improve the calibration of SAM data and boost the efficiency of SAM observations because it does not require any change of the instrument setup and avoids overheads caused by calibrator observations.

5.2.4. SAM IMAGE RECONSTRUCTION

IMAGE reconstruction from the interferometric data was performed with the BSMEM package (see, e.g., Buscher, 1994; Lawson et al., 2004). This code uses a maximum-entropy algorithm. Table 5.2 lists the number of iterations and the reduced χ^2 values at the end of the deconvolution process for all sources. The size of the beam used in the reconstruction procedure is $\theta=60$ mas, which corresponds to the nominal angular resolution reached by this technique for the filters we used. The pixel scale used for the reconstruction process was 13 mas/px.

5.3. PROPER MOTIONS

TO measure the proper motions of the stellar sources at the center of the bow shocks we used VLT/NACO K_s -band AO imaging data obtained between 2002 and 2011 (see

Table 5.1). Schödel et al. (2009) obtained proper motion measurements of our sources using PSF fitting to measure their stellar positions. This method is not suited for extended sources like the bow shocks that we analyze here, however. Instead, we measured the stellar positions by centroiding the emission maxima of the central stars in circular apertures of with a radius of 4, 5, and 6 pixels. The positions and their uncertainties were taken as the mean of the three measurements and its corresponding uncertainty. Note that measuring stellar positions by aperture centroiding is significantly less susceptible to systematic errors caused by (moderate) saturation or nonlinearity than is PSF fitting. Moreover, since the bow shocks are extended targets, PSF fitting to their central stars is very difficult and prone to systematic errors.

Astrometric alignment was achieved with the help of the known positions and proper motions of a sample of about 200 stars contained in all images. The astrometric reference stars were selected from the list published by Schödel et al. (2009). The stars had to be brighter than $K_s = 12$, with no companion within $0.3''$ and the uncertainty of each component of the proper motions of the reference stars had to be smaller than $< 30 \text{ km s}^{-1}$. These criteria ensure accurate aperture measurements of their positions. We transformed the stellar positions into the astrometric reference frame via a second-order polynomial fit (see Appendix A in Schödel et al., 2009). A Monte Carlo approach was used to estimate the uncertainty of this alignment procedure, with 1000 trials. For each trial the positions of the reference stars were varied randomly, with the offsets drawn from Gaussian distributions with standard deviations corresponding to the positional uncertainty of each star at each epoch.

After obtaining the stellar positions for each epoch, we fitted the data points by linear motions. The reduced χ^2 was generally significantly larger than 1. There were some sources of uncertainty that were not specifically taken into account, such as errors introduced by camera distortion into the mosaics, the shape of the bow shocks, pixel saturation, or faint secondary stars within the aperture laid over the bow shocks. Hence, the uncertainties of the stellar positions may have been under-estimated. This is no serious problem, however, because we can be certain that linear motions are accurate models to describe the proper motions. Therefore, the uncertainties of the linear fits were all rescaled to a reduced $\chi^2 = 1$. This procedure avoids underestimating the uncertainties (see Schödel et al., 2009, for a more elaborate discussion). The measured angular velocities were converted into km s^{-1} by assuming a GC distance of 8 kpc (e.g., Schödel et al., 2010). Plots of position vs. time along with the linear fits for the proper motions are shown in Appendix A.1.

Table 5.3 lists the proper motions of the bow-shock sources and of the stars IRS 16NW and IRS 33N as determined here and by Schödel et al. (2009). IRS 16NW and IRS 33N are two point-like sources that we used as a reference point to compare our method and Schödel et al. (2009). The measurements of IRS 16NW and IRS 33N and of the bow-shock sources all agree within their 1σ uncertainties, with the exception of IRS 1W. We believe that the discrepancy on the latter source is probably due to the PSF fitting tech-

nique used by Schödel et al. (2009), which is poorly suited to strongly resolved/extended sources like IRS 1W. Moreover, IRS 1W is one of the brightest sources in the field and is affected by saturation in many images. Aperture fitting is suited to both extended and (moderately) saturated sources. We therefore believe that the proper motions for the bow-shocks' stellar sources that we have derived here may be more accurate than those published by Schödel et al. (2009). Tanner et al. (2005) measured the proper motions of IRS 21, IRS 1W, and IRS 10W, which are also listed in Table 5.3. Their measurements generally agree with ours within the quoted 1σ uncertainties, with the exception of the velocity along the right ascension of IRS 21. Note that the proper motions of Tanner et al. (2005) suffer from very large uncertainties, possibly because of the small FOV that they used for determining the proper motions and because they used images reconstructed from speckle observations that have a significantly lower signal-to-noise ratio than we used (AO imaging).

5.4. MODELING THE BOW SHOCKS

5

5.4.1. BOW-SHOCK IMAGES

IN Fig. 5.5 we show a compilation of our images of the bow-shock sources IRS 1W, IRS 5, IRS 10W, and IRS 21. The bow shock is clearly resolved in almost all sources in at least one wavelength. IRS 21 and IRS 10W are more clearly resolved than in the work of Tanner et al. (2005), which can be attributed to technological progress. While Tanner et al. (2005) used low Strehl shift-and-add reconstructed speckle data, here we use high Strehl and high signal-to-noise AO images and images reconstructed from AO assisted Sparse Aperture Masking, a technique that provides a precise calibration of the PSFs. Note that Buchholz et al. (2011) and Buchholz et al. (2013) presented a resolved image of the bow shock around IRS 21. Hence, this source is not seen face-on as hypothesized by Tanner et al. (2005) (see also Tanner et al., 2002).

The extended emission becomes stronger toward longer wavelengths, a consequence of the temperature of the dust in the bow shocks. Tanner et al. (2002) derived a dust temperature of ~ 1000 K for IRS 21. Viehmann et al. (2006) also showed that the temperatures of the bow-shock sources peak at around $4\text{--}10\ \mu\text{m}$, consistent with a dust temperature of a few hundred degrees. On the other hand, the central star is only detected at the shorter wavelengths (see Fig. 5.5).

5.4.2. BOW-SHOCK SHAPE

THE shape of the bow shocks results from the interaction between the stellar wind and the surrounding ISM, taking into account the relative motion of the star with respect to the ISM. Assuming a steady-state model, the shape of the bow shock results directly from the stand-off distance, R_0 , where the ram pressure from the relative motion

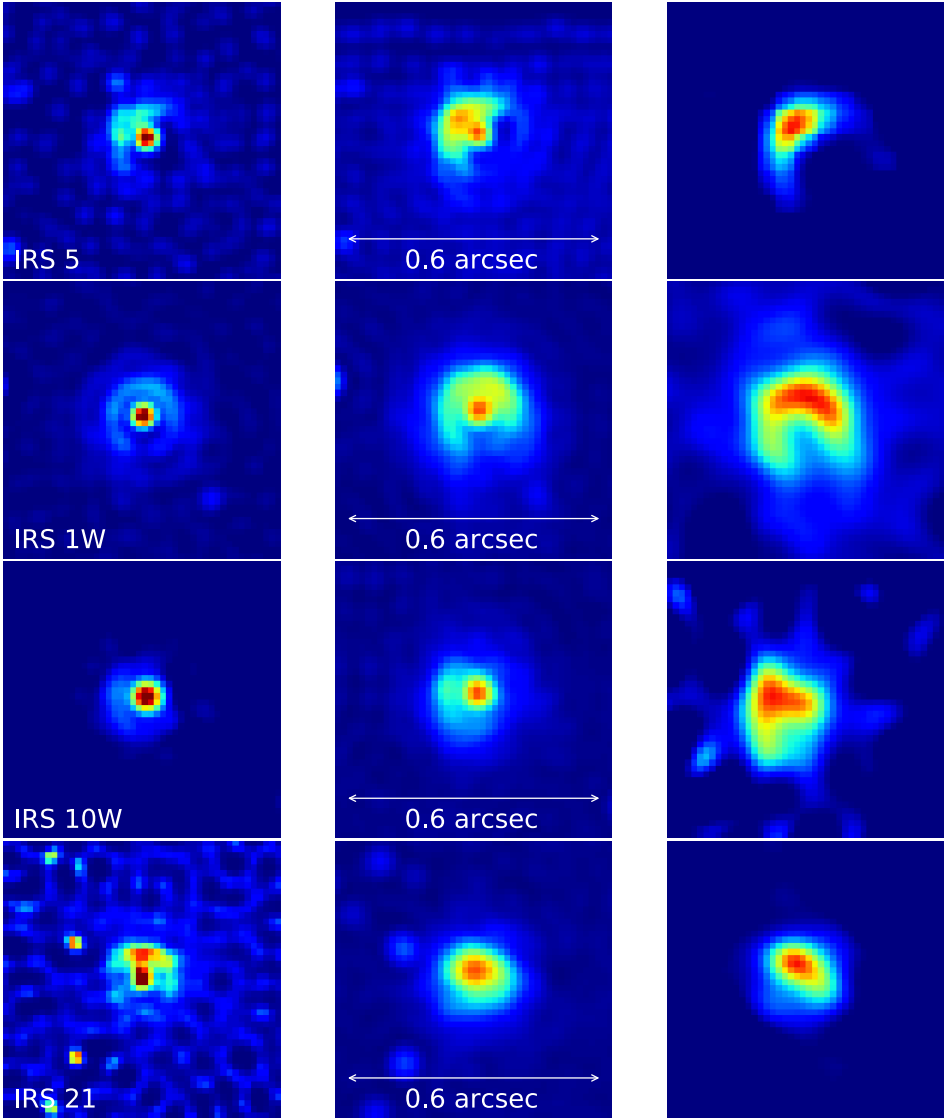


Figure 5.5: Images of the bow-shock sources. Each line corresponds to a different source, while the three columns show the Lucy-Richardson and beam-restored images in the H - and K_s -bands, and the image reconstructed from the L' -band SAM observations.

Table 5.3: Measured proper motions in km/s of reference stars and bow-shock sources.

| Name | $v_{R.A.}^a$ | $v_{Dec.}^a$ | $v_{R.A.,S09}^b$ | $v_{Dec.,S09}^b$ | $v_{R.A.,T05}^c$ | $v_{Dec.,T05}^c$ |
|----------|---------------|---------------|------------------|------------------|------------------|------------------|
| IRS 1W | -164 ± 35 | 309 ± 22 | 54 ± 52 | 167 ± 55 | -170 ± 30 | 320 ± 60 |
| IRS 5 | 54 ± 18 | 26 ± 25 | 57 ± 4 | 32 ± 12 | | |
| IRS 10W | -21 ± 21 | 216 ± 14 | -43 ± 5 | 223 ± 7 | -160 ± 110 | 10 ± 210 |
| IRS 21 | -165 ± 13 | 57 ± 33 | | | -300 ± 30 | 100 ± 30 |
| IRS 16NW | 225 ± 10 | 26 ± 11 | 195 ± 5 | 40 ± 2 | | |
| IRS 33N | 110 ± 17 | -239 ± 18 | 97 ± 4 | -229 ± 2 | | |

^a Proper motion measured in this work.

^b Proper motion measured by [Schödel et al. \(2009\)](#).

^b Proper motion measured by [Tanner et al. \(2005\)](#).

through the ISM is balanced by the pressure from the stellar wind,

$$R_0 = \sqrt{\frac{\dot{m}_* v_w}{4\pi \rho_{\text{ISM}} v_*^2}}, \quad (5.2)$$

where \dot{m}_* is the mass-loss rate of the star, v_w is the velocity of the stellar wind, ρ_{ISM} is the density of the surrounding ISM, and v_* is the relative velocity between the star and the ISM.

To obtain a steady-state solution for the bow-shock shell, [Wilkin \(1996\)](#) assumed (i) that the bow-shock shape is determined by the momentum of the shocking winds, (ii) that the cooling process is instantaneous, (iii) that the shell is a thin layer of negligible width, and (iv) that the interacting winds are homogeneous and do not change with time. The 2D polar canonical form of a bow shock, under the previous conditions, is then defined by

$$R(\theta) = R_0 \csc \theta \sqrt{3(1 - \theta \cot \theta)}, \quad (5.3)$$

where θ is defined as the angle from the axis of symmetry to any point on the 2D-shell's surface. To extend the previous relation from 2D to 3D, we let the locus of $R(\theta)$ rotate by angle ϕ as shown in [Fig. 5.6](#), hence

$$R_{3D}(\theta, \phi) = \text{rot}\{R(\theta), \phi\}, \quad 0^\circ \leq \phi \leq 180^\circ. \quad (5.4)$$

The cells of the bow shock are defined by sampling $R_{3D}(\theta, \phi)$ with increments in θ and ϕ of 0.5° (see [Fig. 5.6](#)).

5.4.3. BOW-SHOCK EMISSION

POLARIZATION AND EMISSION MECHANISMS

[Buchholz et al. \(2013\)](#) described that the bow-shock sources, particularly IRS 21 and IRS 1W, exhibit strong polarization levels at NIR wavelengths. The polarization increases

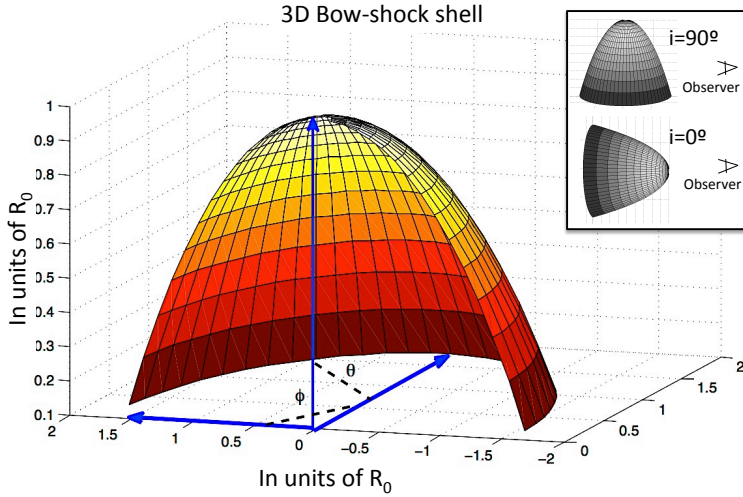


Figure 5.6: 3D Diagram of the bow-shock shell created by our model. The diagram is sliced and the interior of the bow shock is visible. The two polar angles ϕ and θ are shown (see Eqs. 5.3 and 5.4). The blue axis is centered on the position of the star and the scale is in multiples of R_0 . The inset in the upper-right part of the diagram shows the change in bow shock inclination angle as seen from the observer.

from shorter to longer wavelengths, highlighting the importance of the extended dust component. Polarization of the extended emission and of the embedded bow-shock sources in the Northern Arm (NA) reaches its maximum in the MIR (see Buchholz et al., 2013, 2011; Glasse et al., 2003). Buchholz et al. (2011) found that the polarization of the bow-shock sources IRS21 and IRS 1W agrees with the orientation of the magnetic field in the NA. These authors also suggested that the ordered magnetic field is responsible for the dust grain alignment in the bow-shock shells. The polarization measurements from NIR to MIR thus support the assumption that the emission in the bow shocks is produced by the dust IR thermal emission, which is reprocessed UV light from the central star.

BOW-SHOCK EMISSION MODEL

ALTHOUGH the previously mentioned findings suggest that the bow-shock emission is mainly produced by thermal emission, we also explored the role of scattered light in the bow-shock emission, particularly at shorter wavelengths. The procedure used to simulate the emission maps was similar to the one developed by Mužić et al. (2010). The dust thermal emission, L_{th} , was assumed to have a blackbody source function attenuated by the corresponding optical depth, that is, $L_{th} \propto B(T_d)(1 - e^{-\tau_{abs}})$. The dust temperature distribution in the bow shock (T_d) is assumed to be created by heating the dust by the stellar photospheric UV photons from the central source. Therefore, under this condition, T_d is computed via the van Buren and McCray (1988) solution,

$$T_d = 27 a_{\mu m}^{-1/6} L_{*,38}^{1/6} r_{pc}^{-1/3} K, \quad (5.5)$$

where $a_{\mu m}$ is the grain size in microns, $L_{*,38}$ is the star UV luminosity in units of 10^{38} erg/s and r_{pc} is the distance to the dust from the star in parsecs. After calculating the contribution from each cell, the total L_{th} was normalized to one.

The scattering emission was computed using the normalized [Henyey and Greenstein \(1941\)](#) source function modified by the optical depth, $L_{sca} \propto r_{cm}^{-2} P(\theta_{sca}) e^{-\tau_{sca}}$, where r_{cm} is the distance to the dust from the star in centimeters. The scattered light is described by

$$P(\theta_{sca}) = \frac{(1 - g^2)}{(1 + g^2 - 2g \cos(\theta_{sca}))^{3/2}}, \quad (5.6)$$

where g is a dimensionless term that depends on the scattering angle θ_{sca} , with $g = 0$ when the scattering is fully isotropic and $g < 1$ when the scattered light preserves the angle of incidence. After calculating the contribution from each cell, the total L_{sca} was normalized to one. The previous treatment of the scattering emission does not take into account the polarization of light, only the deflection angle of the incident radiation in the dust. A more detailed model of the scattering emission is beyond the scope of this work. The total bow-shock emission, L_{tot} , at every cell in the model was computed adding the previously normalized thermal and scattering emissions, $L_{tot} = \epsilon_{sca} L_{sca} + \epsilon_{th} L_{th}$. The coefficients ϵ_{th} and ϵ_{sca} are the relative efficiencies ($\epsilon_{th} + \epsilon_{sca} = 1$) of the thermal and scattering contribution. The optical depths, $\tau_{abs}(\lambda)$ and $\tau_{sca}(\lambda)$, at every cell of the 3D bow-shock shell are calculated as

$$\tau_{abs}(\lambda) = \int_{a-}^{a+} n_d(a) C_{abs}(a, \lambda) da, \quad (5.7)$$

$$\tau_{sca}(\lambda) = \int_{a-}^{a+} n_d(a) C_{sca}(a, \lambda) da, \quad (5.8)$$

where $C_{abs}(a, \lambda)$ and $C_{sca}(a, \lambda)$ are the dust thermal and scattering extinction coefficients. They are calculated as $C_{abs}(a, \lambda) = \pi a^2 (Q_{abs})$ and $C_{sca}(a, \lambda) = \pi a^2 (Q_{sca})$. The values of the thermal and scattering efficiencies, Q_{abs} and Q_{sca} , were obtained from the Draine database on the optical properties of interstellar dust grains¹ for a standard mixture of 50% graphite and 50% silicate (see [Draine and Lee, 1984](#); [Mathis, 1990](#)). The grain size distribution used, $n_d(a)$, follows an MRN ([Mathis et al., 1977](#)) power-law with the grain size a ranging from $a- = 0.005 \mu m$ to $a+ = 0.25 \mu m$.

5.4.4. BOW-SHOCK FITTING

W^E used the 3D steady-state model and the dust emission processes described in the two preceding sections to create models of the bow-shock shells and fit them

¹<http://www.astro.princeton.edu/~draine/dust/dust.diel.html>

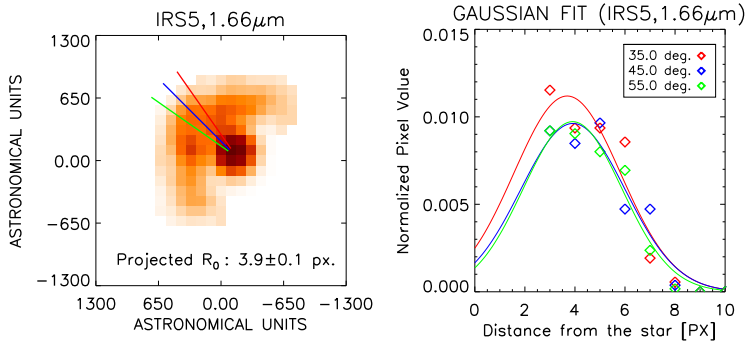


Figure 5.7: *Left*: H -band image of IRS5 with the three radial cuts used to estimate R'_0 marked in colors. *Right*: Gaussian fitted to the emission of the bow shock in the direction of the three radial cuts. The position angle (E of N), used for each cut, is identified in different colors.

to the images. The best-fitting models were found by a χ^2 -minimization as implemented in the IDL *MPFIT* package by C. Markwardt (Markwardt, 2009). Masks were applied to the bow-shock images to suppress features that are not related to the actual bow shocks. Each masked image was normalized to unity inside the applied mask. The same normalization was applied to the projected and masked models. A central point-source was included in the model (with free parameters for its position and flux). This point-like source concentrates most of the NIR-flux and dominates the model fitting at the shortest wavelengths. We note that the pixel uncertainties are hard (or impossible) to determine in Lucy-Richardson deconvolved images and in the BSMEM reconstructed images. In addition, there are several sources of systematic uncertainties, such as faint point sources or ISM features that may be confused with the bow shocks. Therefore, both uniform and flux-weighting schemes were tested to determine the model with the lowest uncertainties that is least affected by the systematics previously discussed. Our tests show that a flux-weighting scheme produced better fits in H and K_s while a uniform weighting works better in L' . The final uncertainties of the best-fit parameters are obtained from their standard deviation of the fits to the statistically independent images from the three different filters. We also expect this procedure to reliably take care of possible contamination from stars and extended emission because the former are expected to be faint at L' and the latter at H .

The stand-off distance R_0 (reported in Table 5.4), which is strongly degenerated with the inclination of the bow shock, was linked in our fitting code to the projected stand-off distance in the plane of the sky, $R'_0 = R_0 / \cos(i - 90^\circ)$, where i is the bow-shock inclination angle between the LOS and the bow-shock apex. When the bow-shock apex is pointing to the observer $i = 0^\circ$ and when the bow-shock shell is projected in the plane of the sky $i = 90^\circ$ (see inset in Fig. 5.6). R'_0 was obtained from the mean of a Gaussian fit to the emission obtained by three radial cuts along the bow-shock structure. The central cut

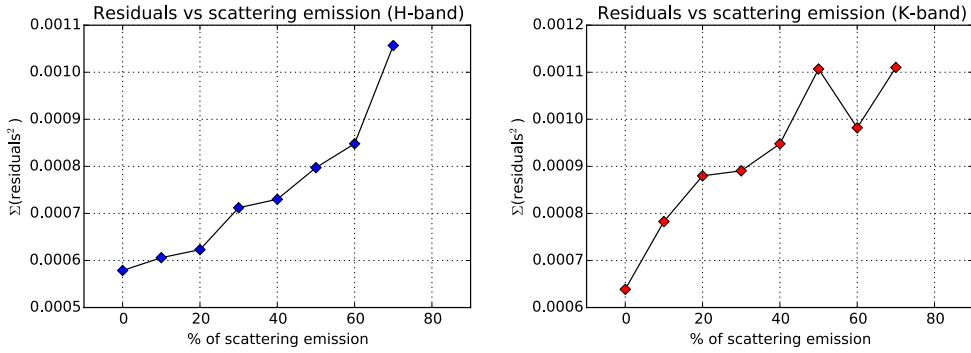


Figure 5.8: Sum of the squared residuals of the best-fit models with increasing relative contribution of scattering emission. The left panel corresponds to the residuals in the H -filter and the right one to the residuals in the K_s -filter for isotropic scattering.

was made along the symmetry axis of the bow shock, the two additional cuts were at -10° and $+10^\circ$ from the position of the central cut. Figure 5.7 shows as an example the radial cuts, the fitted Gaussian, and the R'_0 mean value obtained for IRS5 in the H -filter. A similar procedure was performed for the other sources. The rest of the parameters described in Table 5.4 were fitted directly to the image described at the beginning of this section.

5.4.5. CONTRIBUTION FROM DUST SCATTERING TO THE BOW-SHOCK EMISSION

To quantitatively approximate their relative importance, we investigated the effect of different relative thermal and scattering efficiencies on our models. Since IRS 5 appears to resemble the canonical steady-state bow-shock model most, we used the images of this source in H and K_s to perform this test. We fit different sets of models with fixed efficiencies for thermal and scattering emission at different wavelengths and considered cases of isotropic and anisotropic scattering. For each wavelength, model fitting was performed with increments of 10% in the scattering efficiency from 0 to 70% of the total emission observed. We tested the cases for $g=0$ in the scattering source function (isotropic scattering) and for $g=0.5$ (partially anisotropic scattering).

The best-fit bow-shock model was found in each trial with the procedure described in Sect. 5.4.4. Residual images were obtained by subtracting the models from the original image. Figure 5.8 displays the sum of the squared pixel values of the residual image for each trial in H and K_s for the isotropic case. In both bands, we found that the residuals increase with the scattering contribution, the model with 0% scattering had the lowest residuals. Similar results were found for the anisotropic scattering contribution ($g=0.5$). As indicated in Sect. 5.4.1, we expect the main contribution to the bow-shock emission to be thermal emission from the dust grains. Our tests here are consistent with this picture.

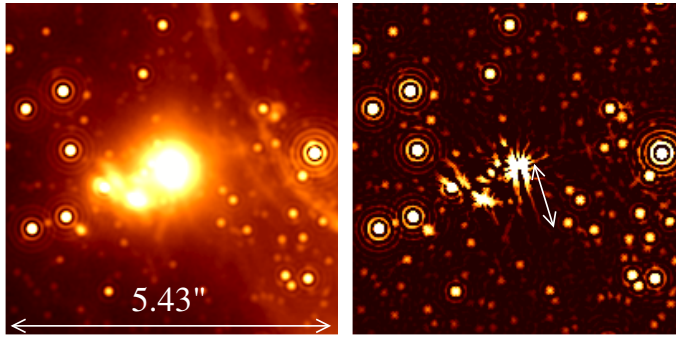


Figure 5.9: Left: L' -band image of the surroundings of IRS 1W. Right: highpass-filtered version of the image. The white arrow in the right panel shows the length of the bow-shock tail. It has a length of $\sim 0.8''$, or 6400 AU. The radial lines emanating from the apex of the bow shock of IRS 1W are artifacts of the high-pass filtering.

5

Therefore, all the models obtained for this work were fit only for the thermal emission of the dust.

5.4.6. PROPERTIES OF THE INDIVIDUAL SOURCES

HERE, we discuss the individual bow-shock sources in detail. Their morphologies can be examined in Fig. 5.5, while Fig. 5.12 shows the best-fit bow-shock models overplotted to the images.

IRS 5: This bright bow shock displays similar morphologies in the H , K_s , and L' filters. The central star is clearly identified in H and K_s . The projected bow-shock shape is axially symmetrical in the plane of the sky with the vector from the central star to the stagnation point. IRS 5 is the source in our sample that can best be described with the isotropic wind steady-state model. Table 5.4 describes the best-fit parameters for the different wavelengths. Here, and for the other bow-shock sources, we conservatively estimate the uncertainties of the best-fit parameters from their standard deviation that results from the fits to the images at the different wavelengths (i.e., we did not use the uncertainty of the mean). The small uncertainties support the model assumption of a bow shock in the steady-state phase. Our results suggest that the bow shock of IRS 5 is inclined at $\sim 130^\circ$. From the interaction of IRS 5 with the NA and using the NA model of Paumard et al. (2004), we estimate a position of $z=3.81'' \pm 2.66''$ along the LOS, where $z=0$ corresponds to the plane of the sky. Assuming that IRS 5 is gravitationally bound to Sgr A*, we calculate a 3σ upper limit of $\pm 336 \text{ km s}^{-1}$ for its LOS velocity.

IRS 1W: as Fig. 5.5 shows, the target is resolved at the three wavelengths. It has a clear bow-shock structure in K_s and L' , but also deviates from the analytical bow-shock model that we used here: first, a rounded shell appears around the central star that is open on its southern edge and is clearly visible at H and K_s . It is not observed in L' , however. Instead, the tails of the bow shock are better distinguished. The origin of this more rounded shell in the H and K_s images is unclear. Second, the shape near the apex

Table 5.4: Best-fit parameters of our bow-shock models for IRS 5 (spherically symmetric stellar wind).

| Parameter | H | K_s | L' | σ_{rms} |
|---------------------------------|-------|-------|-------|----------------|
| R_0 [AU] | 445.0 | 517.0 | 575.0 | $\pm 53.0^a$ |
| P.A. [deg] ^b | 50.0 | 46.9 | 47.0 | $\pm 1.6^a$ |
| Inclination [deg] ^c | 116.0 | 139.9 | 144.6 | $\pm 12.5^a$ |
| FWHM [px] ^d | 2.0 | 2.23 | 4.6 | - |
| Bow-shock flux [%] ^e | 60.0 | 90.0 | 100.0 | - |

^a The standard deviation of the measurements obtained in the three filters.

^b Position angle increasing E of N.

^c Angle between the the bow-shock symmetry axis and the observer's line of sight. 0° - the bow-shock apex is toward the observer, 90° - the bow-shock is projected on the plane of the sky.

^d Full width at half maximum of the beam at different wavelengths in pixels. The FWHM reported for the L' -band is fixed and corresponds to the synthesized beam of the SAM observations.

^e Percentage of the total emission that corresponds to the extended emission. The rest of the emission corresponds to the central source.

is slightly asymmetrical in L' , with the maximum of the emission shifted to the west of the apex. Possible causes are confusion with a star or some feature in the mini-spiral, or an asymmetrical outflow from IRS 1W. To investigate this point further, the left panel in Fig. 5.9 shows a close-up of the surroundings of IRS 1W from a NACO L' -band image. The right panel shows a highpass-filtered version of the same image. IRS 1W does not appear to be contaminated by a typical mini-spiral feature such as a thin filament, nor by any bright star (see also Fig. 5.5). We therefore do not find any obvious or easily testable explanation for the observed asymmetry, but note here that the mini-spiral is generally a complex region with many knots and features in the ISM that may be confused in projection and/or interact with the bow shock. Third, IRS 1W displays a long, tightly closed tail. The tail of IRS 1W is clearly visible in the highpass-filtered image and has a length of approximately $0.8''$, or 6400 AU.

IRS 1W shows a remarkable interaction with the ISM of the NA. The proper motion of IRS 1W is $350 \pm 25 \text{ km s}^{-1}$ at an angle $332 \pm 5^\circ$ E of N. Assuming a mass of $4.2 \pm 0.3 \times 10^6 M_\odot$ for SgrA* (Gillessen et al., 2009; Yelda et al., 2011), the escape velocity at the projected distance, $R = 5.30 \pm 0.01''$, of IRS 1W is $419 \pm 15 \text{ km s}^{-1}$. The LOS distance of IRS 1W can be estimated from its interaction with the Northern Arm of the mini-spiral. Using the model of Paumard et al. (2004), we estimate a LOS distance of $z = 7.37 \pm 1.5''$ for IRS 1W and obtain an escape velocity of $320 \pm 29 \text{ km s}^{-1}$ at its 3D position. Although this is lower than its proper motion, both values overlap well within their 1σ uncertainties. Using the 3σ upper limit in the escape velocity and the 3σ lower limit on the proper motion, we can set a firm upper limit of $V_z = 300 \text{ km s}^{-1}$ on the LOS velocity of IRS 1W (assuming that it is bound to SgrA*, of course). This corresponds to a maximum inclination of its velocity vector of 137° , corresponding to 47° out of the plane of the sky, moving away from the

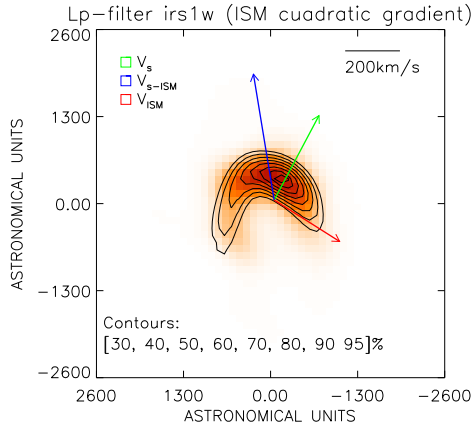


Figure 5.10: Model of a bow shock in an ISM with a quadratic density gradient. The L' image of IRS 1W is represented in color and the best-fit gradient model is overplotted as contours. The colored vectors represent the velocity of the star (V_s ; green arrow), the relative motion of the star through the ISM (V_{s-ISM} ; blue arrow) and the dust motion of the ISM obtained with our bow-shock model (V_{ISM} ; red arrow).

5

observer. Here, the ambiguity between motion toward or away from the observer is broken by our best-fit bow-shock model. From the model of [Paumard et al. \(2004\)](#) we can calculate the properties of the gas flow. At the position of IRS 1W, the gas in the NA has a proper motion of $226 \pm 70 \text{ km s}^{-1}$ at an angle $207 \pm 13^\circ$ E of N. The orientation of the tail-like feature agrees well with the relative proper motion between star and gas. The angle of the gas flow out of the plane of the sky is a mere 7° , with the gas moving toward the observer, which means that the NA flow is practically within the plane of the sky at the position of IRS 1W. We note that with a relative proper motion between star and gas on the order of 550 km s^{-1} the channel-like feature that is marked by the tail of IRS 1W may trace the motion of IRS 1W over the past ~ 50 years. With such short timescales at work, IRS 1W may be an ideal probe for the conditions of the ISM in the NA, for instance, for the homogeneity of the gas density.

Table 5.5 shows our best-fit bow-shock model for IRS 1W using our steady-state model. The second row of images in Fig. 5.12 corresponds to the steady-state isotropic wind-fitted models. As can be clearly seen, our model cannot fit the tail of IRS 1W well (specially in L') because it is much narrower than what can be produced with this model. Possible explanations of this problem include (i) changes in the density of the ISM at the shocking points, (ii) variations in the mass-loss rate and wind velocity, (iii) anisotropic winds, or (iv) that because of the short interaction times the bow shock in IRS 1W has not yet reached the steady-state bow-shock solution (see [Mohamed et al., 2012](#)). The large scatter in the best-fit position angles in Table 5.5 also suggests that the isotropic wind model is not suitable to reproduce the observed morphology of IRS 1W.

To examine whether there are other models that provide a better fit to the IRS 1W

morphology, we decided to perform a model fitting using the narrow solution of a steady-state bow-shock shell described in [Zhang and Zheng \(1997\)](#). We assumed that the central source has a wind bound inside a cone with an opening angle of 40° along the polar axis. Table 5.6 displays the fitted parameters and the third row of images in Figure 5.12 represents the best-fits for the narrow solution. A comparison between the isotropic wind model and the narrow solution (see Fig. 5.12) demonstrates that the latter fits the observed emission of IRS 1W better, with the main difference being in a smaller R_0 and different inclination. The narrow solution models have considerably lower residuals and result in best-fit parameters with very low scatter between the different observing wavelengths.

Another plausible explanation for the shape of IRS 1W can be changes in the density of the ISM. This condition is not rare in complex environments like the NA where filaments and clumps of gas/dust are observed. For example, [Rauch et al. \(2013\)](#) determined the geometry and emission of the asymmetric IRS 8 bow shock using a shell solution for a quadratic density gradient in the NA ISM. Figure 5.10 displays our best-fit solution to IRS 1W in L' for an ISM density gradient. The density gradient function has the form $\rho = \rho_0(1 + a_1x + a_2x^2)$, where ρ_0 is the mean density of the ISM and x the direction of the ρ_0 increment. In our model, the density increased from east to west and the values of the coefficients a_1 and a_2 were fixed to 2.0 and 5.0, respectively.

This bow-shock gradient solution produced residuals on the order of those of the narrow solution. Similar values were obtained between the narrow and the gradient solution for the fitted parameters. The best-fit gradient solution produced a $R_0=533$ AU, and inclination of $i=103^\circ$ and a $PA=9^\circ$. Nevertheless, to perform a complete least-squares fitting to bow-shock solutions with free gradient coefficients and/or different gradient functions creates strong degeneracies among the fitted parameters. Hence, we did not investigate other gradient solutions and decided to use the narrow solution best-fit model for the following analysis. Although we cannot fully distinguish between the physical mechanisms that produce the observed shape of IRS 1W, our narrow and gradient models suggest that inhomogeneities in the stellar wind and/or ISM are important in shaping the structure of this particular bow shock.

Table 5.5: Best-fit parameters of our bow-shock models for IRS 1W (spherically symmetric stellar wind)

| Parameter | H | K_s | L' | σ_{rms} |
|--------------------|-------|-------|-------|----------------|
| R_0 [AU] | 689.0 | 606.0 | 651.0 | ± 34.0 |
| PA. [deg] | 3.0 | -13.0 | 27.0 | ± 16.0 |
| Inclination [deg] | 131.0 | 121.0 | 127.0 | ± 4.0 |
| FWHM [px] | 2.0 | 3.24 | 4.6 | - |
| Bow-shock flux [%] | 49.0 | 79.0 | 100.0 | - |

IRS 10W: the extended emission around this source presents a particularly different morphology in L' , more so than in H and K_s . The central star is detected in the H and

Table 5.6: Best-fit parameters of our bow-shock models for IRS 1W (narrow solution).

| Parameter | H | K_s | L' | σ_{rms} |
|--------------------|-------|-------|-------|----------------|
| R_0 [AU] | 520.0 | 523.0 | 523.0 | ± 1.2 |
| PA. [deg] | 13.0 | 2.0 | 5.0 | ± 5.0 |
| Inclination [deg] | 88.0 | 96.0 | 84.0 | ± 5.0 |
| FWHM [px] | 2.0 | 3.42 | 4.6 | - |
| Bow-shock flux [%] | 50.0 | 79.0 | 100.0 | - |

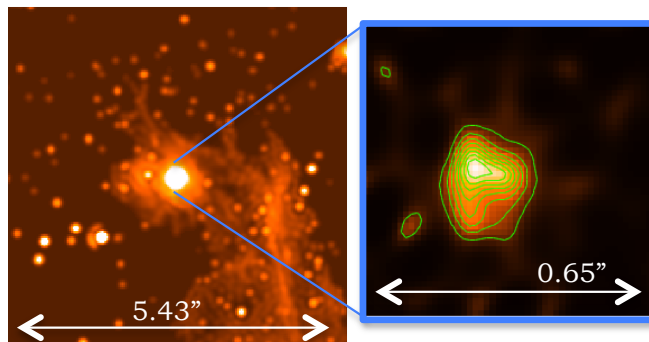


Figure 5.11: *Left*: L' -band image of the surroundings of IRS 10W. The filamentary structure of the NA is appreciated as well as some additional close-by stars with extended emission. *Right*: the reconstructed SAM image of IRS 10W in L' band. An asymmetric structure can be seen. Contours represent 10, 20, 30, 40, 50, 60, 70, 80, and 90% of the peak flux.

K_s filters. Extended emission is observed at the position of the central source in L' . It is unclear whether this emission is related to the central star or not. The projected emission in H and K_s displays a symmetric structure, while in L' the southward pointing tail is more extended than the northward pointing one. This feature may be related to inhomogeneities in the NA ISM at the location of IRS 10W (see Fig. 5.11). The radio image mapped at 1.3 cm by Zhao et al. (2009, see their Fig. 10) suggests that IRS 10W is part of the NA and is surrounded by ionized gas in a shell-like structure with a completely different morphology than the one observed at NIR wavelengths, showing no clear evidence of a bow-shock.

Because of the asymmetric shape of IRS 10W in L' , we decided to apply the model fitting only to the H and K_s images. Table 5.7 shows the best-fit parameters. The fourth row of images in Figure 5.12 displays the best-fit models in contours. Although the extended emission around IRS 10W can be interpreted as a bow shock, a more detailed analysis of the IRS 10W proper motion and of the NA motion (at the position of IRS 10W) does not support the idea of a bow shock produced by the relative motion of the star throughout the ISM.

IRS 10W has a proper motion of $217 \pm 14 \text{ kms}^{-1}$ with a PA of 355° E of N (see Fig. 5.12

and Table 5.3). Paumard et al. (2004) reported a gas flow of $189 \pm 84 \text{ kms}^{-1}$ with a PA of 188° E of N at the position of IRS 10W, while the values according to Zhao et al. (2009) are $229 \pm 49 \text{ kms}^{-1}$ with a PA of 191° . Therefore, the relative proper motion of IRS 10W with respect to the NA is $403 \pm 86 \text{ kms}^{-1}$ at a PA of 1° E of N, or $441 \pm 37 \text{ kms}^{-1}$ at a PA of 3° E of N, that is, at a PA perpendicular to the direction of the possible bow-shock symmetry axis (around $\sim 90^\circ$). This suggests that the extended emission around IRS 10W is not produced by the bow-shock model described in Sect. 5.4, which implies that the relative motion and the bow-shock axis must be parallel. Alternative explanations for the observed extended emission are (i) a shock between the stellar wind with a dust knot or filament of the NA, (ii) a shock between the stellar winds of IRS 10W and a secondary source, or (iii) a chance superposition of a some NA feature with IRS 10W. These hypotheses are plausible since IRS 10W is located in a very mixed environment of the extended emission in the NA, some filaments can be observed superimposed along the source position and, additionally, some close-by stars have extended emission (see Fig. 5.11).

Table 5.7: Best-fit parameters of our bow-shock models for IRS 10W.

| Parameter | H | K_s | L' | σ_{rms} |
|--------------------|-------|-------|------|----------------|
| R_0 [AU] | 620.0 | 525.0 | - | ± 48.0 |
| P.A. [deg] | 107.0 | 98.0 | - | ± 9.0 |
| Inclination [deg] | 123.0 | 89.0 | - | ± 13.0 |
| FWHM [px] | 2.88 | 3.60 | - | - |
| Bow-shock flux [%] | 26.0 | 45.0 | - | - |

IRS 21: the bow-shock of this source can be clearly seen at all wavelengths and is similar to the deconvolved K_s -band image presented by Buchholz et al. (2011). IRS 21 is best resolved in H band, where the central star is also unambiguously detected. We can discard the hypothesis, made by Tanner et al. (2005), that IRS 21 is seen face-on, since these authors could not resolve its structure in their lower Strehl no-AO observations. In our K_s and L' images the central source is not detected and the bow-shock morphology is less clearly observed because of the lack of angular resolution. We therefore decided to apply the model fitting only to the H -band image. The steady-state model fits the morphology observed in the H -band very well. The proper motions of the star and of the NA environment are consistent with the relative motion of the bow shock obtained from our model. Table 5.8 lists the best-fit parameters.

Since we only performed the model fitting to the IRS 21 H -band image, the uncertainties in the fitted parameters were estimated in a different way than for the other bow shocks, for which we have at least two models in two different filters. For IRS 21, the uncertainties reported in Table 5.8 were estimated by testing three different starting values for the bow-shock inclination angle. We chose this approach because the inclination angle strongly affects the determination of the bow-shock stand-off distance. In fact, it is degenerated for low- and high-inclinations and therefore, our code works best at in-

intermediate values of inclination angles ($40^\circ \leq i \leq 160^\circ$). Very low- or high-inclination angles result in bow-shock shapes that resemble spherical shells. Thereupon, our code cannot compute the stand-off distance since it strongly depends on the inclination angle (see Section 5.4.4). For IRS 21 we tested the code with initial conditions of $i = 50^\circ, 90^\circ, 145^\circ$. The fitted parameters are reported in Table 5.8 and their errors are the standard deviation of the three trials. Although the model did not always converge to the same solution, which can be largely explained by degeneracies between the model parameters, the best-fit parameters, resulting from the runs with significantly different starting values for the inclination, have overall similar best-fit parameters with a low scatter between them.

Table 5.8: Best-fit parameters of our bow-shock models for IRS 21 (spherically symmetric wind).

| Parameter | $H_{i=50^\circ}$ | $H_{i=90^\circ}$ | $H_{i=145^\circ}$ | σ_{rms} |
|--------------------|------------------|------------------|-------------------|----------------|
| R_0 [AU] | 432.0 | 417.0 | 462.0 | ± 22.0 |
| P.A. [deg] | -8.5 | -4.0 | -6.3 | ± 2.2 |
| Inclination [deg] | 106.0 | 95 | 116 | ± 10.0 |
| FWHM [px] | 2.14 | 2.11 | 2.05 | ± 0.04 |
| Bow-shock flux [%] | 68.0 | 62.0 | 65.0 | ± 3.0 |

5.5. ISM VELOCITY FIELD AND BOW-SHOCK ORBITAL PARAMETERS

5.5.1. NORTHERN ARM DUST MOTION

OUR best-fit bow-shock models provide estimates of the local motion of the ISM in the NA. Assuming that our objects are Wolf-Rayet stars (Tanner et al., 2005) with a mass-loss rate on the order of $\dot{m}_* \sim 1.2 \times 10^{-5} M_\odot/\text{yr}$ and stellar winds with velocities around $v_w \sim 1000 \text{ km s}^{-1}$, and that the density in the NA has a mean particle number $n_H \sim 3 \times 10^4 \text{ cm}^{-3}$ (see Rauch et al., 2013; Tanner et al., 2002), we first calculated the relative velocity between star and ISM with Eq. 5.2. Subsequently, we used the measured proper motion of the central star to calculate the proper motion of the ISM at the position of the bow-shocks. Figure 5.12 shows the projected motion of the ISM, V_{ISM} (red vector), the relative motion of the bow shock, $V_{s-\text{ISM}}$, according to our best-fit model (blue vector), and the proper motion, V_s , of the central source (green vector) for all our targets. All our ISM motion measurements (magnitude and position angle) agree to within $1-\sigma$ with the models of Paumard et al. (2004) and/or Zhao et al. (2009) except for IRS 10W, which supports our hypothesis that IRS 10W does not represent a standard bow shock (see Sect. 5.4). Table 5.9 summarizes the NA projected motions obtained in this work and the previously published models of gas and dust. These results corroborate the hypothesis of Wolf-Rayet stars as the central sources of the bow shocks. For comparison, if we

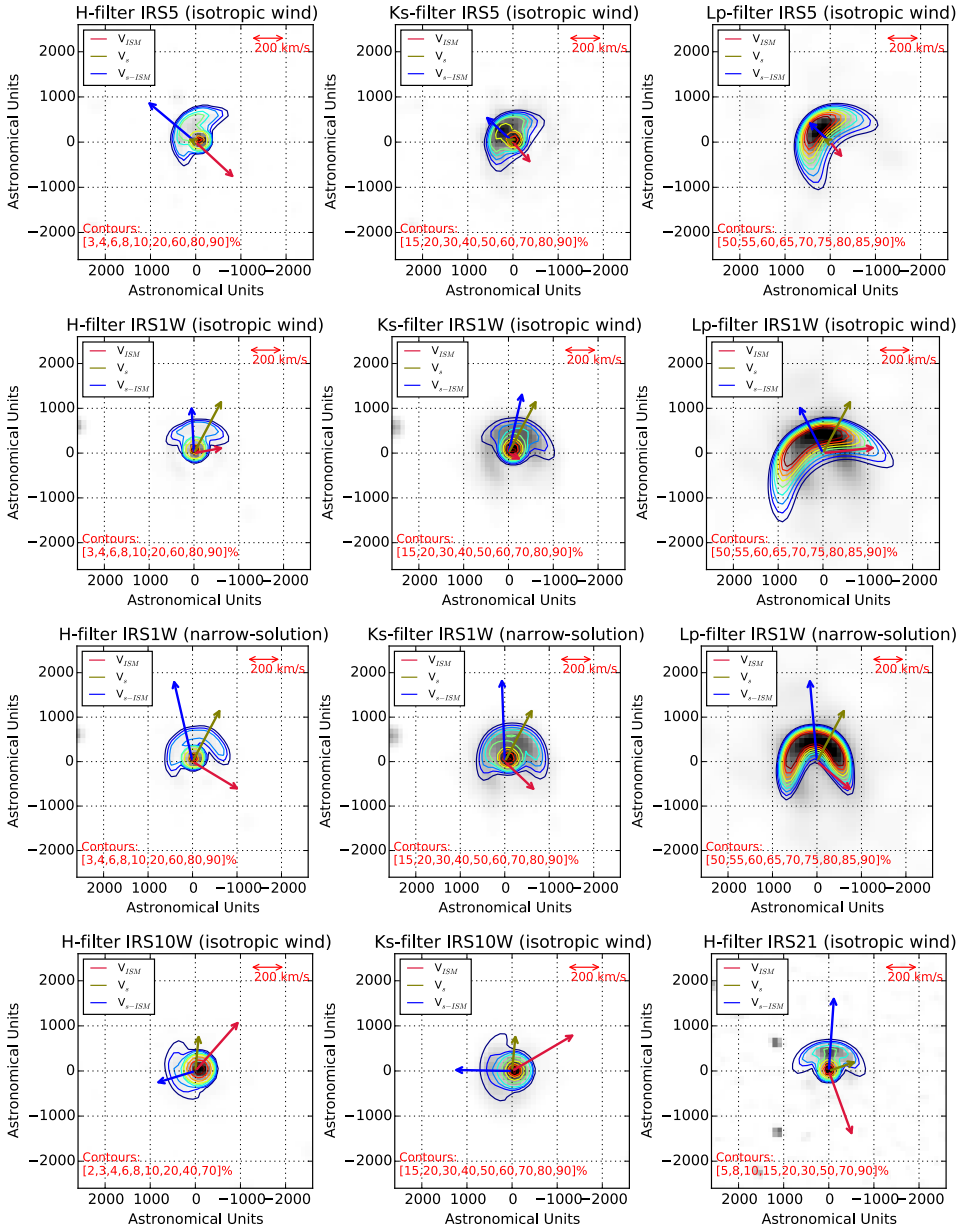


Figure 5.12: Bow-shock fitting of IRS 1W, IRS 5, IRS 10W and IRS 21 in H, K_s and L wavelengths. We represent in gray scale the real image and in contours the best model obtained. The colored vectors represent the velocity of the star (V_s ; green arrow), the relative motion of the star through the ISM (V_{s-ISM} ; blue arrow) and the dust motion of the ISM obtained with our bow-shock model (V_{ISM} ; red arrow).

Table 5.9: Velocities of the NA ISM considering the bow-shock model used in this work, the Paunard et al. (2004), and the Zhao et al. (2009) models.

| Source | Bow-shock model NA velocities [km s ⁻¹] | | | | | | Position angles [deg.] | | |
|---------|-----------------------------------------------------|-------------------------|---------------------------|---------------------------|---------------------------|---------------------------|----------------------------|------------------------------|------------------------------|
| | $v_{\text{ISM-RA}}^a$ | $v_{\text{ISM-Dec.}}^a$ | $v_{\text{ISM-R.A.P.}}^b$ | $v_{\text{ISM-Dec.P.}}^b$ | $v_{\text{ISM-R.A.Z.}}^c$ | $v_{\text{ISM-Dec.Z.}}^c$ | PA_{ISM}^a | $\text{PA}_{\text{ISM,P}}^b$ | $\text{PA}_{\text{ISM,Z}}^c$ |
| IRS 5 | -136±76 | -143±56 | -0.88±67 | -133±91 | -54±20 | -141±13 | 223±33 | 0.4±207 | 201±8 |
| IRS 1W | -220±48 | -169±4 | -73±49 | -213±69 | -218±13 | -110±13 | 232±16 | 199±19 | 243±15 |
| IRS 10W | -305±74 | 248±54 | -28.54±63 | -187±85 | -44±29 | -225±50 | 310±76 | 189±19 | 191±11 |
| IRS 21 | -123±16 | -331±41 | -127±54 | -325±51 | -275±28 | -250±66 | 200±13 | 201±17 | 228±80 |

^a Motion of the ISM and its position angle measured in this work.

^b Motion of the ISM and its position angle measured by Paunard et al. (2004).

^c Motion of the ISM and its position angle measured by Zhao et al. (2009).

compute the projected NA motions using O-stars, ($\dot{m}_* \sim 10^{-7} M_\odot/\text{yr}$; $v_w \sim 2000 \text{ km s}^{-1}$; [Prinja et al., 1990](#)) as the central engines of the bow-shocks, the resulting NA motions are a factor of $\sim 5\text{-}10$ lower than the observationally inferred values. Hence, we discard the idea of O-stars as the central sources of the bright NA bow shocks.

5.5.2. ORBITAL MOTION OF THE BOW-SHOCK SOURCES

THE location of our sources within the NA and the determination of their geometry with the models used here provide valuable information to determine the probability density distribution (PDF) of their orbital parameters, $PDF(a, e, i, \Omega, \omega, P, T_0)$. We used the methodology described by [Lu et al. \(2009\)](#) and the same definitions for the orbital elements ([Appendix A.2](#) describes in detail the equations to calculate the keplerian orbital elements of a star around a given gravitational potential). This method consists of a Monte Carlo simulation of 10^4 trials to convert the 3D positions and velocities of the sources into their six orbital parameters. The projected positions of the bow shocks are obtained from the astrometric measurements used to compute their proper motions (see [Sect. 5.3](#)). The distances of the bow shocks along the LOS and their respective uncertainties were obtained from the NA model of [Paumard et al. \(2004\)](#). The LOS velocities were constrained in two different ways. On the one hand, they were constrained by assuming that the sources are tied to the gravitational potential of SgrA* and have a 3D motion lower than their escape velocities. This method provides an upper limit for the magnitude of the LOS velocity but with an ambiguity in its sign. The PDFs of the orbital parameters were therefore constructed using both signs for the LOS velocities. The second method computes the LOS velocity using the relative velocity of the sources through the ISM obtained from our model fitting (see [Sects. 5.4.2, 5.5.1](#)). With this method we determined an allowed $3\text{-}\sigma$ range of LOS velocities. Furthermore, this approximation helped us eliminate the degeneracy of sign presented in the derivation of the LOS velocity using the first method. The computed escape velocities, the 3D positions, the proper motions, and the $3\text{-}\sigma$ ranges for the LOS velocities are reported in [Table 5.10](#). The 3D positions and proper motions use a Gaussian distribution as prior, while the LOS velocity uses a uniform distribution. These parameters allowed us to determine the $PDF(a, e, i, \Omega, \omega, P, T_0)$ of each one of our sources.

After obtaining the PDFs of the orbital parameters, we computed the orientation of the sources' orbital planes in the sky, as viewed from SgrA*. The orientation of the orbital planes can be described by a unitary vector (\vec{s}) originating at the position of SgrA* and normal to the source's orbital plane. To determine the Cartesian components of \vec{s} , the PDFs of the inclination angle, i , and the ascending node, Ω , were used according to the following expression:

$$\vec{s} = \begin{pmatrix} s_x \\ s_y \\ s_z \end{pmatrix} = \begin{pmatrix} \sin i \cos \Omega \\ -\sin i \sin \Omega \\ -\cos i \end{pmatrix}. \quad (5.9)$$

Figure 5.13 displays the pointing vectors obtained with the PDFs of the orientation of the sources' orbital planes using a Hammer projection. The left column of the maps shows the vectors of the PDF(i, Ω) of the bow shocks using the computed $3\text{-}\sigma$ LOS range. The right column shows the vectors of the PDF(i, Ω) using only the $3\text{-}\sigma$ LOS upper limit determined from the escape velocity. For IRS 10W we only computed its probability distribution using the $3\text{-}\sigma$ LOS upper limit since this source was not clearly identified as a bow shock. Additionally, we included the PDF(i, Ω) of IRS 16CC, a source previously studied by Lu et al. (2009), to check the validity of our code. We obtain similar results to those previously published, which confirms the accuracy of our code. Each map in Fig. 5.13 displays the $1\text{-}\sigma$ and $2\text{-}\sigma$ confidence levels of the PDFs in red and blue. The confidence levels were computed using only orbital solutions tied to Sgr A*. The ellipses plotted in different colors represent the $1\text{-}\sigma$ contour of the orbital planes of some of the main dynamical structures at the GC. Table 5.11 shows the peak values of the PDFs for the sources identified as bow shocks.

The plots in the left and right columns of Fig. 5.13 clearly show that the PDFs based on the modeling of the bow-shocks constrain the orbital planes significantly better than those obtained with the constraints from the escape velocities alone. The PDF(i, Ω) of IRS 5 is the best constrained. The derived LOS velocity range of IRS 5 fully eliminates the ambiguity in the sign of the LOS velocity. Conversely, IRS 1W exhibits very similar PDFs using both methods. This effect can be explained by the fact that we only took into account orbits gravitationally bound to Sgr A*. Furthermore, most of the IRS 1W bound orbits obtained from our MC simulation have LOS velocities within the $3\text{-}\sigma$ range derived from our bow-shock modeling. From this analysis we also observe that IRS 5 and IRS 21 clearly are not part of the CWS or the CCWS. IRS 1W and IRS 10W are relatively close to the position of the CWS but still on the edge of the CWS $1\text{-}\sigma$ limits. Hence, we cannot establish with certainty whether they are CWS members or not. None of the sources are moving in the same plane of the NA.

5.6. DISCUSSION AND CONCLUSIONS

THE AO facilities and the sparse aperture masking mode of NACO at the ESO VLT allowed us to perform a NIR multiwavelength campaign to study with high-angular resolution the structure, circumstellar matter, and kinematics of some of the brightest and most embedded sources in the central parsec of the GC. We used AO-deconvolved and beam-restored images in H and K_s and reconstructed SAM images in L' to determine the morphology of IRS 5, IRS 1W, IRS 10W, and IRS 21. We presented a new technique for calibrating SAM data of dense star fields that does not require observations of an off-target calibrator source. Our new procedure, called the synthesized calibrator, uses our a priori information of the stars in the field and constructs a median superposition of bona-fide point-like sources to build the final calibrator. This method allowed us to minimize the noise, poor background estimates, and problems in the PSF stability. It is also an alternative way of calibrating SAM observations where traditional calibra-

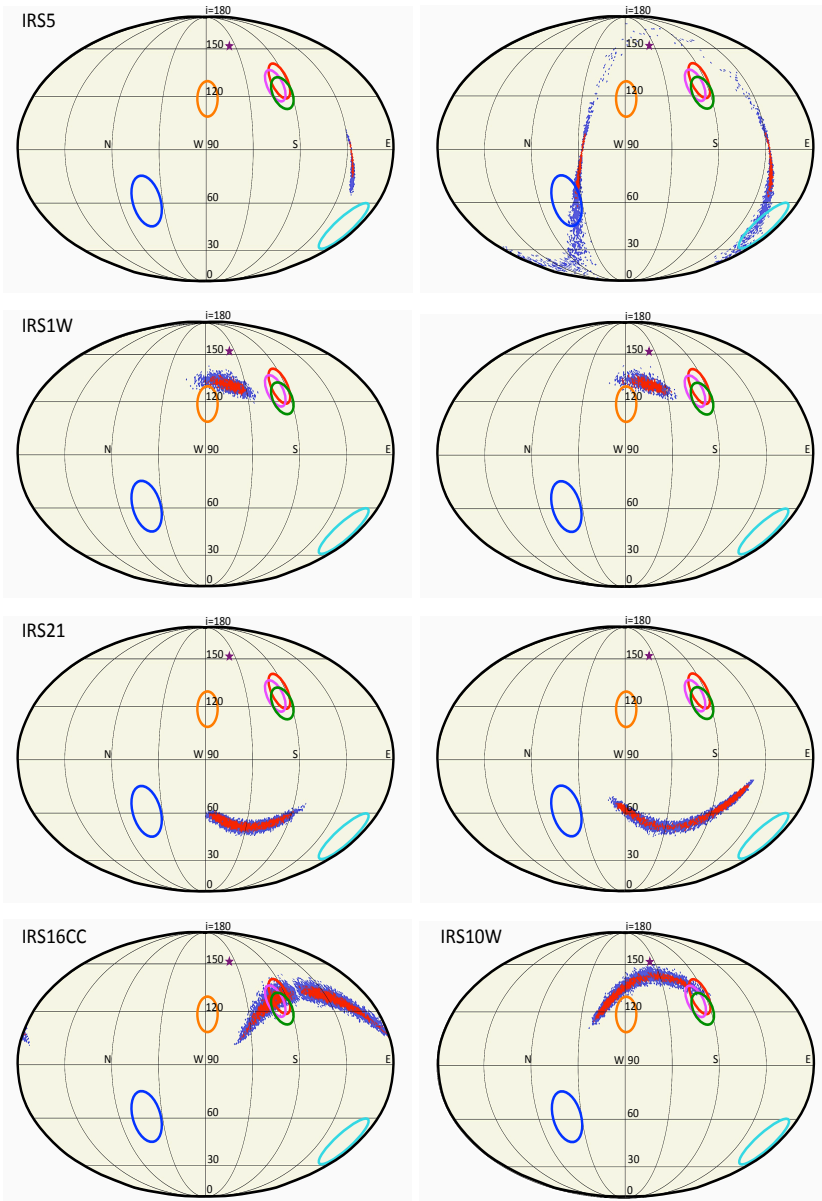


Figure 5.13: Distribution of the orbital planes of IRS 5, IRS 1W, IRS 21, IRS 10W, and IRS 16CC. The $1\text{-}\sigma$ and $2\text{-}\sigma$ confidence levels are shown in red and blue. The ellipses represent the $1\text{-}\sigma$ position of the CCW, CCWS, and the NA orbital planes: the NA is represented by the light-blue ellipse (Bartko et al., 2009; Paumard et al., 2006); the green ellipse corresponds to the CWS according to Lu et al. (2009); the red, pink, and orange ellipses display the CWS according to Bartko et al. (2009) for stars at $0.8''\text{-}12''$, $0.8''\text{-}3.5''$, and $7''\text{-}12''$ projected distances, respectively; the purple star represents the position of the CWS for stars at $3.5''\text{-}7''$ projected distance from Sgr A* (Bartko et al., 2009), and the blue ellipse displays the position of the CCWS according to Paumard et al. (2006).

Table 5.10: 3D coordinates and velocities of IRS 1W, IRS 10W, IRS 21, and IRS 5.

| Star | IRS 1W | IRS 5 | IRS 10W | IRS 21 |
|--------------------------------|-------------|------------|-------------|-------------|
| x [arcsec] ^a | 5.26±0.009 | 8.62±0.02 | 6.5±0.01 | -2.35±0.001 |
| y [arcsec] ^a | 0.616±0.016 | 9.83±0.032 | 5.15±0.02 | -2.69±0.001 |
| z [arcsec] ^b | 7.53±1.53 | 3.81±2.66 | 6.43±1.5 | 4.45±1.07 |
| v_e [km/s] ^c | 320±29 | 266±7 | 303±13 | 412±30 |
| $v_{R.A.}$ [km/s] ^d | -164±35 | 54±18 | -21±21 | 165±13 |
| $v_{Dec.}$ [km/s] ^d | 309±22 | 26±25 | 216±14 | 57±33 |
| v_{LOS} [km/s] ^e | [-18, 18] | [113, 334] | [-307, 307] | [-79, 261] |

^a Projected distances from SgrA*.

^b LOS distance from the plane containing SgrA*, using the NA model of [Paumard et al. \(2004\)](#).

^c 3D escape velocity at the position of the source.

^d Proper motion measured in this work.

^e 3- σ range on the LOS velocity of the bow shocks.

5

tors are too dim or located far away from the science target, like in the case of the GC. Additionally, we used AO observations in K_s between 2002 to 2011 to derive the proper motions of our sources.

We interpreted our observations with 3D steady-state bow-shock models and confirmed that three of them (IRS 5, IRS 1W, and IRS 21) are bow shocks associated with the relative motion of Wolf-Rayet stars through the ISM. Although this conclusion was suggested previously, our models give the best constraints on the bow-shock shell and kinematics so far because of our detailed modeling, new proper motion data, and the inclusion of new NA proper motion data from [Zhao et al. \(2009\)](#), which allowed us an additional consistency check. In contrast to [Tanner et al. \(2005\)](#), we also found a good model fit to the IRS 1W. On the other hand, the extended emission around IRS 10W does not appear to trace a bow shock, but may be produced by the shock of two stellar winds, or there may be a chance superposition with a mini-spiral feature, or the star may heat a nearby mini-spiral filament. We also confirmed that IRS 21 is an edge-on bow shock, not a face-on bow shock, as was previously hypothesized by [Tanner et al. \(2005\)](#).

Our results support the idea that the observed NIR bow-shock emission is thermal emission from hot dust grains. [Tanner et al. \(2002\)](#) fit a 1000 K black-body to the spectral energy distribution of IRS 21. Dust can easily reach such temperatures in the local environs of massive (O/WR) stars since they are strong UV radiation emitters. For our bow-shock sources, which have IR luminosities of $L \sim 10^4 - 10^5 L_\odot$ ([Tanner et al., 2005](#)), the smallest distance from the central source at which dust can exist without evaporation, r_{evap} , can be calculated, at first glance, as ([Barvainis, 1987](#)):

$$r_{evap} = 1.3 \sqrt{L_{UV,39}} T_{1500}^{-2.8} pc, \quad (5.10)$$

where $L_{UV,39}$ is in units of 10^{39} watts and T_{1500} in units of 1500 K. Hence, r_{evap} for our sources is $\sim 8 \times 10^{-5} - 25 \times 10^{-5}$ pc or 16-52 AU. This lies well inside the measured size of the bow-shock shells of our targets at scales lower than our angular resolution. Taking into account the grain sizes used in our study, we can also compute r_{evap} using Eq. 5.5. In this case, the smallest distance at which dust can exist is about 24-75 AU for the given luminosities. Both approximations are consistent, also with the observed bow-shock sizes. From Eq. 5.5 we obtain a rough estimate of 470 K for the temperature near the apices of the bow shocks. These calculations, together with our scattering and thermal-emission modeling, support the assumption that the radiation in the GC bow-shock sources arises from thermal emission in dust grains. Therefore, the mechanism responsible for the observed polarization is the alignment of asymmetric/elongated dust grains. The alignment mechanism implies a compression of the magnetic field of the Northern Arm in the environs of the bow shocks and the increment of the local field density. These changes produce a rapid magnetic alignment of the grains (Buchholz et al., 2013). From the best-fit bow-shock stand-off distances, we have established that their central sources are massive objects (WR stars) with supersonic stellar wind velocities and strong mass-loss rates. They are therefore short-lived objects and have probably formed during the most recent starburst event at the GC.

Table 5.11: Maxima of the PDFs orbital planes for the inclination angle (i) and angle of the line of nodes in the sky (Ω).

| Source | i [deg] ^a | Ω [deg] ^a |
|--------|------------------------|-----------------------------|
| IRS 1W | 132 | 154 |
| IRS 5 | 78 | 37 |
| IRS 21 | 51 | 95 |

^a Angle between the orbit and the plane of sky.

^b Angle between North and the line of ascending nodes, increasing East of North.

One of the main sources of uncertainty in determining the orbital planes of the population of massive stars around the GC is the lack of information of the stellar LOS distances (see e.g., Lu et al., 2009; Yelda et al., 2014). Therefore, their LOS distances are significantly better constrained by the result that the extended emission of our sources are bow shocks produced by the interaction of the stellar source with the NA. This characteristic, unique in this sources, along with their LOS velocity from our best-fit models, their proper motions and models of the ISM in the NA, allowed us to perform a Monte Carlo analysis of the sources' orbital planes.

IRS 1W stands out from the other sources because of its unusual morphology (see Sect. 5.4.6), in particular its long tail, which we expect to trace the relative motion between IRS 1W and NA in the past 50 years. From studying the orbital-plane, we derived that the most probable orbit for this source peaks at an inclination of 132° with an as-

ending node angle of 154° . Since the NA orbital plane has an inclination of 45° with an ascending node of 15° , we discovered that both the IRS 1W and the NA orbital planes are approximately perpendicular to each other. Therefore, IRS 1W is crossing the NA and its tail traces the thickness of the NA stream. Since the projected tail has an extension of 6400 AU, the NA thickness probably is on the order of ~ 9000 AU at the position of this source.

The derived orbital planes suggest that our sources are not part of any of the suggested disks of young stars in the GC, but our results are consistent with the most recent detailed work on the orbital distribution of the young stars in the GC by [Yelda et al. \(2014\)](#). These authors suggested that only about 20% of 116 O/WR stars, at a projected distances of $0.8''$ to $12''$ from Sgr A*, are part of the CWS. Hence, if our bow shocks were members of the CWS, the number of disk members would be increased by about 20%. However, our results show that the targeted bow-shock sources probably do not form part of the CWS. Therefore, our results provide new evidence for the complexity of the population of young massive stars in the central parsec of the GC and highlight that the disk members are only a small fraction of the young massive stars around Sgr A*. We conclude that models that intend to explain the formation of the young massive stars in the central parsec of the GC and/or their dynamical evolution need to be adjusted to explain the presence of a considerable number of massive stars with apparently random distribution of their orbital planes, which suggests that either not all stars formed in a disk, or that the disk is rapidly dissolving.

6

CONCLUSIONS

But the years of anxious searching in the dark for a truth that one feels but cannot express, the intense desire and the alternations of confidence and misgiving, and the final emergence into light - only who have experienced it can appreciate it.

Albert Einstein

IN this thesis, I have presented the results of my research in the study of various aspects of massive stars using high-angular resolution techniques, particularly optical interferometry. I have made use of near-infrared data obtained with standard Adaptive Optics NACO/VLT observations, with NACO/VLT in its “Fizeau” interferometric mode, with AMBER/VLTI, and with CRIRES/VLT. All these data were analyzed to perform spectra and image manipulation, as well as the obtaining of observables from optical interferometry data. Nevertheless, since optical interferometry is still a field under development, much of the code used in my analysis was developed by myself. In the following lines, I present the main key conclusions obtained of this dissertation:

- Throughout this thesis, I have demonstrated that stellar interferometry provides unique information to resolve compact structures and/or stellar companions associated with massive stars, which cannot be resolved by any other technique.
- In my work on the young massive stellar object IRS 9A, I have presented new 2.2 and 3.8 μm NACO/SAM data, in addition to the already existing mid-infrared interferometric data, with the aim to resolve the compact component at the core of this object previously detected with MIDI/VLTI. Additionally, I have complemented these SAM observations with near-infrared spectroscopic data obtained with CRIRES/VLT of the H_2 and $\text{Br}\gamma$ lines. The trend observed in the visibilities

supports the presence of a compact component with an angular size of the order of ~ 30 mas at the core of IRS 9A, that might be associated with the presence of a disk-like structure. Observed spectroastrometric displacements of the Br γ line are of the same order than the angular size of the interferometrically detected compact component around IRS 9A. The presence of over-resolved flux is detected in the SAM data. This over-resolved flux is consistent with the presence of an extended envelope with a diameter of $\sim 1''$ around IRS 9A, previously observed with mid-infrared interferometric data taken with the T-ReCS/Gemini camera. Moreover, the spectroastrometric signal of the H $_2$ also traces the material in the envelope, exhibiting centroid-flux displacements between 150-300 mas, depending on the sampled position angle.

- The presented radiative transfer model (applied simultaneously to the near- and mid-infrared interferometric data, and to the spectral energy distribution of the target) suggests that IRS 9A has a morphology similar to the Class I young stellar objects described by [Whitney et al. \(2003\)](#). This supports the idea of a central star surrounded by a compact disk and an outer envelope with bipolar cavities. Nevertheless, in addition to the inadequate angular resolution of the data used to measure the spectral energy distribution, my model still possesses important limitations due to the possible complexity of the target, like (a) the presence of inhomogeneities in the disk, (b) the presence of additionally unresolved stellar companions, and (c) the asymmetrical structure of the envelope.
- During this thesis, I have analyzed long-baseline optical interferometric data of two multiple massive systems: Herschel36 and HD 150 136, with the objective of resolving, by first time, their outer-most component from the spectroscopic binary. For this purpose, I have used AMBER/VLTI observations, covering three bands (J, H, and K) from 1.19 to 2.56 μm . The observed V^2 and closure phases exhibit the typical cosine signature of a binary system (an unresolved spectroscopic binary + outer component). Geometrical models of a binary composed of two unresolved sources allowed us to determine the projected position angles of the components in the plane of the sky and their flux-ratio. Interferometric image reconstruction was performed using a maximum entropy method.
- For Herschel36, the outer component Aa was separated by ~ 2 mas from the spectroscopic binary Ab , suggesting that the components are close to the periastron. The flux ratio between both components are almost equal to unity, suggesting that Aa is more massive than each one of the components in the spectroscopic binary. This configuration is not common in triple hierarchical systems, in which most of the mass in the system is contained by the spectroscopic binary. This would indicate that the formation mechanism of Herschel36 might be different from the one of other triple hierarchical systems. On the other hand, HD 150 136 has an angular separation between the spectroscopic binary and the tertiary component T of ~ 7

mas, with a flux ratio of four, confirming the simultaneous findings by [Sana et al. \(2013\)](#) with PIONIER/VLTI. The flux ratio obtained from my AMBER/VLTI observations allowed us to perform a photometric analysis and to determine the age of the system of around ~ 1 Ma, consistently with the presence of an O3 V star in the target.

- I studied the bright-massive stars at the central parsec of the Galactic center which exhibit a bow-shock structure. For this study, I made use of adaptive optics observations and Sparse Aperture Masking data taken with the NACO/VLT instrument. The central parsec of the Galactic center is one of the most violent environments in the Galaxy. My study determined the morphology of the bow-shock sources, the main processes responsible of their infrared emission, as well as their orbital planes. From my analysis, I confirmed that the morphology of the Wolf-Rayet stars IRS 1W, IRS 5 and IRS 21 can be modelled by a parabolic shell around them produced by the relative motion of the targets in the interstellar medium (i.e., the so-called mini-spiral). The 3D position of the shell is consistent with previous measurements and models of the gas and dust of the interstellar medium, at the position of the sources. In contrast, the morphology of IRS 10W can not be reproduced by my bow-shock model. The morphology of this target might be formed by the shock of two stellar winds and/or by the superposition of a dusty clump or filament in the mini-spiral.
- My steady-state radiative transfer model of the bow-shock sources suggests that their emission observed in the H , K_s and L' data are produced only by thermal emission of the dust in the bow-shock shells, which have a temperature of ~ 470 K near their apices of the shells. This suggests that the polarization observed in the sources is produced by alignment of the dust grains. My Monte-Carlo analysis of the orbital motion of the bow-shock sources shows that they are not part of the population of massive stars that rotates in a projected clockwise disk around SgrA*. Thus, in agreement with other work, my study adds evidence that either all the massive stars do not form in the clockwise system or that the latter is dissolving rapidly.
- To perform the calibration of the aperture masking data in crowded fields, I developed a new technique called the “synthetic calibrator”. In crowded fields, the presence of additional components to the targets of interest can be used to calibrate the data. Thus, the calibrator is constructed by a median superposition of the known point-like sources in the field. This method can help to minimize possible variations in the PSF at different regions of the field-of-view, and it also boosts the efficiency of aperture masking observations by getting rid of the necessity to alternate between calibrator and target observations in different pointings.
- As part of the research performed in this thesis, image reconstruction was per-

formed several times. The expertise that I was able to acquire during these different image reconstruction exercises was decisive for winning the “2014 Beauty Contest” in interferometric image reconstruction.

7

FUTURE WORK

The known is finite, the unknown is infinite; intellectually we stand on an islet in the midst of an illimitable ocean of inexplicability. Our business in every generation is to reclaim a little more land.

T.H. Huxley

Follow-up work on the study of massive stars presented in this thesis includes the following projects:

- **Determination of the orbital motion of stellar components in massive multiple systems:** This line of research focuses on the study of the orbital motion of stellar components in massive triple hierarchical systems. Coplanarity of the orbits in massive multiple systems typically indicates that they were formed by the collapse of the same protostellar cloud (e.g. via Raleigh-Taylor instabilities in the accretion disk). In contrast, non-coplanar orbits usually indicate that the systems were formed most probably due to dynamical interactions. The goal is to characterize the orbital motion of massive hierarchical triple systems to test for coplanarity. To accomplish this goal, I will continue working with the monitoring program of the orbital motion of Herschel36 and HD 150 136 through spectroscopic and VLTI observations. Nevertheless, I plan to increase the number of triple hierarchical systems to test the relative inclination of the orbits. I have submitted a proposal to observe another four triple systems with PIONIER/VLTI and with SPHERE/VLT to determine their orbits.
- **A comprehensive study of the morphology of MYSOs:** This project focuses on the study of the hot central regions (~ 50 -100 AU) of MYSOs. The current observations

and models of MYSOs suggest that there exists an “interpretation gap” between SED modeling and the geometry of the structures observed with optical/infrared interferometry. In the case of NGC3603 IRS9A*, I have found that although several disk + envelope models fit the SED, many of them do not reproduce the observed interferometric visibilities. This problem most probably arises because SED fitting is a degenerate problem since SEDs do not contain any spatial information about the origin of the emission. Bridging this “interpretation gap” by fitting SED and interferometric data simultaneously is a necessary requirement to obtain complete and consistent models of MYSOs. This requires (a) a comprehensive search for disks and companions in these objects by using high angular resolution data across the infrared regime, and (b) a consistent combination of SED models with interferometric data. My initial approach will focus on the analysis of new photometric and VLTI observations with the second generation of VLTI instruments. For this I plan to use GRAVITY and MATISSE to resolve the compact, possibly disk-like structure at the core of IRS 9A and compare its properties with models and SED data. Finally, I also plan to extend this methodology to a larger sample of MYSOs.

- **Search for low-mass companions around massive stars:** This project aims at pushing the limits of our understanding of high mass star formation and multiplicity in massive stars. The main observational goal is to search for low- and intermediate-mass companions in a range from 50 to 500 mas (or 10^2 - 10^3 AU at a distance of 2 kpc) around massive stars, using high-contrast observations. This observational regime will fill out the observational gap in the brightness ratio of the SAM and AO-imaging data presented in the state-of-the-art study of multiplicity in massive stars (see Fig. 4.2 in Chapter 4). From the astrophysical point of view, this project aims at providing important observational evidence to test the validity of the current massive star formation scenarios. The detection of low mass companions will support the core collapse scenario, while the non-detection will hold up to the competitive accretion model.

I will survey nearby (≤ 4 kpc) massive stars with magnitudes $R \leq 9$ in the H and K filters. The target selection is going to be performed from the GOSC catalog (Maíz-Apellániz, 2004). The reason to use a sample limited by magnitude is because this will guarantee excellent AO-performance and thus the required contrast (this project requires a contrast ratio of 10^3 - 10^4 or $8 < \Delta m < 10$). Therefore, state-of-the-art instruments with extreme AO-systems and low-photon noise detectors are required. Hence, I will make use of the new NIR planetary imagers: SPHERE/VLT and the Gemini Planetary Imager (GPI). This project will be one of the first attempts to obtain a complete view of multiplicity in massive stars at the lower end of the mass distribution of companions. SPHERE/VLT and the GPI/Gemini have unique observing modes that are perfectly suited to perform this study. I will use a combination of these different observing modes to ensure the optimal contrast

ratio for all the sampled spatial scales. To search for companions at scales between $0.5 \lambda/D$ and $4 \lambda/D$, I will use Sparse Aperture Masking and Kernel Phases. At scales larger than $4 \lambda/D$ and lower than $8 \lambda/D$, I will survey using angular differential imaging with coronagraphy. These observations will be combined with a statistical analysis of the detected companions, and radiative transfer simulations to explain the physical scenarios of the observed distribution of low-mass stars.

- **Software to perform SAM data reduction and image reconstruction:** From my experience with the current facilities to reduce and analyze sparse aperture masking data, I found that there are still significant improvements that should be implemented to make this technique more accessible to the community. The idea to create a new SAM data reduction package that will allow to choose between the traditional calibration scheme and the synthetic calibrator. Moreover, I would like to include implementations of geometrical models in order to perform simple model fitting with the same package. In a similar fashion, I noticed that the current software to perform image reconstruction in optical interferometry needs additional capabilities. For example, the ability to select certain spatial frequencies from which the image reconstruction would be performed, flagging bad data and outliers, and the option to implement new regularizers. This software is planned to be written in an open source language, like Python, to make it available to the community.

A

GALACTIC CENTER ORBITS AND PROPER MOTIONS (APPENDIX)

A.1. PROPER MOTION MEASUREMENTS

Figures A.1 and A.2 display the proper motions of the reference stars and of the bow-shock sources, respectively.

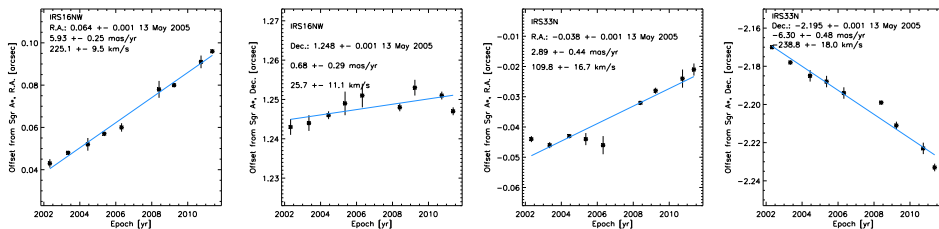


Figure A.1: Proper motion measurements. Measured positions vs. time in right ascension and declination offsets from Sagittarius A* for the stars IRS 16NW and IRS 33N.

A.2. THIELE-INNES METHOD TO DETERMINE ORBITAL PARAMETERS

Once the position (\vec{r}) and velocity (\vec{v}) in 3D space of an orbiting star around a supermassive black hole (where $M_{BH} \ll M_{star}$) are known, the Keplerian orbital elements: period (P), eccentricity (e), time of the periapsis passage (T_0), inclination (i), angle of the ascending node (Ω), and the angle of the periapsis (ω) can be calculated. The eccentricity

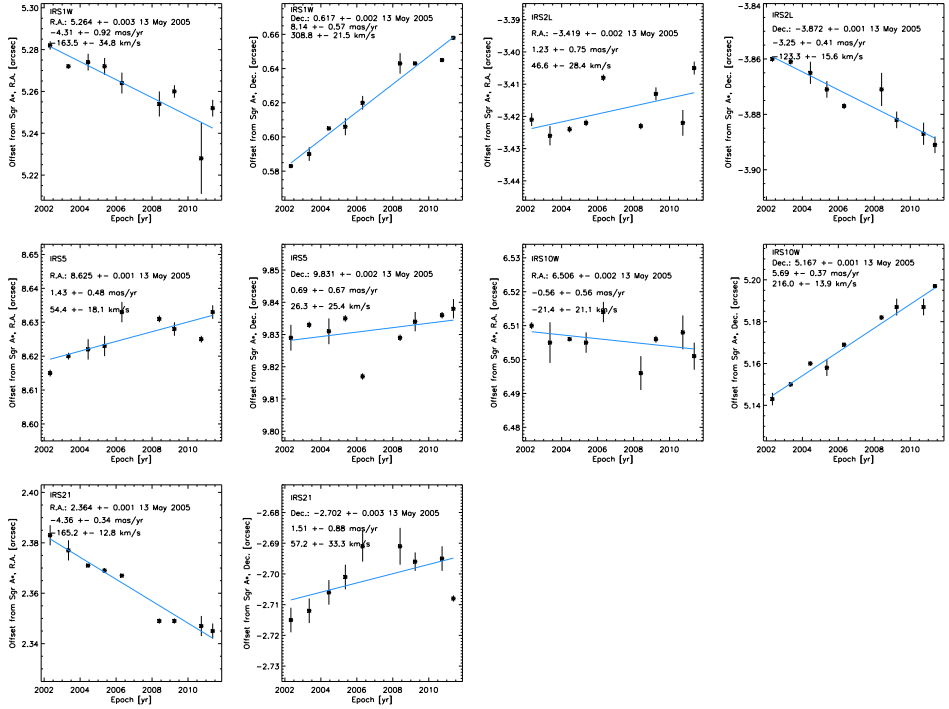


Figure A.2: Proper motion measurements. Measured positions vs. time in right ascension and declination offsets from Sagittarius A* for the bow-shock sources IRS 1W, IRS 5, IRS 2L, IRS 10W, and IRS 21.

(e) describes how elongated is the orbit. The period (P) is the time necessary to complete an orbit. The periapsis passage (T_0) describes the position of the body in the orbit at a given reference time. The inclination angle (i) describes the angle between the orbital plane and a reference plane (usually the plane of the sky). The angle of the ascending node (Ω) determines the orientation of the ascending node (the point in the orbit where the orbiting body crosses through the plane of reference) from a reference direction (usually the north, frequently called the vernal point). The angle of the periapsis (ω) measures the angle between the ascending node to the periapsis (the minimum separation in the orbital ellipse between the orbiting bodies). Figure A.3 displays a schematic representation of the three important angles in the set of Keplerian orbital elements.

As described in Lu et al. (2009), the reference frame to compute the orbital elements of our stars situates SgrA* at the origin of the coordinate system. Right ascension and declination are parallel to the x and y axes. The z -axis increases towards the observer. The orbital parameters are thus computed in the following way:

First, some intermediate quantities are calculated:

The specific angular momentum vector (\vec{h}): This quantity is equivalent to the total angular momentum of the two orbiting bodies divided by the reduced mass. This vector

is constant in magnitude and direction. The direction of \vec{h} is normal to the plane of the orbit.

$$\vec{h} = \vec{r} \times \vec{v} \quad (\text{A.1})$$

The eccentricity vector:(\vec{e}): The magnitude of this vector equals the scalar eccentricity of the orbit. \vec{e} is a constant of the orbital motion and points from the center of mass towards the periapsis. G is the gravitational constant, and M the total mass of the system.

$$\vec{e} = \frac{\vec{v} \times \vec{h}}{GM} - \frac{\vec{r}}{|\vec{r}|} \quad (\text{A.2})$$

The ascending node vector:($\vec{\Omega}$): This vector points toward the ascending node. \hat{z} is the unit vector that lies on the z -axis.

$$\vec{\Omega} = \vec{h} \times \hat{z} \quad (\text{A.3})$$

The semi-major axis:(a):

$$a = \left[\frac{2}{|\vec{r}|} - \frac{|\vec{v}|^2}{GM} \right]^{-1} \quad (\text{A.4})$$

Once the previous intermediate quantities are calculated, then the computation of the orbital parameters is straight-forward:

$$i = \arccos \left(\frac{-\vec{h} \cdot \hat{z}}{|\vec{h}|} \right) \quad (\text{A.5})$$

$$e = |\vec{e}| \quad (\text{A.6})$$

$$\omega = \left[\frac{(\hat{z} \times \vec{h}) \cdot \vec{e}}{|\hat{z} \times \vec{h}| |\vec{e}|} \right] \quad (\text{if } \vec{e} \cdot \hat{z} \text{ then } \omega = 2\pi - \omega) \quad (\text{A.7})$$

$$\Omega = \arctan \left(\frac{\vec{\Omega} \cdot \hat{x}}{\vec{\Omega} \cdot \hat{y}} \right) \quad (\text{A.8})$$

$$\left(\frac{P}{[yr]} \right) = \sqrt{\left(\frac{a}{[AU]} \right)^3 \left(\frac{[M_{\odot}]}{M} \right)} \quad (\text{A.9})$$

To compute T_0 , it is necessary to calculate the Thiele-Innes constants:

$$A = a(\cos\omega\cos\Omega - \sin\omega\sin\Omega\cos i) \quad (\text{A.10})$$

$$B = a(\cos\omega\sin\Omega + \sin\omega\cos\Omega\cos i) \quad (\text{A.11})$$

$$F = a(-\sin\omega\cos\Omega - \cos\omega\sin\Omega\cos i) \quad (\text{A.12})$$

$$G = a(-\sin\omega\sin\Omega + \cos\omega\cos\Omega\cos i) \quad (\text{A.13})$$

$$\cos E = \frac{Gr_y - Fr_x}{AG - BF} + e \quad (\text{A.14})$$

$$\sin E = \frac{-r_x - Br_y}{A} \frac{AG - BF}{\sqrt{1 - e^2}} \quad (\text{A.15})$$

$$E = \arctan\left(\frac{\sin E}{\cos E}\right) \quad (\text{A.16})$$

Finally, T_0 is obtained with the following expression, where t_{ref} is the reference epoch (in this case we use J2000).

$$T_0 = t_{ref} - \frac{P}{2\pi}(E - e\sin E) \quad (\text{A.17})$$

Keplerian orbital elements

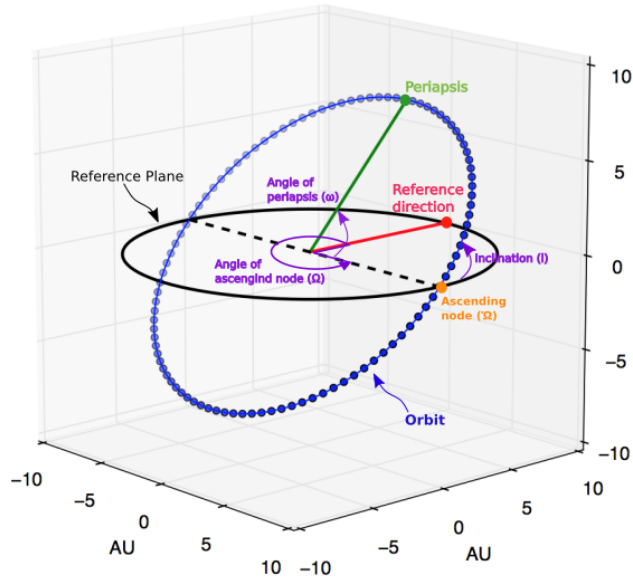


Figure A.3: Schematic of some of the Keplerian orbital elements. The figure illustrates the convention for Ω, ω, i in a given orbit. Additionally, some other important orbital points are labeled.

REFERENCES

- Alexander, T. (2005). "Stellar processes near the massive black hole in the Galactic center [review article]". *astro-ph/0508106*, 419:65–142.
- Alves, J., Lombardi, M., and Lada, C. J. (2007). "The mass function of dense molecular cores and the origin of the IMF". *A&A*, 462:L17–L21.
- Arias, J. I., Barbá, R. H., Gamen, R. C., Morrell, N. I., Maíz Apellániz, J., Alfaro, E. J., Sota, A., Walborn, N. R., and Moni Bidin, C. (2010). "On The Multiplicity of the Zero-Age Main-Sequence O Star Herschel 36". *ApJ*, 710:L30–L34.
- Arias, J. I., Barbá, R. H., Maíz Apellániz, J., Morrell, N. I., and Rubio, M. (2006). "The infrared Hourglass cluster in M8*†". *MNRAS*, 366:739–757.
- Bailey, J. (1998). "Detection of pre-main-sequence binaries using spectro-astrometry". *MNRAS*, 301:161–167.
- Baldwin, J. E., Beckett, M. G., Boysen, R. C., Burns, D., Buscher, D. F., Cox, G. C., Haniff, C. A., Mackay, C. D., Nightingale, N. S., Rogers, J., Scheuer, P. A. G., Scott, T. R., Tuthill, P. G., Warner, P. J., Wilson, D. M. A., and Wilson, R. W. (1996). "The first images from an optical aperture synthesis array: mapping of Capella with COAST at two epochs.". *A&A*, 306:L13.
- Baldwin, J. E., Haniff, C. A., Mackay, C. D., and Warner, P. J. (1986). "Closure phase in high-resolution optical imaging". *Nature*, 320:595–597.
- Bally, J., Ginsburg, A., Silvia, D., and Youngblood, A. (2015). "The Orion Fingers: Near-IR Adaptive Optics Imaging of an Explosive Protostellar Outflow". *ArXiv e-prints: 1502.04711*.
- Bally, J. and Zinnecker, H. (2005). "The Birth of High-Mass Stars: Accretion and/or Mergers?". *AJ*, 129:2281–2293.
- Barbá, R. H., Gamen, R., Arias, J. I., Morrell, N., Maíz Apellániz, J., Alfaro, E., Walborn, N., and Sota, A. (2010). "Spectroscopic survey of galactic O and WN stars. OWN Survey: new binaries and trapezium-like systems". *Revista Mexicana de Astronomía y Astrofísica Conference Series*, 38:30–32.
- Baron, F. and Kloppenborg, B. (2010). "GPU-accelerated image reconstruction for optical and infrared interferometry". *Society of Photo-Optical Instrumentation Engineers (SPIE) Conference Series*, 7734:4.

- Baron, F. and Young, J. S. (2008). "Image reconstruction at Cambridge University". *Society of Photo-Optical Instrumentation Engineers (SPIE) Conference Series*, 7013:3.
- Bartko, H., Martins, F., Fritz, T. K., Genzel, R., Levin, Y., Perets, H. B., Paumard, T., Nayakshin, S., Gerhard, O., Alexander, T., Dodds-Eden, K., Eisenhauer, F., Gillessen, S., Mascetti, L., Ott, T., Perrin, G., Pfuhl, O., Reid, M. J., Rouan, D., Sternberg, A., and Trippe, S. (2009). "Evidence for Warped Disks of Young Stars in the Galactic Center". *ApJ*, 697:1741–1763.
- Bartko, H., Martins, F., Trippe, S., Fritz, T. K., Genzel, R., Ott, T., Eisenhauer, F., Gillessen, S., Paumard, T., Alexander, T., Dodds-Eden, K., Gerhard, O., Levin, Y., Mascetti, L., Nayakshin, S., Perets, H. B., Perrin, G., Pfuhl, O., Reid, M. J., Rouan, D., Zilka, M., and Sternberg, A. (2010). "An Extremely Top-Heavy Initial Mass Function in the Galactic Center Stellar Disks". *ApJ*, 708:834–840.
- Barvainis, R. (1987). "Hot dust and the near-infrared bump in the continuum spectra of quasars and active galactic nuclei". *ApJ*, 320:537–544.
- Beckers, J. M. (1993). "Adaptive optics for astronomy - Principles, performance, and applications". *ARA&A*, 31:13–62.
- Becklin, E. E. and Neugebauer, G. (1975). "High-resolution maps of the galactic center at 2.2 and 10 microns". *ApJ*, 200:L71–L74.
- Beltrán, M. T., Cesaroni, R., Neri, R., Codella, C., Furuya, R. S., Testi, L., and Olmi, L. (2005). "A detailed study of the rotating toroids in G31.41+0.31 and G24.78+0.08". *A&A*, 435:901–925.
- Berger, J. P. and Segransan, D. (2007). "An introduction to visibility modeling". *New A Rev.*, 51:576–582.
- Bernat, D., Martinache, F., Ireland, M., Tuthill, P., and Lloyd, J. (2012). "The Use of Spatial Filtering with Aperture Masking Interferometry and Adaptive Optics". *ApJ*, 756:8.
- Beuther, H., Schilke, P., Menten, K. M., Motte, F., Sridharan, T. K., and Wyrowski, F. (2002). "High-Mass Protostellar Candidates. II. Density Structure from Dust Continuum and CS Emission". *ApJ*, 566:945–965.
- Beuther, H. and Shepherd, D. (2005). "Precursors of UCHII Regions and the Evolution of Massive Outflows". *Cores to Clusters: Star Formation with Next Generation Telescopes*, eds., Kumar, M. S. N. and Tafalla, M. and Caselli, P., pages 105–119.
- Black, J. H. and van Dishoeck, E. F. (1987). "Fluorescent excitation of interstellar H₂". *ApJ*, 322:412–449.

- Blanco Cárdenas, M. W., Käufel, H. U., Guerrero, M. A., Miranda, L. F., and Seifahrt, A. (2014). "CRIRES-VLT high-resolution spectro-astrometry as a tool in the search for disks inside the cores of planetary nebulae". *A&A*, (566):A133.
- Boley, P. A., Linz, H., van Boekel, R., Henning, T., Feldt, M., Kaper, L., Leinert, C., Müller, A., Pascucci, I., Robberto, M., Stecklum, B., Waters, L. B. F. M., and Zinnecker, H. (2013). "The VLTI/MIDI survey of massive young stellar objects . Sounding the inner regions around intermediate- and high-mass young stars using mid-infrared interferometry". *A&A*, 558:A24.
- Bonneau, D., Clause, J.-M., Delfosse, X., Mourard, D., Cetre, S., Chelli, A., Cruzalèbes, P., Duvert, G., and Zins, G. (2006). "SearchCal: a virtual observatory tool for searching calibrators in optical long baseline interferometry. I. The bright object case". *A&A*, 456:789.
- Bonneau, D., Delfosse, X., Mourard, D., Lafrasse, S., Mella, G., Cetre, S., Clause, J.-M., and Zins, G. (2011). "SearchCal: a Virtual Observatory tool for searching calibrators in optical long-baseline interferometry. II. The faint-object case". *A&A*, 535:A53.
- Bonnell, I. and Bastien, P. (1992). "A binary origin for FU Orionis stars". *ApJ*, 401:L31–L34.
- Bonnell, I. A. (2005). "The Formation of Massive Binary Stars". *ArXiv Astrophysics e-prints: 0501260*.
- Bonnell, I. A. and Bate, M. R. (2006). "Star formation through gravitational collapse and competitive accretion". *MNRAS*, 370:488–494.
- Bonnell, I. A., Bate, M. R., Clarke, C. J., and Pringle, J. E. (2001). "Competitive accretion in embedded stellar clusters". *MNRAS*, 323:785–794.
- Bonnell, I. A., Vine, S. G., and Bate, M. R. (2004). "Massive star formation: nurture, not nature". *MNRAS*, 349:735–741.
- Brown, L. R., Troutman, M. R., and Gibb, E. L. (2013). "Spectro-astrometry of Water in DR Tauri". *ApJ*, 770:L14.
- Buchholz, R. M., Witzel, G., Schödel, R., and Eckart, A. (2013). "Ks- and Lp-band polarimetry on stellar and bow-shock sources in the Galactic center". *A&A*, 557:A82.
- Buchholz, R. M., Witzel, G., Schödel, R., Eckart, A., Bremer, M., and Mužić, K. (2011). "Adaptive-optics assisted near-infrared polarization measurements of sources in the Galactic center". *A&A*, 534:A117.
- Burch, S. F., Gull, S. F., and Skilling, J. (1983). "Image Restoration by a Powerful Maximum Entropy Method". *Computer Vision Graphics and Image Processing*, 23:113–128.

- Buscher, D. F. (1994). "Direct maximum-entropy image reconstruction from the bispectrum". *Very High Angular Resolution Imaging; eds. Robertson, J. G. and Tango, W. J.*, 158:91.
- Carlotti, A. and Groff, T. (2010). "New approaches to the design of non-redundant aperture masks". *Society of Photo-Optical Instrumentation Engineers (SPIE) Conference Series*, page 3.
- Carlotti, A., Kasdin, N. J., Vanderbei, R. J., and Delorme, J.-R. (2012). "Optimized shaped pupil masks for pupil with obscuration". *Society of Photo-Optical Instrumentation Engineers (SPIE) Conference Series*, 8442:54.
- Chelli, A., Utrera, O. H., and Duvert, G. (2009). "Optimised data reduction for the AMBER/VLTI instrument". *A&A*, 502:705–709.
- Christopher, M. H. and Scoville, N. Z. (2003). "OVRO High Resolution Imaging of Dense Molecular Clouds in the Central Three Parsecs of the Galaxy". *Active Galactic Nuclei: From Central Engine to Host Galaxy; eds: Collin, S. and Combes, F. and Shlosman, I.*, 290:389.
- Clarke, A. J., Oudmaijer, R. D., and Lumsden, S. L. (2005). "Tycho-2 stars with infrared excess in the MSX Point Source Catalogue". *MNRAS*, 363:1111–1124.
- Cl enet, Y., Rouan, D., Gendron, E., Lacombe, F., Lagrange, A.-M., Mouillet, D., Magnard, Y., Rousset, G., Fusco, T., Montri, J., Genzel, R., Sch odel, R., Ott, T., Eckart, A., Marco, O., and Tacconi-Garman, L. (2004). "The infrared L'-band view of the Galactic Center with NAOS-CONICA at VLT". *A&A*, 417:L15–L19.
- Colavita, M. M., Hines, B. E., Shao, M., Klose, G. J., and Gibson, B. V. (1991). "Prototype high speed optical delay line for stellar interferometry". *Delay Lines, Interferometers, Very Long Base Interferometry, Control Systems Design, Prototypes; eds: Ealey, M. A.*, 1542:205–212.
- Crowther, P. A., Schnurr, O., Hirschi, R., Yusof, N., Parker, R. J., Goodwin, S. P., and Kasim, H. A. (2010). "The R136 star cluster hosts several stars whose individual masses greatly exceed the accepted $150M_{\text{Solar}}$ stellar mass limit". *MNRAS*, 408:731–751.
- Danchi, W. C., Bester, M., Greenhill, L. J., Degiacomi, C. G., and Townes, C. H. (1994). "Analysis of visibility data from the University of California/Berkeley Infrared Spatial Interferometer: radiative transfer modeling and results on fifteen stars". *Amplitude and Intensity Spatial Interferometry II: Society of Photo-Optical Instrumentation Engineers (SPIE) Conference Series*, 2200:286–303.
- de Mink, S. E., Cantiello, M., Langer, N., Pols, O. R., Brott, I., and Yoon, S.-C. (2009). "Rotational mixing in massive binaries. Detached short-period systems". *A&A*, 497:243–253.

- de Wit, W. J., Hoare, M. G., Oudmaijer, R. D., and Mottram, J. C. (2007). "VLTI/MIDI 10 μm Interferometry of the Forming Massive Star W33A". *ApJ*, 671:L169–L172.
- de Wit, W. J., Hoare, M. G., Oudmaijer, R. D., Nürnberger, D. E. A., Wheelwright, H. E., and Lumsden, S. L. (2011). "Mid-infrared interferometry towards the massive young stellar object CRL 2136: inside the dust rim". *A&A*, 526:L5.
- de Wit, W. J., Testi, L., Palla, F., Vanzi, L., and Zinnecker, H. (2004). "The origin of massive O-type field stars. I. A search for clusters". *A&A*, 425:937–948.
- di Benedetto, G. P. and Rabbia, Y. (1987). "Accurate angular diameters and effective temperatures for eleven giants cooler than K0 by Michelson interferometry". *A&A*, 188:114–124.
- Diolaiti, E., Bendinelli, O., Bonaccini, D., Close, L. M., Currie, D. G., and Parmeggiani, G. (2000). "StarFinder: an IDL GUI-based code to analyze crowded fields with isoplanatic correcting PSF fitting". *Society of Photo-Optical Instrumentation Engineers (SPIE) Conference Series*, 4007(astro-ph/0004101):879–888.
- Doeleman, S. S., Shen, Z.-Q., Rogers, A. E. E., Bower, G. C., Wright, M. C. H., Zhao, J. H., Backer, D. C., Crowley, J. W., Freund, R. W., Ho, P. T. P., Lo, K. Y., and Woody, D. P. (2001). "Structure of Sagittarius A* at 86 GHz using VLBI Closure Quantities". *AJ*, 121:2610–2617.
- Doeleman, S. S., Weintraub, J., Rogers, A. E. E., Plambeck, R., Freund, R., Tilanus, R. P. J., Friberg, P., Ziurys, L. M., Moran, J. M., Corey, B., Young, K. H., Smythe, D. L., Titus, M., Marrone, D. P., Cappallo, R. J., Bock, D. C.-J., Bower, G. C., Chamberlin, R., Davis, G. R., Krichbaum, T. P., Lamb, J., Maness, H., Niell, A. E., Roy, A., Strittmatter, P., Werthimer, D., Whitney, A. R., and Woody, D. (2008). "Event-horizon-scale structure in the supermassive black hole candidate at the Galactic Centre". *Nature*, 455:78–80.
- Draine, B. T. and Lee, H. M. (1984). "Optical properties of interstellar graphite and silicate grains". *ApJ*, 285:89–108.
- Eckart, A., Schoedel, R., and Straubmeier, C. (2005). *"The black hole at the center of the Milky Way"*. Imperial College Press.
- Edgar, R. and Clarke, C. (2004). "The effect of radiative feedback on Bondi-Hoyle flow around a massive star". *MNRAS*, 349:678–686.
- Ekers, R. D., van Gorkom, J. H., Schwarz, U. J., and Goss, W. M. (1983). "The radio structure of SGR A". *A&A*, 122:143–150.
- Frater, R. H., Robertson, J. G., and O'Sullivan, J. D. (1986). "High resolution interferometric imaging using a large optical telescope". *International Topical Meeting on Image Detection and Quality*, pages 255–258.

- Frey, S. and Mosoni, L. (2009). "A short introduction to radio interferometric image reconstruction". *New A Rev.*, 53:307–311.
- García, B., Malaroda, S., Levato, H., Morrell, N., and Grosso, M. (1998). "Frequency of Binaries in the Open Cluster Trumpler 14". *PASP*, 110:53–59.
- Geballe, T. R., Najarro, F., Rigaut, F., and Roy, J.-R. (2006). "The K-Band Spectrum of the Hot Star in IRS 8: An Outsider in the Galactic Center?". *ApJ*, 652:370–375.
- Genzel, R., Eisenhauer, F., and Gillessen, S. (2010). "The Galactic Center massive black hole and nuclear star cluster". *Reviews of Modern Physics*, 82:3121–3195.
- Genzel, R., Thatte, N., Krabbe, A., Kroker, H., and Tacconi-Garman, L. E. (1996). "The Dark Mass Concentration in the Central Parsec of the Milky Way". *ApJ*, 472:153.
- Gezari, D. Y., Backman, D. E., and Werner, M. W. (1998). "Mid-Infrared Imaging of Orion BN/KL. II. Luminosity Sources, Extinction Distribution, and the Nature of IRc2". *ApJ*, 509:283–298.
- Ghez, A. M., Klein, B. L., Morris, M., and Becklin, E. E. (1998). "High Proper-Motion Stars in the Vicinity of Sagittarius A*: Evidence for a Supermassive Black Hole at the Center of Our Galaxy". *ApJ*, 509:678–686.
- Ghez, A. M., Salim, S., Hornstein, S. D., Tanner, A., Lu, J. R., Morris, M., Becklin, E. E., and Duchêne, G. (2005). "Stellar Orbits around the Galactic Center Black Hole". *ApJ*, 620:744–757.
- Gieles, M., Sana, H., and Portegies Zwart, S. F. (2010). "On the velocity dispersion of young star clusters: super-virial or binaries?". *MNRAS*, 402:1750–1757.
- Gies, D. R. (1987). "The kinematical and binary properties of association and field O stars". *ApJS*, 64:545–563.
- Gillessen, S., Eisenhauer, F., Trippe, S., Alexander, T., Genzel, R., Martins, F., and Ott, T. (2009). "Monitoring Stellar Orbits Around the Massive Black Hole in the Galactic Center". *ApJ*, 692:1075–1109.
- Girard, J. H. V., Kasper, M., Quanz, S. P., Kenworthy, M. A., Rengaswamy, S., Schödel, R., Gallenne, A., Gillessen, S., Huerta, N., Kervella, P., Kornweibel, N., Lenzen, R., Mérand, A., Montagnier, G., O’Neal, J., and Zins, G. (2010). "Status and new operation modes of the versatile VLT/NaCo". *Society of Photo-Optical Instrumentation Engineers (SPIE) Conference Series*, 7736:2.
- Glasse, A. C. H., Aitken, D. K., and Roche, P. F. (2003). "The magnetic field in the central parsec". *Astronomische Nachrichten Supplement*, 324:563–566.

- Goto, M., Stecklum, B., Linz, H., Feldt, M., Henning, T., Pascucci, I., and Usuda, T. (2006). "High-Resolution Infrared Imaging of Herschel 36 SE: A Showcase for the Influence of Massive Stars in Cluster Environments". *ApJ*, 649:299–305.
- Grellmann, R., Ratzka, T., Kraus, S., Linz, H., Preibisch, T., and Weigelt, G. (2011). "Mid-infrared interferometry of the massive young stellar object NGC 2264 IRS 1". *A&A*, 532:A109.
- Grønbech, B. and Olsen, E. H. (1976). "Four-color uvby photometry for bright O to G0 type stars south of declination +10 .". *A&AS*, 25:213–270.
- Hanbury Brown, R., Davis, J., and Allen, L. R. (1967a). "The stellar interferometer at Narrabri Observatory I. A. description of the instrument and the observational procedure". *MNRAS*, 137:375.
- Hanbury Brown, R., Davis, J., Allen, L. R., and Rome, J. M. (1967b). "The stellar interferometer at Narrabri Observatory-II. The angular diameters of 15 stars". *MNRAS*, 137:393.
- Haniff, C. A., Mackay, C. D., Titterton, D. J., Sivia, D., and Baldwin, J. E. (1987). "The first images from optical aperture synthesis". *Nature*, 328:694–696.
- Heney, L. G. and Greenstein, J. L. (1941). "Diffuse radiation in the Galaxy". *ApJ*, 93:70–83.
- Herbst, W. and Havlen, R. J. (1977). "ARA OB1, NGC 6193 and ARA R1 - an optical study of a very young southern complex". *A&AS*, 30:279–295.
- Hillwig, T. C., Gies, D. R., Bagnuolo, Jr., W. G., Huang, W., McSwain, M. V., and Wingert, D. W. (2006). "Binary and Multiple O-Type Stars in the Cassiopeia OB6 Association". *ApJ*, 639:1069–1080.
- Högbom, J. A. (1974). "Aperture Synthesis with a Non-Regular Distribution of Interferometer Baselines". *A&AS*, 15:417.
- Ireland, M. J. (2013). "Phase errors in diffraction-limited imaging: contrast limits for sparse aperture masking". *MNRAS*, 433:1718–1728.
- Ireland, M. J., Monnier, J. D., and Thureau, N. (2006). "Monte-Carlo imaging for optical interferometry". *Society of Photo-Optical Instrumentation Engineers (SPIE) Conference Series*, 6268:1.
- Jennison, R. C. (1958). "A phase sensitive interferometer technique for the measurement of the Fourier transforms of spatial brightness distributions of small angular extent". *MNRAS*, 118:276.

- Käufel, H.-U., Ballester, P., Biereichel, P., Delabre, B., Donaldson, R., Dorn, R., Fedrigo, E., Finger, G., Fischer, G., Franza, F., Gojak, D., Huster, G., Jung, Y., Lizon, J.-L., Mehrgan, L., Meyer, M., Moorwood, A., Pirard, J.-F., Paufique, J., Pozna, E., Siebenmorgen, R., Silber, A., Stegmeier, J., and Wegerer, S. (2004). "CRIRES: a high-resolution infrared spectrograph for ESO's VLT". *Society of Photo-Optical Instrumentation Engineers (SPIE) Conference Series*, Moorwood, A. F. M. and Iye, M., 5492:1218–1227.
- Kim, S.-H., Martin, P. G., and Hendry, P. D. (1994). "The size distribution of interstellar dust particles as determined from extinction". *ApJ*, 422:164–175.
- Kishimoto, M., Hönl, S. F., Antonucci, R., Kotani, T., Barvainis, R., Tristram, K. R. W., and Weigelt, G. (2009). "Exploring the inner region of type 1 AGNs with the Keck interferometer". *A&A*, 507:L57–L60.
- Kraus, S., Hofmann, K.-H., Menten, K. M., Schertl, D., Weigelt, G., Wyrowski, F., Meilland, A., Perraut, K., Petrov, R., Robbe-Dubois, S., Schilke, P., and Testi, L. (2010). "A hot compact dust disk around a massive young stellar object". *Nature*, 466:339–342.
- Kraus, S., Weigelt, G., Balega, Y. Y., Docobo, J. A., Hofmann, K.-H., Preibisch, T., Schertl, D., Tamazian, V. S., Driebe, T., Ohnaka, K., Petrov, R., Schöller, M., and Smith, M. (2009). "Tracing the young massive high-eccentricity binary system θ^1 Orionis C through periastron passage". *A&A*, 497:195–207.
- Kroupa, P. (2000). "Stellar Dynamics of Young Star Clusters". *Massive Stellar Clusters; eds. Lançon, A. and Boily, C. M.*, 211:233.
- Krumholz, M. R. (2006). "Radiation Feedback and Fragmentation in Massive Protostellar Cores". *ApJ*, 641:L45–L48.
- Krumholz, M. R., Klein, R. I., and McKee, C. F. (2007a). "Radiation-Hydrodynamic Simulations of Collapse and Fragmentation in Massive Protostellar Cores". *ApJ*, 656:959–979.
- Krumholz, M. R., Klein, R. I., McKee, C. F., and Bolstad, J. (2007b). "Equations and Algorithms for Mixed-frame Flux-limited Diffusion Radiation Hydrodynamics". *ApJ*, 667:626–643.
- Krumholz, M. R., Klein, R. I., McKee, C. F., Offner, S. S. R., and Cunningham, A. J. (2009). "The Formation of Massive Star Systems by Accretion". *Science*, 323:754.
- Krumholz, M. R., McKee, C. F., and Klein, R. I. (2005). "The formation of stars by gravitational collapse rather than competitive accretion". *Nature*, 438:332–334.
- Kuiper, R., Yorke, H. W., and Turner, N. J. (2014). "Protostellar Outflows and Radiative Feedback from Massive Stars". *ArXiv e-prints:1412.6528*.

- Labeyrie, A. (1975). "Interference fringes obtained on VEGA with two optical telescopes". *ApJ*, 196:L71–L75.
- Labeyrie, A., Lipson, S. G., and Nisenson, P. (2006). An introduction to optical stellar interferometry. *Cambridge University Press*.
- Lacour, S., Thiébaud, E., and Perrin, G. (2007). "High dynamic range imaging with a single-mode pupil remapping system: a self-calibration algorithm for redundant interferometric arrays". *MNRAS*, 374:832–846.
- Lacour, S., Tuthill, P., Amico, P., Ireland, M., Ehrenreich, D., Huelamo, N., and Lagrange, A.-M. (2011). "Sparse aperture masking at the VLT. I. Faint companion detection limits for the two debris disk stars HD 92945 and HD 141569". *A&A*, 532:A72.
- Lada, C. J. (1987). "Star formation - From OB associations to protostars". *Star Forming Regions*, Peimbert, M. and Jugaku, J., 115:1–17.
- Lane, B. F., Kuchner, M. J., Boden, A. F., Creech-Eakman, M., and Kulkarni, S. R. (2000). "Direct detection of pulsations of the Cepheid star ζ Gem and an independent calibration of the period-luminosity relation". *Nature*, 407:485–487.
- Langer, N., Cantiello, M., Yoon, S.-C., Hunter, I., Brott, I., Lennon, D., de Mink, S., and Verheijdt, M. (2008). "Rotation and Massive Close Binary Evolution". *IAU Symposium; eds. Bresolin, F and Crowther, P. A. and Puls, J.*, 250:167–178.
- Lawson, P. R. (2000). "Principles of Long Baseline Stellar Interferometry". *Course notes from the 1999 Michelson Summer School, held August 15-19, 1999*.
- Lawson, P. R., Cotton, W. D., Hummel, C. A., Monnier, J. D., Zhao, M., Young, J. S., Thorsteinsson, H., Meimon, S. C., Mugnier, L. M., Le Besnerais, G., Thiebaud, E. M., and Tuthill, P. G. (2004). "An interferometry imaging beauty contest". *New Frontiers in Stellar Interferometry: Society of Photo-Optical Instrumentation Engineers (SPIE) Conference Series*, 5491:886.
- Lejeune, T. and Schaerer, D. (2001). "Database of Geneva stellar evolution tracks and isochrones for (UBV)_J(RI)_C JHKLL'M, HST-WFPC2, Geneva and Washington photometric systems". *A&A*, 366:538–546.
- Levin, Y. and Beloborodov, A. M. (2003). "Stellar Disk in the Galactic Center: A Remnant of a Dense Accretion Disk?". *ApJ*, 590:L33–L36.
- Linder, N., Rauw, G., Sana, H., De Becker, M., and Gosset, E. (2007). "The Struve-Sahade effect in the optical spectra of O-type binaries. I. Main-sequence systems". *A&A*, 474:193–204.
- Lo, K. Y. and Claussen, M. J. (1983). "High-resolution observations of ionized gas in central 3 parsecs of the Galaxy - Possible evidence for infall". *Nature*, 306:647–651.

- Lu, J. R., Do, T., Ghez, A. M., Morris, M. R., Yelda, S., and Matthews, K. (2013). "Stellar Populations in the Central 0.5 pc of the Galaxy. II. The Initial Mass Function". *ApJ*, 764:155.
- Lu, J. R., Ghez, A. M., Hornstein, S. D., Morris, M. R., Becklin, E. E., and Matthews, K. (2009). "A Disk of Young Stars at the Galactic Center as Determined by Individual Stellar Orbits". *ApJ*, 690:1463–1487.
- Lucy, L. B. (1974). "An iterative technique for the rectification of observed distributions". *AJ*, 79:745.
- Mac Low, M.-M. and Klessen, R. S. (2004). "Control of star formation by supersonic turbulence". *Reviews of Modern Physics, astro-ph/0301093*, 76:125–194.
- Maeder, A. and Behrend, R. (2002). "Formation and pre-MS Evolution of Massive Stars with Growing Accretion". *Hot Star Workshop III: The Earliest Phases of Massive Star Birth*; eds. Crowther, P., 267:179.
- Mahy, L., Gosset, E., Sana, H., Damerdji, Y., De Becker, M., Rauw, G., and Nitschelm, C. (2012). "Evidence for a physically bound third component in HD 150136". *A&A*, 540:A97.
- Mahy, L., Nazé, Y., Rauw, G., Gosset, E., De Becker, M., Sana, H., and Eenens, P. (2009). "Early-type stars in the young open cluster NGC 2244 and in the Monoceros OB2 association. I. The multiplicity of O-type stars". *A&A*, 502:937–950.
- Maíz-Apellániz, J. (2004). "CHORIZOS: A χ^2 Code for Parameterized Modeling and Characterization of Photometry and Spectrophotometry". *PASP*, 116:859–875.
- Maíz Apellániz, J. (2010). "High-resolution imaging of Galactic massive stars with AstraLux. I. 138 fields with $\delta > -25$ deg.". *A&A*, 518:A1.
- Maíz Apellániz, J. (2013a). "A multipurpose 3-D grid of stellar models". *Highlights of Spanish Astrophysics VII*; eds. Guirado, J. C. and Lara, L. M. and Quilis, V. and Gorgas, J., page 657.
- Maíz Apellániz, J. (2013b). "Do we need a new family of optical-NIR extinction laws?". *Highlights of Spanish Astrophysics VII*; eds. Guirado, J. C. and Lara, L. M. and Quilis, V. and Gorgas, J., pages 583–589.
- Markwardt, C. B. (2009). "Non-linear Least-squares Fitting in IDL with MPFIT". *Astronomical Society of the Pacific Conference Series, Bohlender, D. A. and Durand, D. and Dowler, P.*, arXiv 0902.2850:251.
- Martinache, F. (2010). "Kernel Phase in Fizeau Interferometry". *ApJ*, 724:464–469.

- Martinache, F. (2011). "Kernel-phases for high-contrast detection beyond the resolution limit". *Society of Photo-Optical Instrumentation Engineers (SPIE) Conference Series*, 8151:11.
- Martinache, F. (2014). "Kernel-phase for interferometry with a rich aperture". *Improving the Performances of Current Optical Interferometers Future Designs*, eds: Arnold, L. and Le Coroller, H. and Surdej, J., (235-244).
- Martins, F., Schaerer, D., and Hillier, D. J. (2005). "A new calibration of stellar parameters of Galactic O stars". *A&A*, 436:1049–1065.
- Mason, B. D., Hartkopf, W. I., Gies, D. R., Henry, T. J., and Helsel, J. W. (2009). "The High Angular Resolution Multiplicity of Massive Stars". *AJ*, 137:3358–3377.
- Mathis, J. S. (1990). "Interstellar dust and extinction". *ARA&A*, 28:37–70.
- Mathis, J. S., Rumpl, W., and Nordsieck, K. H. (1977). "The size distribution of interstellar grains". *ApJ*, 217:425–433.
- McKee, C. F. and Tan, J. C. (2002). "Massive star formation in 100,000 years from turbulent and pressurized molecular clouds". *Nature*, 416:59–61.
- Millan-Gabet, R., Schloerb, F. P., and Traub, W. A. (2001). "Spatially Resolved Circumstellar Structure of Herbig AE/BE Stars in the Near-Infrared". *ApJ*, 546:358–381.
- Moeckel, N. and Bally, J. (2007). "Capture-formed Binaries via Encounters with Massive Protostars". *ApJ*, 656(275-286).
- Mohamed, S., Mackey, J., and Langer, N. (2012). "3D simulations of Betelgeuse's bow shock". *A&A*, 541:A1.
- Monin, J.-L., Clarke, C. J., Prato, L., and McCabe, C. (2007). "Disk Evolution in Young Binaries: From Observations to Theory". *Protostars and Planets V*, pages 395–409.
- Monnier, J. D. (2003). "Optical interferometry in astronomy". *Reports on Progress in Physics: astro-ph/0307036*, 66:789–857.
- Monnier, J. D. and Allen, R. J. (2013). "Radio and Optical Interferometry: Basic Observing Techniques and Data Analysis". *Planets, Stars and Stellar Systems*, by Oswald, Terry D.; Bond, Howard E., ISBN 978-94-007-5617-5. Springer Science+Business Media Dordrecht, 2013, p. 325, page 325.
- Monnier, J. D., Berger, J.-P., Le Bouquin, J.-B., Tuthill, P. G., Wittkowski, M., Grellmann, R., Müller, A., Renganswany, S., Hummel, C., Hofmann, K.-H., Schertl, D., Weigelt, G., Young, J., Buscher, D., Sanchez-Bermudez, J., Alberdi, A., Schoedel, R., Köhler, R., Soulez, F., Thiébaud, É., Kluska, J., Malbet, F., Duvert, G., Kraus, S., Kloppenborg, B. K., Baron, F., de Wit, W.-J., Rivinius, T., and Merand, A. (2014). "The 2014

- interferometric imaging beauty contest". *Society of Photo-Optical Instrumentation Engineers (SPIE) Conference Series*, 9146:1.
- Monnier, J. D. and Millan-Gabet, R. (2002). "On the Interferometric Sizes of Young Stellar Objects". *ApJ*, 579:694–698.
- Monnier, J. D., Tuthill, P. G., Lopez, B., Cruzalebes, P., Danchi, W. C., and Haniff, C. A. (1999). "The Last Gasp of VY Canis Majoris: Aperture Synthesis and Adaptive Optics Imagery". *ApJ*, 512:351–361.
- Monnier, J. D., Zhao, M., Pedretti, E., Thureau, N., Ireland, M., Muirhead, P., Berger, J.-P., Millan-Gabet, R., Van Belle, G., ten Brummelaar, T., McAlister, H., Ridgway, S., Turner, N., Sturmman, L., Sturmman, J., and Berger, D. (2007). "Imaging the Surface of Altair". *Science*, 317:342.
- Mužić, K., Eckart, A., Schödel, R., Buchholz, R., Zamaninasab, M., and Witzel, G. (2010). "Comet-shaped sources at the Galactic center. Evidence of a wind from the central 0.2 pc". *A&A*, 521:A13.
- Mužić, K., Eckart, A., Schödel, R., Meyer, L., and Zensus, A. (2007). "First proper motions of thin dust filaments at the Galactic center". *A&A*, 469:993–1002.
- Najarro, F., Hillier, D. J., Kudritzki, R. P., Krabbe, A., Genzel, R., Lutz, D., Drapatz, S., and Geballe, T. R. (1994). "The nature of the brightest galactic center HeI emission line star". *A&A*, 285:573–584.
- Narayan, R. and Nityananda, R. (1986). "Maximum entropy image restoration in astronomy". *ARA&A*, 24:127–170.
- Niemela, V. S. and Gamen, R. C. (2005). "The nearest star of spectral type O3: a component of the multiple system HD 150136". *MNRAS*, 356:974–978.
- Nürnberger, D. E. A. (2003). "Infrared observations of NGC 3603. III. The enigmatic, highly reddened sources of IRS 9". *A&A*, 404:255–265.
- Nürnberger, D. E. A. (2008). "High mass star formation to the extremes: NGC 3603 at high angular resolution in the near-infrared". *Journal of Physics Conference Series*, 131(1):012025.
- Ott, T., Eckart, A., and Genzel, R. (1999). "Variable and Embedded Stars in the Galactic Center". *ApJ*, 523:248–264.
- Paresce, F. (1996). "Science with the VLT Interferometer". *Proceedings of the ESO workshop held at Garching, Germany, 18-21 June 1996*, pages 13–34.
- Pauls, T. A., Young, J. S., Cotton, W. D., and Monnier, J. D. (2005). "A Data Exchange Standard for Optical (Visible/IR) Interferometry". *PASP*, 117:1255–1262.

- Paumard, T., Genzel, R., Martins, F., Nayakshin, S., Beloborodov, A. M., Levin, Y., Trippe, S., Eisenhauer, F., Ott, T., Gillessen, S., Abuter, R., Cuadra, J., Alexander, T., and Sternberg, A. (2006). "The Two Young Star Disks in the Central Parsec of the Galaxy: Properties, Dynamics, and Formation". *ApJ*, 643:1011–1035.
- Paumard, T., Maillard, J.-P., and Morris, M. (2004). "Kinematic and structural analysis of the Minispiral in the Galactic Center from BEAR spectro-imagery". *A&A*, 426:81–96.
- Penny, L. R., Gies, D. R., Hartkopf, W. I., Mason, B. D., and Turner, N. H. (1993). "The frequency of binary stars in the young cluster Trumpler 14". *PASP*, 105:588–594.
- Perrin, G., Lacour, S., Woillez, J., and Thiébaud, É. (2007). "High dynamic range imaging by pupil single-mode filtering and remapping". *MNRAS*, 373:747–751.
- Perrin, M. D., Soummer, R., Elliott, E. M., Lallo, M. D., and Sivaramakrishnan, A. (2012). "Simulating point spread functions for the James Webb Space Telescope with WebbPSF". *Society of Photo-Optical Instrumentation Engineers (SPIE) Conference Series*, 8442:3.
- Peterson, D. M., Hummel, C. A., Pauls, T. A., Armstrong, J. T., Benson, J. A., Gilbreath, G. C., Hindsley, R. B., Hutter, D. J., Johnston, K. J., Mozurkewich, D., and Schmitt, H. R. (2006). "Vega is a rapidly rotating star". *Nature*, 440:896–899.
- Petrov, R. G., Malbet, F., Weigelt, G., Antonelli, P., Beckmann, U., Bresson, Y., Chelli, A., Dugué, M., Duvert, G., Gennari, S., Glück, L., Kern, P., Lagarde, S., Le Coarer, E., Lisi, F., Millour, F., Perraut, K., Puget, P., Rantakyö, F., Robbe-Dubois, S., Roussel, A., Salinari, P., Tatulli, E., Zins, G., Accardo, M., Acke, B., Agabi, K., Altariba, E., Arezki, B., Aristidi, E., Baffa, C., Behrend, J., Blöcker, T., Bonhomme, S., Busoni, S., Cas-saing, F., Clause, J.-M., Colin, J., Connot, C., Delboulbé, A., Domiciano de Souza, A., Driebe, T., Feautrier, P., Ferruzzi, D., Forveille, T., Fossat, E., Foy, R., Fraix-Burnet, D., Gallardo, A., Giani, E., Gil, C., Glentzlin, A., Heiden, M., Heininger, M., Hernandez Utrera, O., Hofmann, K.-H., Kamm, D., Kiekebusch, M., Kraus, S., Le Contel, D., Le Contel, J.-M., Lesourd, T., Lopez, B., Lopez, M., Magnard, Y., Marconi, A., Mars, G., Martinot-Lagarde, G., Mathias, P., Mège, P., Monin, J.-L., Mouillet, D., Mourard, D., Nussbaum, E., Ohnaka, K., Pacheco, J., Perrier, C., Rabbia, Y., Rebattu, S., Reynaud, F., Richichi, A., Robini, A., Sacchetti, M., Schertl, D., Schöller, M., Solscheid, W., Spang, A., Stee, P., Stefanini, P., Tallon, M., Tallon-Bosc, I., Tasso, D., Testi, L., Vakil, E., von der Lühe, O., Valtier, J.-C., Vannier, M., and Ventura, N. (2007). "AMBER, the near-infrared spectro-interferometric three-telescope VLT instrument". *A&A*, 464:1–12.
- Pontoppidan, K. M., Blake, G. A., and Smette, A. (2011). "The Structure and Dynamics of Molecular Gas in Planet-forming Zones: A CRIRES Spectro-astrometric Survey". *ApJ*, 733:84.

- Pontoppidan, K. M., Blake, G. A., van Dishoeck, E. F., Smette, A., Ireland, M. J., and Brown, J. (2008). "Spectroastrometric Imaging of Molecular Gas within Protoplanetary Disk Gaps". *ApJ*, 684:1323–1329.
- Pope, B., Martinache, E., and Tuthill, P. (2013). "Dancing in the Dark: New Brown Dwarf Binaries from Kernel Phase Interferometry". *ApJ*, 767:110.
- Poveda, A., Ruiz, J., and Allen, C. (1967). "Run-away Stars as the Result of the Gravitational Collapse of Proto-stellar Clusters". *Boletín de los Observatorios Tonantzintla y Tacubaya*, (4):86–90.
- Prinja, R. K., Barlow, M. J., and Howarth, I. D. (1990). "Terminal velocities for a large sample of O stars, B supergiants, and Wolf-Rayet stars". *ApJ*, 361:607–620.
- Quirrenbach, A., Mozurkewich, D., Buscher, D. F., Hummel, C. A., and Armstrong, J. T. (1996). "Angular diameter and limb darkening of Arcturus.". *A&A*, 312(160-166).
- Rauch, C., Mužić, K., Eckart, A., Buchholz, R. M., García-Marín, M., Sabha, N., Straubmeier, C., Valencia-S., M., and Yazici, S. (2013). "A peek behind the dusty curtain: K_S-band polarization photometry and bow shock models of the Galactic center source IRS 8". *A&A*, 551:A35.
- Readhead, A. C. S., Nakajima, T. S., Pearson, T. J., Neugebauer, G., Oke, J. B., and Sargent, W. L. W. (1988). "Diffraction-limited imaging with ground-based optical telescopes". *AJ*, 95:1278–1296.
- Reipurth, B. and Zinnecker, H. (1993). "Visual binaries among pre-main sequence stars". *A&A*, 278:81–108.
- Rieke, G. H. and Low, F. J. (1973). "Infrared maps of the galactic nucleus.". *ApJ*, 184:415–425.
- Rivilla, V. M., Jiménez-Serra, I., Martín-Pintado, J., and Sanz-Forcada, J. (2013a). "The role of low-mass star clusters in forming the massive stars in DR 21". *MNRAS*, 437:1561–1575.
- Rivilla, V. M., Martín-Pintado, J., Jiménez-Serra, I., and Rodríguez-Franco, A. (2013b). "The role of low-mass star clusters in massive star formation. The Orion case". *A&A*, 554:A48.
- Robitaille, T. P. (2011). "HYPERION: an open-source parallelized three-dimensional dust continuum radiative transfer code". *A&A*, 536:A79.
- Robitaille, T. P., Whitney, B. A., Indebetouw, R., and Wood, K. (2007). "Interpreting Spectral Energy Distributions from Young Stellar Objects. II. Fitting Observed SEDs Using a Large Grid of Precomputed Models". *ApJS*, 169:328–352.

- Robitaille, T. P., Whitney, B. A., Indebetouw, R., Wood, K., and Denzmore, P. (2006). "Interpreting Spectral Energy Distributions from Young Stellar Objects. I. A Grid of 200,000 YSO Model SEDs". *ApJS*, 167:256–285.
- Roddier, F. (1986). "Triple correlation as a phase closure technique". *Optics Communications*, 60:145–148.
- Roddier, F. (2004). "Adaptive Optics in Astronomy". *Adaptive Optics in Astronomy, Edited by François Roddier, pp. 419. ISBN 0521612144. Cambridge, UK: Cambridge University Press, November 2004.*
- Rogers, A. E. E., Doeleman, S., Wright, M. C. H., Bower, G. C., Backer, D. C., Padin, S., Phillips, J. A., Emerson, D. T., Greenhill, L., Moran, J. M., and Kellermann, K. I. (1994). "Small-scale structure and position of Sagittarius A(*) from VLBI at 3 millimeter wavelength". *ApJ*, 434:L59–L62.
- Rudin, L. I., Osher, S., and Fatemi, E. (1992). "Nonlinear total variation based boise removal algorithms". *PhysicaD*, 60:259–268.
- Sana, H., de Mink, S. E., de Koter, A., Langer, N., Evans, C. J., Gieles, M., Gosset, E., Izard, R. G., Le Bouquin, J.-B., and Schneider, F. R. N. (2012). "Binary Interaction Dominates the Evolution of Massive Stars". *Science*, 337:444.
- Sana, H. and Evans, C. J. (2011). "The multiplicity of massive stars". *IAU Symposium, eds. Neiner, C. and Wade, G. and Meynet, G. and Peters, G. , 272:474–485.*
- Sana, H., Gosset, E., and Evans, C. J. (2009). "The massive star binary fraction in young open clusters - II. NGC6611 (Eagle Nebula)". *MNRAS*, 400:1479–1492.
- Sana, H., Gosset, E., Nazé, Y., Rauw, G., and Linder, N. (2008). "The massive star binary fraction in young open clusters - I. NGC 6231 revisited". *MNRAS*, 386:447–460.
- Sana, H., Gosset, E., and Rauw, G. (2006). "The OB binary HD152219: a detached, double-lined, eclipsing system". *MNRAS*, 371:67–80.
- Sana, H., James, G., and Gosset, E. (2011). "The massive star binary fraction in young open clusters - III. IC 2944 and the Cen OB2 association". *MNRAS*, 416:817–831.
- Sana, H., Le Bouquin, J.-B., Lacour, S., Berger, J.-P., Duvert, G., Gauchet, L., Norris, B., Olofsson, J., Pickel, D., Zins, G., Absil, O., de Koter, A., Kratter, K., Schnurr, O., and Zinnecker, H. (2014). "Southern Massive Stars at High Angular Resolution: Observational Campaign and Companion Detection". *ApJS*, 215:15.
- Sana, H., Le Bouquin, J.-B., Mahy, L., Absil, O., De Becker, M., and Gosset, E. (2013). "Three-dimensional orbits of the triple-O stellar system HD 150136". *A&A*, 553:A131.

- Sanchez-Bermudez, J., Alberdi, A., Schödel, R., Hummel, C. A., Arias, J. I., Barbá, R. H., Maíz Apellániz, J., and Pott, J.-U. (2014a). "Resolving the stellar components of the massive multiple system Herschel 36 with AMBER/VLTI". *A&A*, 572:L1.
- Sanchez-Bermudez, J., Hummel, C. A., Tuthill, P., Alberdi, A., Schödel, R., and Lacour, S. (2014b). "Unveiling the near-infrared structure of the massive-young stellar object NGC 3603 IRS 9A with sparse aperture masking and spectroastrometry". *ArXiv e-prints: 1409.2831*.
- Sanchez-Bermudez, J., Schödel, R., Alberdi, A., Barbá, R. H., Hummel, C. A., Maíz Apellániz, J., and Pott, J.-U. (2013). "Direct detection of the tertiary component in the massive multiple HD 150136 with VLTI". *A&A*, 554:L4.
- Sanchez-Bermudez, J., Schödel, R., Alberdi, A., Muzić, K., Hummel, C. A., and Pott, J.-U. (2014c). "Properties of bow-shock sources at the Galactic center". *A&A*, 567:A21.
- Sánchez-Monge, Á., Cesaroni, R., Beltrán, M. T., Kumar, M. S. N., Stanke, T., Zinnecker, H., Etoke, S., Galli, D., Hummel, C. A., Moscadelli, L., Preibisch, T., Ratzka, T., van der Tak, F. F. S., Vig, S., Walmsley, C. M., and Wang, K.-S. (2013). "A candidate circumbinary Keplerian disk in G35.20-0.74 N: A study with ALMA". *A&A*, 552:L10.
- Schertl, D., Balega, Y. Y., Preibisch, T., and Weigelt, G. (2003). "Orbital motion of the massive multiple stars in the Orion Trapezium". *A&A*, 402:267–275.
- Schödel, R., Merritt, D., and Eckart, A. (2009). "The nuclear star cluster of the Milky Way: proper motions and mass". *A&A*, 502:91–111.
- Schödel, R., Najarro, F., Muzic, K., and Eckart, A. (2010). "Peering through the veil: near-infrared photometry and extinction for the Galactic nuclear star cluster. Accurate near infrared H, Ks, and L' photometry and the near-infrared extinction-law toward the central parsec of the Galaxy". *A&A*, 511:A18.
- Schödel, R., Ott, T., Genzel, R., Eckart, A., Mouawad, N., and Alexander, T. (2003). "Stellar Dynamics in the Central Arcsecond of Our Galaxy". *ApJ*, 596:1015–1034.
- Schödel, R., Ott, T., Genzel, R., Hofmann, R., Lehnert, M., Eckart, A., Mouawad, N., Alexander, T., Reid, M. J., Lenzen, R., Hartung, M., Lacombe, F., Rouan, D., Gendron, E., Rousset, G., Lagrange, A.-M., Brandner, W., Ageorges, N., Lidman, C., Moorwood, A. F. M., Spyromilio, J., Hubin, N., and Menten, K. M. (2002). "A star in a 15.2-year orbit around the supermassive black hole at the centre of the Milky Way". *Nature*, 419:694–696.
- Schödel, R., Yelda, S., Ghez, A., Girard, J. H., Labadie, L., Rebolo, R., Pérez-Garrido, A., and Morris, M. R. (2013). "Holographic imaging of crowded fields: high angular resolution imaging with excellent quality at very low cost". *MNRAS*, 429:1367–1375.

- Schutz, A., Ferrari, A., Mary, D., Soulez, F., Thiébaud, É., and Vannier, M. (2014). "PAINTER: a spatio-spectral image reconstruction algorithm for optical interferometry". *ArXiv e-prints: 1407.1885*.
- Schutz, A., Ferrari, A., Mary, D., Thiébaud, E., and Soulez, F. (2015). "Large Scale 3D Image Reconstruction in Optical Interferometry". *ArXiv e-prints: 1503.01565*.
- Schwarz, U. J. (1978). "Mathematical-statistical Description of the Iterative Beam Removing Technique (Method CLEAN)". *A&A*, 65:345.
- Seifried, D., Banerjee, R., Klessen, R. S., Duffin, D., and Pudritz, R. E. (2011). "Magnetic fields during the early stages of massive star formation - I. Accretion and disc evolution". *MNRAS*, 417:1054–1073.
- Seifried, D., Banerjee, R., Klessen, R. S., Duffin, D., and Pudritz, R. E. (2012). "Erratum: Magnetic fields during the early stages of massive star formation - I. Accretion and disc evolution". *MNRAS*, 425:1598–1599.
- Shao, M., Colavita, M. M., Hines, B. E., Staelin, D. H., Hutter, D. J., Johnston, K. J., Mozurkewich, D., Simon, R. S., Hershey, J. L., Hughes, J. A., and Kaplan, G. H. (1988). "The Mark III stellar interferometer". *A&A*, 193:357–371.
- Sivaramakrishnan, A., Cheetham, A., Greenbaum, A. Z., Tuthill, P. G., Acton, D. S., Pope, B., Martinache, F., Thatte, D., and Nelan, E. P. (2014). "Non-redundant masking ideas on JWST". *Society of Photo-Optical Instrumentation Engineers (SPIE) Conference Series*, 9143:3.
- Skilling, J. and Bryan, R. K. (1984). "Maximum Entropy Image Reconstruction - General Algorithm". *MNRAS*, 211:111.
- Skrutskie, M. F., Cutri, R. M., Stiening, R., Weinberg, M. D., Schneider, S., Carpenter, J. M., Beichman, C., Capps, R., Chester, T., Elias, J., Huchra, J., Liebert, J., Lonsdale, C., Monet, D. G., Price, S., Seitzer, P., Jarrett, T., Kirkpatrick, J. D., Gizis, J. E., Howard, E., Evans, T., Fowler, J., Fullmer, L., Hurt, R., Light, R., Kopan, E. L., Marsh, K. A., McCallon, H. L., Tam, R., Van Dyk, S., and Wheelock, S. (2006). "The Two Micron All Sky Survey (2MASS)". *AJ*, 131:1163–1183.
- Smith, M. D. (1995). "Predictions for JHK photometry of molecular shocks.". *A&A*, 296:789.
- Smith, R. J., Longmore, S., and Bonnell, I. (2009). "The simultaneous formation of massive stars and stellar clusters". *MNRAS*, 400:1775–1784.
- Sota, A., Maíz Apellániz, J., Morrell, N. I., Barbá, R. H., Walborn, N. R., Gamen, R. C., Arias, J. I., and Alfaro, E. J. (2014). "The Galactic O-Star Spectroscopic Survey (GOSSS). II. Bright Southern Stars". *ApJS*, 211:10.

- Takami, M., Bailey, J., and Chrysostomou, A. (2003). "A spectro-astrometric study of southern pre-main sequence stars. Binaries, outflows, and disc structure down to AU scales". *A&A*, 397:675–691.
- Tallon-Bosc, I., Tallon, M., Thiébaud, E., Béchet, C., Mella, G., Lafrasse, S., Chesneau, O., Domiciano de Souza, A., Duvert, G., Mourard, D., Petrov, R., and Vannier, M. (2008). "LITpro: a model fitting software for optical interferometry". *Society of Photo-Optical Instrumentation Engineers (SPIE) Conference Series*; 10.1117/12.788871, 7013:70131J.
- Tanner, A., Ghez, A. M., Morris, M., Becklin, E. E., Cotera, A., Ressler, M., Werner, M., and Wizinowich, P. (2002). "Spatially Resolved Observations of the Galactic Center Source IRS 21". *ApJ*, 575:860–870.
- Tanner, A., Ghez, A. M., Morris, M. R., and Christou, J. C. (2005). "Stellar Bow Shocks in the Northern Arm of the Galactic Center: More Members and Kinematics of the Massive Star Population". *ApJ*, 624:742–750.
- Tatulli, E., Millour, F., Chelli, A., Duvert, G., Acke, B., Hernandez Utrera, O., Hofmann, K.-H., Kraus, S., Malbet, F., Mège, P., Petrov, R. G., Vannier, M., Zins, G., Antonelli, P., Beckmann, U., Bresson, Y., Dugué, M., Gennari, S., Glück, L., Kern, P., Lagarde, S., Le Coarer, E., Lisi, F., Perraut, K., Puget, P., Rantakyö, F., Robbe-Dubois, S., Rousset, A., Weigelt, G., Accardo, M., Agabi, K., Altariba, E., Arezki, B., Aristidi, E., Baffa, C., Behrend, J., Blöcker, T., Bonhomme, S., Busoni, S., Cassaing, F., Clause, J.-M., Colin, J., Connot, C., Delboulbé, A., Domiciano de Souza, A., Driebe, T., Feautrier, P., Ferruzzi, D., Forveille, T., Fossat, E., Foy, R., Fraix-Burnet, D., Gallardo, A., Giani, E., Gil, C., Glentzlin, A., Heiden, M., Heininger, M., Kamm, D., Kiekebusch, M., Le Contel, D., Le Contel, J.-M., Lesourd, T., Lopez, B., Lopez, M., Magnard, Y., Marconi, A., Mars, G., Martinot-Lagarde, G., Mathias, P., Monin, J.-L., Mouillet, D., Mourard, D., Nussbaum, E., Ohnaka, K., Pacheco, J., Perrier, C., Rabbia, Y., Rebattu, S., Reynaud, F., Richichi, A., Robini, A., Sacchettini, M., Schertl, D., Schöller, M., Solscheid, W., Spang, A., Stee, P., Stefanini, P., Tallon, M., Tallon-Bosc, I., Tasso, D., Testi, L., Vakili, F., von der Lühe, O., Valtier, J.-C., and Ventura, N. (2007). "Interferometric data reduction with AMBER/VLTI. Principle, estimators, and illustration". *A&A*, 464:29–42.
- Thiébaud, E. (2002). "Optimization issues in blind deconvolution algorithms". *Astronomical Data Analysis II*; eds: Starck, J.-L. and Murtagh, F. D., 4847:174–183.
- Thiébaud, E. (2008). "MIRA: an effective imaging algorithm for optical interferometry". *Society of Photo-Optical Instrumentation Engineers (SPIE) Conference Series*, 7013:1.
- Thiébaud, E. (2009). "Image reconstruction with optical interferometers". *New A Rev.*, 53:312–328.

- Thiébaud, É. (2013). "Principles of Image Reconstruction in Interferometry", volume 59. EAS Publications Series.
- Thiébaud, E. and Giovannelli, J.-F. (2010). "Image reconstruction in optical interferometry". *IEEE Signal Processing Magazine*, 27:97–109.
- Thompson, A. R., Moran, J. M., and Swenson, Jr., G. W. (2001). "Interferometry and Synthesis in Radio Astronomy, 2nd Edition". *Interferometry and synthesis in radio astronomy by A. Richard Thompson, James M. Moran, and George W. Swenson, Jr. 2nd ed. New York : Wiley, c2001.xxiii, 692 p. : ill. ; 25 cm. "A Wiley-Interscience publication." Includes bibliographical references and indexes. ISBN : 0471254924*".
- Tikhonov, A. N. and Arsenin, V. Y. (1977). "Solutions of Ill-Posed Problems". *Mathematics for computation*, 32:1320–1322.
- Tuthill, P., Lacour, S., Amico, P., Ireland, M., Norris, B., Stewart, P., Evans, T., Kraus, A., Lidman, C., Pompei, E., and Kornweibel, N. (2010). "Sparse aperture masking (SAM) at NAOS/CONICA on the VLT". *Society of Photo-Optical Instrumentation Engineers (SPIE) Conference Series*, 7735:1.
- Tuthill, P., Lloyd, J., Ireland, M., Martinache, F., Monnier, J., Woodruff, H., ten Brummelaar, T., Turner, N., and Townes, C. (2006). "Sparse-aperture adaptive optics". *Society of Photo-Optical Instrumentation Engineers (SPIE) Conference Series*, 6272:10.1117/12.672342.
- Tuthill, P. G. (2012). "The unlikely rise of masking interferometry: leading the way with 19th century technology". *Society of Photo-Optical Instrumentation Engineers (SPIE) Conference Series*, 8445:2.
- Tuthill, P. G., Monnier, J. D., and Danchi, W. C. (2000). "Aperture masking interferometry on the Keck I Telescope: new results from the diffraction limit". *Society of Photo-Optical Instrumentation Engineers (SPIE) Conference Series, Léna, P. and Quirrenbach, A.*, 4006:491–498.
- Tuthill, P. G., Monnier, J. D., Lawrance, N., Danchi, W. C., Owocki, S. P., and Gayley, K. G. (2008). "The Prototype Colliding-Wind Pinwheel WR 104". *ApJ*, 675:698–710.
- Ulrich, R. K. (1976). "An infall model for the T Tauri phenomenon". *ApJ*, 210:377–391.
- Vaidya, B., Fendt, C., and Beuther, H. (2009). "Accretion Disks Around Massive Stars: Hydrodynamic Structure, Stability, and Dust Sublimation". *ApJ*, 702:567–579.
- van Boekel, R., Min, M., Leinert, C., Waters, L. B. F. M., Richichi, A., Chesneau, O., Dominik, C., Jaffe, W., Dutrey, A., Graser, U., Henning, T., de Jong, J., Köhler, R., de Koter, A., Lopez, B., Malbet, F., Morel, S., Paresce, F., Perrin, G., Preibisch, T., Przygodda, F., Schöller, M., and Wittkowski, M. (2004). "The building blocks of planets within the 'terrestrial' region of protoplanetary disks". *Nature*, 432:479–482.

- van Buren, D. and McCray, R. (1988). "Bow shocks and bubbles are seen around hot stars by IRAS". *ApJ*, 329:L93–L96.
- Vehoff, S., Hummel, C. A., Monnier, J. D., Tuthill, P., Nürnberger, D. E. A., Siebenmorgen, R., Chesneau, O., and Duschl, W. J. (2010). "Mid-infrared interferometry of the massive young stellar object NGC 3603 - IRS 9A". *A&A*, 520:A78.
- Viehmann, T., Eckart, A., Schödel, R., Pott, J.-U., and Moutaka, J. (2006). "Dusty Sources at the Galactic Center the N- and Q-Band Views with VISIR". *ApJ*, 642:861–867.
- Vollmer, B. and Duschl, W. J. (2000). "The Minispiral in the Galactic Center revisited". *New A*, 4:581–590.
- Weigelt, G. P. (1977). "Modified astronomical speckle interferometry 'speckle masking'". *Optics Communications*, 21:55–59.
- Wheelwright, H. E., de Wit, W. J., Weigelt, G., Oudmaijer, R. D., and Ilee, J. D. (2012). "AMBER and CRIRES observations of the binary sgB[e] star HD 327083: evidence of a gaseous disc traced by CO bandhead emission". *A&A*, 543:A77.
- Wheelwright, H. E., Oudmaijer, R. D., de Wit, W. J., Hoare, M. G., Lumsden, S. L., and Urquhart, J. S. (2010). "Probing discs around massive young stellar objects with CO first overtone emission". *MNRAS*, (408):1840–1850.
- Whelan, E. and Garcia, P. (2008). "Spectro-astrometry: The Method, its Limitations, and Applications". *Jets from Young Stars II, Bacciotti, F. and Testi, L. and Whelan, E.*, 742:123.
- Whitney, B. A., Wood, K., Bjorkman, J. E., and Cohen, M. (2003). "Two-dimensional Radiative Transfer in Protostellar Envelopes. II. An Evolutionary Sequence". *ApJ*, 598:1079–1099.
- Wilkin, F. P. (1996). "Exact Analytic Solutions for Stellar Wind Bow Shocks". *ApJ*, 459:L31.
- Wolfire, M. G. and Konigl, A. (1991). "Molecular line emission models of Herbig-Haro objects. I - H₂ emission". *ApJ*, 383:205–225.
- Yelda, S., Ghez, A. M., Lu, J. R., Do, T., Clarkson, W., and Matthews, K. (2011). "Increasing the Scientific Return of Stellar Orbits at the Galactic Center". *The Galactic Astronomical Society of the Pacific Conference Series*, ed. Morris, M. R., Wang, Q. D., Yuan, E, 439:167.
- Yelda, S., Ghez, A. M., Lu, J. R., Do, T., Meyer, L., Morris, M. R., and Matthews, K. (2014). "Properties of the Remnant Clockwise Disk of Young Stars in the Galactic Center". *ApJ*, 783:131.

- Yorke, H. W. and Sonnhalter, C. (2002). "On the Formation of Massive Stars". *ApJ*, 569:846–862.
- Zhang, Q. and Zheng, X. (1997). "The Role of Bow Shocks in Bipolar Molecular Outflows". *ApJ*, 474:719–723.
- Zhao, J.-H., Morris, M. R., Goss, W. M., and An, T. (2009). "Dynamics of Ionized Gas at the Galactic Center: Very Large Array Observations of the Three-dimensional Velocity Field and Location of the Ionized Streams in Sagittarius A West". *ApJ*, 699:186–214.
- Zimmerman, N., Sivaramakrishnan, A., Bernat, D., Oppenheimer, B. R., Hinkley, S., Lloyd, J. P., Tuthill, P. G., Brenner, D., Parry, I. R., Simon, M., Krist, J. E., and Pueyo, L. (2012). "Aperture mask interferometry with an integral field spectrograph". *Society of Photo-Optical Instrumentation Engineers (SPIE) Conference Series*, 8445:2.
- Zinnecker, H. and Bate, M. R. (2002). "Multiplicity of Massive Stars – a Clue to their Origin?". *Hot Star Workshop III: The Earliest Phases of Massive Star Birth*; eds. Crowther, P, 267:209.
- Zinnecker, H. and Yorke, H. W. (2007). "Toward Understanding Massive Star Formation",. *ARA&A*, 45:481–563.